High Fidelity Simulations of Optical Waveguides for Optical Frequency Conversion and Frequency Combs

Yixuan Zhu

Submitted in fulfilment of the requirements for the
Degree of Doctor of Philosophy

School of Engineering
College of Science and Engineering
University of Glasgow

June 2018

Abstract

Conventional silicon-based electronics have developed dramatically in recent years; however, their optimum integration level is reaching its limits. To meet the requirements of dealing with this explosion of data, opto-electronic integrated circuits have provided a way out. Optical waveguides are crucial components which can be applied in opto-electronic integrated circuits to achieve specific functionalities, such as frequency conversion and frequency combs. Frequency conversion offers the possibility of converting the frequency components generated by lasers to a previously inaccessible frequency region in order to extend the application fields, such as gas sensing and optical communications. A frequency comb is a series of equally spaced frequency components, which could be utilized for frequency standards and optical clocks.

This thesis has simulated frequency mixing processes, including second-harmonic generation and four-wave mixing in the optical waveguides based on second- and third-order nonlinearities in order to realize frequency conversion and generation of frequency combs. The focus of this thesis are silicon-based and AlGaAs waveguides because of their particular material characteristics. Silicon is the base of electronic devices so that silicon-based waveguides are complementary metal-oxide-semiconductor compatible and can be integrated with other electronic elements on a single chip. AlGaAs is a direct-band gap semi-conductor and has a small two-photon-absorption co-efficient. Both silicon and AlGaAs have a high refractive index and ensure the confinement of modes in waveguides. In addition, both have strong nonlinearity, leading to efficient nonlinear interactions and significant frequency mixing processes.

This method of simulation was based on the finite-difference time-domain algorithm, incorporating linear dispersion and nonlinearity. Material dispersion was described as Lorentz medium and incorporated through Sellmeier equations. Geometric dispersion was taken into account in mode solver, which was applied in order to produce the fundamental modes for excitation sources. Second- and third-order nonlinearities (including Kerr-nonlinearity and Raman scattering) were incorporated with a piecewise linear recursive convolution method, which was solved by the Newton-Raphson method. In addition, a perfectly matched layer absorbing boundary condition and circular boundary condition were designed in the

simulations. Programs were written in Fortran 95 and parallel computation was applied to improve the efficiency.

This thesis has simulated four-wave mixing of five optical waveguides: GaAs suspended waveguide, deep-etched multi-layer $Al_{0.25}Ga_{0.75}As$ waveguide, $Al_{0.3}Ga_{0.7}As$ -on-insulator waveguide, silicon-on-insulator waveguide and silicon nitride-on-insulator waveguide. Phase matching conditions and phase mismatch factors were discussed for these waveguides. The results of four-wave mixing were observed when the phase matching conditions were satisfied. In deep-etched multi-layer $Al_{0.25}Ga_{0.75}As$ waveguide, Raman scattering was incorporated and the results of simulation showed a good match with experimental data. This thesis has also simulated second-harmonic generation of highly birefringent AlGaAs waveguide. Type-I phase matching condition was achieved so that efficient second-harmonic generation was obtained.

Table of Contents

List of Tables

List of Figures

Acknowledgement

I would like to express my deepest appreciation to my supervisor Professor David C. Hutchings for his patient guidance and continual encouragement. I knew little about this project at the beginning and I had never used MATLAB, Wolfram Methematica, Fortran 95 and HPC before. He, very kindly, explained everything to me and described the goal with patience. I would never have finished my PhD without his advice and support.

My sincere appreciation is extended to Professor Marc Sorel and his PhD student Stuart May. They offered design ideas for some optical waveguides, as well as the measurements in the experiments.

I would also like to express my gratitude to several HPC sources: Miffy and Buckethead (HPC at the University of Glasgow, a partner of ARCHIE-WeSt), Cirrus (EPCC at the University of Edinburgh) and ARCHIE-WeSt, for providing faster computations and saving run time.

Many thanks to my sponsor, the China Scholarship Council, for its three-year financial support.

Finally, this work is dedicated to my family and friends as a token of my deepest gratitude for their love, support and understanding.

Abbreviations

ABC	Absorbing Boundary Condition
BO	Born-Oppenheimer
BPM	Beam Propagation Method
CEM	Computational Electromagnetics
CFL	Courant–Friedrichs–Lewy
CFS	Complex Frequency-Shifted
CMOS	Complementary Metal-Oxide-Semiconductor
CPML	Convolution Perfectly Matched Layer
CW	Continuous-Wave
DDA	Discrete Dipole Approximation
DFG	Difference Frequency Generation
FCA	Free-Carrier-Absorption
FDM	Finite-Difference Method
FDTD	Finite-Difference Time-Domain
FEM	Finite Element Method
FFT	Fast Fourier Transform
FWHM	Full Width at Half Maximum
FWM	Four-Wave Mixing
GVD	Group Velocity Dispersion
GVM	Group Velocity Mismatch
HPC	High-Performance Computation
MoM	Method of Moments
OEICs	Optoelectronic Integrated Circuits
OpenMP	Open Multi-Processing
OPO	Optical Parametric Oscillator
PDE	Partial Differential Equations
PLRC	Piecewise Linear Recursive Convolution
PML	Perfectly Matched Layer
RC	Recursive Convolution
RCS	Radar Cross Section
SFG	Sum Frequency Generation
SHG	Second-Harmonic Generation

SOI	Silicon-on-Insulator
SPM	Self-Phase Modulation
TPA	Two-Photon-Absorption
VLSI	Very-Large-Scale Integration
XPM	Cross-Phase Modulation

Chapter 1

Introduction

1.1 Motivation

As part of the Information Age in which we now all live, the explosion of network and data has led to the rapid development of silicon-based electronics. However, the technology of very-large-scale integration circuits (VLSI) is approaching fundamental limits so that it is difficult to achieve smaller sizes and higher performance. Fortunately, optoelectronic integrated circuits (OEICs)[1] can complement the conventional silicon-based electronics, using light for communication rather than electrons. It is not confined by the limitations and makes possible faster computational speed and higher complexity[2].

In this thesis, there is a focus on the nonlinear effects of optical waveguides, which are treated as components of OEICs with specific functionalities. Different from bulks that can only propagate optical wave with high intensity in a short distance and depends on the beam, optical waveguides is capable of propagating high intensity through the whole length. This thesis aims to simulate the frequency-mixing processes of electromagnetic waves inside optical waveguides and to realize frequency conversion and generation of the frequency comb based on the second-order and third-order nonlinearities.

Given that not all the frequency components are accessible through lasers, frequency conversion is vital to convert accessible frequencies to the desired frequencies. Typical examples are super-continuum generation, parametric oscillation, Raman conversion, sum frequency generation (SFG), difference frequency generation (DFG) and second-harmonic generation (SHG), which is also known as frequency doubling. Frequency conversion provides a way to reach the new light sources and a variety of applications, such as gas sensing and optical communication.

A frequency comb is a laser source that can produce a sequence of discrete frequency components which are equally spaced. The description of frequency components in a frequency comb is as follows:

$$f_n = f_0 + nf_\gamma \qquad (n = 1, 2, 3, 4\ldots) \tag{1.1}$$

where f_0 is the carrier offset frequency; n is an integer; and f_γ is the spacing between comb tooth. Frequency combs have attracted attention and been developed since the 1990s. In 2005, two physicists - John L. Hall[3] and Theodor Wolfgang Hänsch[4] - were awarded one half of the Nobel Prize in Physics for "their contributions to the development of laser-based precision spectroscopy, including the optical frequency comb technique"[5]. There are several ways to generate a frequency comb which have been demonstrated in recent research such as four-wave mixing (FWM)[6]–[11], electro-optic modulation of a continuous-wave (CW) laser[12]–[14] and mode-locked laser[15][16]. Frequency combs became popular because of their attractive applications, where the comb needs to be widened to an octave to ensure the highest frequency in the spectrum at at least twice the lowest frequency.

One typical application of frequency combs is frequency standard[17]. It offers a fundamental frequency with great accuracy for reference or calibration. Therefore, time standard is also achieved based on the frequency standard and is applied in optical clocks[18]–[21], which provide greater precision and stability than normal cesium atomic clocks. Moreover, thanks to the development of the frequency comb, extreme precise laser spectroscopy[13][22] is possible. The previous measurements of spectroscopy limited the precision until the invention of the frequency comb synthesiser by Theodor Wolfgang Hänsch et al[4].

1.2 Introduction of optical waveguides

Optical waveguides are the structures that guide the electromagnetic wave in the optical spectrum and they have attracted an increasing amount of attention in the past two decades because of their optical properties, such as linear dispersion and certain nonlinear effects.

1.2.1 Silicon-on-insulator waveguide

Silicon-on-insulator (SOI) waveguide is a popular waveguide because silicon is a good choice as optical material for OEICs. Silicon has a mature low-cost fabrication technology and it is

transparent in the telecommunication wavelength range 1.3-1.7 μm. In addition, as the base of microelectronic chips, silicon provides the possibility of integrating silicon photonic devices and complementary metal-oxide-semiconductors (CMOS) on the same substrate[23]. Figure1.1 shows a basic structure of SOI strip waveguide, where the electromagnetic wave is mainly propagated in the silicon layer. SOI has shown a high refractive index contrast[24] between the silicon core layer and its oxide cladding layer, as well as the high mode confinement and large nonlinear co-efficient[25]. Much relevant research about frequency-mixing processes of SOI waveguide has been carried out in recent years, such as self-phase modulation (SPM)[26]–[29], cross-phase modulation (XPM)[30][31] , FWM[32]–[40], SFG[41], DFG[42][43] and SHG[44]–[46]. These have indicated that the SOI waveguide has a great potential for a range of applications: wavelength conversion based on FWM[32]–[40] and XPM[31], super-continuum generation[47]–[49], parametric amplifier[50] and de-multiplexing[51][52]. Some engineered SOI waveguides optimize the group velocity dispersion (GVD) in order to satisfy phase matching conditions and improve conversion efficiency[53][54] or to find the balance between nonlinear effects and linear dispersion to generate soliton[55][56], which is known as dispersion-free propagation.

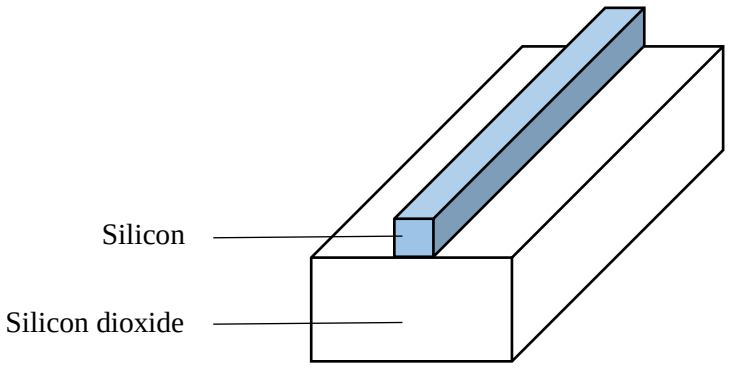

Fig. 1.1 Structure of SOI strip waveguide.

However, silicon has two great limitations. Firstly, it is an indirect-bandgap semi-conductor, with difficulty in producing pumped laser. Secondly, its energy gap is so small that it suffers two-photon-absorption (TPA) and free-carrier-absorption (FCA) in the telecommunication frequency range. TPA is a phenomenon that an electron is excited to a higher energy state by absorbing the energy of two photons, while FCA is a phenomenon that a carrier, an electron or a hole, is excited from an excited energy state to another unoccupied energy state in the same band, both of which lead to a significant loss of power when the optical wave with high power is propagated in SOI waveguide.

Silicon nitride is an alternative form of silicon with a larger energy gap. It is also CMOS compatible and has an obvious Kerr effect[57]. In addition, TPA is not expected in silicon nitride around 1.55 μm. Its refractive index varies from 1.57 to 2.76, depending on the SiH_4/N_2 flow ratio[58][59] and the deposition temperature[60] - much larger than the refractive index of silicon dioxide - and ensures the mode confinement in the waveguide. SPM and GVD of silicon nitride waveguide have been demonstrated[57], as well as frequency comb generation[61], super-continuum generation[62][63] from visible spectrum to near-infrared and SHG[64].

1.2.2 AlGaAs waveguide

AlGaAs is an ideal candidate and is considered as "the silicon of nonlinear optical materials"[65]. Similar to silicon, AlGaAs has a high refractive index so that it is capable of retaining a strong optical confinement mode and ensures sufficient nonlinear interaction inside the AlGaAs waveguide. The refractive index relies on the aluminium concentration, providing a flexible adjusting refractive index in a broad range[66]. In addition, AlGaAs is found to have broadband transparency in the telecommunication frequency range. AlGaAs not only have a high second-order nonlinear co-efficient[67], but also have strong Kerr nonlinearity that the value of nonlinear refractive index n_2 is 500 times higher than that of silica[68]. Apart from the excellent nonlinear performance, AlGaAs is a direct-band gap semi-conductor, which is promising for utilisation in OEICs or all-optical chips as a laser source.

Table 1.1 Comparison of nonlinear properties of optical materials.

Material	Refractive index	$n_2(\mathrm{cm}^2/\mathrm{W})$	α_2(cm/GW)
Silicon	3.48[24]	4×10^{-14}[34]	0.5[34]
Silicon nitride	1.57-2.76[58]	2.4×10^{-15}[69]	Negligible
GaAs	3.37[66]	1.59×10^{-13}[68]	15[70]
$Al_{0.18}Ga_{0.82}As$	3.28[66]	1.5×10^{-13}(TE)[68] 1.43×10^{-13}(TM)[68]	0.05[68]

Table 1.1 shows a comparison between four different optical materials at a wavelength of 1.55 μm, where α_2 is the TPA co-efficient. Silicon shows the highest refractive index and a large nonlinear refractive index, as well as the largest TPA in the table. Although silicon nitride has a lower refractive index and a smaller nonlinear refractive index when compared with silicon, its TPA is negligible. In contrast, GaAs has a relatively high refractive index and the largest nonlinear refractive index. However, its TPA co-efficient is 30 times that of silicon, which may cause the dramatic power loss. Compared with the above materials, AlGaAs is a perfect material for nonlinear optics. Taking $Al_{0.18}Ga_{0.82}As$ as an example, it has a high refractive index, a large nonlinear refractive index and a small TPA co-efficient.

A typical structure of deep-etched AlGaAs multi-layers waveguide is depicted in Figure 1.2, in which the core layer has a lower Al concentration so it has a higher refractive index than those of cladding layers. Two decades ago, a large nonlinear phase shift in AlGaAs waveguides was found[71] and reference [68] measured the nonlinear refractive index for both TE- and TM-polarized modes, as well as the two- and three-photon absorption co-efficients of a AlGaAs channel waveguide, where the core layer is $Al_{0.18}Ga_{0.82}As$. Thanks to the improvement in fabrication technology, much more attention has been focused on AlGaAs waveguide in the past few years; in particular, the nonlinear effects. Many nonlinear frequency-mixing processes have been demonstrated based on the second-order nonlinearity: SHG[72]–[76], SFG[77] and DFG[78][79], and third-order nonlinearity: SPM[80][81], XPM[80]–[83] and FWM[80][84]–[88]. In addition, geometric dispersion and material dispersion were taken into consideration and zero-GVD was studied by engineering the structure of AlGaAs nanowire[89][90].

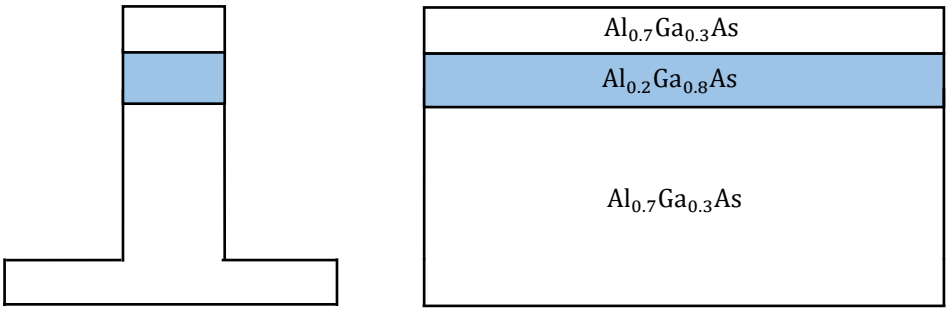

Fig. 1.2 Structure of deep-etched AlGaAs strip waveguide.

1.3 Introduction of computational electromagnetics

Computational electromagnetics (CEM)[91] is a typical technique in order to obtain the effective solution of the approximation to Maxwell's equations, involving the analysis of the interaction in both electric and magnetic fields in the problem domain. Therefore, CEM is applied widely in the simulations of many research fields: Radar Cross Section (RCS), aircraft, antenna, biomedical application and optical waveguides. With regard to optical waveguides, the general utilized methods are classified as the numerical methods of CEM, which include finite element method (FEM), finite-difference time-domain method (FDTD), beam propagation method (BPM), discrete dipole approximation (DDA) and method of moments (MoM). These methods have been developed to calculate the energy flux, power flow direction, radiation, scattering, absorption and normal modes of optical waveguides, simplifying the real irregular and complex structure of devices and simulating the propagation of electromagnetic waves in the realistic three-dimensional models.

Finite element method

The finite element method is a popular computational method based on the approximation solution of partial differential equations (PDE). In this approach, the whole problem domain is divided into a set of small sub-divisions which are called finite elements and each element has its own equations. Final values can be obtained by solving those sets of element equations and combining the results in mathematical ways. The initial concept of FEM was firstly suggested by Courant in 1943[92]. In 1950s and 1960s, a similar approach was proposed by a Chinese scientist Feng and it was called the finite difference method based on variation principle. Many books about FEM have been published since the 1970s[93]–[96]. Compared with other numerical methods, FEM attracts more attention when it is utilized for scientific research and industrial application. It is a good choice for researchers because of its many advantages. It can easily turn complex geometry into a collection of simple elements so that it is efficient in dealing with the various material properties and various desired precisions over the whole problem domain. Moreover, local effects are easily incorporated because of the mesh discretization.

Finite-difference time-domain method

The finite-difference time-domain method is a finite-difference method (FDM) that is applied in the time-domain. It is a grid-based numerical analysis method, computing the central-

difference approximation to the time-dependent partial differential equations, and has been used for simulating electromagnetic models for many years. FDTD can be traced back to 1966, Yee[97] presented a set of difference equations of Maxwell's curl equation, which were discretized in space and time with a central-difference format. Electric and magnetic components were sampled as discrete points in both the space and time domain. Figure 1.3 shows the Yee space lattice with electric and magnetic field vector components in three-dimensional space. Electric components have been placed in the middle of the edges and magnetic components have been placed in the middle of surfaces.

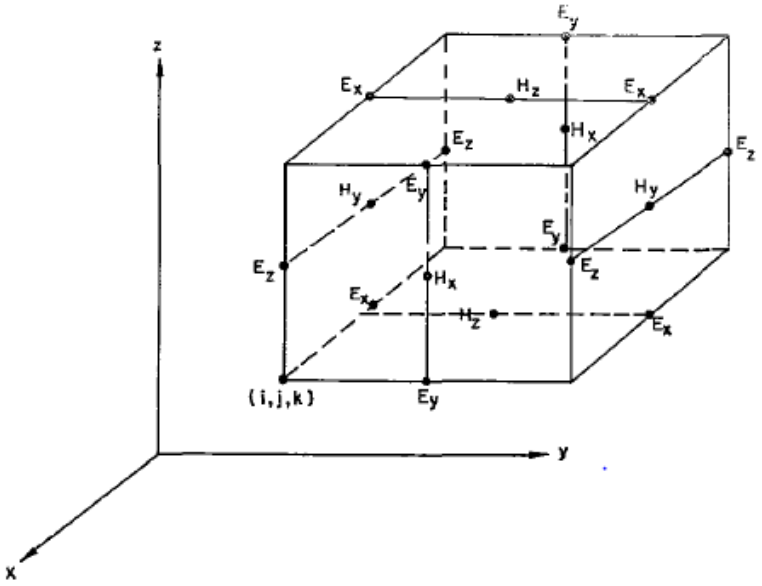

Fig. 1.3 Yee space lattice: position of electric and magnetic field components. Source: K. S. Yee *IEEE Trans. Antennas Propag*, 14(3), 302-307, 1966.

It was Taflove who developed the FDTD acronym in 1980[98]. He introduced the first model of sinusoidal steady-state electromagnetic-penetration in cylindrical metal cavity based on FDTD. In the next year (1981), Mur[99] reported absorbing boundary condition (ABC) which could be used for both two- and three-dimension FDTD models with second-order accuracy. The first simulation of waveguide structures was published by Choi and Hoefer[100] in 1986. After that, the FDTD method began to be utilized for modelling linear dispersive materials (1990-1991)[101]–[103] and simulating the propagation of optical pulses in nonlinear dispersive media between 1992 and 1994[104][105]. In 1994, Berenger[106] presented a form of highly effective ABC that could be applied in two-spatial dimensions, which was known as a perfectly matched layer (PML). In the same year, PML was extended from two dimensions to three dimensions by Katz, Thiele and Taflove[107]. FDTD has been developed and widely

used in many scientific research areas since 1994 and is still one of the most popular numerical methods.

FDTD is a dominant technique in electro-magnetic computation because of its three main advantages. Compared with other numerical methods, FDTD (1) can calculate all points of the problem domain directly and simulate electric and magnetic fields realistically, and (2) is it also able to cover a wide range of frequencies in a single simulation. Since every component of E and H in every time step is calculated, (3) means that displaying the movement of $\vec{E}$ and $\vec{H}$ is possible so that it is not difficult to work out what is going on inside the waveguide to ensure it works correctly.

Beam propagation method

The beam propagation method is a simple and useful way to simulate the propagation of light in optical waveguides based on the slowly varying envelope approximation of differential equations, which are treated as paraxial one-way models. In the 1970s, BPM was first introduced to solve the problem of the propagation of waves in a large domain with long distance, only involving the spatial variable z rather than time. BPM is suitable for both isotropic and general anisotropic[108] optical material. In addition, it can be applied with a finite-difference method (FDM)[109] or FEM[110] in the same simulation.

However, BPM does have limitations. It depends on the slowly varying envelope approximation so it is less valid when utilized in small structures or in waveguides with high refractive-index contrast. Normally, it is applied in paraxial one-way models. It can be used in two-direction propagation with the iterations of reflections, but it may cause the issue of convergence.

Discrete dipole approximation

Discrete dipole approximation is a widely used method in the computation of absorption and scattering of target materials with arbitrary geometry. In 1964, DeVoe[111] proposed the initial idea of DDA, to which was later added retardation effects by Purcell and Pennypacker (1973)[112].They used a set of point dipoles instead of a scatterer. In 1988, Goedecke and O'Brien[113] derived DDA from the integral equations of an electronic field based on the

digitized Green's function algorithm and developed the coupled dipole method in two ways. A scatterer consists of small cubic particles, which are polarized and interact with each other when induced by the electric field[114]. The interaction between these particles and between optical wave and arbitrary structures is taken into consideration in the DDA method. DDA became more popular after Draine and Flatau wrote a DDSCAT package in FORTRAN[115]. The package includes the calculations for interaction between the electromagnetic waves and devices of various shapes (e.g., sphere, ellipsoids, regular tetrahedron, cuboid, cylinder, and hexagonal prism) which is considered as a convenient and simple tool for simulation.

Method of moments

Method of moments[116] is known as a boundary technique. This method involves computing boundary values through utilizing Green's formula to solve linear partial differential equations, which is expressed as a boundary integral equation. Compared s with other numerical methods, MoM is more efficient in many ways because it only focuses on boundary values, rather than the values over the entire problem domain. Firstly, MoM can achieve a reduction in spatial dimensions, meaning reduction in numerical discretization. Secondly, the behaviour of an optical wave can be simulated at infinity automatically in MoM without the approximation of mesh. Thirdly, handling mesh with MoM is much easier when the boundaries are moving[117]. MoM has been popular since the 1980s and is now widely used to obtain numerical results[118]–[120]. MoM, however, is only applicable in solving problems with a small volume ratio. In terms of larger computational domain, volume-discretization techniques, such as FEM and FDM, are more effective than MoM, which will cause rapid growth in storage requirements and time of calculation.

Following the numerical methods introduced above, the mode solver has been developed as a tool to compute the fundamental and high-order TE and TM modes of optical waveguides, as well as their effective indices. Mode solver was proposed primarily based on the FEM[121]–[124] and FDM[125][126]. Thanks to the development and application of these efficient numerical methods, a large amount of simulation results have been obtained and these provide the theoretical support for fabrication and further design of optical waveguides. Although these techniques have been shown to have a big success in the research into optical waveguides, they still face many challenges.

For instance:

(1) Difficulty in incorporating arbitrary material dispersion.

(2) Difficulty in handling optical second- and third-order nonlinearities $\chi^{(2)}$ and $\chi^{(3)}$.

(3) Difficulty in solving waveguide formats, especially in one long spatial dimension.

(4) Difficulty in tackling anisotropy (for instance, birefringence).

This thesis introduces high-fidelity simulations of GaAs/AlGaAs waveguides and silicon-based waveguides with an implementation of FDTD method, incorporating linear dispersion, including geometric- and material-dependent dispersions, and second- and third-order nonlinearities in three-dimension models with one long spatial dimension.

The extant commercial softwares and research codes based on FDTD method, such as Lumerical FDTD solutions and Remcom XFdtd, offering the simulations of three-dimensional waveguides with linear dispersion and nonlinearities. However, they are not capable of simulating wave propagation in six directions (+x, -x, +y, -y, +z, -z) in one time to provide a realistic model, which is handled in the simulations in this thesis. Moreover, in this thesis, a three-dimension model was designed with a cyclic boundary condition so that the memory requirement and computation time are significantly decreased. The current limitation of the code is that the propagation loss and TPA are not incorporated, which will be improved in the future work.

1.4 Overview of the thesis

In Chapter 1, the research background of optical waveguides and the development of typical numerical methods applied for electromagnetic simulations are briefly introduced.

In Chapter 2, the basic finite-difference time-domain method is discussed; starting from the introduction of Maxwell's equations and FDTD updating equations, to the analysis of numerical dispersion and stability. Then the excitation source and PML absorbing boundary condition in FDTD simulation are highlighted. At the end of the chapter, linear dispersion and nonlinearity are described, as well as piecewise linear recursive convolution (PLRC) method.

In Chapter 3, the simulation of optical waveguides is introduced. The basic model, the implementation of FDTD algorithms and the waveguide source computed in mode solver are presented. The approach of incorporating linear dispersion and nonlinearity in FDTD technique is demonstrated where both second- and third-order nonlinearities are considered. In addition, phase matching conditions of FWM and SHG are discussed. Then the parameters of PML are optimized. Finally, the parallel programming based on OpenMP and high-performance computation (HPC) are highlighted.

In Chapter 4, four-wave mixing processes in three optical waveguides - GaAs suspended waveguide, deep-etched multi-layer $Al_{0.25}Ga_{0.75}As$ waveguide and $Al_{0.3}Ga_{0.7}As$-on-insulator waveguide - are simulated. FWM results were observed in all the waveguides with widths that satisfy the phase matching condition, which is discussed based on GVD and phase mismatch factor.

In Chapter 5, four-wave mixing processes in two dielectric waveguides - silicon-on-insulator waveguide and silicon rich silicon nitride-on-insulator waveguide - are simulated. According to GVD and phase mismatch factor, phase matching condition of FWM is discussed. FWM results were observed in all the waveguides when the widths satisfy the phase matching condition.

In Chapter 6, second-harmonic generation in a highly birefringent $Al_{0.3}Ga_{0.7}As$-on-insulator waveguide is simulated. The SHG result was observed in the waveguide when the width achieved the type-I phase matching condition.

In Chapter 7, a conclusion to this research is offered with suggestions for future research.

Chapter 2

The Finite-Difference Time-Domain Method

This chapter presents the basic theory of the finite-difference time-domain method, introducing the updating equations of electric and magnetic fields in multiple dimensions. In addition, numerical dispersion and stability are analyzed and typical excitation sources applied in the simulation are introduced as well as absorbing boundary conditions. Finally, linear dispersion and nonlinearity are incorporated in the updating equations, making them suitable for all linear, dispersive or nonlinear materials.

2.1 Introduction to the FDTD method

FDTD is a popular time-domain numerical algorithm in solving approximation values of electric and magnetic fields in Maxwell's equations. In this method, the whole problem domain is formed of discrete points and every field components of each point is calculated at each time step from the values of the previous time steps, simulating the propagation of optical pulses in waveguides.

2.1.1 Maxwell's equations

Generally, FDTD is based on the differential form of Maxwell's equations in time domain:

$$\nabla \times \vec{H} = \frac{\partial \vec{D}}{\partial t} + \vec{J} \tag{2.1a}$$

$$\nabla \times \vec{E} = -\frac{\partial \vec{B}}{\partial t} - \vec{M} \tag{2.1b}$$

$$\nabla \cdot \vec{D} = \rho_e \tag{2.1c}$$

$$\nabla \cdot \vec{B} = \rho_m \tag{2.1d}$$

where $\vec{E}$ is the electric field (V/m); $\vec{D}$ is the electric flux density (C/m^2); $\vec{H}$ is the magnetic field (A/m); $\vec{B}$ is the magnetic flux density (Wb/m^2); $\vec{J}$ is the electric current density (A/m^2);

$\vec{M}$ is the magnetic current density (V/m^2); ρ_e is the electric charge density (C/m^3); and ρ_m is the magnetic charge density (Wb/m^3). Formula (2.1a-b) is the curl of the electromagnetic field, being used for derivation to obtain updating equations in FDTD, while formulas (2.1c-d) are divergence of the electromagnetic field and are employed to check the simulation results of FDTD. In the first two equations, $\vec{J}$ and $\vec{M}$ can be expressed as follows:

$$\vec{J} = \vec{J}_i + \sigma^e \vec{E} \tag{2.2a}$$

$$\vec{M} = \vec{M}_i + \sigma^m \vec{H} \tag{2.2b}$$

where $\vec{J}_i$ and $\vec{M}_i$ are independent sources of electric and magnetic field energy; σ^e is the electric conductivity (S/m); and σ^m is the magnetic conductivity (Ω/m). It is noted that $\vec{M}$, ρ_m and σ^m are non-physical and will always be zero because the existence of magnetic monopole has not yet been proven. However, when we consider a magnetic current source or magnetic loss, they are treated as having equivalent magnetic current density and equivalent magnetic conductivity.

In general, the constitutive relationships between $\vec{D}$, $\vec{B}$ and $\vec{E}$, $\vec{H}$ in the time domain are described as:

$$\vec{D}(t) = \left[\, \varepsilon\left(t, \vec{E}\,\right)\right] * \vec{E}(t) \tag{2.3a}$$

$$\vec{B}(t) = [\, \mu(t)] * \vec{H}(t) \tag{2.3b}$$

where ε is the electric permittivity (F/m); and μ is the magnetic permeability (H/m). $\vec{D}$ is the convolution of permittivity and $\vec{E}$, while $\vec{B}$ is the convolution of permeability and $\vec{H}$. If we consider the medium is anisotropic, the dielectric permittivity and the magnetic permeability are tensors. When the medium is linear, isotropic and non-dispersive, the permittivity and the permeability are constants, so the relationships are codirectional and proportionate,

$$\vec{D}(t) = \varepsilon\vec{E}(t) = \varepsilon_r\varepsilon_0\vec{E}(t) \tag{2.4a}$$

$$\vec{B}(\mathrm{t}) = \mu\vec{H}(t) = \mu_r\mu_0\vec{H}(t) \tag{2.4b}$$

where ε_r is the relative permittivity; ε_0 is free-space permittivity (8.85×10^{-12} F/m); μ_r is the relative permeability; and μ_0 is the free-space permeability ($4\pi \times 10^{-7}$ H/m). When equations

(2.2a-b) and (2.3a-b) are substituted into equations (2.1a-b), Maxwell's curl equations are re-written as:

$$\nabla \times \vec{H} = \varepsilon \frac{\partial \vec{E}}{\partial t} + \vec{J}_i + \sigma^e \vec{E} \tag{2.5a}$$

$$\nabla \times \vec{E} = -\mu \frac{\partial \vec{H}}{\partial t} - \vec{M}_i - \sigma^m \vec{H} \tag{2.5b}$$

As a result, in three dimensional space, these two vector equations can be decomposed as six scalar equations in a Cartesian co-ordinate system, taking E_x and H_x as examples:

$$\frac{\partial E_x}{\partial t} = \frac{1}{\varepsilon_x}\left(\frac{\partial H_z}{\partial y} - \frac{\partial H_y}{\partial z} - \sigma_x^e E_x - J_{ix}\right) \tag{2.6a}$$

$$\frac{\partial H_x}{\partial t} = \frac{1}{\mu_x}\left(\frac{\partial E_y}{\partial z} - \frac{\partial E_z}{\partial y} - \sigma_x^m H_x - M_{ix}\right) \tag{2.6b}$$

2.1.2 FDTD updating equations

To further solve the value of electric and magnetic fields in scalar formulas, difference approximation is utilized, which is effective for continuum functions. Table 2.1 shows the expressions and accuracy of three typical methods: forward difference, backward difference and central difference. The errors of forward and backward difference are determined by Δx, but in contrast, the main error of central difference is caused by $(\Delta x)^2$ so that it achieves higher order accuracy.

Table 2.1 Comparison between three types of difference approximations.

Types	Expression	Accuracy
Forward difference	$f'(x) \approx \frac{f(x+\Delta x) - f(x)}{\Delta x}$	First - order accuracy
Backward difference	$f'(x) \approx \frac{f(x) - f(x-\Delta x)}{\Delta x}$	First - order accuracy
Central difference	$f'(x) \approx \frac{f\left(x+\frac{\Delta x}{2}\right) - f(x-\frac{\Delta x}{2})}{\Delta x}$	Second - order accuracy

Central difference approximation is used in FDTD to obtain approximation values of Maxwell's equations according to Yee grid. It is noted that field components $\vec{E}$ and $\vec{H}$ are not

coincident in space or time. In general, the electric field is sampled at each time step: 0, Δt, $2\Delta t$, $3\Delta t$, …nΔt, while the magnetic field is sampled at each half time step: $\frac{1}{2}\Delta t$, $(1+\frac{1}{2})\Delta t$, $(2+\frac{1}{2})\Delta t$, $(3+\frac{1}{2})\Delta t$, … $(n+\frac{1}{2})\Delta t$. Distributions of $\vec{E}$ and $\vec{H}$ in various dimensional space are depicted in the following Figures.

In the one dimensional case, position does not change in two directions (take *y*-direction and *z*-direction as an example), so derivatives with respect to *y* and *z* should be equal to zero. Therefore, one-dimension problems can be classified as two separate types: one is involved in the components E_y and H_z and the other one is involved in E_z and H_y.

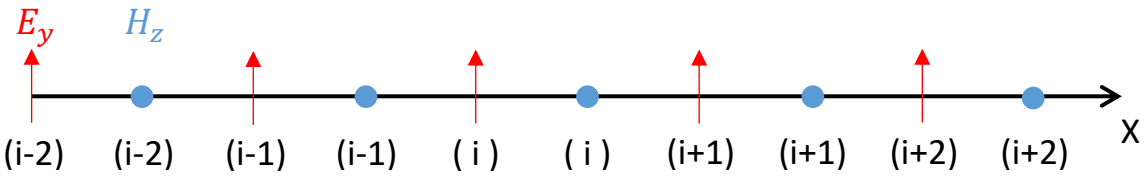

Fig. 2.1a Electric and magnetic components E_y and H_z of FDTD in one dimension.

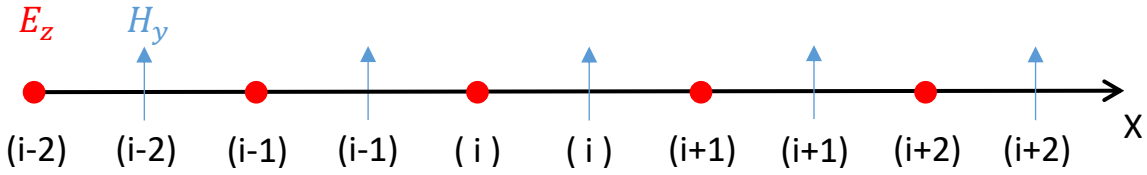

Fig. 2.1b Electric and magnetic components E_z and H_y of FDTD in one dimension.

According to the distribution of the positions of electric and magnetic field components in one-dimension space as shown in Figure 2.1 and central difference approximation, it is possible to obtain the updating equations of $\vec{E}$ and $\vec{H}$. Taking E_y and H_z for instance,

$$\frac{\partial E_y}{\partial t} = \frac{1}{\varepsilon_y}\left(-\frac{\partial H_z}{\partial x} - \sigma_y^e E_y - J_{iy}\right)$$

$$\frac{E_y^{n+1}(i) - E_y^n(i)}{\Delta t} = \frac{1}{\varepsilon_{y(i)}}\left[-\frac{H_z^{n+\frac{1}{2}}(i) - H_z^{n+\frac{1}{2}}(i-1)}{\Delta x} - \sigma_y^e E_y^{n+\frac{1}{2}}(i) - J_{iy}^{n+\frac{1}{2}}(i)\right] \quad (2.7)$$

where the electric field at (n+0.5) Δt is expressed as average values of those at (n+1) Δt and nΔt.

$$E_y^{n+\frac{1}{2}}(i) = \frac{E_y^{n+1}(i) + E_y^n(i)}{2} \quad (2.8)$$

As a consequence, electric field components are updated by their values at the previous time step and the values of the magnetic field, as well as current source. Similarly, updating equations of the magnetic field are simplified as:

$$\frac{\partial H_z}{\partial t} = \frac{1}{\mu_z}\left(-\frac{\partial E_y}{\partial x} - \sigma_z^m H_z - M_{iz}\right)$$

$$\frac{H_z^{n+\frac{1}{2}}(i) - H_z^{n-\frac{1}{2}}(i)}{\Delta t} = \frac{1}{\mu_z(i)}\left[-\frac{E_y^n(i+1) - E_y^n(i)}{\Delta x} - \sigma_z^m H_z^n(i) - M_{iz}^n(i)\right] \quad (2.9)$$

where the magnetic field at nΔt can be expressed as average values of those at (n+0.5) Δt and (n-0.5) Δt.

$$H_z^n(i) = \frac{H_z^{n+\frac{1}{2}}(i) + H_z^{n-\frac{1}{2}}(i)}{2} \quad (2.10)$$

Therefore, magnetic field components are updated by their values at the previous time step and the values of the electric field, as well as current source.

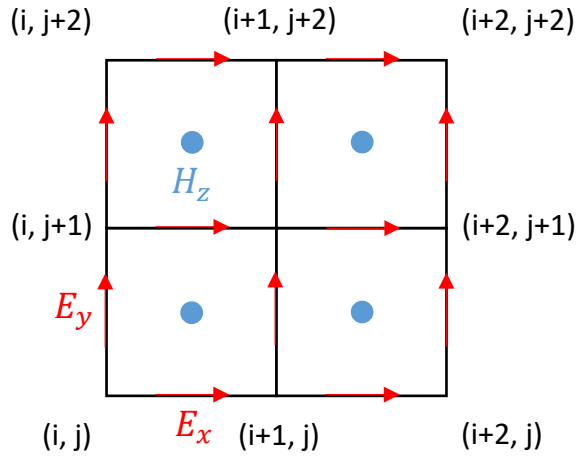

Fig. 2.2a Electric and magnetic components of FDTD in two-dimension TE_z mode.

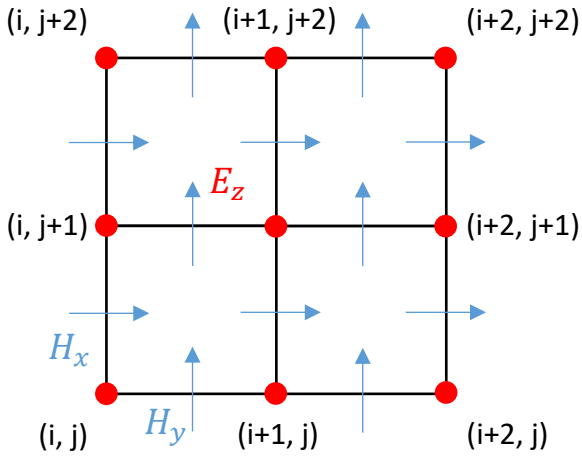

Fig. 2.2b Electric and magnetic components of FDTD in two-dimension TM_z mode.

When the problem domain increases to a two-dimension space, the position does not change in one direction (take z-direction for an example), so derivatives with respect to z should be equal to zero. Scalar equations are simplified as two separate modes: transverse-electric mode with respect to z (TE_z mode) which is involved in three components E_x, E_y and H_z and transverse-magnetic mode with respect to z (TM_z mode) which is involved in the other three components H_x, H_y and E_z. The distribution of the positions of the field components in the two modes are depicted in Figures 2.2a and 2.2b respectively.

With regard to a three-dimension space, all six field components are taken into consideration. Figure 2.3 shows the positions of $\vec{E}$ and $\vec{H}$ components. Every $\vec{H}$ component is surrounded by four $\vec{E}$ components. In the meantime, the $\vec{E}$ component is surrounded by four $\vec{H}$ components. According to the Yee grid in Fig. 2.3, scalar equations of six field components are simplified with central difference approximation of derivatives of time and space. Taking E_x and H_x as examples,

$$\frac{\partial E_x}{\partial t} = \frac{1}{\varepsilon_x}\left(\frac{\partial H_z}{\partial y} - \frac{\partial H_y}{\partial z} - \sigma_x^e E_x - J_{ix}\right)$$

$$\frac{E_x^{n+1}(i,j,k) - E_x^n(i,j,k)}{\Delta t} = \frac{1}{\varepsilon_{x(i,j,k)}}\left[\frac{H_z^{n+\frac{1}{2}}(i,j,k) - H_z^{n+\frac{1}{2}}(i,j-1,k)}{\Delta y} - \frac{H_y^{n+\frac{1}{2}}(i,j,k) - H_y^{n+\frac{1}{2}}(i,j,k-1)}{\Delta z} - \sigma_x^e E_x^{n+\frac{1}{2}}(i,j,k) - J_{ix}^{n+\frac{1}{2}}(i,j,k)\right] \quad (2.11)$$

$$\frac{\partial H_x}{\partial t} = \frac{1}{\mu_x}\left(\frac{\partial E_y}{\partial z} - \frac{\partial E_z}{\partial y} - \sigma_x^m H_x - M_{ix}\right)$$

$$\frac{H_x^{n+\frac{1}{2}}(i,j,k) - H_x^{n-\frac{1}{2}}(i,j,k)}{\Delta t} = \frac{1}{\mu_x(i,j,k)}\left[\frac{E_y^n(i,j,k+1) - E_y^n(i,j,k)}{\Delta z} - \frac{E_z^n(i,j+1,k) - E_z^n(i,j,k)}{\Delta y} - \sigma_x^m H_x^n(i,j,k) - M_{ix}^n(i,j,k)\right] \quad (2.12)$$

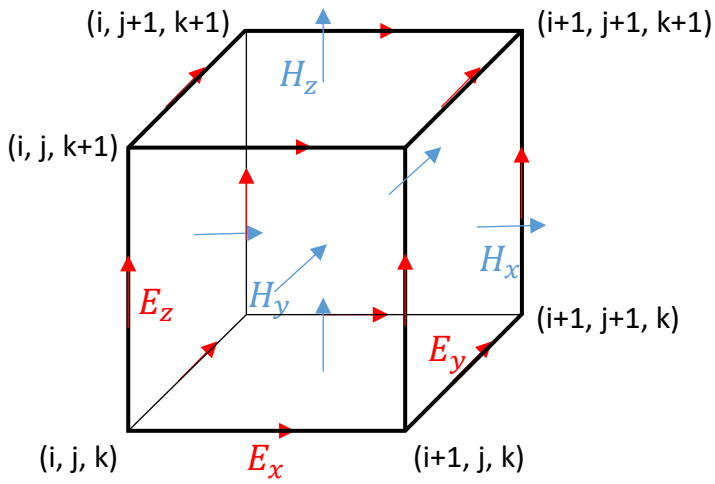

Fig. 2.3 Distribution of electric and magnetic components of FDTD in three dimensions.

2.2 Numerical dispersion and stability

2.2.1 Numerical stability

Given that the points of the electric field and the magnetic field are discrete in the problem domain, the sampling period is important. To ensure the stability of the values, the relationship between the time step and the size of grid must obey the Courant–Friedrichs–Lewy (CFL) condition[127]. According to the CFL condition,

$$\mathrm{C} = \Delta\mathrm{t} * \sum_{i=1}^{n} \frac{u_{xi}}{\Delta_{xi}} \ll \mathrm{C}_{\max} \qquad \text{(n=1, 2, 3)} \qquad (2.13)$$

where C is the courant number; Δt is the time step (s); u_{xi} is the magnitude of velocity (m/s); Δ_{xi} is the size of grid (m); and n is the number of dimensions. Typically, the maximum of the courant number is 1. Therefore, formula (2.13) can be re-written for a three dimensional FDTD case[128]:

$$\Delta t \ll \frac{1}{\frac{c}{n}\sqrt{\frac{1}{(\Delta x)^2}+\frac{1}{(\Delta y)^2}+\frac{1}{(\Delta z)^2}}} \qquad (2.14)$$

where c is the velocity of light in free space (m/s); and n is the refractive index. If $\Delta x = \Delta y = \Delta z$, formula (2.14) is simplified:

$$\Delta t \ll \frac{n\Delta x}{c\sqrt{3}} \qquad (2.15)$$

Nevertheless, the CFL condition ensures the stability rather than the accuracy. It only provides a basic relationship between grid size and time step.

2.2.2 Numerical dispersion

Generally, FDTD is a good approximation of a realistic electro-magnetic field. However, difference approximation causes error, leading to biased phase velocity, which is so-called numerical dispersion. A one-dimensional formula of numerical dispersion is described as:

$$\left[\frac{1}{c\Delta t}\sin\left(\frac{\omega\Delta t}{2}\right)\right]^2 = \left[\frac{1}{\Delta x}\sin\left(\frac{k_x\,\Delta x}{2}\right)\right]^2 \qquad (2.16)$$

where ω is the angular frequency (rad/s); and k_x is the wave number. It is not difficult to extend to the three-dimension case:

$$[\frac{1}{c\Delta t}\sin\left(\frac{\omega\Delta t}{2}\right)]^2 = [\frac{1}{\Delta x}\sin\left(\frac{k_x\Delta x}{2}\right)]^2 + [\frac{1}{\Delta y}\sin\left(\frac{k_y\Delta y}{2}\right)]^2 + [\frac{1}{\Delta z}\sin\left(\frac{k_z\Delta z}{2}\right)]^2 \quad (2.17)$$

When $\Delta x \to 0$, $\Delta y \to 0$, $\Delta z \to 0$, $\Delta t \to 0$, an ideal three-dimension dispersion formula is obtained based on L'Hopital's rule:

$$k_x^2 + k_y^2 + k_z^2 = (\frac{\omega}{c})^2 \quad (2.18)$$

Hence, the smaller the grid size and time step are, the better the results are. Because of numerical dispersion, different frequency components have different phase velocities. Over time, the shape of the pulse changes. Therefore, to ensure the stability of late-time propagation of the optical pulse, the size of the grid also depends on the frequency. Generally, in the reasonable FDTD simulations, the corresponding wavelength of the highest frequency component should be at least 20 times larger than the size of the cell.

2.3 Excitation source

The excitation source is established by assigning a time function to a source point in the waveguide, giving initial values of the electro-magnetic pulse in the time domain. Then the optical wave carries the desired frequency and propagates in six directions from the source point. Generally, according to a feature of the source point, the excitation source is divided into two types: hard source and current source. Moreover, on the basis of different pulses, the excitation source has many types and those typical for the FDTD method are sinusoidal pulse and Gaussian pulse.

2.3.1 Hard source and current source

Hard source is defined in that the source point of the excitation source is a specific component of $\vec{E}$ or $\vec{H}$ in the FDTD grid. For example, in a one-dimensional space, E_y hard source is set up as:

$$E_y(i_s) = E_0\, f(t) \quad (2.19)$$

where i_s is the position of the source point; E_0 is the amplitude; and $f(t)$ is the independent time function. The pulse would propagate in both +x and –x directions from the source point.

In contrast, in current sources, the source point is a component of $\vec{J}_i$ and $\vec{M}_i$, but the way to build the excitation source is similar to the formula (2.19). For example, in a three-dimensional space, $\vec{J}_i$ current source is set up as:

$$J_{ix}(i_s, j_s, k_s) = J_0 f(t) \tag{2.20}$$

where (i_s, j_s, k_s) is the position of the source point in the Yee grid; and J_0 is the amplitude. Current source is independent of other parameters in the waveguide. According to the equation (2.6), electric field and magnetic field are updated by $\vec{J}_i$ and $\vec{M}_i$ so that the source would propagate in all six directions from the source point.

2.3.2 Sinusoidal pulse and Gaussian pulse

In the FDTD algorithm, the time function in the formulas (2.19) and (2.20) is usually considered as a sinusoidal pulse or Gaussian pulse. Theoretically, the sinusoidal pulse is an ideal single-frequency pulse. Nevertheless, the excitation source of the FDTD method has limited time, which means the sinusoidal pulse would have additional frequency components. As a consequence, the sinusoidal pulse is utilized to simulate CW excitation.

As for the modelling of pulsed laser excitation, the bandpass Gaussian pulse is a suitable choice. It can build a pulse that contains a certain range of frequency and the bandwidth is easy to adjust. In addition, it is simple to set two or three frequencies in the Gaussian pulse to simulate frequency mixing processes. The expression of Gaussian-shaped pulse (based on cosine wave) is:

$$f(t) = \cos\left(\omega_c(t - t_0)\right) \mathrm{e}^{-\left(\frac{t-t_0}{\tau}\right)^2} \tag{2.21}$$

where ω_c is the central frequency; t_0 is the time of delay and used for moving pulse to the positive time domain, making sure that the incident wave starts from zero value; and τ is the parameter involving bandwidth. To have a better understanding of the Gaussian pulse, we do Fourier transform of formula (2.21) and obtain the frequency domain:

$$f(\omega) = \frac{\tau\sqrt{\pi}}{2} e^{-\left(\frac{\tau(\omega-\omega_c)}{2}\right)^2} + \frac{\tau\sqrt{\pi}}{2} e^{-\left(\frac{\tau(\omega+\omega_c)}{2}\right)^2} \tag{2.22}$$

To build an example of Gaussian pulse that contains a wavelength from 1.3 μm to 1.8 μm, the first step is to obtain the value of parameter τ. It is important to consider that the amplitude of the effective highest or lowest frequency component is one tenth of the central frequency and according to the formula (2.22), τ should satisfy:

$$0.1 = e^{-\left(\frac{\tau(\omega_{\max}-\omega)}{2}\right)^2} \tag{2.23}$$

where $\omega_{\max} = 2\pi f_{\max}$, so

$$\tau = \frac{2\sqrt{2.3}}{\pi\,\Delta f} \quad ; \quad \Delta f = f_{\max} - f_{\min} \tag{2.24}$$

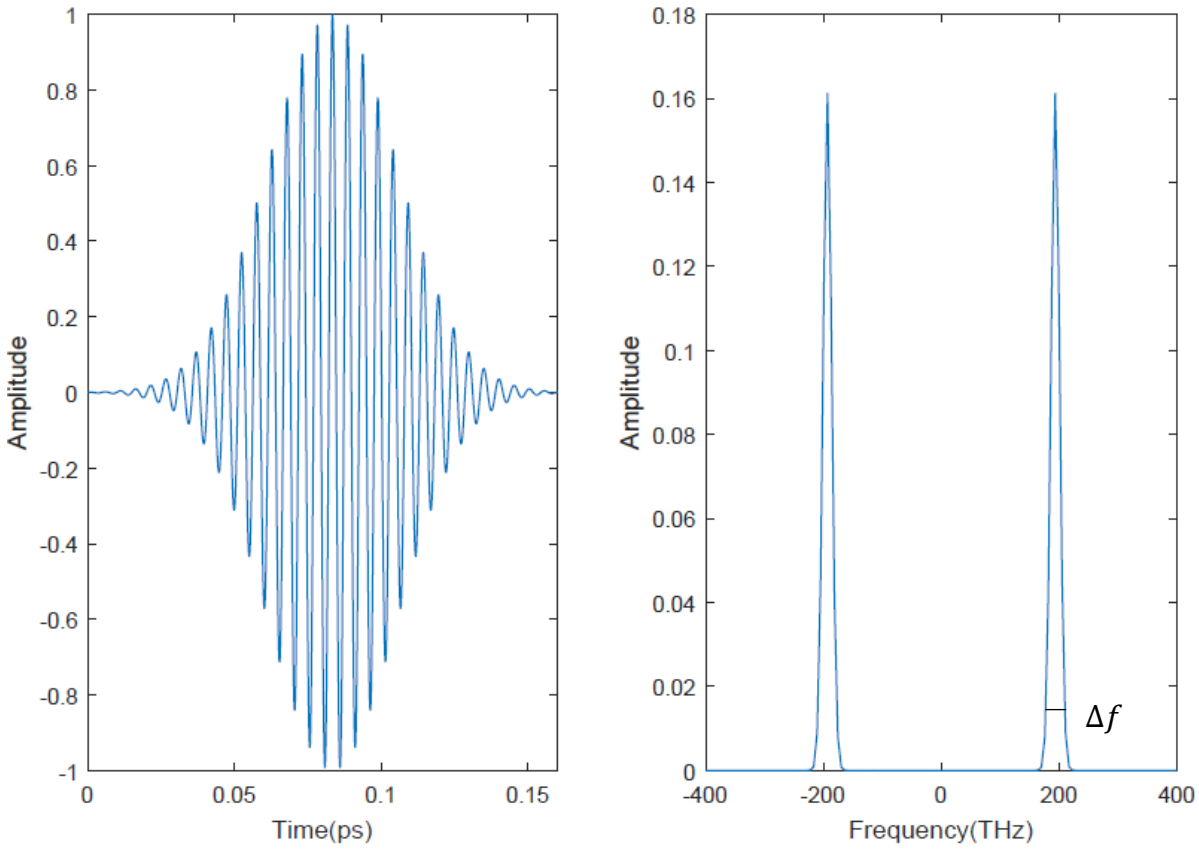

Fig. 2.4 Time domain and frequency domain of Gaussian pulse. The central wavelength is 1.55 μm.

Once τ is gained, it is easy to build the desired Gaussian pulse, as long as the delay constant t_0 is big enough to ensure that the pulse starts from a neglectable value. As is shown in Figure 2.4, Gaussian pulse with a central wavelength 1.55 μm has zero value when t=0, and the whole pulse is finished in 160 fs. The corresponding bandwidth Δf is highlighted in the frequency domain, which is decided by the width of the frequency at one tenth of the peak value.

Another way to determine the values of parameters in Gaussian pulse is based on the laser source used in the experiments. Once the duration of the pulse has been obtained, the time-delay constant and bandwidth are obtained.

2.4 Absorbing boundary conditions

Given the discretization and computational burden of the FDTD algorithm, it is impossible to simulate infinite problem space, otherwise the computer storage and running time would be major issues. To address these issues, boundary conditions have been created to cut the problem domain as necessary. In order to build a realistic environment of propagation for the optical pulse in both the waveguide and the air, the special boundary conditions must ensure that the radiation energy of the waveguide is absorbed at the boundary without any reflections.

2.4.1 Perfectly matched layer

Compared to other absorbing boundary conditions, a perfectly matched layer is the best choice in this case[129]. To update the electric and magnetic field, every component of $\vec{H}$ and $\vec{D}$ should be divided as two sub-components[130]. Taking $\vec{H}$ as an example,

$$\mu\frac{\partial H_{xy}}{\partial t}+\sigma_{my}H_{xy}=-\frac{\partial E_z}{\partial y} \tag{2.25a}$$

$$\mu\frac{\partial H_{xz}}{\partial t}+\sigma_{mz}H_{xz}=\frac{\partial E_y}{\partial z} \tag{2.25b}$$

$$\mu\frac{\partial H_{yx}}{\partial t}+\sigma_{mx}H_{yx}=\frac{\partial E_z}{\partial x} \tag{2.25c}$$

$$\mu\frac{\partial H_{yz}}{\partial t}+\sigma_{mz}H_{yz}=-\frac{\partial E_x}{\partial z} \tag{2.25d}$$

$$\mu\frac{\partial H_{zx}}{\partial t}+\sigma_{mx}H_{zx}=-\frac{\partial E_y}{\partial x} \tag{2.25e}$$

$$\mu\frac{\partial H_{zy}}{\partial t}+\sigma_{my}H_{zy}=\frac{\partial E_x}{\partial y} \tag{2.25f}$$

where the values of conductivity σ are as follows:

$$\sigma_{mx}=\sigma_{my}\neq 0 \tag{2.26a}$$

$$\sigma_{mz}=0 \tag{2.26b}$$

In addition, the values of ε,μ, σ_{ex}, σ_{ey}, σ_{mx} and σ_{my} should satisfy the impedance matching conditions:

$$\frac{\sigma_{ex}}{\varepsilon} = \frac{\sigma_{mx}}{\mu} \tag{2.27a}$$

$$\frac{\sigma_{ey}}{\varepsilon} = \frac{\sigma_{my}}{\mu} \tag{2.27b}$$

Figure 2.5 shows the distribution of conductivity in the electric and the magnetic fields of two dimensional PML. In x direction, conductivity σ_{ey} and σ_{my} are required and in y-direction, conductivity σ_{ex} and σ_{mx} are required. Every corner contains four components of conductivity. If we combine formula (2.25a-f) and Figure 2.5, updating equations of $\vec{E}$ and $\vec{H}$ in the PML area are obtained.

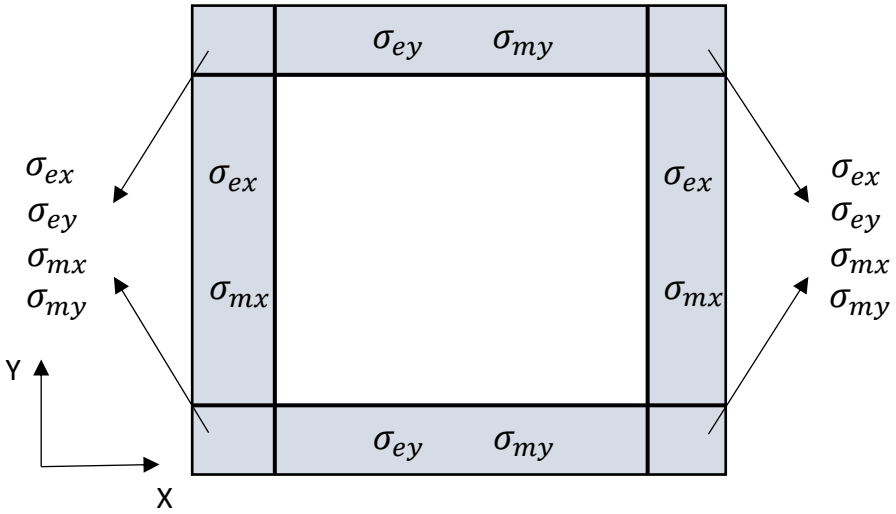

Fig. 2.5 Conductivity distribution of PML in two dimension.

However, significant wave reflection at PML surface is observed when σ is a constant [131]. To weaken the reflection error and improve the modelling results, a polynomial grading method and geometric grading method of increasing PML loss parameter from zero at the interface were proposed by Berenger in the reference [129]. The loss parameter of polynomial-graded PML is defined as:

$$\sigma(\rho) = \sigma_{\max}(\frac{\rho}{\delta})^{n_{\text{pml}}} \tag{2.28a}$$

$$\sigma_{\max} = -\frac{(n_{\text{pml}}+1)\varepsilon_0 c \ln R(0)}{2\Delta s N} \tag{2.28b}$$

where δ is the thickness of PML. σ increases from zero at $\rho = 0$, the inner surface of PML, to $\sigma = \sigma_{\max}$ at $\rho = \delta$, when $n_{\text{pml}} = 1$, formula (2.28a) is a linear function. For many optimal FDTD simulations, $n = 2$, 3 or 4. In the formula (2.28b), Δs is the size of PML mesh and N is the number of PML cells. $R(0)$ is the reflection factor. It is demonstrated in the reference [132] that for 10-cell-thick PML and 5-cell-thick PML, the optimal values of $R(0)$ are e^{-16} and e^{-8}, respectively.

Similarly, the loss parameter of geometric-graded PML is defined as:

$$\sigma(\rho) = \sigma_0(g^{\frac{\rho}{\Delta s}}) \tag{2.29a}$$

$$\sigma_0 = -\frac{\varepsilon_0 c \ln g}{2\Delta s(g^N - 1)} \ln R(0) \tag{2.29b}$$

where σ_0 is the starting value of PML conductivity; and g is the geometric scaling factor.

2.4.2 Convolution perfectly matched layer

Although PML works well for most FDTD cases, it is ineffective in absorbing an evanescent wave unless it is placed far away from the obstacle[133]. Nevertheless, this solution increases the requirement of memory and runtime. Another issue is that it suffers from late-time reflections when the simulation field is too large or running time is too long. Convolution perfectly matched layer (CPML)[134] is an implementation of complex frequency-shifted (CFS) PML[135], which is efficient in absorbing an evanescent wave and stabilises the longer propagation. In general, in the stretched co-ordinate, updating equations of the electric and magnetic fields of PML in the frequency domain are expressed as [136]. Taking E_x as an example,

$$\mathrm{j}\omega\varepsilon E_x + \sigma E_x = \frac{1}{s_{ey}} \frac{\partial}{\partial y} H_z - \frac{1}{s_{ez}} \frac{\partial}{\partial z} H_y \tag{2.30}$$

where σ is the conductivity of lossy medium; s_{ey} and s_{ez} are the stretched-coordinate metrics,

$$s_{ey} = 1 + \frac{\sigma_{ey}}{\mathrm{j}\omega\varepsilon_0} \quad ; \quad s_{ez} = 1 + \frac{\sigma_{ez}}{\mathrm{j}\omega\varepsilon_0} \tag{2.31}$$

In formula (2.31), σ_{ey} and σ_{ez} are conductivities of PML. Here the method proposed by Kuzouglu and Mittra[134] is applied to describe s_{ey} and s_{ez} ,

$$s_{ey} = \kappa_{ey} + \frac{\sigma_{ey}}{\alpha_{ey}+\mathrm{j}\omega\varepsilon_0} \quad ; \quad s_{ez} = \kappa_{ez} + \frac{\sigma_{ez}}{\alpha_{ez}+\mathrm{j}\omega\varepsilon_0} \tag{2.32}$$

where $\kappa_{ey} \geq 1$, $\kappa_{ez} \geq 1$, $\alpha_{ey} \geq 0$, $\alpha_{ez} \geq 0$. As with the formula (2.27a-b), the conductivity of electric and magnetic field should satisfy the matching conditions:

$$\kappa_{ei} = \kappa_{mi} \quad ; \quad \frac{\sigma_{ei}}{\varepsilon_0} = \frac{\sigma_{mi}}{\mu_0} \quad ; \quad \frac{\alpha_{ei}}{\varepsilon_0} = \frac{\alpha_{mi}}{\mu_0} \qquad (\mathrm{i} = \mathrm{x}, \mathrm{y}, \mathrm{z}) \tag{2.33}$$

In the FDTD method, the relationship between $\vec{D}$ and $\vec{H}$ is fixed and simple no matter whether the media are dispersive or nonlinear. Thus, in the simulation of waveguide in this thesis, values of magnetic fields are used for updating $\vec{D}$ instead of updating $\vec{E}$, so equation (2.30) is modified:

$$\frac{\partial D_x}{\partial t} + \sigma \frac{D_x}{\varepsilon} = \overline{s_{ey}} * \frac{\partial}{\partial y} H_z - \overline{s_{ez}} * \frac{\partial}{\partial z} H_y \tag{2.34}$$

where $\overline{s_{ey}}$ and $\overline{s_{ez}}$ are the Laplace transform of $\frac{1}{s_{ey}}$ and $\frac{1}{s_{ez}}$, so the multiplication in the frequency domain becomes a convolution in the time domain. Taking $\overline{s_{ey}}$ for instance,

$$\overline{s_{ey}} = \frac{\delta(t)}{\kappa_{ey}} + \xi_{ey}(t) \tag{2.35a}$$

$$\xi_{ey}(t) = -\frac{\sigma_{ey}}{\varepsilon_0 {\kappa_{ey}}^2} e^{\left[-\left(\frac{\sigma_{ey}}{\varepsilon_0 \kappa_{ey}} + \frac{\alpha_{ey}}{\varepsilon_0}\right) t\right]} u(t) \tag{2.35b}$$

Substitute formula (2.35a) for $\overline{s_{ey}}$ in formula (2.34),

$$\frac{\partial D_x}{\partial t} + \sigma \frac{D_x}{\varepsilon} = \frac{1}{\kappa_{ey}} \frac{\partial}{\partial y} H_z - \frac{1}{\kappa_{ez}} \frac{\partial}{\partial z} H_y + \xi_{ey}(t) * \frac{\partial}{\partial y} H_z - \xi_{ez}(t) * \frac{\partial}{\partial z} H_y \tag{2.36}$$

In order to further solve the convolution in the formula (2.36), it is important to utilize the discrete-time convolution to simplify it:

$$\int_{m\Delta t}^{(m+1)\Delta t} \xi_{ey}(t)\, dt = \int_{m\Delta t}^{(m+1)\Delta t} \frac{-\sigma_{ey}}{\varepsilon_0 {\kappa_{ey}}^2} e^{\left[-\left(\frac{\sigma_{ey}}{\varepsilon_0 \kappa_{ey}} + \frac{\alpha_{ey}}{\varepsilon_0}\right) t\right]}\, dt$$

$$= a_{ey}\, e^{\left[-\left(\frac{\sigma_{ey}}{\varepsilon_0 \kappa_{ey}} + \frac{\alpha_{ey}}{\varepsilon_0}\right) m\Delta t\right]} \tag{2.37}$$

where

$$b_{ey} = e^{\left[-\left(\frac{\sigma_{ey}}{\varepsilon_0 \kappa_{ey}} + \frac{\alpha_{ey}}{\varepsilon_0}\right) \Delta t\right]} \tag{2.38a}$$

$$a_{ey} = \frac{\sigma_{ey}}{\sigma_{ey}\kappa_{ey} + \alpha_{ey}\kappa_{ey}^{\,2}}\ (b_{ey} - 1) \tag{2.38b}$$

With formula (2.37-2.38), the convolution in the formula (2.36) becomes a sum function:

$$\xi_{ey}(t) * \frac{\partial}{\partial y} H_z = \sum_{m=0}^{n-1} a_{ey}\, e^{\left[-\left(\frac{\sigma_{ey}}{\varepsilon_0 \kappa_{ey}} + \frac{\alpha_{ey}}{\varepsilon_0}\right) m\Delta t\right]} \frac{\partial}{\partial y} H_z^{n-m+1/2} \tag{2.39}$$

However, formula (2.39) indicates that at every time step, the values of $\vec{H}$ need to be stored and the sum function has to be calculated, which is memory and time-consuming. Thanks to the recursive convolution (RC) method[137], it is not necessary to save the values in every time step, as long as the value at the previous time step is stored . As a consequence, formula (2.36) is simplified:

$$\frac{\partial D_x}{\partial t} + \sigma \frac{D_x}{\varepsilon} = \frac{1}{\kappa_{ey}} \frac{\partial}{\partial y} H_z - \frac{1}{\kappa_{ez}} \frac{\partial}{\partial z} H_y + \psi_{ey}^{n+1/2} - \psi_{ez}^{n+1/2} \tag{2.40}$$

where

$$\psi_{ey}^{n+1/2} = b_{ey} \psi_{ey}^{n-1/2} + a_{ey} \frac{\partial}{\partial y} H_z \tag{2.41a}$$

$$\psi_{ez}^{n+1/2} = b_{ez} \psi_{ez}^{n-1/2} + a_{ez} \frac{\partial}{\partial z} H_y \tag{2.41b}$$

where b_{ey} and a_{ey} are defined in the formula (2.38a-b), b_{ez} and a_{ez} are expressed in similar ways. Values of parameters σ, κ , and α are analyzed and optimized in the reference [134][138].

2.5 Linear material dispersion

When the optical pulse propagates in the dispersive material, the velocities of frequency components vary. Different frequencies have different dielectric permittivities, leading to various refractive indices, which decides the velocity inside the medium:

$$v = \frac{c}{n} \quad ; \quad n = \sqrt{\frac{\varepsilon}{\varepsilon_0}} \tag{2.42}$$

In the earlier sections, the relationship between $\vec{D}$ and $\vec{E}$, $\vec{B}$ and $\vec{H}$ was treated as a simple collinear equation. However, in a linear and non-dispersive medium, it has a more complicated expression. Generally, the relationship is expressed as the equation (2.3), where $\vec{D}$ is the convolution of permittivity and $\vec{E}$. It is known that convolution requires all values from earlier times, which increases the computer storage burden. Debye relaxation[139] and Lorentzian resonance are employed to describe the material dispersion and both of them have an exponentially decaying envelope, therefore, only require the previous value. In this thesis, Lorentz dispersion was chosen as linear material dispersion because its susceptibility is a decaying exponential sinusoidal function and it is easy to implement in the time domain.

2.5.1 Lorentz dispersion

In general, in a linear, dispersive and isotropic medium, the electric flux density $\vec{D}$ in the time domain is expressed as the convolution:

$$\vec{D}(t) = \varepsilon_0 \varepsilon_\infty \vec{E}(t) + \varepsilon_0 \int_{\tau=0}^{t} \vec{E}(t-\tau)\chi^{(1)}(\tau)d\tau \tag{2.43}$$

where $\chi^{(1)}(t)$ is the linear susceptibility. The relative permittivity of Lorentz medium with P pole pairs in the frequency domain is:

$$\varepsilon(\omega) = \varepsilon_\infty + \sum_{p=1}^{P} \frac{(\varepsilon_{s,p} - \varepsilon_\infty)\omega_p^2}{\omega_p^2 + 2j\omega\delta_p - \omega^2} \tag{2.44}$$

where ε_∞ is the relative permittivity at infinite frequency; $\varepsilon_{s,p}$ is the relative permittivity at zero frequency of p'th pole pair; ω_p is the frequency of p'th pole pair, which is undamped resonant frequency; and δ_p is the damping coefficient of p'th pole pair. By doing inverse Fourier transform of the equation (2.44), the linear susceptibility of each pole pair in the time domain is obtained:

$$\chi^{(1)}(t) = \frac{(\varepsilon_s - \varepsilon_\infty)\omega_0^2}{\sqrt{\omega_0^2 - \delta^2}}\, e^{-\delta t} \sin(\sqrt{\omega_0^2 - \delta^2}\, t)\mathrm{U}(t) \tag{2.45}$$

As a result, equation (2.43) is re-written as:

$$\vec{D}(t) = \varepsilon_0 \varepsilon_\infty \vec{E}(t) + \varepsilon_0 \sum_{p=1}^{P} \int_{\tau=0}^{t} \vec{E}(t-\tau)\chi_p^{(1)}(\tau)d\tau \tag{2.46}$$

2.5.2 Piecewise linear recursive convolution of linear medium

Piecewise linear recursive convolution (PLRC) method was firstly presented in 1996 by Kelley and Luebbers[140] to analyse the linear dispersive media and it is an implement of RC. PLRC owns the advantages of RC, such as fast speed, few requirements for memory and an easy application in multiple poles. In addition, it improves the accuracy of RC and it is no longer a drawback. In this thesis, PLRC is the primary technique for computing the linear susceptibility functions and was subsequently extended to solve the nonlinear case in Section 2.6.

Using the PLRC method, $\vec{E}(t)$ is assumed to be linear in a time interval:

$$\vec{E}(t) = E^n + \frac{E^{n+1} - E^n}{\Delta t}(t - n\Delta t)$$

$$n\Delta t \le t \le (n+1)\Delta t \tag{2.47}$$

Similarly,

$$\vec{E}(n\Delta t - \tau) = E^{m+1} + \frac{E^m - E^{m+1}}{\Delta t}[\tau - (n-m-1)\Delta t]$$

$$(n-m-1)\Delta t \le \tau \le (n-m)\Delta t \tag{2.48}$$

If we make $\vec{D}(t) = \vec{D}(n\Delta t)$ and $\vec{E}(t) = \vec{E}(n\Delta t)$, then the formula (2.46) is modified as:

$$D^n = \varepsilon_0 \varepsilon_\infty E^n + \varepsilon_0 \sum_{p=1}^{P} \sum_{m=0}^{n-1} [E^{m+1} (\psi_{p,0}^L)^{n,m} + (E^m - E^{m+1}) (\psi_{p,1}^L)^{n,m}] \tag{2.49}$$

where,

$$(\psi_{p,0}^L)^{n,m} = \int_{(n-m-1)\Delta t}^{(n-m)\Delta t} \chi_p^{(1)}(\tau)d\tau \tag{2.50a}$$

$$(\psi_{p,1}^{L})^{n,m} = \frac{1}{\Delta t}\int_{(n-m-1)\Delta t}^{(n-m)\Delta t}[\tau - (n-m-1)\Delta t]\chi_p^{(1)}(\tau)\, d\tau \tag{2.50b}$$

However, $\chi_p^{(1)}(\tau)$ is defined in the formula (2.45) and it cannot apply RC directly to update values. According to the solution proposed by Luebbers in Reference[137], a complex format of susceptibility is defined as follows:

$$\hat{\chi}_p^{(1)}(t) = \alpha_p^L\, e^{-\gamma_p^L t} \tag{2.51a}$$

$$\chi_p^{(1)}(t) = Re\,[\,\hat{\chi}_p^{(1)}(t)\,] \tag{2.51b}$$

Compared to the formula (2.44), it is simple to determine the parameters in the formula (2.51):

$$\alpha_p^L = -\,j\frac{(\,\varepsilon_s - \varepsilon_\infty\,)\,\omega_0^2}{\sqrt{\omega_0^2 - \delta^2}} \tag{2.52}$$

$$\gamma_p^L = \delta - j\sqrt{\omega_0^2 - \delta^2} \tag{2.53}$$

where $j = \sqrt{-1}$. Now that the linear susceptibility is expressed in exponential form, it is possible to utilize PLRC to update parameters:

$$(\psi_{p,0}^{L})^{n+1,m} = (\psi_{p,0}^{L})^{n,m}\, e^{-\gamma_p^L \Delta t} \tag{2.54a}$$

$$(\psi_{p,1}^{L})^{n+1,m} = (\psi_{p,1}^{L})^{n,m}\, e^{-\gamma_p^L \Delta t} \tag{2.54b}$$

Then, the RC approach can be employed to solve the sum function in formula (2.49), which is simplified as:

$$D^n = \varepsilon_0\varepsilon_\infty E^n + \sum_{p=1}^{P}(P_p^L)^n \tag{2.55}$$

$$(P_p^L)^n = (P_p^L)^{n-1}e^{-\gamma_p^L \Delta t} + \varepsilon_0[\,E^n(\psi_{p,0}^{L})^{n,n-1} + (E^{n-1} - E^n)\,(\psi_{p,1}^{L})^{n,n-1}] \tag{2.56}$$

By substituting equation (2.56) into equation (2.55), a linear updating equation is obtained. Once the value of D^n has been obtained, together with the values of the previous time step $(P_p^L)^{n-1}$ and E^{n-1}, it is possible to gain a linear equation of E^n which is simple to solve.

2.6 Nonlinearity

When electromagnetic waves are propagated in a nonlinear medium, some special characteristics appear and these are described as nonlinearity. This is usually observed at a very high intensity. A variability of material's dielectric permittivity with the intensity of electric field or magnetic field leads to various velocities. The typical nonlinear optical effects are frequency-mixing processes, such as second-order nonlinear effects and third-order nonlinear effects. This approach to incorporate nonlinearity into FDTD algorithm is discussed in this section.

2.6.1 Nonlinear electric susceptibility theory

In Section 2.5.1, the electric polarization vector $\vec{P}$ was highlighted in the linear dispersion. There are higher-order terms in the nonlinear case:

$$\vec{P} = \varepsilon_0(\chi^{(1)}\vec{E} + \chi^{(2)}\vec{E}^2 + \chi^{(3)}\vec{E}^3 + \cdots) \tag{2.57}$$

where $\chi^{(1)}$ is the first-order(linear) dielectric susceptibility; $\chi^{(2)}$ is the second-order dielectric susceptibility; and $\chi^{(3)}$ is the third-order dielectric susceptibility. Second-order and higher order dielectric susceptibilities are nonlinear. The even-order susceptibility only exists in those crystals that are anisotropic and non-centrosymmetric; in contrast, the odd-order crystals exist in all types of materials.

2.6.2 Second-order nonlinear effects

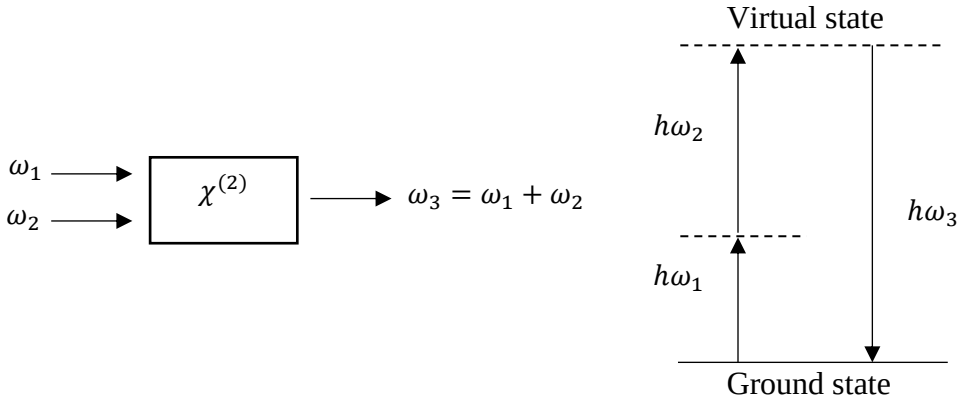

Fig. 2.6 Sum-frequency generation in second-order nonlinear crystal.

In the second-order nonlinear crystal, there are three-wave mixing processes: sum-frequency generation, difference-frequency generation and second-harmonic generation. Figure 2.6 describes the process of SFG. After propagation through the second-order nonlinear medium, the incident pulse which carries two different frequency components ω_1 and ω_2 would generate a new frequency ω_3, the sum of ω_1 and ω_2. SHG is a special case of SFG when $\omega_1 = \omega_2$.

SFG is also explained using a quantum transition description[141]. In the energy-level diagram (Figure 2.6) a molecule jumps from the ground state to an intermediate state by absorbing the energy of a photon whose frequency is ω_1, then this molecule leaves the intermediate state for a virtual state by absorbing the energy of another photon whose frequency is ω_2. With the annihilation of the two photons, the molecule is excited. After that, the excited molecule returns to the initial ground state and in the meantime, a new photon of sum frequency is generated.

In order to incorporate second-order nonlinearity into FDTD technique, the second term of polarization vector in equation (2.57) is simplified in Reference[142]. The only purely electronic and instantaneous part which is obtained is:

$$\vec{P}_i(t)^{(2)} = \varepsilon_0 \chi^{(2)} \vec{E}_j(t) \vec{E}_k(t) \tag{2.58}$$

where the second-order nonlinear susceptibility $\chi^{(2)}$ is an electric constant. The quadratic equation (2.58) is easily added in updating equations of the electric field.

2.6.3 Third-order nonlinear effects

In general, third-order non-linear effects are caused by instantaneous Kerr-type nonlinearity and Raman scattering. Kerr effect results in four-wave mixing, self-phase modulation and cross-phase modulation.

2.6.3.1 Introduction

In the third-order non-linear optical system, the relationship between $\vec{D}$ and $\vec{E}$ is expressed as:

$$\vec{D}(t) = \varepsilon_0 \varepsilon_\infty \vec{E}(t) + \varepsilon_0 \sum_{p=1}^{P} \int_{\tau=0}^{t} \vec{E}(t-\tau) \chi_p^{(1)}(\tau) d\tau$$

$$+ \varepsilon_0 \sum_{p=1}^{P} \iiint_0^t \vec{E}(t-\tau)\vec{E}(t-\tau_1)\vec{E}(t-\tau_2)\chi_p^{(3)}(t,\tau,\tau_1,\tau_2)\, d\tau d\tau_1 d\tau_2 \quad (2.59)$$

where $\chi_p^{(3)}(t,\tau,\tau_1,\tau_2)$ is the third-order susceptibility function. Using Born-Oppenheimer (BO) approximation[142], $\chi_p^{(3)}(t,\tau,\tau_1,\tau_2)$ is simplified as the following expression:

$$\chi_p^{(3)}(t,\tau,\tau_1,\tau_2) = \delta(t-\tau_1)\,\delta(\tau_2-\tau)\,[\,R_{p'}^{(3)}(\tau_1-\tau_2) + K_{p'}^{(3)}\delta(\tau_1-\tau_2)\,] \quad (2.60)$$

where δ is the Dirac delta function; $R_{p'}^{(3)}$ is the parameter represents Raman scattering[143]; and $K_{p'}^{(3)}$ is a constant, representing Kerr-type nonlinearity[144]. Substitute formula (2.60) to formula (2.59), $\vec{D}$ is modified as follows:

$$\vec{D}(t) = \varepsilon_0\varepsilon_\infty\vec{E}(t) + \varepsilon_0 \sum_{p=1}^{P} \int_{\tau=0}^{t} \vec{E}(\tau)\chi_p^{(1)}(t-\tau)d\tau$$
$$+ \varepsilon_0\,\vec{E}(t) \sum_{p=1}^{P} \int_{\tau=0}^{t} \left|\vec{E}(\tau)\right|^2 [\,R_{p'}^{(3)}(t-\tau) + K_{p'}^{(3)}\delta(t-\tau)\,]d\tau \quad (2.61)$$

2.6.3.2 Optical Kerr effect

In 1875, John Kerr[145] found a new relationship between electricity and light, which is considered as quadratic electro-optic effect and it took his family name. The Kerr effect is instantaneous nonlinearity, leading to an induced change in the refractive index that depends on the intensity or the square of the electric field. Therefore, the refractive index is given by

$$n = n_0 + n_2 I \quad (2.62)$$

where n_0 is the linear refractive index of material; n_2 is the nonlinear refractive index; and I is the intensity of the wave:

$$I = \frac{\varepsilon_0 c n_0}{2} E^2 \quad (2.63)$$

As a consequence, permittivity is expressed as:

$$\varepsilon = \varepsilon_0\varepsilon_r = \varepsilon_0(n_0 + \Delta n)^2 \approx \varepsilon_0\,(n_0^2 + 2n_0 n_2 I) \quad (2.64)$$

It is known that, in a linear case, the relationship between $\vec{D}$ and $\vec{E}$ is:

$$\vec{D}(t) = \varepsilon_0 \vec{E}(t) + \vec{P}(t)^{(1)} = \varepsilon_0 [1 + \text{Re}(\chi^{(1)})] \vec{E}(t)$$
$$= \varepsilon_0 \varepsilon_r{}' \vec{E}(t) \quad (2.65)$$

where

$$\varepsilon_r{}' = n_0^2 = 1 + \text{Re}(\chi^{(1)}) \quad (2.66)$$

When it is extended to the nonlinear case, the polarization vector is modified as:

$$\vec{P}(t) = \vec{P}(t)^{(1)} + \vec{P}(t)^{(3)} = \varepsilon_0 [\text{Re}(\chi^{(1)}) + \text{Re}(K^{(3)})|\vec{E}(t)|^2] \vec{E}(t) \quad (2.67)$$

As a consequence, equation (2.65) has been re-written as:

$$\vec{D}(t) = \varepsilon_0 \vec{E}(t) + \vec{P}(t) = \varepsilon_0 [1 + \text{Re}(\chi^{(1)}) + \text{Re}(K^{(3)}) |\vec{E}(t)|^2] \vec{E}(t)$$
$$= \varepsilon_0 [\varepsilon_r{}' + \text{Re}(K^{(3)})|\vec{E}(t)|^2] \vec{E}(t) = \varepsilon \vec{E}(t) \quad (2.68)$$

By substituting formula (2.66) and (2.68) for ε in formula (2.64), then:

$$\varepsilon_0 (n_0^2 + 2 n_0 n_2 I) = \varepsilon_0 [n_0^2 + \text{Re}(K^{(3)})|\vec{E}(t)|^2] \quad (2.69)$$

By replacing *I* with equation (2.63), it becomes possible to gain the real part of third-order nonlinear susceptibility (Kerr coefficient):

$$\text{Re}(K^{(3)}) = n_0^2 n_2 \varepsilon_0 c \quad (2.70)$$

2.6.3.3 Four-wave mixing

Four-wave mixing is an attractive frequency-mixing process caused by the Kerr effect. If the input wave contains three frequencies ω_1, ω_2 and ω_3, output wave obtained would contain frequencies $\pm\omega_1 \pm \omega_2 \pm \omega_3$. However, the newly generated frequencies that most influence optical wave are the frequencies $\omega_\text{i} + \omega_\text{j} - \omega_\text{k}$. FWM is also presented in the interaction

between the two frequency components. Figure 2.7 shows the quantum transition of the FWM process. A molecule jumps from the ground state to virtual state by absorbing the energy of two photons of frequencies ω_1 and ω_2, and then returns to the ground state and releases energy; in the meantime, two new photons of new frequencies ω_3 and ω_4 are created. The second sub-figure in Figure 2.7 indicates the values of incident frequency components and new generated frequency components. It is noted that ($\omega_1 > \omega_2$):

$$\omega_3 = 2\omega_1 - \omega_2 \quad ; \quad \omega_4 = 2\omega_2 - \omega_1 \tag{2.71}$$

It is interesting that the interval between the two adjacent frequencies is constant and is equal to the difference in the original two frequencies. Over time, more new frequency components are produced so that a frequency comb is generated.

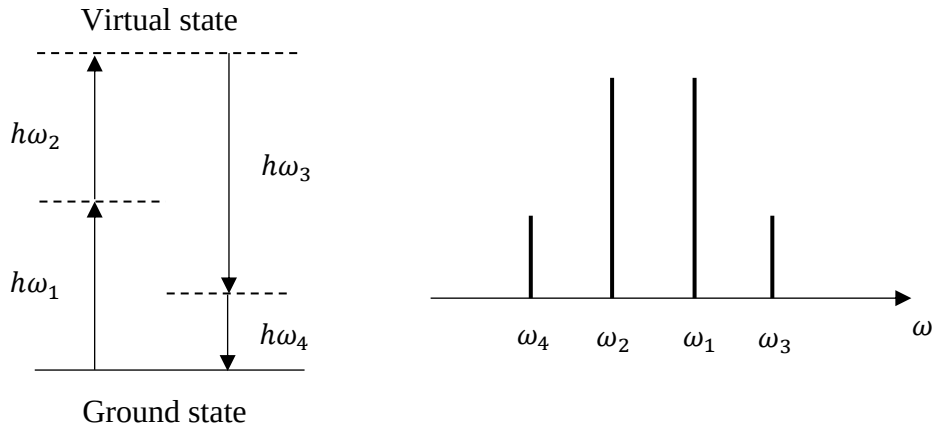

Fig. 2.7 Four-wave mixing in third-order nonlinear medium.

2.6.3.4 Self-phase modulation and cross-phase modulation

In third-order nonlinear medium, apart from four-wave mixing, self-phase modulation and cross-phase modulation are also primary frequency-mixing processes. All of these three effects result from Kerr nonlinearity. The comparison of polarization vectors of three effects is as follows:

$$\text{FWM: } \vec{P}(t)^{(3)} = \varepsilon_0 \left[\text{Re}\left(K^{(3)}\right)\left|\vec{E}_i(t)\right|^2\right]\vec{E}_j^*(t) \quad (i \neq j) \tag{2.72a}$$

$$\text{SPM: } \vec{P}(t)^{(3)} = \varepsilon_0 \left[\text{Re}\left(K^{(3)}\right)\left|\vec{E}_i(t)\right|^2\right]\vec{E}_i(t) \tag{2.72b}$$

$$\text{XPM: } \vec{P}(t)^{(3)} = \varepsilon_0 \left[\text{Re}\left(K^{(3)}\right)\left|\vec{E}_i(t)\right|^2\right]\vec{E}_j(t) \quad (i \neq j) \tag{2.72c}$$

SPM is the phase shift which happens in the optical wave, leading to a wider frequency spectrum. It is applied to spectral broadening and super-continuum. In contrast, XPM is the interaction and the one frequency component that affects the phase of another frequency component in the optical wave.

2.6.3.5 Raman scattering

Raman scattering is a phenomenon where the frequency of optical wave changes after it is scattered. In general, a photon exhibits Rayleigh scattering when it is scattered from a molecule or atom and has the same frequency as the incident pulse. However, a fairly small portion of photons exchange their energy with the molecule or atom, having a lower frequency than incident pulse. Reference [128] gives an equation to describe Raman response:

$$R^{(3)}(t) = R_0^{(3)} \frac{\tau_1^2+\tau_2^2}{\tau_1\tau_2^2} e^{-\frac{t}{\tau_2}} \sin(\frac{t}{\tau_1})\text{U}(t) \tag{2.73}$$

where $R_0^{(3)}$ is the strength of Raman scattering; $1/\tau_1$ is the optical phonon frequency; and τ_2 is the lifetime of the optical phonon.

2.6.4 Piecewise linear recursive convolution of nonlinear medium

As with the linear case, a nonlinear medium also employs PLRC to compute the approximation value of an electric field based on the value of the electric flux density. Equation (2.57) indicates the polarization vector which has higher-order terms. In this thesis, second and third-order susceptibility are considered. Second-order nonlinearity is applied only when focusing on the SHG process and it is simple to incorporate it in the FDTD method. Thus, in most cases, optical waveguide has only linear dispersion and third-order non-linearity. So the relationship between $\vec{D}$ and $\vec{E}$ is given by:

$$\vec{D}(t) = \varepsilon_0\varepsilon_\infty\vec{E}(t) + \sum_{p=1}^{P}\vec{P}_p^L(t) + \vec{E}(t)\sum_{p'=1}^{P'}\vec{P}_{p'}^{NL}(t) + \varepsilon_0 K_{p'}^{(3)}\left|\vec{E}(t)\right|^2\vec{E}(t) \tag{2.74}$$

where

$$\vec{P}_p^L(t) = \varepsilon_0 \int_{\tau=0}^{t} \vec{E}(\tau)\chi_p^{(1)}(t-\tau)d\tau \quad (2.75)$$

$$\vec{P}_{p'}^{NL}(t) = \varepsilon_0 \int_{\tau=0}^{t} \left|\vec{E}(\tau)\right|^2 R_{p'}^{(3)}(t-\tau)d\tau \quad (2.76)$$

Formula (2.75) is solved in Section 2.5.2. Similarly, using equation (2.48), it is possible to obtain a further expression of the formula (2.76):

$$(P_{p'}^{NL})^n = \varepsilon_0 \sum_{m=0}^{n-1}[\,(E^{m+1})^2\,(\psi_{p',0}^{NL})^{n,m} + 2E^{m+1}(E^m - E^{m+1})(\psi_{p',1}^{NL})^{n,m} + (E^m - E^{m+1})^2(\psi_{p',2}^{NL})^{n,m}\,] \quad (2.77)$$

where,

$$(\psi_{p',0}^{NL})^{n,m} = \int_{(n-m-1)\Delta t}^{(n-m)\Delta t} R_{p'}^{(3)}(\tau)d\tau \quad (2.78a)$$

$$(\psi_{p',1}^{NL})^{n,m} = \frac{1}{\Delta t}\int_{(n-m-1)\Delta t}^{(n-m)\Delta t}[\tau - (n-m-1)\Delta t]\, R_{p'}^{(3)}(\tau)\, d\tau \quad (2.78b)$$

$$(\psi_{p',2}^{NL})^{n,m} = \frac{1}{(\Delta t)^2}\int_{(n-m-1)\Delta t}^{(n-m)\Delta t}[\tau - (n-m-1)\Delta t]^2\, R_{p'}^{(3)}(\tau)\, d\tau \quad (2.78c)$$

In order to utilize RC approach, it is possible to define a complex format of non-linear susceptibility as a linear case as presented in reference [137]:

$$\hat{R}_{p'}^{(3)}(t) = \alpha_{p'}^{NL}\, e^{-\gamma_{p'}^{NL} t} \quad (2.79)$$

$$R_{p'}^{(3)}(t) = Re\,[\,\hat{R}_{p'}^{(3)}(t)] \quad (2.80)$$

According to the equation (2.73),

$$\alpha_p^{NL} = -\mathrm{j}\,\frac{\tau_1^2+\tau_2^2}{\tau_1\tau_2^2}R_0^{(3)} \quad (2.81)$$

$$\gamma_p^{NL} = \frac{1}{\tau_2} - j\frac{1}{\tau_1} \quad (2.82)$$

Therefore, the exponential form in equation (2.79) gives the following recursive iteration:

$$(\psi_{p',0}^{NL})^{n+1,m} = (\psi_{p',0}^{NL})^{n,m}\, e^{-\gamma_{p'}^{NL}\Delta t} \quad (2.83a)$$

$$(\psi_{p',1}^{NL})^{n+1,m} = (\psi_{p',1}^{NL})^{n,m}\, e^{-\gamma_{p'}^{NL}\Delta t} \tag{2.83b}$$

$$(\psi_{p',2}^{NL})^{n+1,m} = (\psi_{p',2}^{NL})^{n,m}\, e^{-\gamma_{p'}^{NL}\Delta t} \tag{2.83c}$$

Then, it is possible to employ the RC approach to solve the sum function in formula (2.77), which is re-written as:

$$(P_{p'}^{NL})^{n} = (P_{p'}^{NL})^{n-1} e^{-\gamma_{p'}^{NL}\Delta t} + \varepsilon_0 \left[(E^n)^2 (\psi_{p',0}^{NL})^{n,n-1} \right.$$

$$\left. + 2E^n (E^{n-1} - E^n)(\psi_{p',1}^{NL})^{n,n-1} + (E^{n-1} - E^n)^2 (\psi_{p',2}^{NL})^{n,n-1} \right] \tag{2.84}$$

As a consequence, the updating equation of electric field in dispersive and nonlinear medium is a cubic equation, which could be solved by Newton's iteration.

This chapter introduced the FDTD algorithm and PLRC method in incorporating linear dispersion and nonlinearity. Together with the excitation source and PML absorbing boundary condition, simulation of optical waveguide is possible to obtain, which will be demonstrated in Chapter 3.

Chapter 3

Simulation for Optical Waveguides

This chapter introduces the methods of simulation adopted for nonlinear optical waveguides, presents the way to incorporate linear dispersion and nonlinearity and analyses the optimization of PML absorbing boundary conditions. In addition, parallel programing and high−performance computation are applied.

3.1 Basic simulation of optical waveguide

3.1.1 Basic model

Based on the FDTD algorithm, the simulations of optical waveguides started from simple one-dimensional cases and subsequently extended to two- and three-dimensional space.

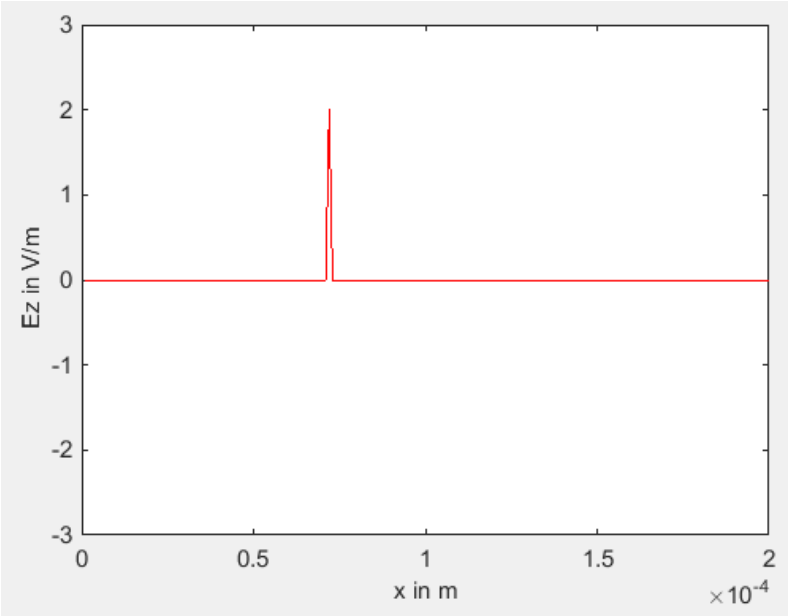

Fig. 3.1 Values of E-field in one-dimension program in MATLAB.

One-dimension program without linear dispersion and nonlinearity was done in MATLAB to validate the code. The movement of optical pulse was revealed based on the values of

component E_z. The excitation source was set at the beginning of E-field and its amplitude is 2 V/m. Figure 3.1 shows the values of E-field when the pulse propagates 75 μm in +*x* direction and the peak value of pulse is 2 V/m. In the lossless propagation, the peak value of pulse maintains 2 V/m, which is in agreement with the theory result.

Because an optical waveguide is now treated as a transmission medium of an optical pulse, even in three dimensional cases, the main energy of pulse propagates in one dimension. Therefore, the basic model of optical waveguides in the simulations has one extended longitudinal dimension. Perfectly matched layer is applied to limit the transverse simulation dimensions while circular boundary condition is applied on the longitudinal dimension.

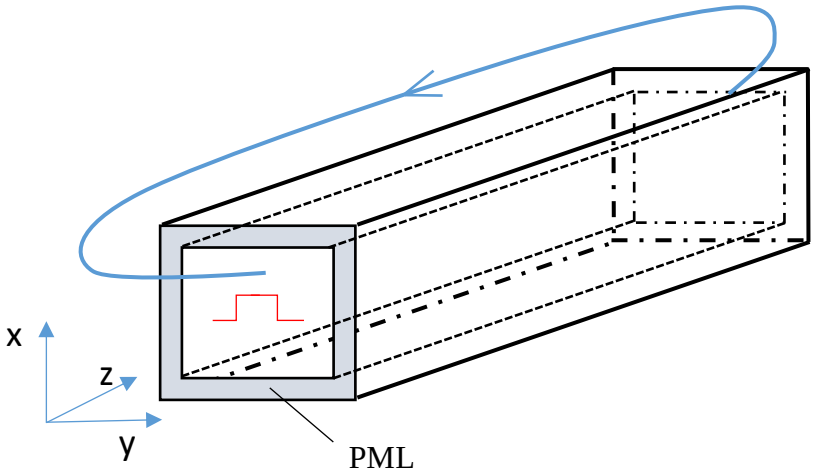

Fig. 3.2 A three-dimensional model of optical waveguides in the simulation. *X-y* plane is bounded with PML absorbing boundary conditions while *z*-direction has circular boundary.

A basic three−dimensional model of optical waveguides in the simulation is shown in Figure 3.2. The circular boundary condition is designed for the longitudinal dimension to re-use the channel for many times as long as the beginning of the optical pulse cannot catch up with the tail. This does not only reduce the size of the problem domain and dramatically decrease memory requirement, but also save the time for computation. At this point the transverse dimensions, *x-y* plane, are surrounded by PML absorbing boundary conditions so that the radiation energy is propagated in *x*- and *y*-directions and would be absorbed eventually without reflections.

Figure 3.3 shows how the circular boundary condition works. In order to exhibit the propagation of the energy of an optical pulse, energy flux is introduced. Energy flux is the sum

of Poynting vector ($\vec{S} = \vec{E} \times \vec{H}$) over the whole cross-section, representing the rate of energy transfer along the longitudinal direction in Figure 3.2, which is defined by:

$$\iint (\vec{E} \times \vec{H})\, \mathrm{dS} \tag{3.1}$$

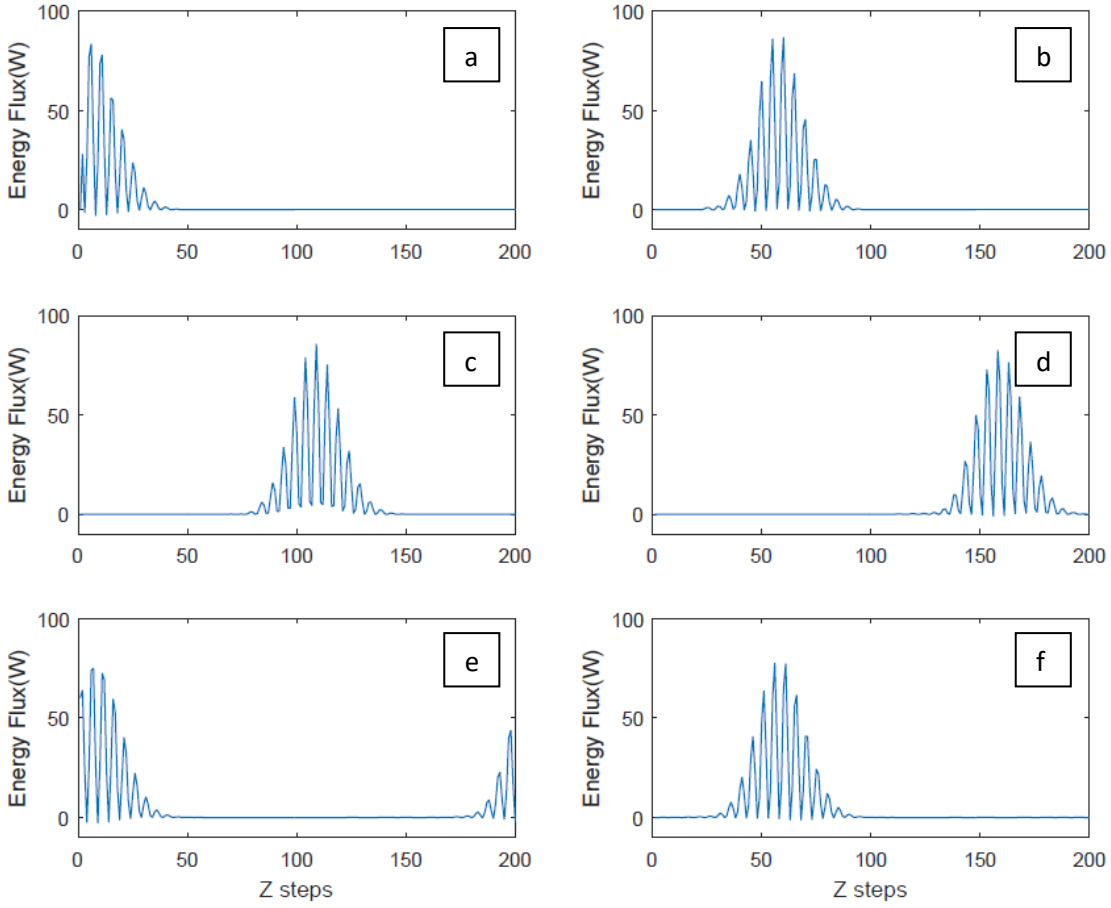

Fig. 3.3 Propagation of energy flux over *x*-*y* plane in optical waveguide with circular boundary condition in *z*-direction. Sub-figures (a)-(f) represent the distribution of energy flux in *z*-direction at 600, 1000, 1400, 1800, 2200 and 2600 time steps, respectively.

In Figure 3.3, six sub-figures represent the energy flux over transverse dimensions in a optical waveguide at various time steps. In sub-figure (a), the pulse starts from the left end of the waveguide at 600 time steps. Over time, it propagates longer distance and reaches the right side at around 1800 time steps. Thanks to the cyclic boundary condition, the pulse continues to propagate and occurs at the left-beginning again. Therefore, although the pulse seems at the same position in sub-figures (b) and (f), the propagation time is 1000 and 2600 time steps respectively. Indeed, the propagation distance in sub-figure (f) is 200 grids longer. As a consequence, long-distance propagation does not require a waveguide with the actual length in the simulation.

3.1.2 Implementation of FDTD algorithm

In general, only the electric field $\vec{E}$ and the magnetic field $\vec{H}$ are updated in the FDTD algorithm. Since the updating equation between $\vec{H}$ and $\vec{D}$ stays the same in all the simulations in this thesis and the relationship of $\vec{D}$ and $\vec{E}$ varies in the different mediums, $\vec{D}$ is updated as an intermediate step. The main steps of the FDTD approach in the simulation are briefly shown as a flow diagram in Figure 3.4.

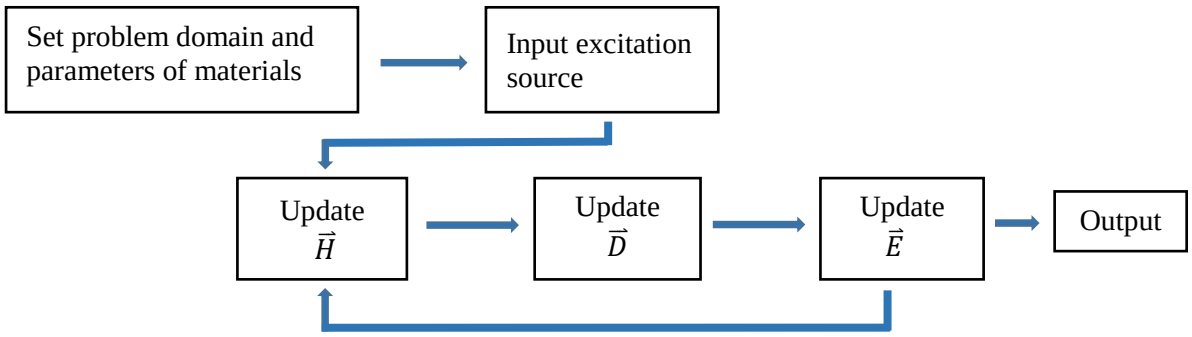

Fig. 3.4 Flow diagram of the simulation of waveguides

The first step is setting the problem domain and the values of parameters, such as the structure of the waveguide and the linear dispersion or nonlinear characteristics of the medium. The models of optical waveguides vary depending on the materials and design. For instance, deep-etched AlGaAs waveguide consists of multiple layers of AlGaAs with different Al concentrations, bounded by both air layer and PML. In contrast, silicon nitride nanowire may be built of core layer (silicon nitride), cladding layer (silicon dioxide) and PML absorbing boundary condition. The following sections in this chapter introduce the way to incorporate the parameters of materials, including linear dispersion and nonlinearity.

The second step is inputting excitation sources to the optical waveguide. The incident source of waveguides is usually calculated with the mode solver in MATLAB (this will be further discussed in Section 3.2). Thus, the optical wave is initially propagated inside the waveguide as a well-confined mode so that the main energy is maintained in propagation.

The third step is running the updating loop. At each time step, $\vec{H}$, $\vec{D}$ and $\vec{E}$ of all the spatial points are updated. In the updating loop, magnetic field $\vec{H}$ is the first to be updated by the

values of $\vec{E}$, and then $\vec{D}$ is updated by the values of $\vec{H}$. After that, $\vec{\mathrm{E}}$ is updated based on the values of $\vec{D}$. Because the excitation source is set as a hard source in the simulations, $\vec{J}$ and $\vec{M}$ are equal to zero. As a result, Maxwell's equations are modified as:

$$\nabla \times \vec{E} = -\mu \frac{\partial \vec{H}}{\partial t} \tag{3.2a}$$

$$\nabla \times \vec{H} = \frac{\partial \vec{D}}{\partial t} \tag{3.2b}$$

According to the formulae (3.2a-b), updating equations of $\vec{H}$ and $\vec{D}$ are obtained and remain the same in various mediums. As for the updating equation of $\vec{E}$, it is simple in the cases of linear and non-dispersive material, where permittivity is a constant and $\vec{E}$ is updated:

$$\vec{E} = \frac{\vec{D}}{\varepsilon} \tag{3.3}$$

While in birefringence material, the permittivity is a tensor. In the dispersive and nonlinear medium, $\vec{D}$ is the convolution of $\vec{E}$ and permittivity, solved by PLRC (as was introduced in the previous chapter).

The final step is output. It is important to focus on the energy flux, which is defined in formula (3.1), rather than the electric or magnetic field. To analyse the output data, firstly, fast Fourier transform (FFT) is used to describe energy flux in the frequency domain. Secondly, self-deconvolution is utilized to depict the actual power spectrum of the output wave, because in the FFT convolution, multiplication in the time domain corresponds to the convolution in the frequency domain.

3.1.3 Numerical stability

To ensure the numerical stability in the simulations of optical waveguides, CFL conditions must be fulfilled. In the practical simulations, in order to save memory and runtime, grid sizes of the three dimensions are not always uniform. Therefore, for a three-dimensional case, the common choice of grid size and time step satisfy the condition:

$$\Delta t = \frac{\Delta_{\min}}{2c} \tag{3.4}$$

where Δmin is the minimum value of grid sizes. Another possible cause of unstable values is that the grid size is not small enough when it is compared to the wavelength. As was shown in Section 2.2.2, the maximum value of the grid size should be:

$$\Delta_{\max} \ll \frac{\lambda_{\min}}{20} \tag{3.5}$$

The numerical stability of simulation is guaranteed by the formulae (3.4) and (3.5). The size of grid could be adjusted based on the geometry of waveguide and cuboidal grids with significantly difference values in each dimension does not cause instability.

Besides, Lorentz resonance may lead to numerical instability so that one should either be careful when fitting the refractive index into Sellmeier equation or engineer the damping coefficient to avoid the instability.

3.2 Waveguide source

The excitation source was described in the time domain and discussed in Section 2.3. Simulating the CW case, the sinusoidal wave is the ideal choice. While simulating the pulsed laser source, Gaussian pulse is the most suitable because it can create an optical wave with the desired frequency. Now that the simulations of the optical waveguide in this thesis are three-dimensional, incident sources should be analysed in the space domain as well.

To launch a polarized mode in simulation to achieve efficient propagation, mode solver[146] is applied to calculate the fundamental mode of optical waveguides. Mode solver is a toolbox running in MATLAB. Having the width and height of waveguide, as well as the refractive indices of all the materials, mode solver is able to compute the fundamental and higher-order modes of waveguides with the full- or semi-vector finite difference method. In this thesis, all the waveguides are simulated in three dimensions and all six components of electric and magnetic fields are updated, so the full-vector technique is applied. What mode solver provides is not only the effective index of waveguide, but also the magnitude of all the components of $\vec{E}$ and $\vec{H}$. It is shown in Figure 3.5 that the TE fundamental mode of a silicon channel waveguide is calculated in mode solver using full-vector method. The core layer of the waveguide is silicon and its height and width are 200 nm and 400 nm, respectively. The upper cladding layer is air layer while the lower cladding layer is silicon dioxide. Six components of

the fundamental mode are plotted in the six sub-figures. Therefore, the main energy of mode is propagated in H_y and E_x components, in contrast, other components have relatively smaller magnitudes. Once the mode of the waveguide is obtained, the values of the fundamental mode are treated as the peak values of incident pulse. Together with the Gaussian pulse, the waveguide source in space and time domain is determined.

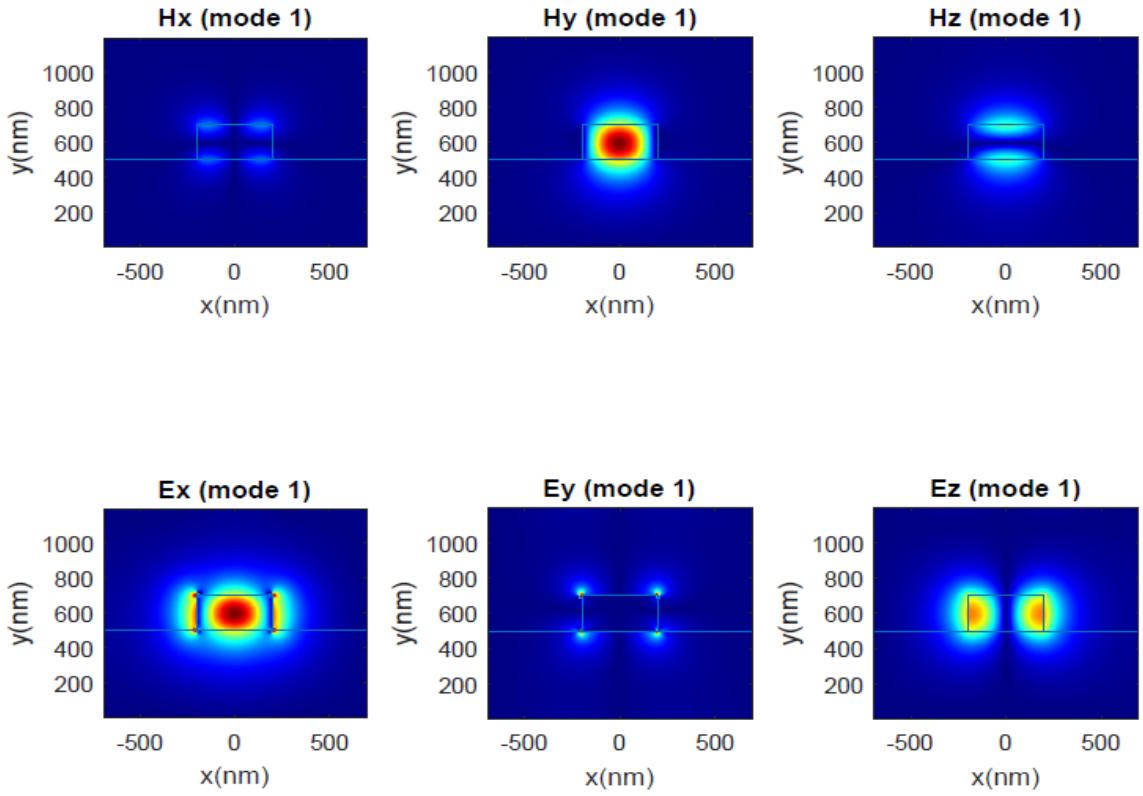

Fig. 3.5 TE fundamental mode in Silicon channel waveguide. Electric field components and magnetic field components which is computed with full-vector method in mode solver in MATLAB.

3.3 Incorporating linear material dispersion

As was highlighted in Section 2.5.1, the linear material dispersion is considered as Lorentzian resonance. To incorporate Lorentz dispersion in the simulation, it is necessary to fit the experimental measurements of refractive index into the Sellmeier equation over a specified wavelength range. The Sellmeier equation is defined as:

$$n^2 = A + \frac{B1*\lambda^2}{\lambda^2 - C1} + \frac{B2*\lambda^2}{\lambda^2 - C2} + \frac{B3*\lambda^2}{\lambda^2 - C3} \tag{3.6}$$

where n is the refractive index and parameters A, B, C are the fitting co-efficients. Equation (3.6) is an example of three pole pairs and the number of pole pairs could be adjusted to provide a good fit.

The Sellmeier equation has a similar description to equation (2.44). Equation (2.44) depicts the Lorentz resonance in the frequency domain while equation (3.6) depicts Lorentz resonance in the wavelength domain. By comparing these two equations, it is relatively simple to get the values of relative permittivity at zero- or infinite-frequency, as well as the resonant frequency of each pole pair. Therefore, the linear susceptibility in the equation (2.45) is obtained. Furthermore, updating equations of $\vec{E}$ in the linear dispersive medium can be gained based on the formulas (2.48-2.56).

3.4 Incorporating nonlinearity

In the simulation of second-order nonlinear cases, the only required parameter is the second-order nonlinear susceptibility. Therefore, the second-order polarization vector defined in the quadratic equation (2.58) is obtained and easily incorporated. In the simulation of third-order nonlinear cases, both the Kerr effect and Raman scattering are taken into consideration. According to the formula (2.70), the real part of Kerr-type nonlinearity is gained as long as the nonlinear refractive index of material is measured. With regard to the Raman-type nonlinearity, all the parameters in the formula (2.73) should be provided, including Raman strength, phonon frequency and phonon lifetime. After that, third-order nonlinearity is incorporated in the simulation on the basis of equations (2.74-2.84) and a cubic equation is obtained.

In general, materials have odd-order susceptibilities, such as linear dispersion and third-order nonlinearity. Second-order nonlinearity only exists in anisotropic and non-centrosymmetric material. Because the higher-order nonlinearities are not included in the simulations in this thesis, the updating equation of $\vec{E}$ is usually a cubic equation whether the second-order nonlinearity exists or not. To further solve the cubic equation of $\vec{E}$, the Newton-Raphson method is applied and it is effective in finding the real root, which is expressed as:

$$x_1 = x_0 - \frac{f(x_0)}{f\prime(x_0)} \quad \ldots \quad x_{n+1} = x_n - \frac{f(x_n)}{f\prime(x_n)} \tag{3.7}$$

where x_0 is the initial guess of the root. In this simulation of optical waveguides, x_0 is the value of $\vec{E}$ at the previous time step and $\vec{E}$ is updated through several iterations. In general FDTD cases, three iterations could guarantee 10^{-4} convergence criterion[147].

3.5 Phase matching conditions

In the optical waveguide, frequency-mixing processes caused by nonlinearity have attracted much attention. Generally, phase matching conditions should be fulfilled to attain efficient interactions among waves inside the waveguide. Otherwise, even strong nonlinearity cannot ensure the generation of new frequency components. Therefore, the phase matching conditions of SHG and FWM need to be discussed.

3.5.1 Phase matching condition of SHG

In the second-order nonlinear medium, the electric field $\vec{E}(\omega)$ of the incident wave and the electric field $\vec{E}(2\omega)$ of the generated frequency-doubled wave of SHG case are described as:

$$\vec{E}_1(\omega, z) = a_1 A_1(z) e^{ik_1 z} \tag{3.8a}$$

$$\vec{E}_2(2\omega, z) = a_2 A_2(z) e^{ik_2 z} \tag{3.8b}$$

where a_1, a_2 are the unit vectors along the polarization direction; $A_1(z)$, $A_2(z)$ are the amplitude functions; and k_1 and k_2 are the magnitude of wave vectors of two waves. The phase mismatch factor of SHG is defined as:

$$\Delta k = 2k_1 - k_2 \tag{3.9}$$

Therefore, coherence length - the effective interaction length - is determined by Δk:

$$l_c = \frac{\pi}{\Delta k} \tag{3.10}$$

It is noted that $\Delta k \neq 0$ is in the equation (3.10). When $\Delta k = 0$, the coherence length is infinite, so it is called phase matching condition. The comparison of the efficiency of SHG in waveguides is indicated in the Figure 3.6: the red line means the second-harmonic power

against distance in the phase-matched waveguide while the blue line means the second-harmonic power against distance in the phase-mismatched waveguide.

When the phase matching condition is satisfied, the second-harmonic power grows significantly from zero value as the propagation distance increases. In contrast, in the phase-mismatched waveguide, the second-harmonic power grows gradually from zero value when the propagation distance increases from zero to a coherence length l_c. However, as the propagation distance grows from l_c to $2l_c$, the second-harmonic power drops from the peak to zero value again. The change is periodic and repeated every two coherence lengths.

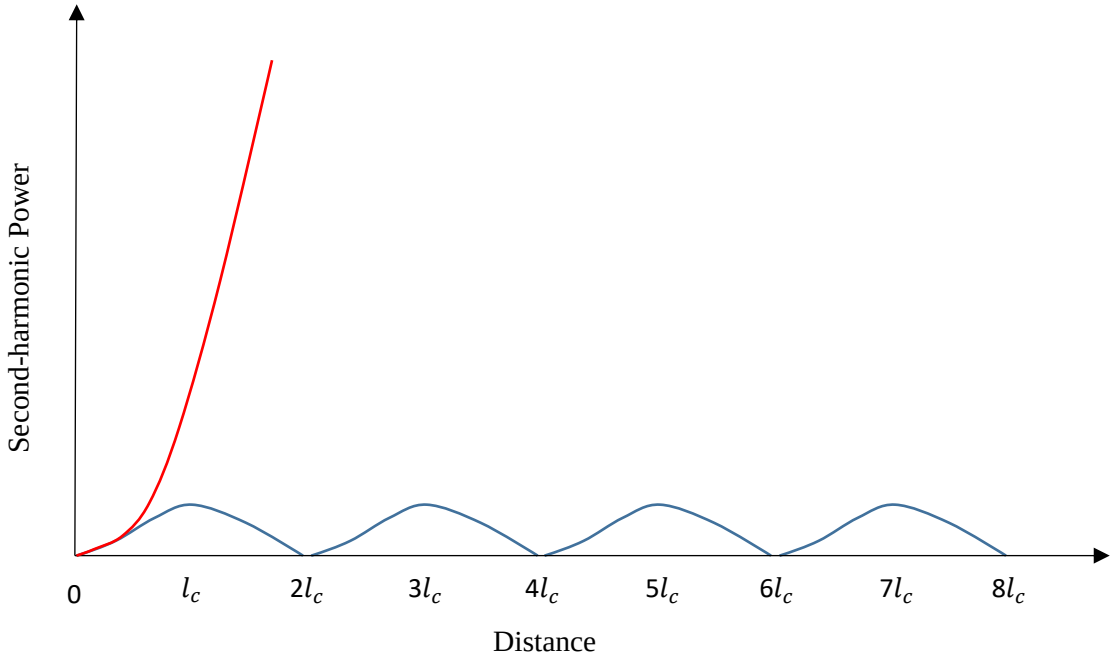

Fig. 3.6 Second-harmonic power. The red line represents phase-matched waveguide and the blue line represents phase-mismatched waveguide.

In order to attain efficient SHG, the phase matching condition should be satisfied. When the optical pulse is propagated inside a second-order medium, in phase-matched SHG frequency-mixing processes, conservation of energy and momentum is maintained within the interaction among three waves:

$$\hbar\omega_1 + \hbar\omega_1 = \hbar\omega_2 \tag{3.11}$$

$$k_1 + k_1 = k_2 \tag{3.12}$$

where $\hbar$ is the Plank constant. Substitute $\lambda = \frac{2\pi c}{\omega}$ and $k = \frac{2\pi n}{\lambda}$ into equation (3.11-3.12), and equations are modified as:

$$\lambda_1 = 2\lambda_2 \tag{3.13}$$

$$\frac{4\pi n_{\omega_1}}{\lambda_1} = \frac{2\pi n_{2\omega_1}}{\lambda_2} \tag{3.14}$$

As a consequence, the phase matching requirement of SHG is:

$$n_{\omega_1} = n_{2\omega_1} \tag{3.15}$$

where n means the refractive index. However, the optical waveguide has multiple layers of different materials, so n is not decided by a certain material but by the effective refractive index of the waveguide. Generally, for normal dispersion, if the frequency increases, the effective index of waveguide should also increase. Thus, it seems impossible to achieve the phase matching condition described in the equation (3.15) unless the polarization of the initial wave and generated wave are different. According to the difference in the effective index caused by different polarizations, there are two ways to fulfill phase matching conditions.

Table 3.1 Two types of phase matching condition of SHG (TE and TM modes are fundamental).

Type \ Wave	Wave 1	Wave 2	Wave 3
Type I	TE (ω_1)	TE (ω_1)	TM ($2\omega_1$)
Type II	TE (ω_1)	TM (ω_1)	TE ($2\omega_1$)
Phase matching condition	$n_{(\text{eff1})} + n_{(\text{eff2})} = 2n_{(\text{eff3})}$		

Table 3.1 indicates two types of phase matching conditions in SHG. In the Type I phase matching condition the incident wave has TE polarization while the generated wave has TM polarization with doubled frequency. In the Type II phase matching condition, for [001] – grown zinc-blende crystalline structure, the incident wave consists of two perpendicular linear polarizations - TE fundamental mode and TM fundamental mode - while the second-harmonic wave consists of TE polarization.

3.5.2 Phase matching condition of FWM

In the third-order nonlinear medium, FWM is the essential frequency-mixing process. The input wave contains two or three frequency components and new frequency components are produced. Similar to the equation (3.8) in the SHG case, (taking two incident frequency components as an example) the electric field $\vec{E}(\omega_i)$ of the incident wave and the electric field $\vec{E}(\omega_j)$ of the generated wave are described as:

$$\vec{E}_i(\omega_i, z) = a_i A_i(z) e^{ik_i z} \qquad (i = 1,2) \tag{3.16a}$$

$$\vec{E}_j(\omega_j, z) = a_j A_j(z) e^{ik_j z} \qquad (j = 3,4) \tag{3.16b}$$

As a result, the phase mismatch factor of FWM is defined as:

$$\Delta k = k_1 + k_2 - k_3 - k_4 \tag{3.17}$$

The previous section explained that $\Delta k = 0$ was required for phase matching. While in the phase-matched FWM process, conservation of energy and momentum is maintained within the interaction among four waves:

$$\hbar\omega_1 + \hbar\omega_2 = \hbar\omega_3 + \hbar\omega_4 \tag{3.18}$$

$$k_1 + k_2 = k_3 + k_4 \tag{3.19}$$

As for general FWM cases, it is difficult to achieve the phase matching condition described in the formulae (3.18-3.19). A key parameter GVD is introduced and applied in order to evaluate the efficiency of interaction among frequency components in FWM. First, wave vector is defined as:

$$k(\omega) = \frac{n(\omega)\,\omega}{c} \tag{3.20}$$

For small changes in frequency, the Taylor series is appropriate for the expression of the approximation value of the wave vector:

$$k(\omega) = \frac{n(\omega_0)\omega_0}{c} + \frac{n'(\omega_0)\omega_0 + n(\omega_0)}{c}(\omega - \omega_0) + \frac{1}{2}\frac{n''(\omega_0)\omega_0 + 2n'(\omega_0)}{c}(\omega - \omega_0)^2 + \cdots$$

$$= k(\omega_0) + k'(\omega_0)(\omega - \omega_0) + \frac{1}{2} k''(\omega_0)(\omega - \omega_0)^2 + O(\omega - \omega_0)^3 \quad (3.21)$$

where ω_0 is the central frequency; $k(\omega_0)$ is inversely proportional to the phase velocity; $k'(\omega_0)$ is the reciprocal of group velocity; and $k''(\omega_0)$ is known as group velocity dispersion [148]. Phase velocity depicts the velocity of phase of any one frequency component in the propagating wave while group velocity describes the velocity of the wave envelope. Usually, GVD is utilized to describe how the duration of the propagating wave is affected by the dispersion of the waveguide, including material and geometric dispersion. Indeed, it is a parameter which depicts the difference among the wave velocities in the wave that carry different frequencies. Large GVD means the difference is significant, which results in a small overlap among waves, even walk-off effect. Walk-off effect means that there is no overlap and no interaction between waves with various velocities. As a consequence, there are few effective interactions among the waves so that the frequency-mixing processes caused by nonlinearity are weak. On the contrary, small GVD provides large overlap and effective interactions among waves. Hence, zero-GVD point is the phase matching condition of FWM.

Equation (3.21) has demonstrated GVD as the second order derivative of wave vector with respect to frequency. As long as the effective index in equation (3.20) is expressed as a function of frequency, GVD could be calculated. Now that the effective index of waveguide is decided by linear dispersion, which is caused by material-dependent dispersion and geometry-dependent dispersion, the zero-GVD point is looked for by engineering the structure of the waveguide.

With mode solver, a sequence of effective indices for optical waveguides is computed through changing the wavelength of incident wave and the corresponding refractive index of materials. Then the data is fitted into the following formula over a limited wavelength range:

$$n(\lambda) = \mathrm{b0} + \mathrm{b1}(\lambda - \lambda_0) + \mathrm{b2}(\lambda - \lambda_0)^2 + \mathrm{b3}(\lambda - \lambda_0)^3 + \mathrm{b4}(\lambda - \lambda_0)^4 \quad (3.22)$$

where λ_0 is the central wavelength and b0-b4 are the co-efficients of fitting. According to the equation (3.21), the value of GVD is easily gained. To find the zero-point of GVD, the structure of the waveguide is engineered. For example, the height of the waveguide is set as constant and the width is changed to check GVD values. When comparing the values of GVD among different structures, zero-GVD could be finally achieved by adjusting the geometry.

3.6 Optimization of PML

PML and CPML absorbing boundary conditions were proposed in Section 2.4. PML works well in short-time simulations but it is memory-consuming for long-time cases, in which the thickness of PML should increase a lot to avoid reflection. CPML is a better choice to save the memory and to absorb the evanescent wave when the runtime of simulation is lengthy. However, calculation of CPML is much more complicated than PML, which means the times of calculation are significantly increased and the simulation with CPML is time-consuming. As a consequence, it is a compromise between memory and time. To evaluate the values of coefficients in PML, optimization in a one-dimension PML test was carried out.

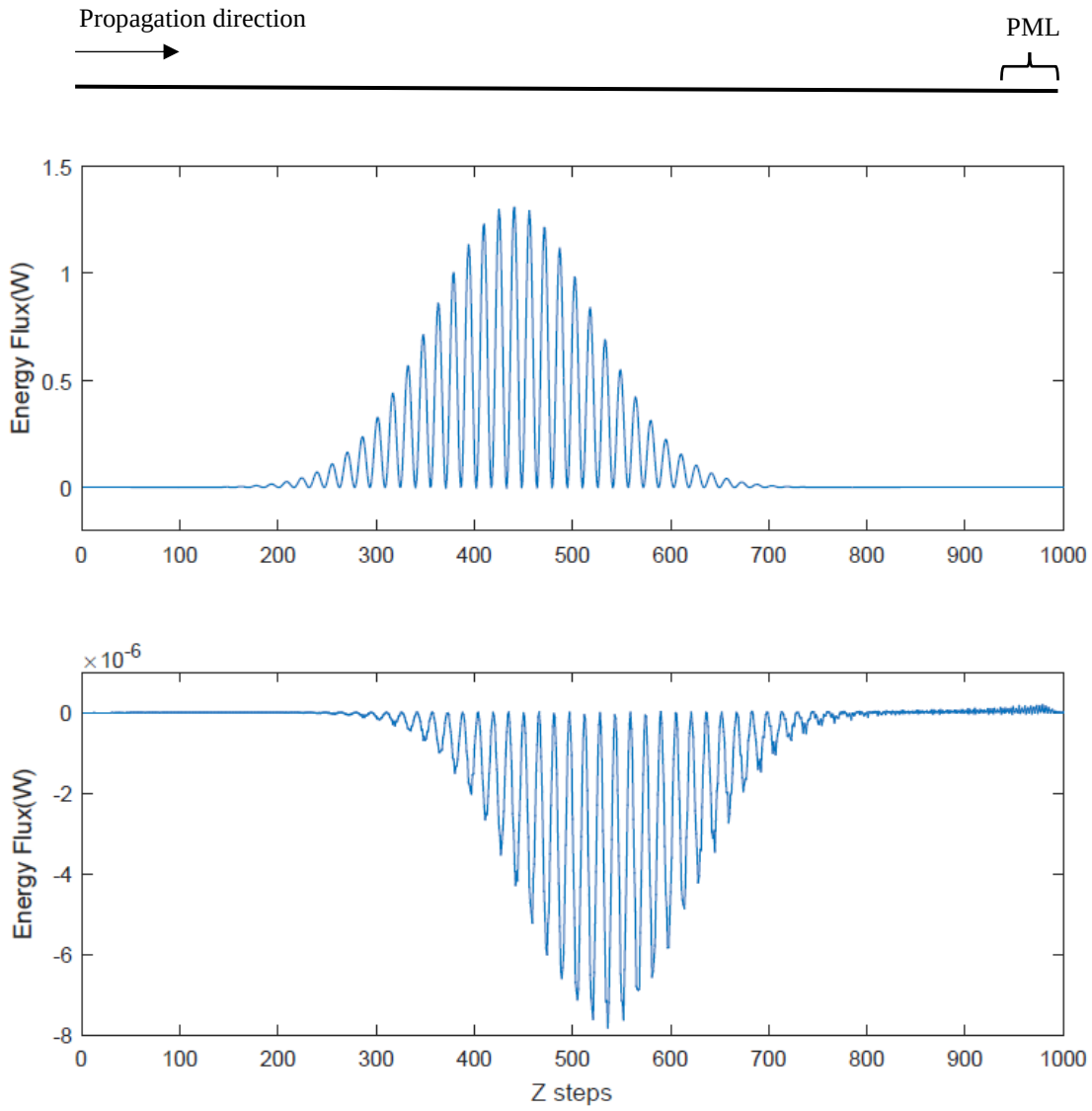

Fig. 3.7 (a) PML in one-dimension model in the simulation; (b) Energy flux of waveguide in one-dimension polynomial-graded PML test. The thickness of PML is 30 grids. The coefficient of polynomial n=2.5 and the maximum of conductivity is 2×10^4.

Figure 3.7a indicates the structure of a one-dimensional model with PML. PML is set at the right end of the waveguide. Figure 3.7b displays a result in one-dimension polynomial-graded PML test where the thickness of PML is 30 cells. Therefore, the peak value of energy flux in the waveguide is approximately 1.3 W . When the pulse reaches PML, most energy is absorbed and the reflected energy flux is -8 $\times 10^{-6}$ W, so the reflection ratio is 6 $\times 10^{-6}$. With regard to normal PML, the reflection at the boundary determines how long the program can run without instability being caused by PML. In Section 2.4.1, there was discussion about the significant wave reflection at PML surface which was observed when the conductivity was a constant. In the simulation of 10-cell thick PML, if the conductivity is a constant, the smallest reflection ratio can be as large as 0.01 so geometric-graded and polynomial-graded conductivity are considered in this section.

Geometric-graded PML is defined in the equation (2.29). In principle, both g and σ_0 could affect the reflection, so the comparison of reflection ratio with various combinations of co-efficients in 10-cell geometric-graded PML are shown in Table 3.2. Values of g are decreased from 4 to 1.5, then the value of σ_0 is selected when the smallest reflection ratio is gained in several tests. Apparently, the best reflection ratio obtained in Table 3.2 is 7.5 $\times 10^{-4}$ when g =1.8 and σ_0 = 5 $\times 10^{4}$.

Table 3.2 Comparison of reflection ratio in 10-cell geometric-graded PML.

PML / Parameters	g	σ_0	Reflection ratio
Geometric Grading	4	2×10^{5}.	1.4×10^{-2}.
	3	5×10^{4}	7.1×10^{-3}.
	2	5×10^{4}	1.5×10^{-3}
	1.8	5×10^{4}	7.5×10^{-4}
	1.5	5×10^{4}	3.5×10^{-3}

In contrast, polynomial-graded PML got better results than geometric-graded PML. Polynomial-graded PML is defined in the equation (2.28). The example in Figure 3.6 has the co-efficient of polynomial-graded PML n = 2.5 and the maximum of conductivity $\sigma_{\max}$ = 2

$\times 10^4$, which is the optimum choice for 30-cell thick PML. The second row in Table 3.3 represents the best result for 10-cell case in polynomial grading method. The reflection ratio is 2.5×10^{-4}, only one third of the value in geometric grading method. Furthermore, Table 3.3 presents more results of reflection error and optimum values of parameters for various thicknesses of polynomial-graded PML. It is apparent that the reflection ratio drops rapidly from 2.5×10^{-4} to 6×10^{-6} as the thickness increases gradually from 10 cells to 30 cells.

According to the convergence criterion of Newton iteration in FDTD cases, which was discussed in Section 3.4, reflection ratio 10^{-4} is reasonable. Therefore, in the simulations in this thesis, the thickness of PML is usually set as 10 cells with polynomial grading model.

Table 3.3 Comparison of reflection ratio in polynomial-graded PML.

PML / Parameters	Thickness	n	$\sigma_{\max}$	Reflection ratio
Polynominal Grading	10 cells	2.5	5×10^4	2.5×10^{-4}
	12 cells	2.5	4.5×10^4	1.8×10^{-4}
	16 cells	2.5	3×10^4	9.2×10^{-5}
	20 cells	2.5	2.5×10^4	2.0×10^{-5}
	30 cells	2.5	2×10^4	6×10^{-6}

3.7 OpenMP and high-performance computation

In this thesis, all the simulations have been programmed with Fortran 95 and compiled with GCC on an Eclipse platform. However, when the problem domain contains too many points or the propagation distance is long, the FDTD algorithm requires a large amount of memory and this also leads to much more computational burden. Therefore, OpenMP is applied in the simulation. Compared to the normal calculation, OpenMP is a parallel computing method, providing a possibility that multiple threads are calculated at the same time with shared memory.

Thanks to OpenMP, the run time of simulations has been reduced dramatically. For instance, the run time of a program is 180 hours in the normal way. When the program is compiled with OpenMP and runs with 8 threads, its run time is decreased to 28 hours. Figure 3.8 indicates the operating principle of OpenMP. At the beginning, the program runs with the master thread. When in the parallel regions, it runs with four threads with shared memory, then the four threads join together again until the next parallel region.

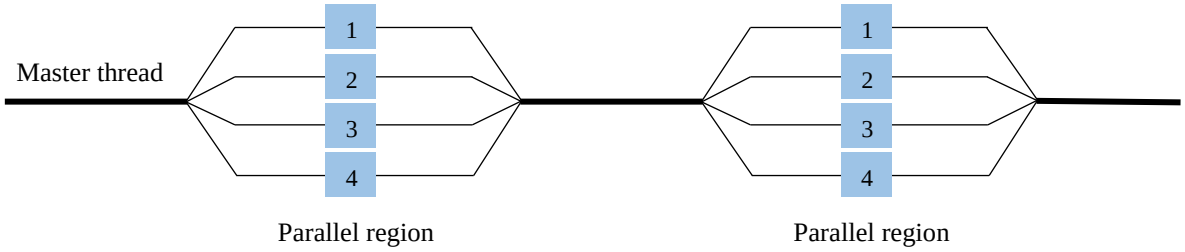

Fig. 3.8 Operating principle of OpenMP with four threads.

To further improve the efficiency of the simulation, high performance computation is utilized. HPC is treated as a supercomputer, having many nodes and each node has many cores. For example, Miffy and Buckethead are parts of HPC at the University of Glasgow. Miffy provides 1256 cores over 156 compute nodes, where two nodes have 12 cores and other nodes have 8 cores. In contrast, Buckethead provides 444 cores over 49 nodes. Most nodes have 4 cores and other nodes have 28 or 32 cores. The degree of parallelization of OpenMP is determined by the number of cores on one node, so that the parallel computation accelerates significantly with HPC. Moreover, cloud computation makes it possible to remotely use HPC on users' own computers, which is convenient and efficient. Simulations in this thesis have used three HPC sources: Miffy and Buckethead (HPC at the University of Glasgow, a partner of ARCHIE-WeSt), Cirrus (EPCC at the University of Edinburgh) and ARCHIE-WeSt.

This chapter presented the main steps of simulations for optical waveguides, introduced details of obtaining excitation source and incorporating linear dispersion and nonlinearity, and demonstrated the optimization of PML. Moreover, the specific HPC sources applied in the simulations were introduced. Based on this chapter, six optical waveguides are simulated and proposed in the following chapters.

Chapter 4

Four-Wave Mixing of GaAs/AlGaAs Waveguides

This chapter presents simulations of the four-wave mixing process for three optical waveguides: the GaAs suspended waveguide, the deep-etched multi-layer $Al_{0.25}Ga_{0.75}As$ waveguide and the $Al_{0.3}Ga_{0.7}As$-on-insulator waveguide. Models and excitation sources are introduced. The method of incorporating linear dispersion and nonlinearity are also presented. Either linear dispersion or nonlinearity could be turned on or turned off so that it was flexible enough to check the linear and nonlinear characteristics. FWM was observed in these waveguides based on Kerr effects and Raman scattering.

4.1 GaAs suspended waveguide

GaAs suspended waveguide was carried out in the simulation as a relatively simple and well-bounded example. GaAs has a high refractive index and provides a strong mode confinement in the GaAs suspended waveguide. Material dispersion was incorporated in the simulation through a Sellmerier equation. Then the GVD and phase mismatch factor Δk were discussed, based on material and geometric dispersions, which are the key parameters in evaluating the efficient nonlinear interactions among waves and determining the phase matching condition of FWM. Moreover, Kerr-type nonlinearity was taken into consideration in order to simulate FWM process. Thanks to the large nonlinear refractive index of GaAs, obvious FWM was observed when the excitation source had high intensity and comb generation was achieved in TE fundamental mode.

4.1.1 Basic model

The basic model of GaAs suspended waveguide in the simulation is shown in Figure 4.1, where the cross-section consists of three layers. The core layer is GaAs. Its height is 0.5 μm and its width is 0.5 to 1.0 μm. The height is based on the most nonlinear research of AlGaAs waveguides[84], [89], [149]. The range of width was decided by the mentioned references and mode solver, which was utilized to make sure that only the fundamental modes exist. Once the

waveguide is suspended, 0.5 μm-thick air layer is set as a cladding layer to provide a realistic environment for wave propagation. In addition, the outer layer is 0.5 μm-thick PML absorbing boundary condition, making sure that the problem domain is limited and that the energy which escapes away from the core layer in the propagation would be absorbed eventually. The thickness of air layer was determined in mode solver and it ensures the fundamental modes were not absorbed by the PML but well confined by the waveguide. The grid size is not uniform to three dimensions and the time step is determined by the smallest grid size:

Δx = 40 nm; $\Delta y = \Delta z$ = 50 nm

$$\Delta t = \frac{\Delta x}{2c} \tag{4.1}$$

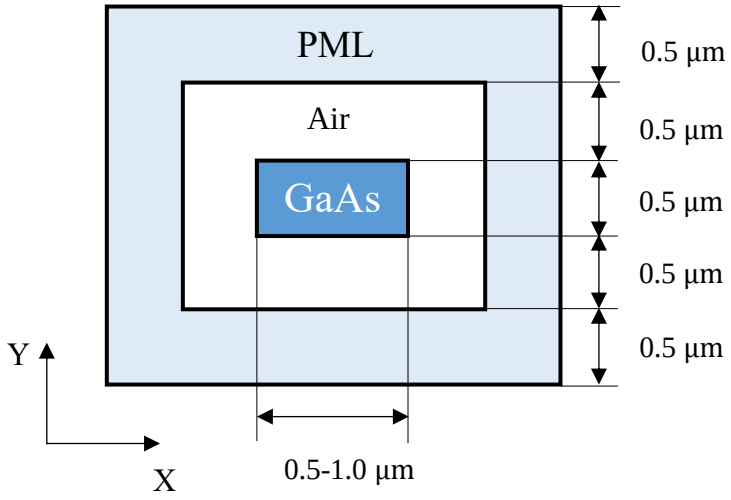

Fig. 4.1 Cross-section of GaAs suspended waveguide in the simulation.

4.1.2 Excitation source

The structure of the GaAs suspended waveguide gives a high refractive index contrast, providing mode confinement for propagation of the optical wave. With the application of a mode solver, geometric dispersion of waveguide can be incorporated and excitation source is obtained. Only the area of the waveguide and the surrounding air layer have an initial value. Peak values of the magnetic field in incident *x-y* plane of GaAs suspended waveguide are described in Figure 4.2 and the width of the core layer is 1 μm. Figure 4.2a shows TE fundamental mode of GaAs suspended waveguide at wavelength 1.55 μm, whose effective index is 3.06, while Figure 4.2b shows TM fundamental mode at the same wavelength with a lower effective index 2.95. It is possible to conclude that both the TE and the TM modes are

well confined and the main energy of optical pulse is propagated in the core layer. As a consequence, together with cosine wave and Gaussian envelope function, an incident wave can be gained, which is defined as:

$$g(t,x,y) = H_0(x,y)\cos\left(\omega_c(t-t_0)\right) e^{-(\frac{t-t_0}{\tau})^2} \quad (4.2)$$

where $H_0(x,y)$ is the values of mode in *x*-*y* plane shown in Figure 4.2, and ω_c is the central frequency of the pulse. If the incident wave contains two separate frequencies ω_1 and ω_2, then the formula (4.2) is modified as:

$$g(t,x,y) = H_0(x,y)\left[\cos\left(\omega_1(t-t_0)\right) + \cos\left(\omega_2(t-t_0)\right)\right] e^{-(\frac{t-t_0}{\tau})^2} \quad (4.3)$$

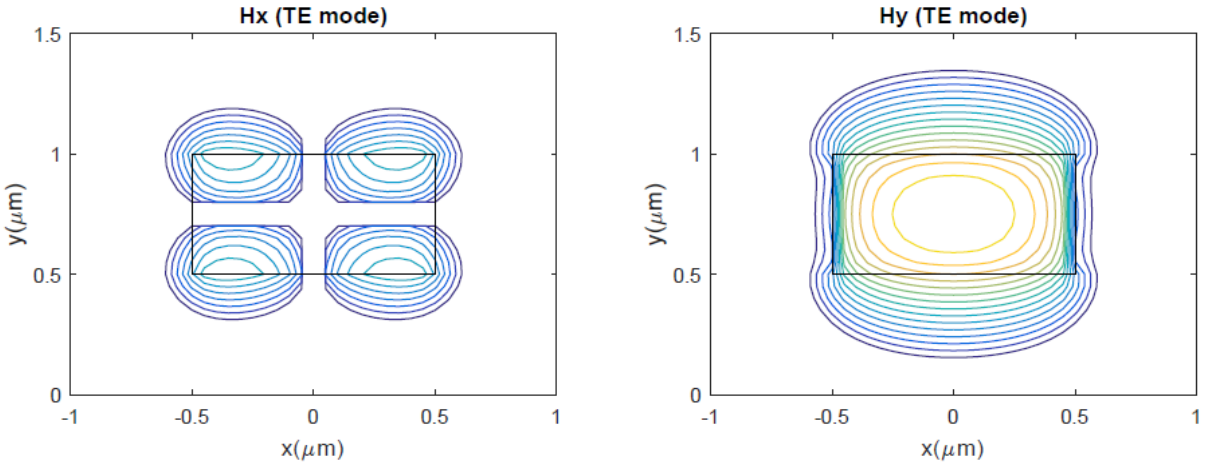

Fig. 4.2a Magnetic field in TE fundamental mode in *x*-*y* plane of GaAs suspended waveguide at wavelength 1.55 μm. The width of core layer is 1.0 μm and the effective index of waveguide is 3.06.

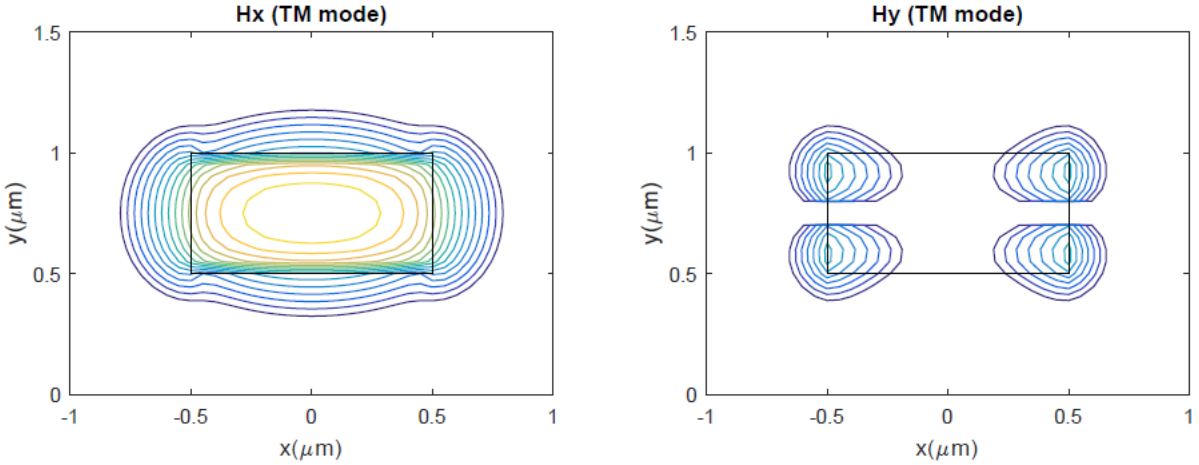

Fig. 4.2b Magnetic field in TM fundamental mode in *x*-*y* plane of GaAs suspended waveguide at wavelength 1.55 μm. The width of core layer is 1.0 μm and the effective index of waveguide is 2.95.

It is noted that the relationship between the duration and spectral bandwidth satisfies a universal inequality[150]:

$$\Delta t \, \Delta\omega \geq \frac{1}{2} \tag{4.4}$$

However, formula (4.4) can lead to the quantum-mechanical time–energy uncertainty principle, which means the bandwidth of frequency must be broad enough to create a Gaussian pulse with a given duration. On the other hand, to build a Gaussian pulse with a narrow bandwidth, the duration must be a certain length. This is especially true in the case described in the formula (4.3) where the incident wave contains two frequencies and, therefore, the bandwidths of both frequencies should be limited. In the reference [150], the Fourier inequality for pulses is expressed as:

$$\Delta\tau \, \Delta\upsilon \geq \mathrm{K} \tag{4.5}$$

where $\Delta\tau$ is the duration at half maximum; $\Delta\upsilon$ is the frequency full width at half maximum (FWHM); and the value of K is 0.441 for Gaussian pulse.

4.1.3 Material dispersion

The material dispersion of GaAs was described as Lorentz medium. In order to determine the parameters and incorporate the linear dispersion in the simulation, the refractive index of GaAs should be expressed as the Sellmeier equation as defined in equation (3.6). Skauli et al [151] measured the refractive index of GaAs in the wavelength range from 0.967 to 17 μm, and fitted the experimental data into a Sellmeier equation with three pole pairs at room temperature. The Sellmeier equation obtained is as follows:

$$n^2(\lambda) = \mathrm{B1} + \frac{\mathrm{B2}\lambda^2}{\lambda^2 - \mathrm{B3}} + \frac{\mathrm{B4}\lambda^2}{\lambda^2 - \mathrm{B5}} + \frac{\mathrm{B6}\lambda^2}{\lambda^2 - \mathrm{B7}} \tag{4.6}$$

where B1=5.3725; B2=5.4667; B3=0.1964; B4=0.0243; B5=0.7650; B6=1.9575; B7=1362.8400; and λ is the wavelength and its unit is μm. The refractive index of GaAs given by formula (4.6) has been plotted in Figure 4.3. It decreases gradually from 3.503 at wavelength 1.0 μm to 3.330 at wavelength 2.1 μm. Therefore, the parameters in the equation (2.43) – permittivities and resonant frequencies – are not difficult to obtain based on equation (4.6):

ε_∞ = 5.3725; ε_{s1} = 10.8393; ε_{s2} = 5.3968; ε_{s3} = 7.3300; (4.7a)

ω_1 = 2.7999 eV; ω_2 = 1.4185 eV; ω_3 = 0.0336 eV (4.7b)

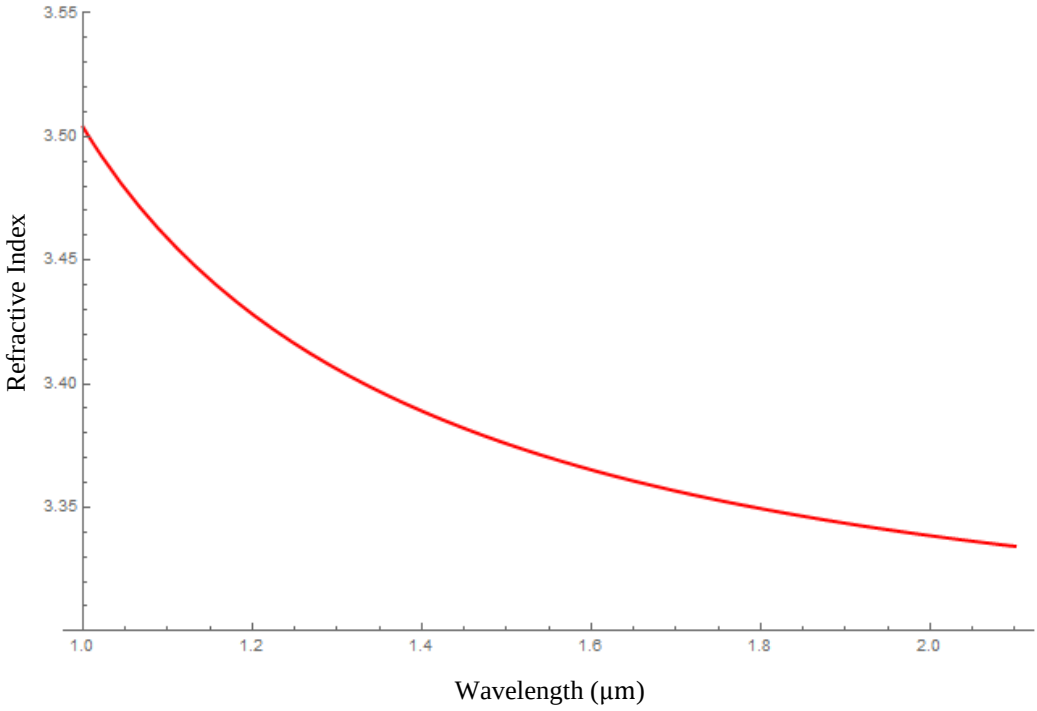

Fig. 4.3 Refractive index of GaAs in the wavelength range from 1.0 to 2.1 μm.

Together with a mode solver, both the geometric and material dispersion of GaAs suspended waveguide could be incorporated in the simulation. Group velocity dispersion is observed in Figure 4.4, in which the pulses contain a range of frequency components. Figure 4.4 shows the propagation of energy flux over four cross-sections of GaAs suspended waveguide in time domain. Sub-figure (a) represents the incident plane while (b) - (d) are cross-sections with 2000 cells, 3000 cells and 4000 cells away from the incident plane, respectively. In addition, FWHM of pulses in the figure are indicated in order to compare the widths. Compared to the shape of input wave in sub-figure (a), waves in sub-figure (b) - (d) have smaller amplitudes and bigger widths in time domain. The input wave has the largest peak value of 80.5 W and the smallest of FWHM 15 fs. Over time, as the propagation distance gradually increases to 4000 cells in sub-figures (b) - (d), the peak value gradually drops to 36.1 W while the FWHM grows to 21 fs. Therefore, the longer distance the optical pulse is propagated, the lower peak value and wider width it has. These results are caused by linear dispersion. In dispersive media, a variability of the material's dielectric permittivity leads to various velocities of a propagating wave with various frequencies. Thus, lower frequency components run faster than higher ones

in GaAs suspended waveguide, resulting in a broadening of the width of wave in time domain as the propagation distance increases. It is noted that the power level in Figure 4.4 was raised to unreasonable values in the simulation in order to confirm the existence of the nonlinear frequency mixing processes.

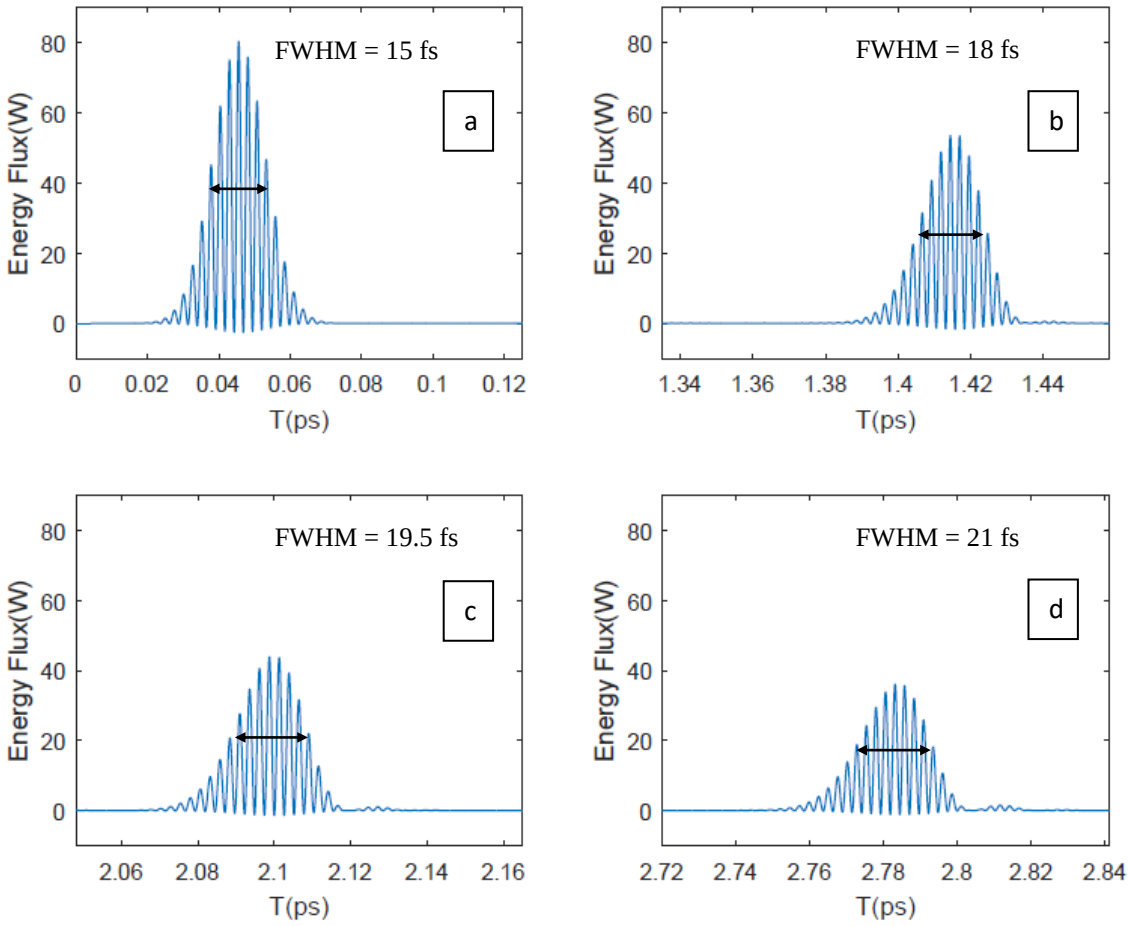

Fig. 4.4 Propagation of energy flux in GaAs suspended waveguide in time domain. Sub-figure (a) is the incident plane while (b), (c) and (d) are cross-sections where the propagation lengths are 2000 Δz , 3000 Δz and 4000 Δz, respectively.

4.1.4 Phase matching condition of FWM

It was suggested in Chapter 3 that phase matching condition allows the infinite coherent length for efficient FWM processing. To achieve phase matching, Δk=0 is required. According to the Taylor expansion in equation (3.21), when the frequency shifts in a small range, the odd terms in the right-hand side are cancelled so that GVD is the primary term. Therefore, Δk is generally a quadratic equation but it would become a quartic equation when GVD is around zero. As a result, both GVD and Δk were taken into account to determine the phase matching condition, being affected by the combination of material and geometric dispersions.

Using the method introduced in Section 3.5.1, GVD of GaAs suspended waveguide with various widths in TE and TM fundamental modes in a wavelength range 1.3-1.8 μm were obtained. Usually, GVD is also defined as a derivative with respect to wavelength rather than angular frequency, which is called group delay dispersion parameter (D parameter). D parameter can be gained as follows:

$$D = -\frac{\lambda}{c}\frac{d^2n}{d\lambda^2} \tag{4.8}$$

GVD is usually specified with a unit of ps·ns/km while D parameter is specified with a unit of ps/nm/km. If D parameter is positive, the waveguide has anomalous dispersion; If D parameter is negative, the waveguide has normal dispersion.

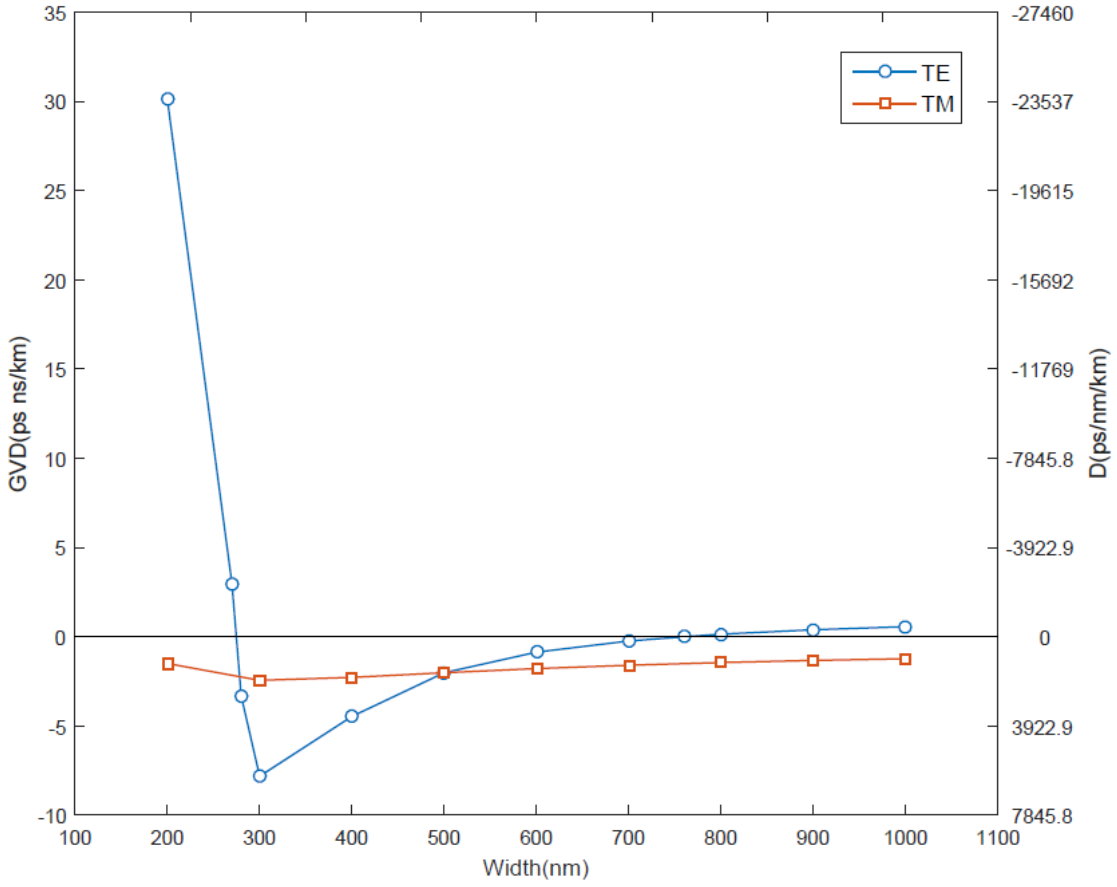

Fig. 4.5 GVD and D of GaAs suspended waveguides with various widths in TE and TM fundamental modes at wavelength 1.55 μm.

In Figure 4.5, GVD and D of GaAs suspended waveguide are plotted with various widths at wavelength 1.55 μm involving two polarizations. The blue line connects several GVD points in TE fundamental mode. It has a relative large positive value about 30 ps·ns/km when the width is as small as 200 nm, then drops sharply to a negative value -8 ps·ns/km at width 300

nm, from which it increases slowly as the width becomes bigger. When the width is around 760 nm, GVD and D of waveguide in TE fundamental mode are close to zero value and it continues to grow to positive value again. Theoretically, there are two zero points of GVD in the figure; one is between 270 and 280 nm, the other is 760 nm. However, as shown in the first sub-figure of Figure 4.6, GVD of waveguide with various widths in TE fundamental modes at a wide wavelength range 1.3-1.8 μm are compared. For small widths, such as 270 nm and 280 nm, higher order dispersion terms become significant. In contrast, in the case of 760 nm, the GVD shows a stable trend and maintains small values in the whole wavelength range. Therefore, 760 nm is better as the zero point of GVD in TE fundamental mode at 1.55 μm.

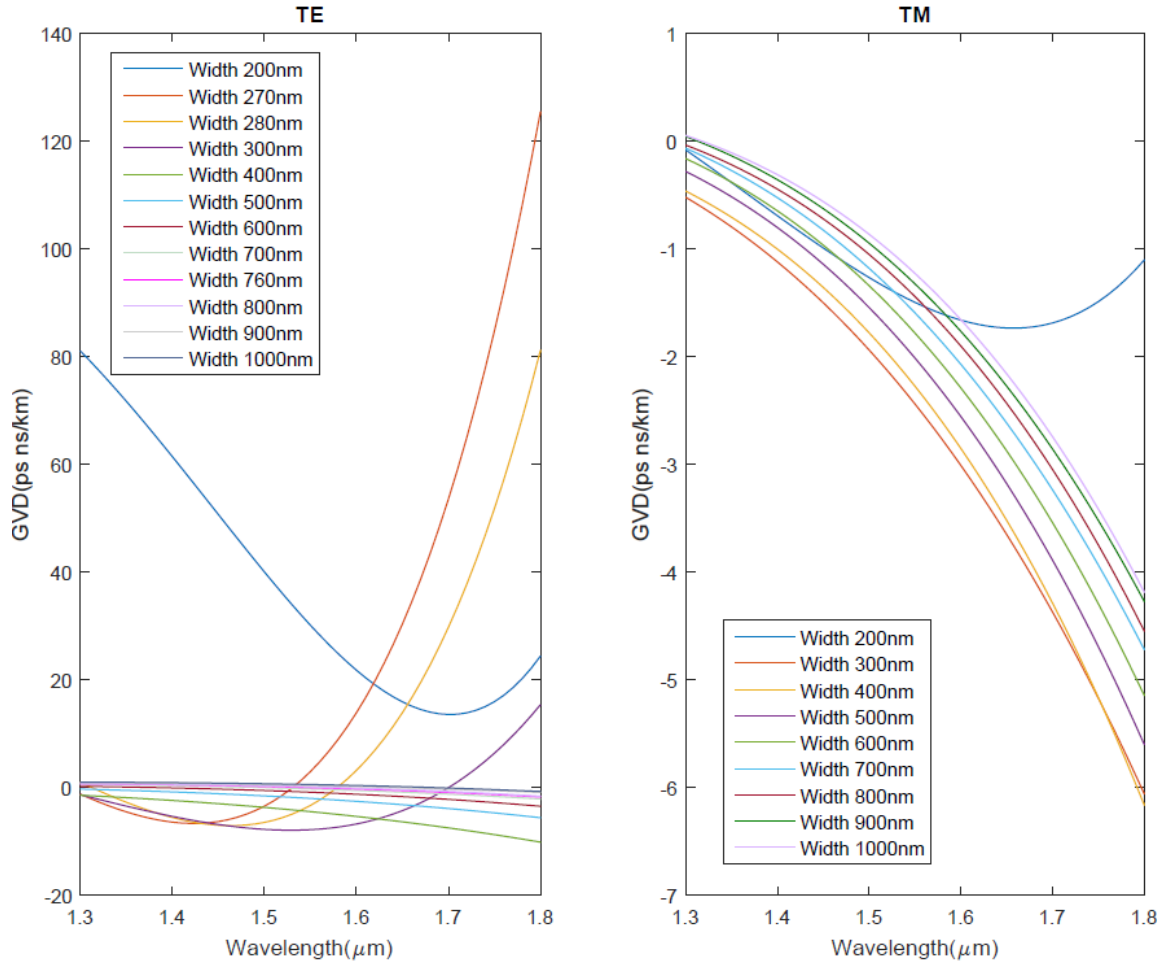

Fig.4.6 GVD of GaAs suspended waveguides with various widths in TE and TM fundamental modes at wavelength 1.3-1.8 μm.

Moreover, according to the D parameter in TE fundamental mode, the waveguide has normal dispersion when the width is less than 280 nm or larger than 760 nm; the waveguide has anomalous dispersion when the width is between 280 and 760 nm. In Figure 4.4, the width of simulated waveguide was 1000 nm and it contained normal dispersion. Therefore, the lower

frequency components propagate faster than the higher ones, meaning the pulse was up-chirped, leading to the increase of the width of optical pulse in time domain. In comparison, there was no broadening in the pulses in Figure 3.2 where the simulation without linear dispersion. The spreading of pulse can be obtained based on GVD and propagation distance:

$$\text{Chirp} = \text{Propagation distance} \times \text{GVD} \times \text{Bandwidth} \tag{4.9}$$

For an example, in Figure 4.4, the bandwidth of excitation source is $\frac{c}{\lambda_1} - \frac{c}{\lambda_2}$, where λ_1 and λ_2 are 1.4 and 1.7 μm, respectively. The GVD of waveguide with a width of 1000 nm is 0.8 ps·ns/km. According to formula (4.9), when the propagation distance is 4000 cells, the chirp is calculated as 6.1 fs, which confirmed the broadening 6 fs in Figure 4.4.

The red line in Figure 4.5 represents the GVD of TM fundamental mode at wavelength 1.55 μm. After decreasing from a negative value -1.5 ps·ns/km at width 200 nm to -2.5 ps·ns/km at width 300 nm, the GVD increases slightly but keeps negative values as the width grows from 300 to 1000 nm. There is no zero-point of GVD and D in the width range. A further look of GVD at a wider wavelength range 1.3-1.8 μm in Figure 4.6, suggests that the GVD of waveguide in TM fundamental mode grows when the wavelength decreases so it could reach the zero value at a shorter wavelength.

Furthermore, in order to prove that the waveguide with width 760 nm has a better situation for phase matching in TE fundamental mode at wavelength 1.55 μm than those with other widths, phase mismatch factor Δk of GaAs suspended waveguides with various widths are compared in Figure 4.7. Optical parametric oscillator (OPO) could convert a pump wave into two waves: signal wave and idler wave. In the FWM process, the relationship between the frequencies of these waves is:

$$\omega_\mathrm{p} + \omega_\mathrm{p} = \omega_\mathrm{s} + \omega_\mathrm{i} \tag{4.10}$$

Therefore, the effective index contrast Δn and phase mismatch factor Δk are defined as:

$$\Delta n = 2n_{\mathrm{eff}}^{\mathrm{p}} - n_{\mathrm{eff}}^{\mathrm{s}} - n_{\mathrm{eff}}^{\mathrm{i}} \tag{4.11}$$

$$\Delta k = 2\pi \left(\frac{2n_{\mathrm{eff}}^{\mathrm{p}}}{\lambda_p} - \frac{n_{\mathrm{eff}}^{\mathrm{s}}}{\lambda_s} - \frac{n_{\mathrm{eff}}^{\mathrm{i}}}{\lambda_i}\right) \tag{4.12}$$

where $n_{\mathrm{eff}}^{\mathrm{p}}$, $n_{\mathrm{eff}}^{\mathrm{s}}$, $n_{\mathrm{eff}}^{\mathrm{i}}$ are the effective index of waveguide when the wave contains pump frequency, signal frequency and idler frequency, respectively.

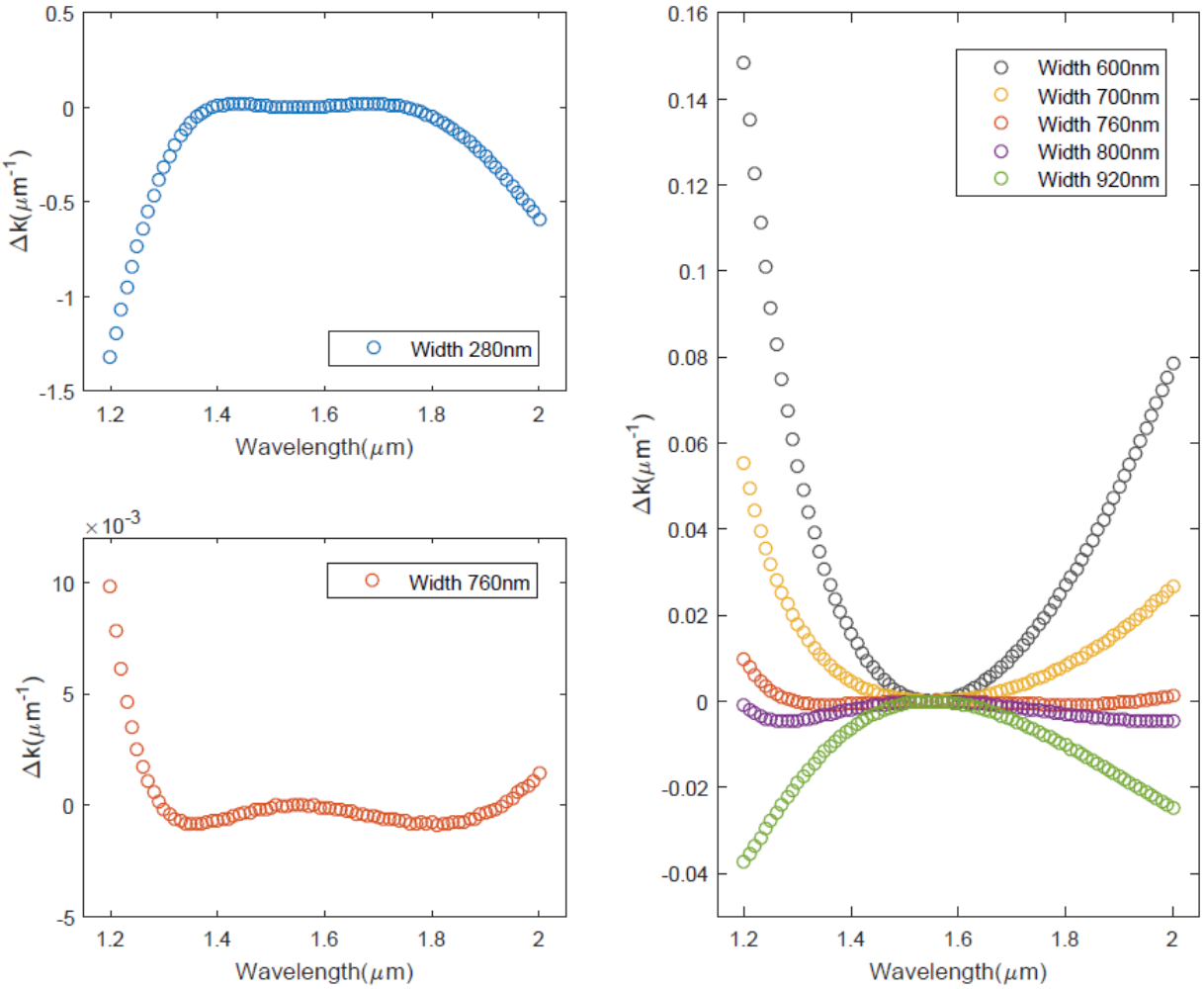

Fig.4.7 Phase mismatch factors of GaAs suspended waveguides with various widths in TE fundamental mode. The pump wavelength is 1.55 μm and the signal wavelength range is 1.2-2.0 μm.

In Figure 4.7, Δk of GaAs suspended waveguide with various widths in TE fundamental mode were obtained at pump wavelength 1.55 μm and signal wavelength 1.2-2.0 μm. Quartic expressions of Δk are revealed when the GVD is around zero value at width 280 nm and 760 nm. However, because of the influence from high order dispersion terms, the absolute value of Δk in the waveguide with a width of 280 nm maintains small values in a narrow wavelength range and increases dramatically as the difference between the signal wavelength and pump wavelength grows. In comparison, when the width is 760 nm, Δk keeps small values in the whole wavelength range, providing a long, coherent length for FWM. In addition, Δk of width 800 nm case is also quartic as a result of the small GVD, but it has larger values than the 760 nm case. With regard to other widths shown in Figure 4.7, Δk is quadratic and has larger

absolute values, in which width 600 nm has the shortest coherent length. In conclusion, width 760 nm is the best choice for the phase matching of FWM process in TE fundamental mode at wavelength 1.55 μm.

4.1.5 Results of FWM

In the simulation of GaAs suspended waveguide, Kerr-type nonlinearity was incorporated. The nonlinear refractive index of GaAs $n_2 = 1.59\times10^{-13}$ $\mathrm{cm}^2 \cdot \mathrm{W}^{-1}$ was demonstrated in the reference [68]. Then, the formula (2.70) was utilized to calculate the real part of Kerr-type nonlinear parameters. Given that the zero-point of GVD in TM fundamental mode at wavelength 1.55 μm does not exist, this section only focuses on TE fundamental mode. The width of the GaAs suspended waveguide was set as 760 nm to simulate the FWM process. A comb generation was obtained and FWM results among waveguides with various widths were compared.

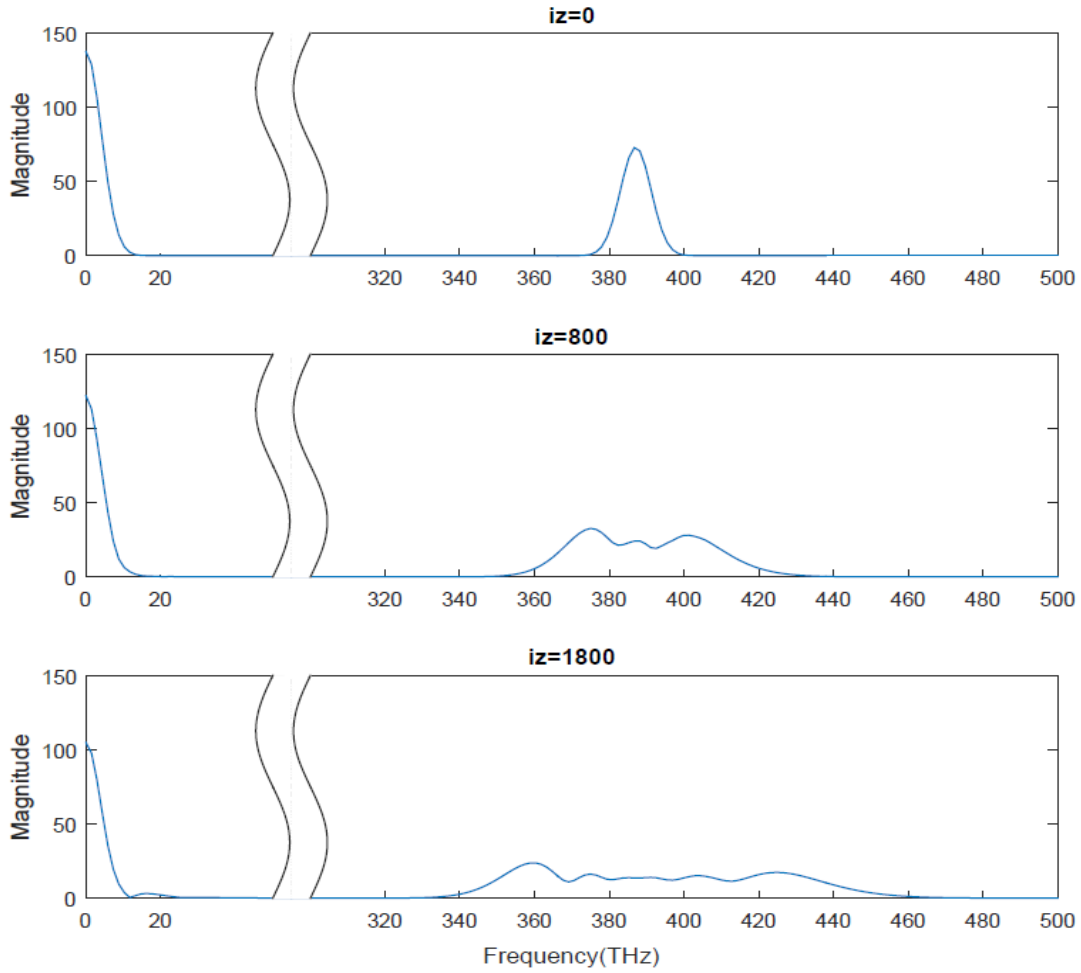

Fig.4.8 FFT of energy flux over three cross-sections of GaAs suspended waveguide with a width of 760 nm. Sub-figures represent the incident plane and cross-sections where the propagation lengths are 800Δz and 1800Δz, respectively.

In Figure 4.8, the excitation source is defined in equation (4.2) with a central wavelength 1.55 μm. Optical pulses were transferred from time domain to frequency domain with FFT algorithm, providing a clear comparison of frequency components. In order to evaluate the propagation of the pulse, energy flux was calculated, which is defined in equation (3.1). Energy flux of three cross-sections in GaAs suspended waveguide were chosen for comparison. The first is the incident plane so that the frequency range is the same as the excitation source whose central frequency is 194 THz. Therefore, the FFT of energy flux shows the sum of frequency 388 THz and the difference frequency in the left pulse. The second cross-section is 800 cells away from the incident plane. The peak values of pulses decreases and frequency ranges became wider. More peaks occur in the right pulse. As for the final sub-figure, the distance of propagation increases to 1800 cells and the change is more significant. Therefore, over time, optical pulse travels much longer and more frequency components are generated because of FWM.

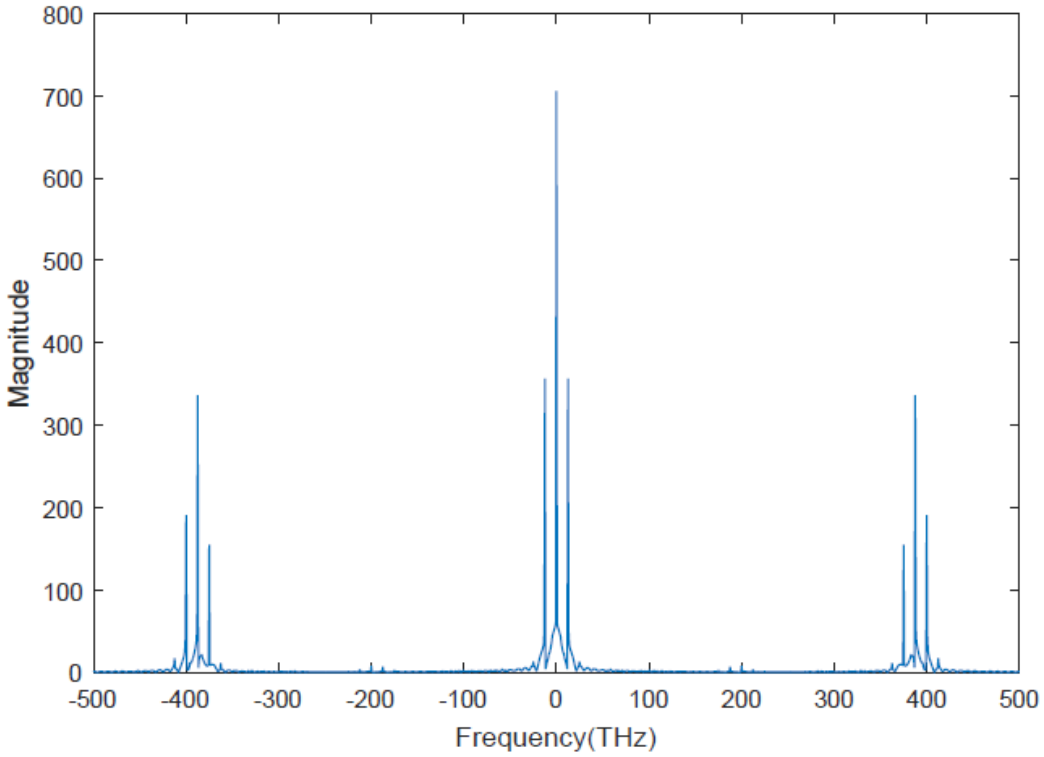

Fig. 4.9 FFT of energy flux over the incident plane of GaAs suspended waveguide with a width of 760 nm.

Different from the above simulation, the excitation source in Figures 4.9 and 4.10 contains two frequencies. Figure 4.9 depicts the FFT of energy flux in the incident plane of GaAs suspended waveguide. The incident two frequencies are 187.5 THz (ω_1) and 200 THz (ω_2), and their corresponding wavelengths are 1.6 μm and 1.5 μm. Therefore, the FFT of energy flux shows the sum frequency of any two frequency components between the pulses: 375 THz ($2\omega_1$), 387.5

THz ($\omega_1 + \omega_2$) and 400 THz ($2\omega_2$), as well as the difference frequency: -12.5 THz ($\omega_1 - \omega_2$), 0 THz ($\omega_1 - \omega_1$ and $\omega_2 - \omega_2$) and 12.5 THz ($\omega_2 - \omega_1$).

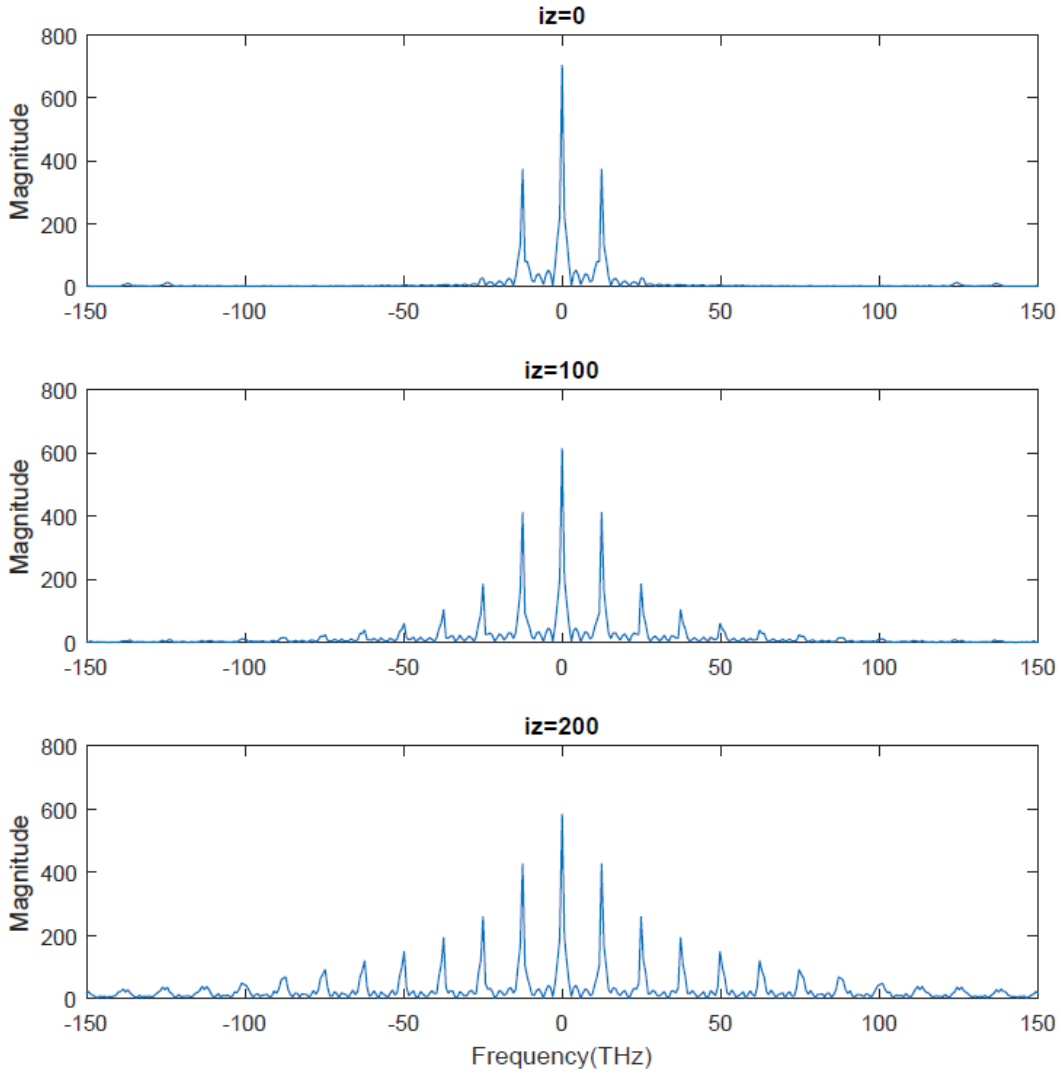

Fig. 4.10 The comparison between the central parts of FFT of energy flux over various cross-sections of GaAs suspended waveguide with a width of 760 nm. Sub-figures represent the incident plane and cross-sections where the propagation lengths are 100Δz and 200Δz, respectively.

In order to have a better understanding of comb generation and newly produced frequency components, Figure 4.10 indicates the central pulse - difference part - of FFT of energy flux in various cross-sections of GaAs suspended waveguide. The cross-section in the first sub-figure is the incident plane so that the frequency range is similar to the excitation source described in Figure 4.9, giving initial frequency pulses for comparison. At this point, the second cross-section is 100 cells away from the incident plane. The peak values of original pulses drop but more frequency pulses are generated. The interval of adjacent pulses is constant and is equal to 12.5 THz, which is exactly the difference of the original two frequencies. When the

propagation distance increases to 200 cells in the third sub-figure, the peak values of pulses generated in the second sub-figure grow and more pulses occur. It is possible to conclude that as the pulse is propagated at a longer distance, more frequency pulses are generated with a constant difference, leading to comb generation.

Furthermore, to confirm the crucial role of the phase matching condition, FWM results between waveguides with various widths were compared. Based on the discussion in the previous section, zero GVD was achieved when the width is 760 nm in TE-polarized fundamental mode at wavelength 1.55 μm. In addition, widths 600 nm and 920 nm were chosen to provide a comparison with 760 nm case. To clearly compare the FWM efficiency between these three waveguides, the focus was on the first newly generated frequency pulse. Therefore, the incident power was set much lower and the frequency bandwidth of the excitation source was larger than those in the simulation of comb generation in Figure 4.9 and Figure 4.10. In the following simulations, the excitation source was based on TE fundamental mode and equation (4.3), including two wavelengths 1.5 μm and 1.6 μm, whose corresponding frequencies are 200 THz and 187.5 THz.

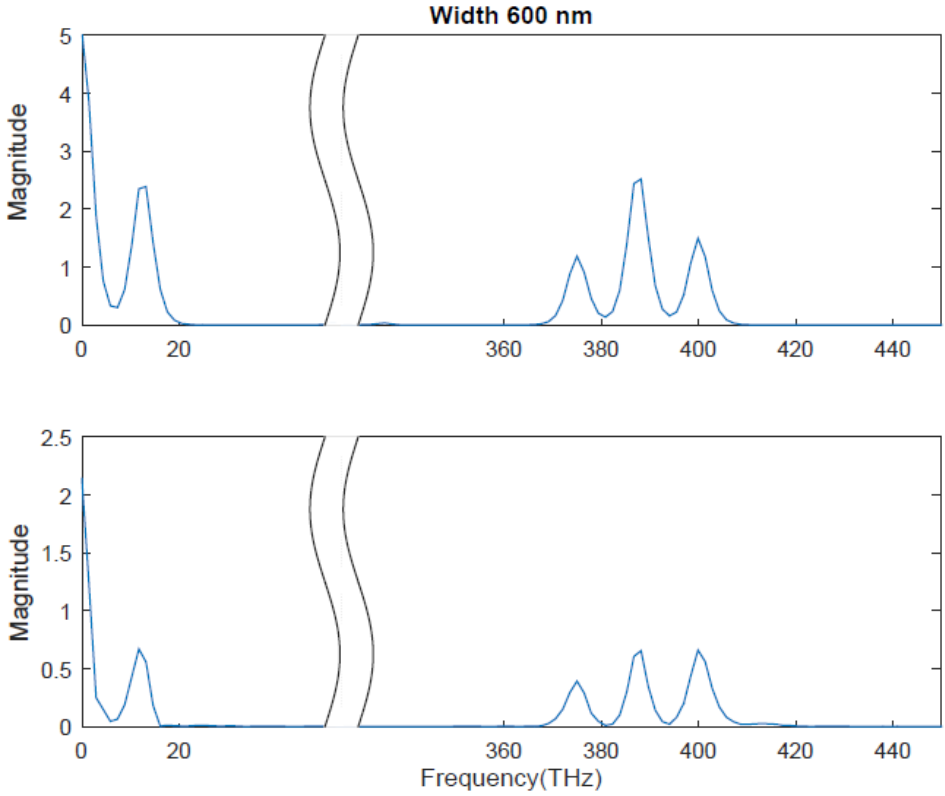

Fig. 4.11 FFT of energy flux of GaAs suspended waveguide with a width of 600 nm. Comparison of frequency components between the incident plane and the cross-section where the propagation length is 2000 cells.

Figure 4.11 shows the FWM results of GaAs suspended waveguide with a width of 600nm. The first sub-figure describes the FFT of energy flux over the incident plane, so the sum and difference frequency of incident pulse are indicated: 375 THz, 387.5 THz and 400 THz, 0 THz and 12.5 THz, respectively. In contrast, the second sub-figure means the FFT of energy flux over the cross-section are 2000 cells away from the incident plane. Although the peak values of original pulses decrease, there is no sign of new frequency components after 2000-cell propagation. In Figure 4.12, the FWM of waveguide with width 760 nm is presented. Compared to the initial pulses in the first sub-figure, a new frequency pulse in the left part is generated and there is an obvious broadening in the sum frequency pulse. The frequency range of two parts significantly spread.

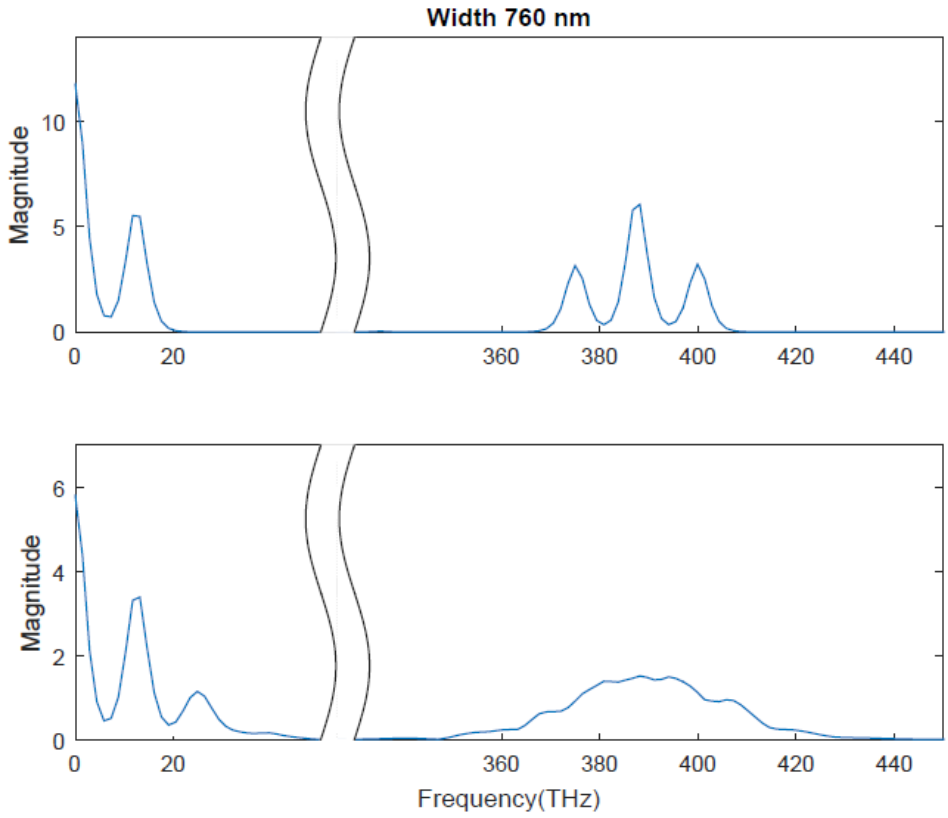

Fig. 4.12 FFT of energy flux of GaAs suspended waveguide with a width of 760 nm. Comparison of frequency components between the incident plane and the cross-section where the propagation length is 2000 cells.

When the width increases to 920 nm in Figure 4.13, the frequency range is slightly broadened in the second sub-figure. There is no newly generated pulse in the left part and the broadenings are much smaller than those in 760 nm case. As a consequence, based on the comparison of the three widths, GaAs suspended waveguide with width 760 nm has the best FWM result in the TE fundamental mode at wavelength 1.55 μm, which agrees with the results of Δk in Figure 4.7. Considering the coherent length is 2000 cells, which is equal to 100 μm, Δk should be less

than 0.01μm^{-1}. When the width is 760 nm, Δk is quartic and maintains the required values in the whole wavelength range: 1.2-2.0 μm. As for widths 600 nm and 920 nm, the ranges of signal wavelength with desired Δk are 1.45-1.67 μm, and 1.36-1.8 respectively. Therefore, the wavelength components involved in nonlinear interaction in coherent length in 760 nm is the greatest, causing the most efficient FWM process. It is noted that two-photon absorption of GaAs is not involved in this simulation, which will have effects in the nonlinear wave mixing process.

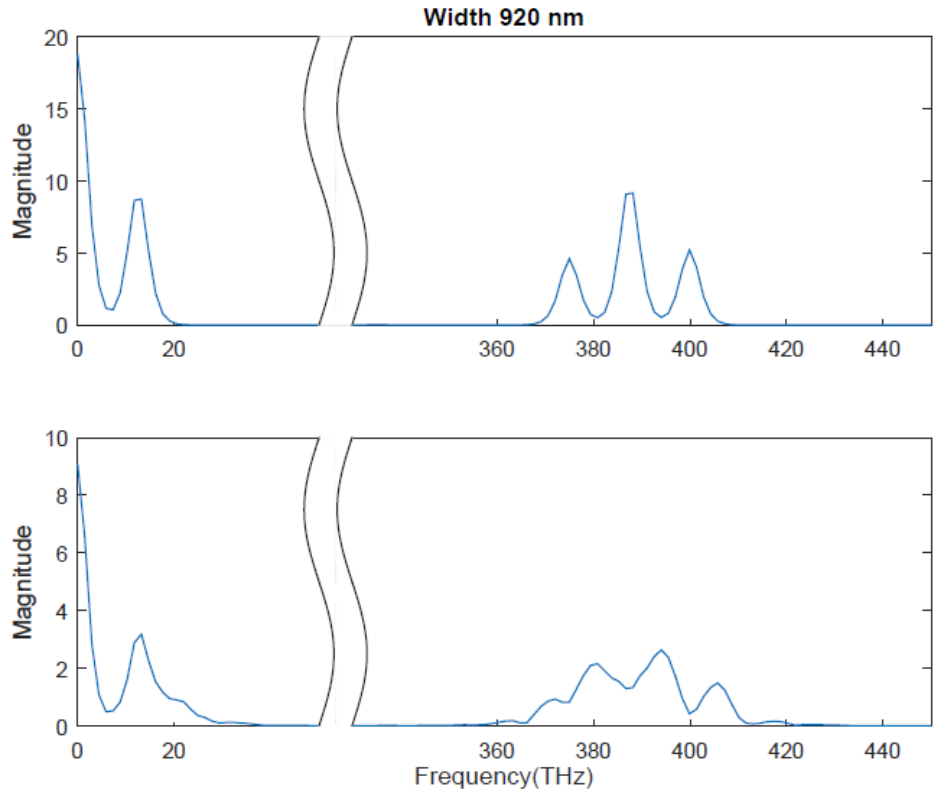

Fig. 4.13 FFT of energy flux of GaAs suspended waveguide with a width of 920 nm. Comparison of frequency components between the incident plane and the cross-section where the propagation length is 2000 cells.

4.2 $Al_{0.25}Ga_{0.75}As$ waveguide

This section introduces the simulation of a deep-etched $Al_{0.25}Ga_{0.75}As$ waveguide[152]. It has a multi-layer structure and all layers consist of AlGaAs. AlGaAs provide a wide range of refractive indices which are flexible and easy to adjust with alloy fraction. As a result of the variation of the refractive index of $Al_xGa_{1-x}As$, the core layer contains a lower concentration of Al while the cladding layers contain a higher concentration. In the simulation, both material and geometric dispersions were incorporated, based on which GVD and phase mismatch factor were obtained as the key parameters to determine the phase matching condition of FWM.

Moreover, Kerr effect and Raman scattering were taken into account to simulate the FWM process. The results of FWM were in good agreement with the measurement of $Al_{0.25}Ga_{0.75}As$ waveguide in the experiment and the comparison is shown in Section 4.2.7.

4.2.1 Basic model

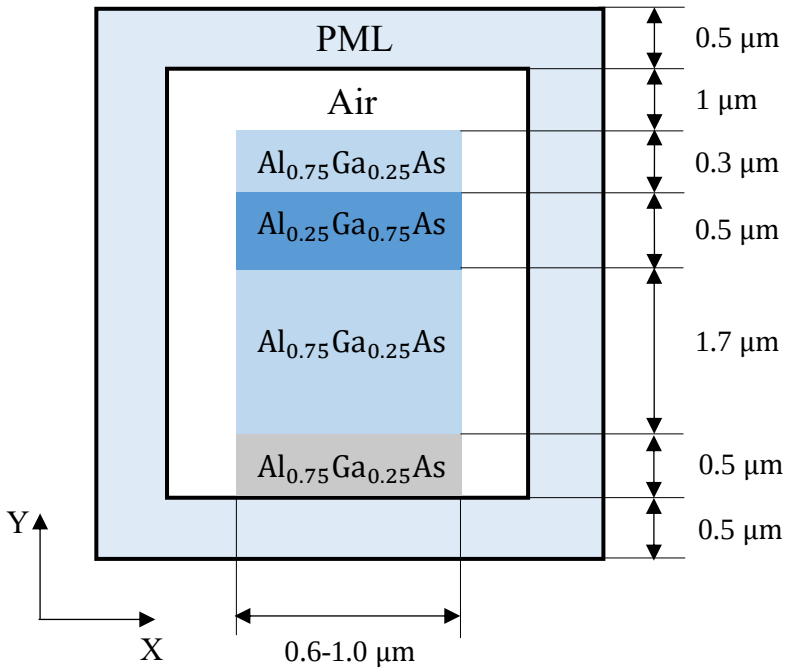

Fig. 4.14 Cross-section of $Al_{0.25}Ga_{0.75}As$ waveguide in the simulation.

The cross-section of the deep-etched $Al_{0.25}Ga_{0.75}As$ waveguide is depicted in Figure 4.14. This waveguide has a multi-layer structure, where the 0.5 μm-thick core layer is $Al_{0.25}Ga_{0.75}As$ and cladding layers are $Al_{0.75}Ga_{0.25}As$. The thickness of upper cladding and lower cladding is 0.3 μm and 1.7 μm, respectively. The width of AlGaAs layers is between 0.6 and 1.0 μm. Apart from the basic structure, a 1.0 μm-thick outer layer of air is designed for the three sides of AlGaAs to simulate the realistic environment of propagation for optical wave. Then 0.5 μm-thick PML absorbing boundaries are set to cut off the problem domain and to make sure that no significant reflection occurs on the boundary. However, considering the lower cladding layer has nonlinearity and PML is nondispersive and an optical pulse would reflect back when it reaches the inner boundary of PML. Therefore, a 0.5 μm-thick buffer layer is set between the lower $Al_{0.75}Ga_{0.25}As$ layer and PML to improve the absorption efficiency of radiation energy. The buffer layer consists of $Al_{0.75}Ga_{0.25}As$ only with linear dispersion. It is noted that for

guided modes, there would be low radiance in the buffer layer. The grid sizes are uniform in the three dimensions and time step is decided by the grid size:

$$\Delta x = \Delta y = \Delta z = 50 \text{ nm}; \qquad \Delta t = \frac{\Delta x}{2c} \tag{4.13}$$

4.2.2 Excitation source

The structure of $Al_{0.25}Ga_{0.75}As$ waveguide gives a high refractive index contrast, providing mode confinement for propagation of an optical wave. Using mode solver, excitation source was obtained. The area of waveguide (including buffer layer) and surrounded air layer have initial values. Values of magnetic fields in the incident *x*-*y* plane of $Al_{0.25}Ga_{0.75}As$ waveguide (width = 0.7 μm) are described in Figures 4.15 and 4.16. Figure 4.15 shows the TE fundamental mode of $Al_{0.25}Ga_{0.75}As$ waveguide at wavelength 1550nm with an effective index of 3. Figure 4.16 shows the TM fundamental mode at the same wavelength with a higher effective index of 3.05. Both TE and TM mode are well confined and the main energy of the optical pulse is propagated in the core layer. Therefore, the incident wave is built of Gaussian pulse and values of mode, which is defined in formula (4.2) and formula (4.3).

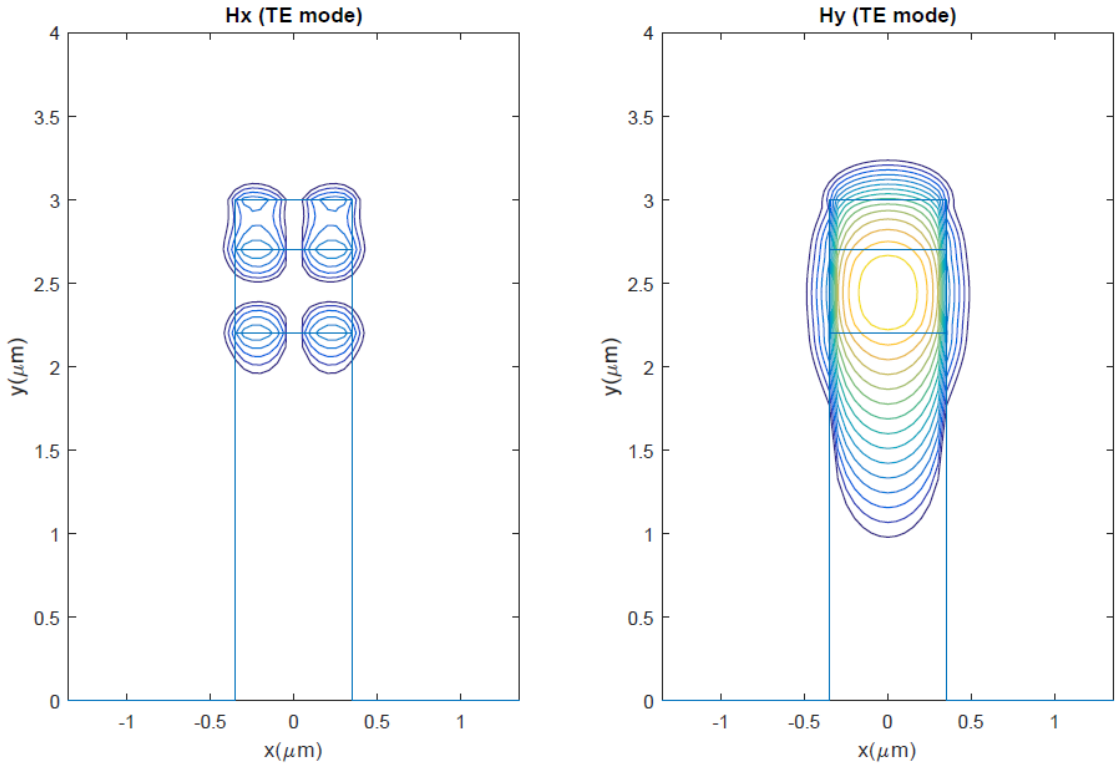

Fig. 4.15 Magnetic field in TE fundamental mode in *x*-*y* plane of $Al_{0.25}Ga_{0.75}As$ waveguide at wavelength 1.55 μm. The width of core layer is 0.7 μm and the effective index of waveguide is 3.00.

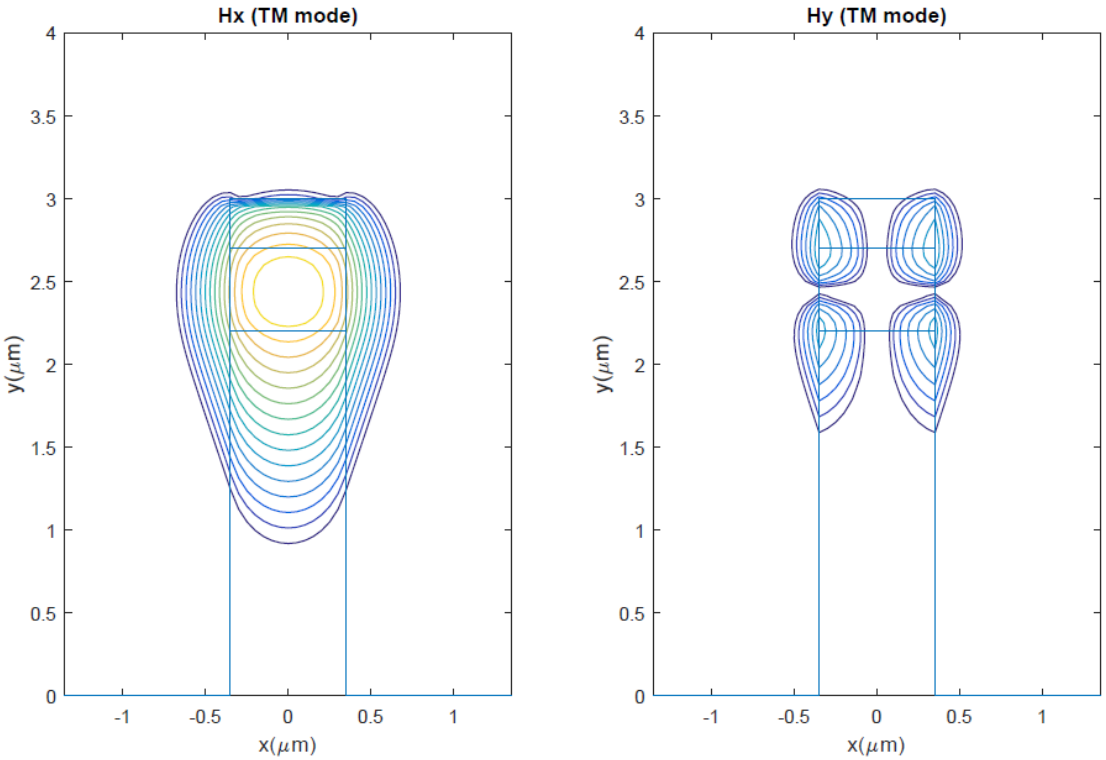

Fig. 4.16 Magnetic fields in TM fundamental mode in *x*-*y* plane of $Al_{0.25}Ga_{0.75}As$ waveguide at wavelength 1.55 μm. The width of core layer 0.7 μm and the effective index of waveguide is 3.05.

4.2.3 Material dispersion

Material dispersion of AlGaAs was described as Lorentz medium. In order to determine the resonances and parameters, the refractive index of AlGaAs should be expressed as Sellmeier equation defined in formula (3.6). It was demonstrated in reference [66] that the experimental data of refractive indices of $Al_xGa_{1-x}As$ were fitted into a modified general function:

$$n^2(x) = A(x) + \frac{C0(x)}{(E0(x)^2 - E^2)} + \frac{C1(x)}{(E1(x)^2 - E^2)} + R(x) \tag{4.14a}$$

$$R(x) = (1 - x)\frac{C2}{(E2^2 - E^2)} + x\frac{C3}{(E3^2 - E^2)} \tag{4.14b}$$

where x is the Al concentration; E0(x) and E1(x) are resonant energies; E = hc/λ is the energy of the photon; R(x) is the reststrahlen correction, E2 and E3 are GaAs-like and AlAs-like transverse phonon energies; A(x), C0(x), C1(x), C2, C3 are fitting co-efficients and values are specified in the reference. When x=0, equation (4.14) describes the refractive index of GaAs with three pole pairs. When x=1, equation (4.14) describes the refractive index of AlAs with

three pole pairs. Generally, for 0<x<1 case, equation (4.14) describes the refractive index of AlGaAs with four pole pairs. It is noted that equation (4.14) is accurate only when 0.176≤x≤1.

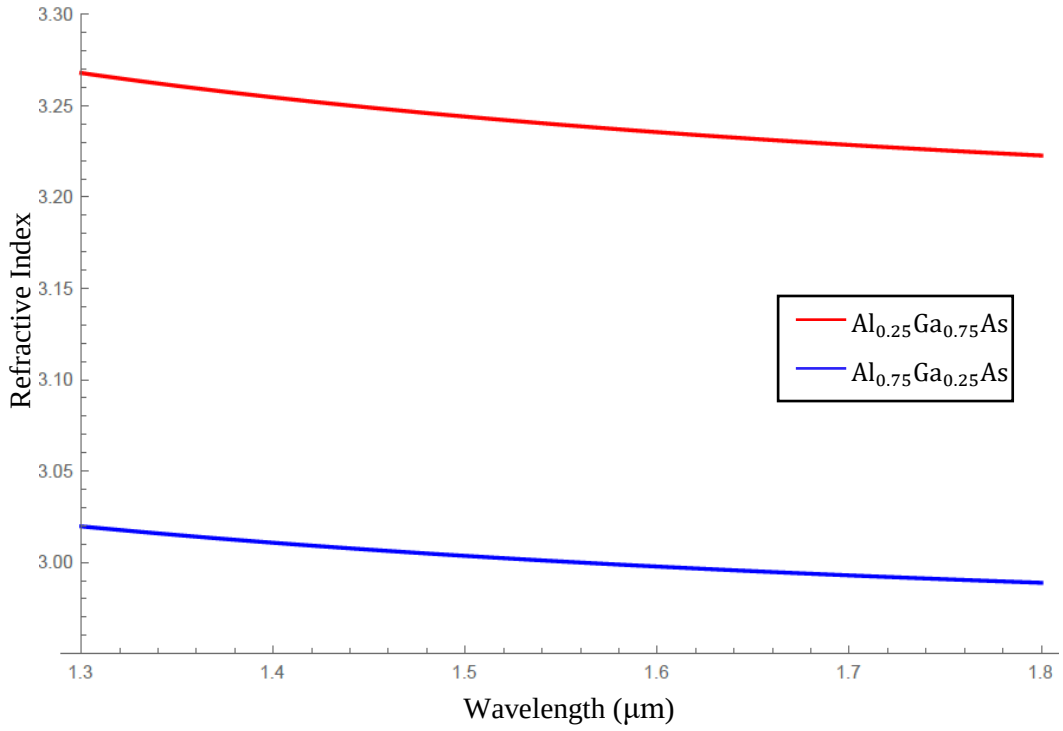

Fig. 4.17 Refractive index of AlGaAs. The Red line represents $Al_{0.25}Ga_{0.75}As$ and the blue line represents $Al_{0.75}Ga_{0.25}As$.

Therefore, according to equation (4.6), the relative permittivities and resonant frequencies of $Al_{0.25}Ga_{0.75}As$ and $Al_{0.75}Ga_{0.25}As$ are obtained:

$Al_{0.25}Ga_{0.75}As$:

$$\varepsilon_\infty = 3.8636;\ \varepsilon_{s1} = 3.8910;\ \varepsilon_{s2} = 10.0758;\ \varepsilon_{s3} = 5.4693;\ \varepsilon_{s4} = 4.3538 \quad (4.15a)$$

$$\omega_1 = 1.7877 \text{ eV}; \qquad \omega_2 = 3.2941 \text{ eV};$$

$$\omega_3 = 0.0333 \text{ eV}; \qquad \omega_4 = 0.04523 \text{ eV} \quad (4.15b)$$

$Al_{0.75}Ga_{0.25}As$:

$$\varepsilon_\infty = 2.4226;\ \varepsilon_{s1} = 2.5184;\ \varepsilon_{s2} = 8.6577;\ \varepsilon_{s3} = 2.9578;\ \varepsilon_{s4} = 3.8933 \quad (4.16a)$$

$$\omega_1 = 2.5778 \text{ eV}; \qquad \omega_2 = 4.1163 \text{ eV};$$

$$\omega_3 = 0.0333 \text{ eV}; \qquad \omega_4 = 0.04523 \text{ eV} \quad (4.16b)$$

Data calculated from the equation (4.16) are plotted in Figure 4.17, in which the refractive indices of $Al_{0.25}Ga_{0.75}As$ and $Al_{0.75}Ga_{0.25}As$ in a limited wavelength range 1.3-1.8 μm are

shown in the red and blue lines. When the wavelength increases, the refractive index of both slowly decreases. It is clear that the core layer has a higher refractive index than cladding layers.

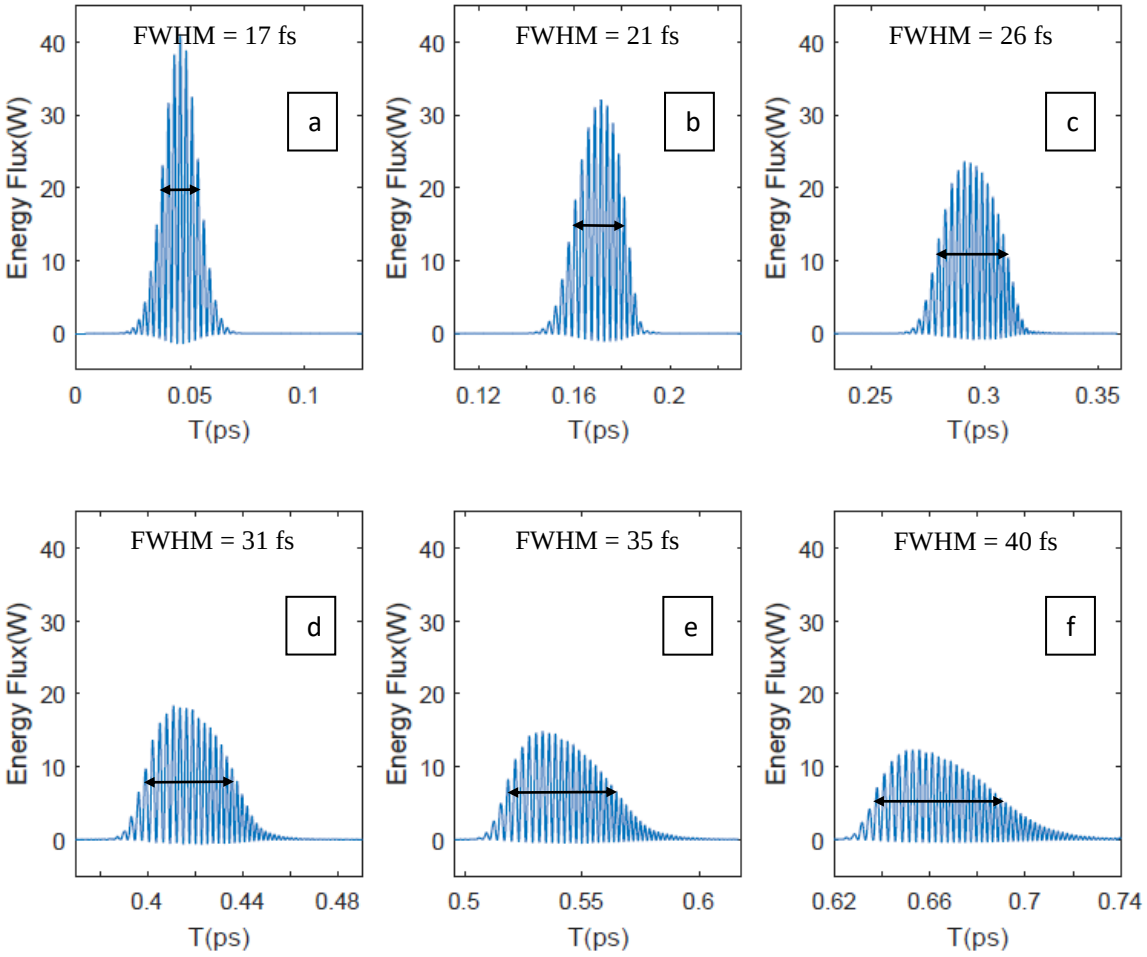

Fig. 4.18 Propagation of energy flux in $Al_{0.25}Ga_{0.75}As$ waveguide in time domain. Subfigure (a) is the incident plane and (b), (c), (d), (e) and (f) are cross-sections where the propagation lengths are 400Δz, 800Δz, 1200Δz, 1600Δz and 2000Δz, respectively.

Group velocity dispersion of $Al_{0.25}Ga_{0.75}As$ waveguide is observed in Figure 4.18, in which the excitation source contains a range of frequency components. Figure 4.18 indicates the propagation of energy flux in $Al_{0.25}Ga_{0.75}As$ waveguide in time domain, as well as the FWHM of pulses. Sub-figure (a) represents the incident plane and the pulse has a peak value of 41 W with FWHM 17 fs. In contrast, sub-figures (b) - (f) are cross-sections at 400 cells, 800 cells, 1200 cells, 1600 cells and 2000 cells away from the incident plane, respectively. Over time, the propagation distance increases to 2000 cells and the peak value of pulses drops gradually to 12 W while the FWHM grows to 40 fs, almost three times as wide as the width of the original pulse in sub-figure (a). The broadening of pulses in the time domain is caused by linear dispersion in that lower frequency components run faster than those at a higher frequency.

4.2.4 Phase matching condition of FWM

Phase matching condition is satisfied when the phase mismatch factor Δk=0. GVD plays an important role in the Taylor expansion of k so its values are plotted in Figure 4.19. D parameter, another expression of GVD, is also indicated. Figure 4.19 shows the GVD and D of $Al_{0.25}Ga_{0.75}As$ waveguide with various widths in TE and TM fundamental modes. The blue line connects the GVD points in TE fundamental mode. GVD starts from a relatively large positive value approximately 18 ps·ns/km at width 200 nm and decreases dramatically to negative value -4 ps·ns/km at width 300 nm. After that, starts to grow gradually as the width increases. GVD approaches zero when the width is 700 nm and keeps increasing to a positive value again as the width increases to 1000 nm. Therefore, it is possible to find two zero points of GVD in the figure; one is between 280 and 290 nm and the other is 700 nm.

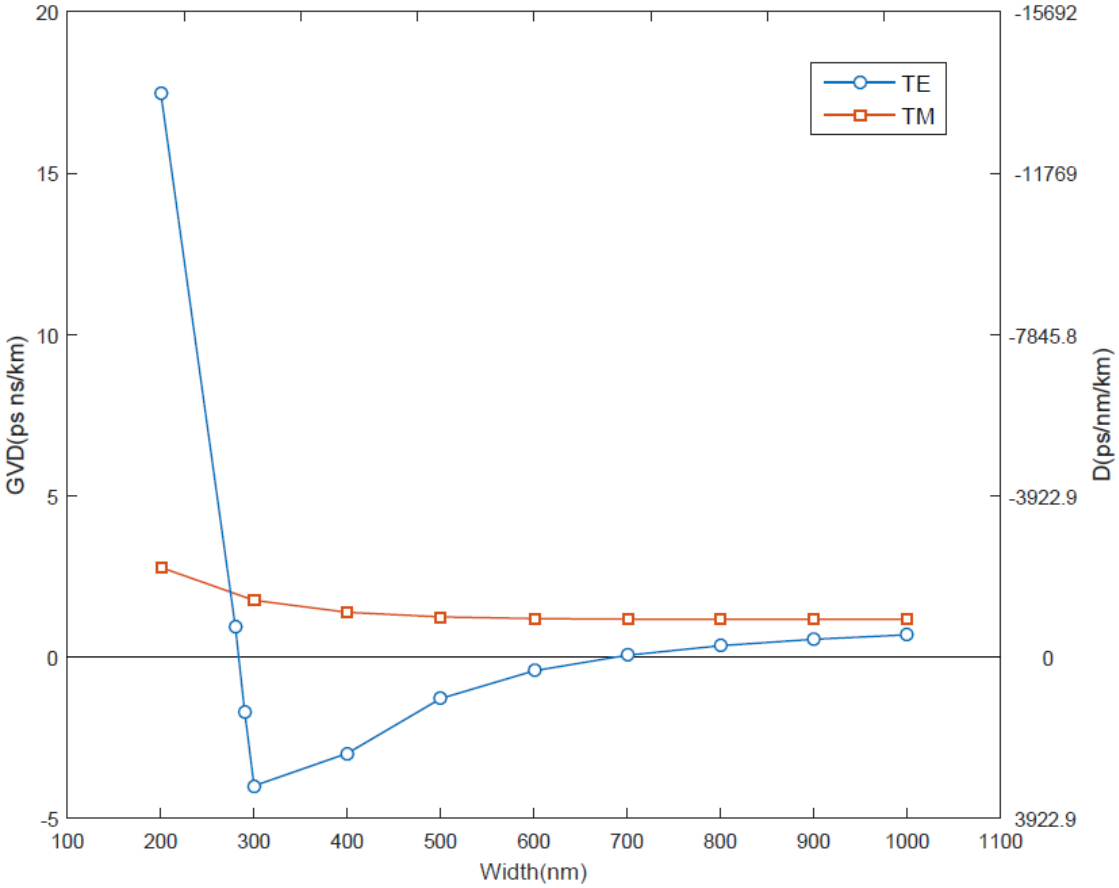

Fig. 4.19 GVD and D of $Al_{0.25}Ga_{0.75}As$ waveguides with various widths in TE and TM fundamental modes at wavelength 1.55 μm.

In order to further analyze these two widths, the left sub-figure in Figure 4.20 depicts GVD of $Al_{0.25}Ga_{0.75}As$ waveguide with various widths in TE fundamental modes in a wavelength

range of 1.3-1.8 μm. When the width is small, such as 280 nm and 290 nm, higher order dispersion terms have a big effect and GVD changes significantly when the wavelength changes. In comparison, for a large width such as 760 nm, GVD has a more stable trend and show small values in the plotted wavelength range. Consequently, 700 nm is better as the width of $Al_{0.25}Ga_{0.75}As$ waveguide for zero-GVD in TE fundamental mode at wavelength 1.55 μm.

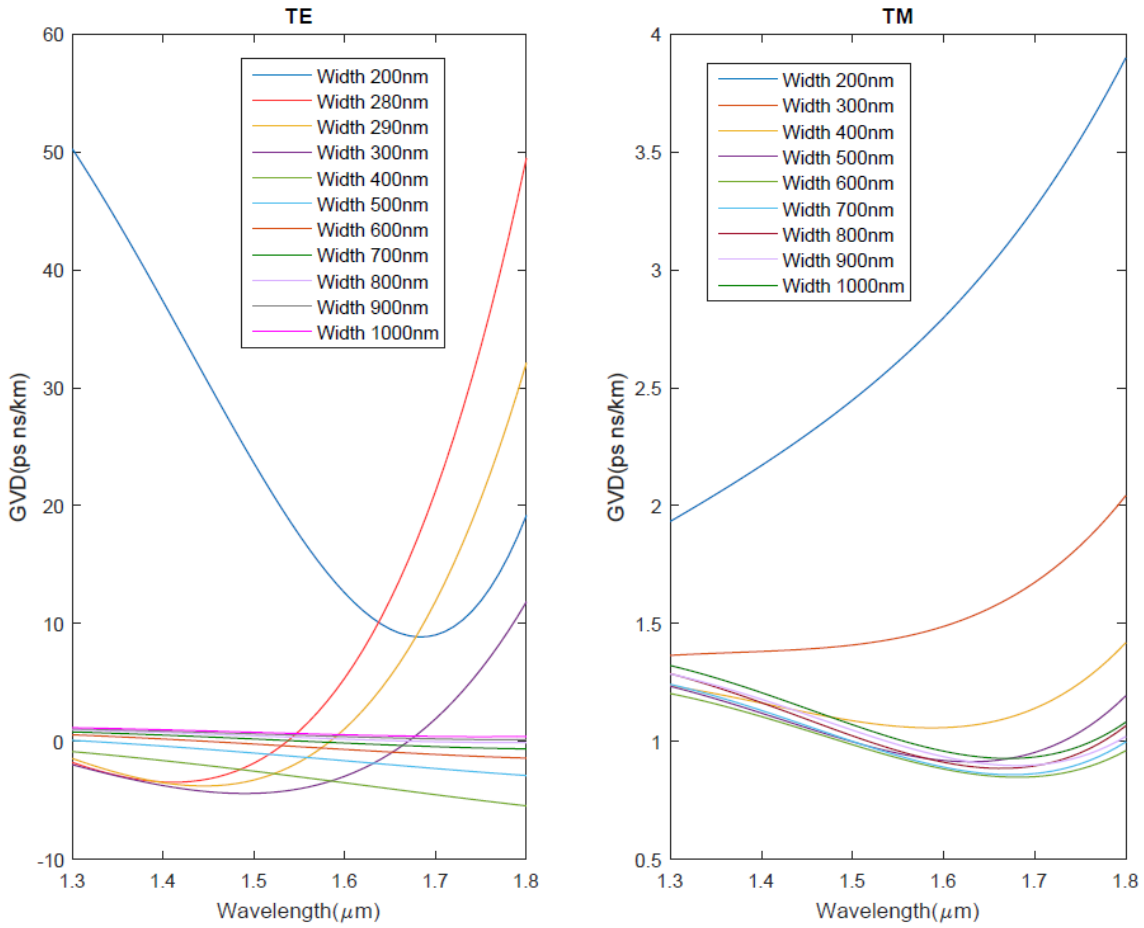

Fig. 4.20 GVD of $Al_{0.25}Ga_{0.75}As$ waveguides with various widths in TE and TM fundamental modes at wavelength 1.3-1.8 μm.

The red line in Figure 4.19 connects the GVD points of waveguides in TM fundamental mode at wavelength 1.55 μm. From a value of 3 ps·ns/km at width 200 nm, GVD decreases slowly to 1 ps·ns/km as the width grows to 1000 nm. Unlike the TE fundamental mode, it is difficult to find a zero-GVD point in TM fundamental mode at wavelength 1.55 μm. In a wider wavelength range 1.3-1.8 μm (shown in Figure 4.20) GVD of $Al_{0.25}Ga_{0.75}As$ waveguide in TM fundamental mode maintains positive values over the limited range. Therefore, phase matching in TM fundamental mode cannot be achieved when the wavelength range is between 1.3 and 1.8 μm. The results of GVD analysis shown in Figures 4.19 and 4.20 have a close match with the GVD of similar AlGaAs waveguides presented in references [84] and [89].

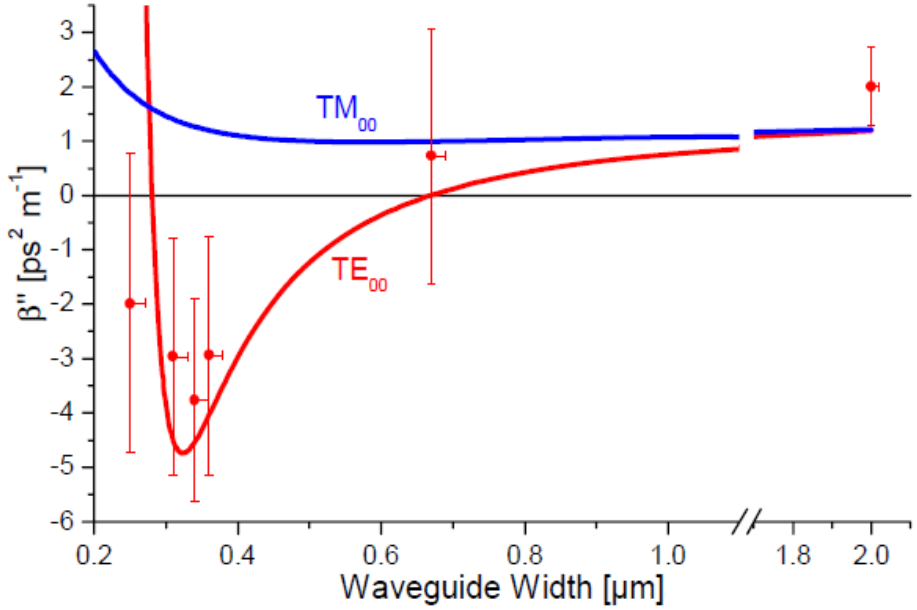

Fig. 4.21 GVD vs. waveguide width for a wavelength of 1.55 μm. Source: J. Meier, W. S. Mohammed, A. Jugessur, L. Qian, M. Mojahedi, and J. S. Aitchison, "Group velocity inversion in AlGaAs nanowires," *Opt. Express*, vol. 15, no. 20, pp. 12755–12762, 2007.

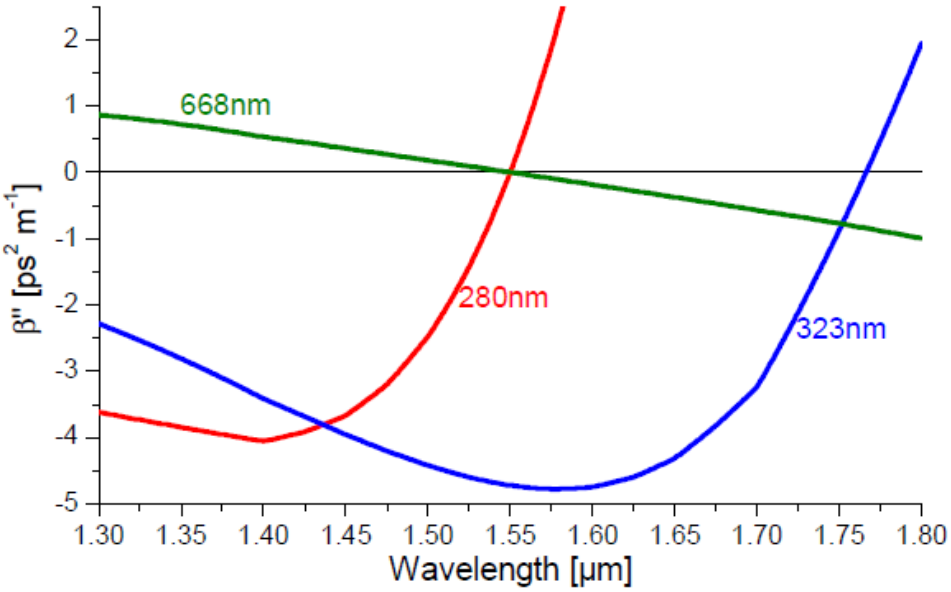

Fig. 4.22 GVD vs. wavelength for width of 668 nm, 323 nm and 280 nm. Source: J. Meier, W. S. Mohammed, A. Jugessur, L. Qian, M. Mojahedi, and J. S. Aitchison, "Group velocity inversion in AlGaAs nanowires," Opt. Express, vol. 15, no. 20, pp. 12755–12762, 2007.

Figure 4.21 and Figure 4.22 depict the GVD of a multi-layer AlGaAs waveguide at wavelength 1.55 μm reported in reference [89]. The core layer is 0.5 μm-thick $Al_{0.2}Ga_{0.8}As$ and the cladding layers are $Al_{0.7}Ga_{0.3}As$. The thickness of upper cladding and lower cladding is 0.2 μm and 2 μm, respectively. Comparing Figure 4.21 against Figure 4.19, the trends of GVD curves are similar. In TM mode, GVD in both figures keep positive values in the width range

200 to 1000 nm. They decrease gradually from a value of around 3 ps·ns/km at a width of 200 nm to around 1 ps·ns/km as the width increases to 1000 nm. In TE mode, GVD in both figures start from positive values at a width of that smaller than 300 nm, drop to the smallest value of around -4.5 ps·ns/km at a width of around 300 nm, and rise to positive values again. In Figure 4.19, zero-GVD is achieved when the width is between 280 and 290 nm or around 700 nm. In comparison, in Figure 4.21, there are also two zero-GVD points, a further look of which is shown in Figure 4.22: one width is 280 nm, the other one width is 668 nm. The trends of GVD lines of waveguides with various widths in a limited wavelength range 1.3 -1.8 μm in Figure 4.22 and Figure 4.20 are in a good agreement. For small widths, such as 280 nm, the GVD is influenced dramatically by the wavelength, which is caused by high-order terms of dispersion. In contrast, when the widths are large, such as 668nm and 700 nm, the GVD decreases gradually as the wavelength increases. In conclusion, the results of GVD of the $Al_{0.25}Ga_{0.75}As$ waveguide simulated in this chapter and those of $Al_{0.2}Ga_{0.8}As$ waveguide proposed in reference [89] are similar.

With regard to D parameter, in TM fundamental mode, it keeps negative values so the waveguide has normal dispersion in the width range. In TE fundamental mode, the waveguide has normal dispersion when the width is less than 290 nm or larger than 700 nm; the waveguide has anomalous dispersion when the width is between 290 and 700 nm. In Figure 4.18, the width of simulated waveguide was 800 nm and the excitation source was based on TM fundamental mode so it contained normal dispersion and the pulse was up-chirped. According to formula (4.9), the spreading of optical pulse could be calculated. The bandwidth of excitation source is $\frac{c}{\lambda_1} - \frac{c}{\lambda_2}$, where λ_1 and λ_2 are 1.1 and 2 μm, respectively. The GVD of waveguide with a width of 800 nm is 1.85 ps·ns/km and the propagation distance is 2000 cells. Therefore, the chirp is calculated as 22.7 fs, which confirmed the broadening 23 fs in Figure 4.18.

In order to further determine the phase matching condition based on the values of Δk, Figure 4.23 depicts Δk of $Al_{0.25}Ga_{0.75}As$ waveguide with four widths in TE fundamental mode when the pump wavelength is 1.55 μm and the signal wavelength range is 1.2-2.0 μm. Points with four colours represent the waveguide with widths 290 nm, 600 nm, 700 nm and 800 nm, respectively. Blue and red points mean widths 290 nm and 700 nm, (as discussed above) and waveguides with both widths close to zero GVD in TE fundamental mode at wavelength 1.55 μm. Therefore, Δk shows quartic curve in both cases. Compared with the 700 nm case, Δk in

290 nm case keeps small values in a shorter wavelength range and its absolute value increases markedly when the wavelength is smaller than 1.4 μm or larger than 1.7 μm, causing shorter coherent length for nonlinear interactions. As a result, 290 nm is not suitable for the FWM process. With regards to the other widths of 600 nm and 800 nm, Δk is quadratic and has larger absolute values when compared with 700 nm case. When the width is 700 nm, Δk maintains small values over the whole wavelength range 1.2-2.0 μm. It is concluded that at wavelength 1.55 μm, width 700 nm provides the best conditions for phase matching of FWM in TE fundamental mode.

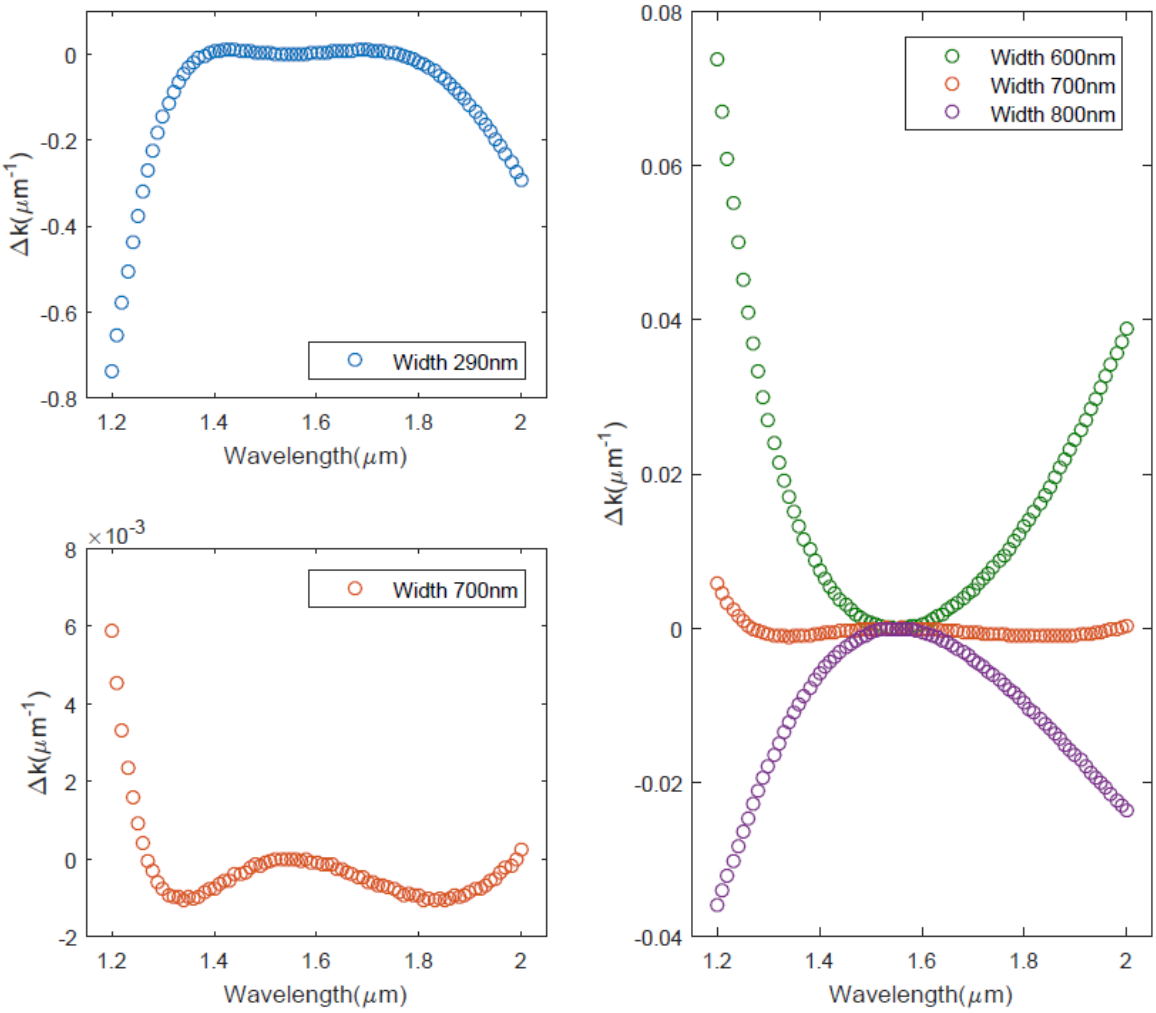

Fig. 4.23 Phase mismatch factors of $Al_{0.25}Ga_{0.75}As$ waveguides with various widths in TE fundamental mode. The pump wavelength is 1.55 μm and the signal wavelength range is 1.2-2.0 μm.

4.2.5 Results of FWM

Phase matching condition of $Al_{0.25}Ga_{0.75}As$ waveguide was analyzed in the previous section so that the width was set as 700 nm to simulate FWM process. The excitation source contains

either two frequencies or one narrow frequency range with a central wavelength 1.55 μm based on TE fundamental mode. Kerr-type nonlinearity was incorporated in the simulation. It was suggested in the reference [152] that the nonlinear refractive index of AlGaAs n_2 = 1.98 ± 0.5 $\times 10^{-13} \mathrm{cm}^2 \cdot \mathrm{W}^{-1}$. Then, the real part of Kerr parameter was gained from formula (2.70).

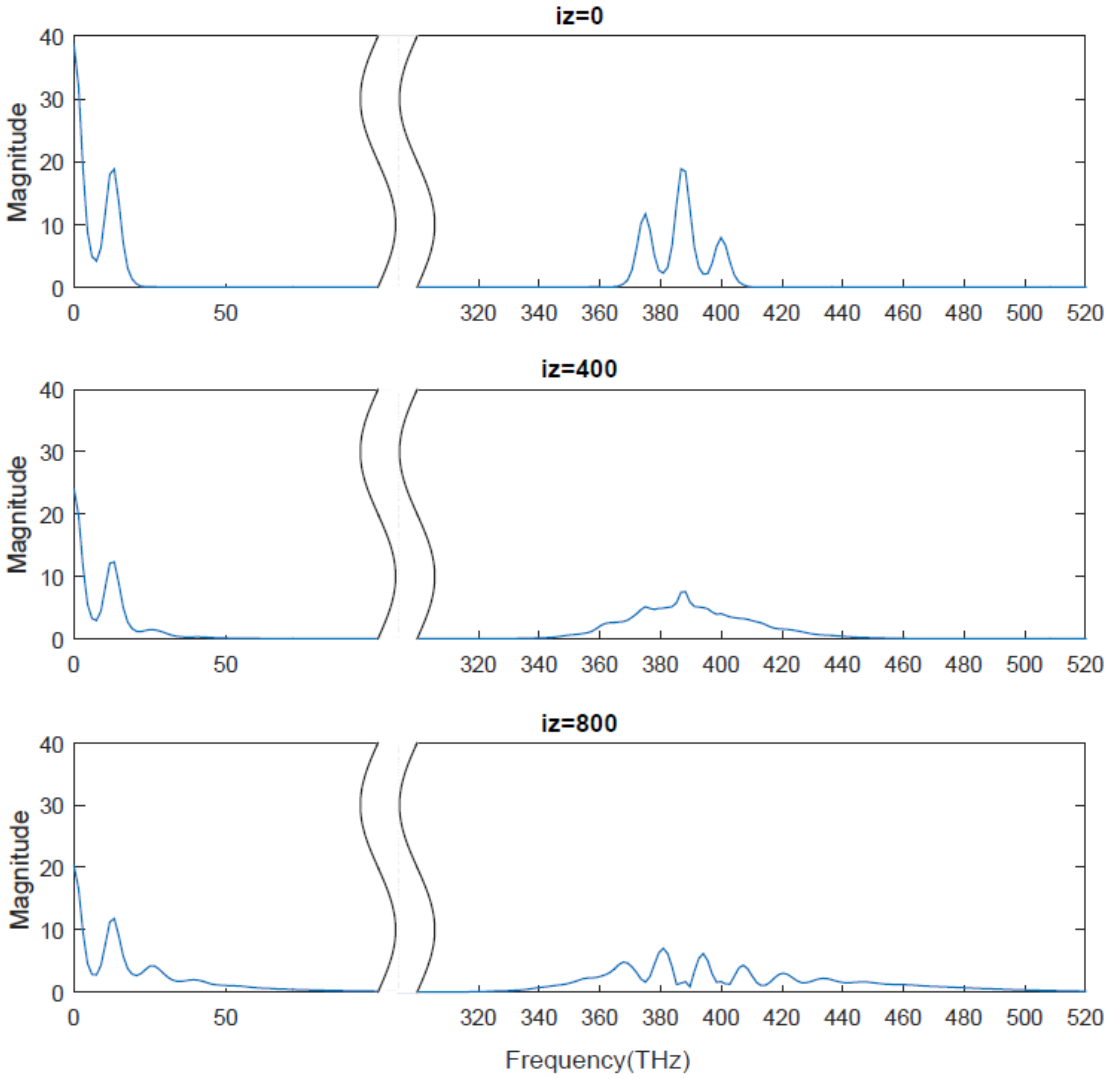

Fig. 4.24 FFT of energy flux in $Al_{0.25}Ga_{0.75}As$ waveguide with a width of 700 nm. Sub-figures represent the incident plane and cross-sections where the propagation lengths are 400Δz and 800Δz, respectively.

Figure 4.24 shows the FFT of energy flux over three cross-sections of the $Al_{0.25}Ga_{0.75}As$ waveguide. The first cross-section represents the incident plane so the frequency range is the same as the excitation source, which contains two frequencies - 187.5 THz and 200 THz - where the corresponding wavelengths are 1.6 and 1.5 μm, respectively. Hence, the FFT of energy flux shows the sum frequencies in the right pulse: 375 THz, 387.5 THz and 400 THz, as well as the difference frequencies in the left pulse: 0 THz and 12.5 THz. Then the second

cross-section is 400 cells away from the incident plane, in which the frequency ranges of pulses broaden and peak values drop. More peaks occur in the sum-frequency pulse and a new small peak is generated in the difference-frequency pulse. As for the last sub-figure, the propagation distance increases to 800 cells and the frequency ranges of pulses spread further. Therefore, over time, the propagation distance grows and more frequency components are generated because of FWM.

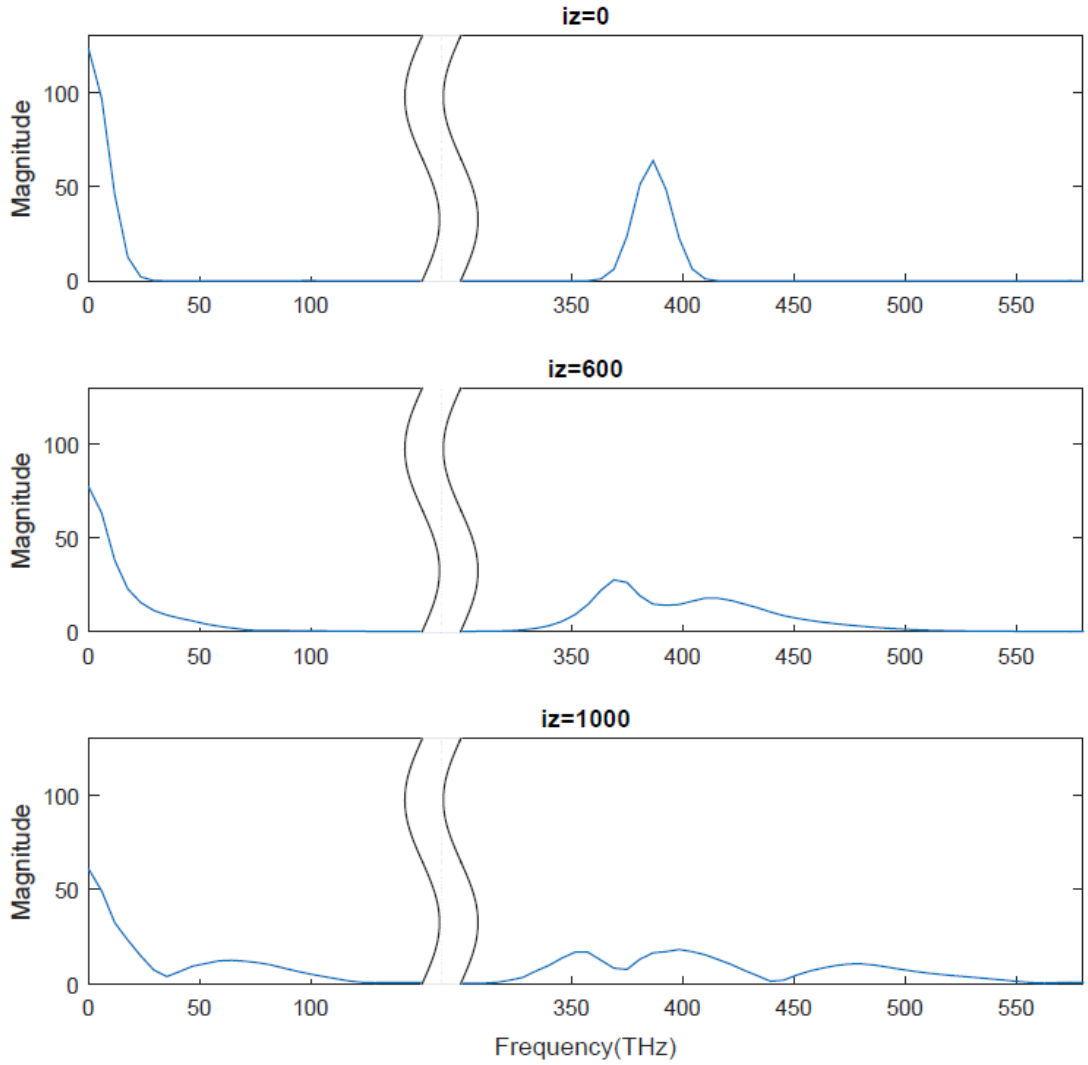

Fig. 4.25 FFT of energy flux over three cross-sections of $Al_{0.25}Ga_{0.75}As$ waveguide with a width of 700 nm. Sub-figures represent the incident plane and cross-sections where the propagation lengths are 600Δz and 1000Δz, respectively.

Different from the excitation source in Figure 4.24, Figure 4.25 contains a narrow range of frequency components. Figure 4.25 indicates the FFT of energy flux over three cross-sections of $Al_{0.25}Ga_{0.75}As$ waveguide with a width of 700 nm. In the first cross-section, which is the incident plane, the frequency range is similar to the excitation source, containing a frequency range with a central frequency of 194 THz. Its corresponding wavelength is 1.55 μm. As a

consequence, the FFT of energy flux shows the sum frequency 388 THz in the right pulse and the difference frequency in the left pulse. When the propagation distance increases to 600 and 1000 cells in the following sub-figures, the peak values of original pulses decrease while the frequency ranges are extended significantly. The final sub-figure has the longest propagation length so it has the widest frequency range, which is caused by the generation of frequency components in FWM process.

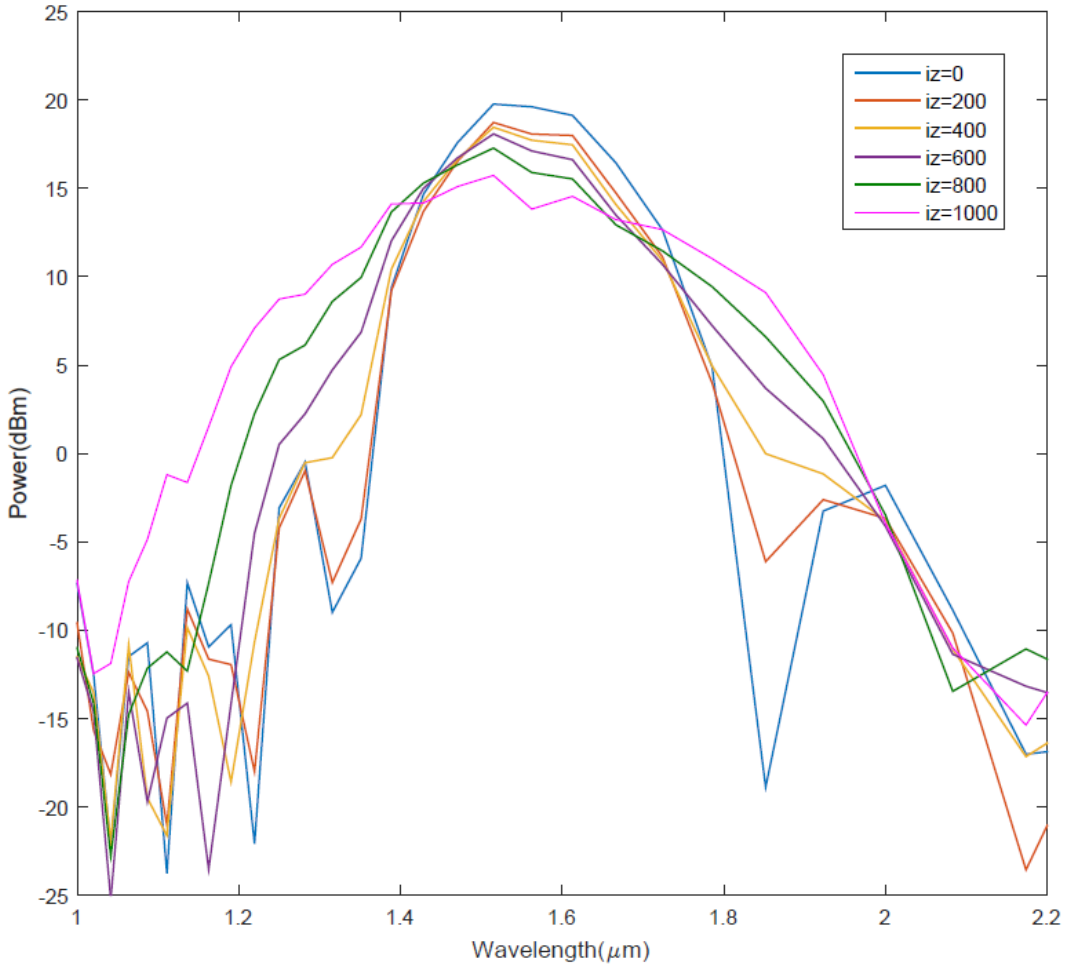

Fig. 4.26 Power spectrums of $Al_{0.25}Ga_{0.75}As$ waveguides with various propagation lengths in wavelength domain. The width of waveguide is 700nm. The lines represent wavelength components of the power propagated through the incident plane and cross-sections where the propagation lengths are 200Δz, 400Δz, 600Δz, 800Δz and 1000Δz, respectively.

Furthermore, the comparison of the power spectrums of $Al_{0.25}Ga_{0.75}As$ waveguides with various lengths in wavelength domain is illustrated in Figure 4.26 to prove the generation of new wavelength components. In order to compare the simulation results with experimental data, power spectrum is described in dBm. In the experiment, optical laser was used as a source of 120-fs (FWHM) optical pulses at a repetition rate of 82 MHz. Power was calculated based on these parameters and energy flux obtained from the simulation. Six lines represent six cross-

sections. The blue line represents the incident plane and it is utilized as the original pulse for comparison. Then the second red line represents the cross-section which is 200 cells away from the incident plane and pulse does not show much difference. When the propagation distance increases to 400 cells, broadenings occur on both sides while the peak value decreases. The broadenings keep spreading and the peak value keeps dropping as the propagation distance grows to 600 cells, 800 cells and 1000 cells. In the shorter wavelength range, the broadening is more obvious than in the longer wavelength range because of the generation of more wavelength components.

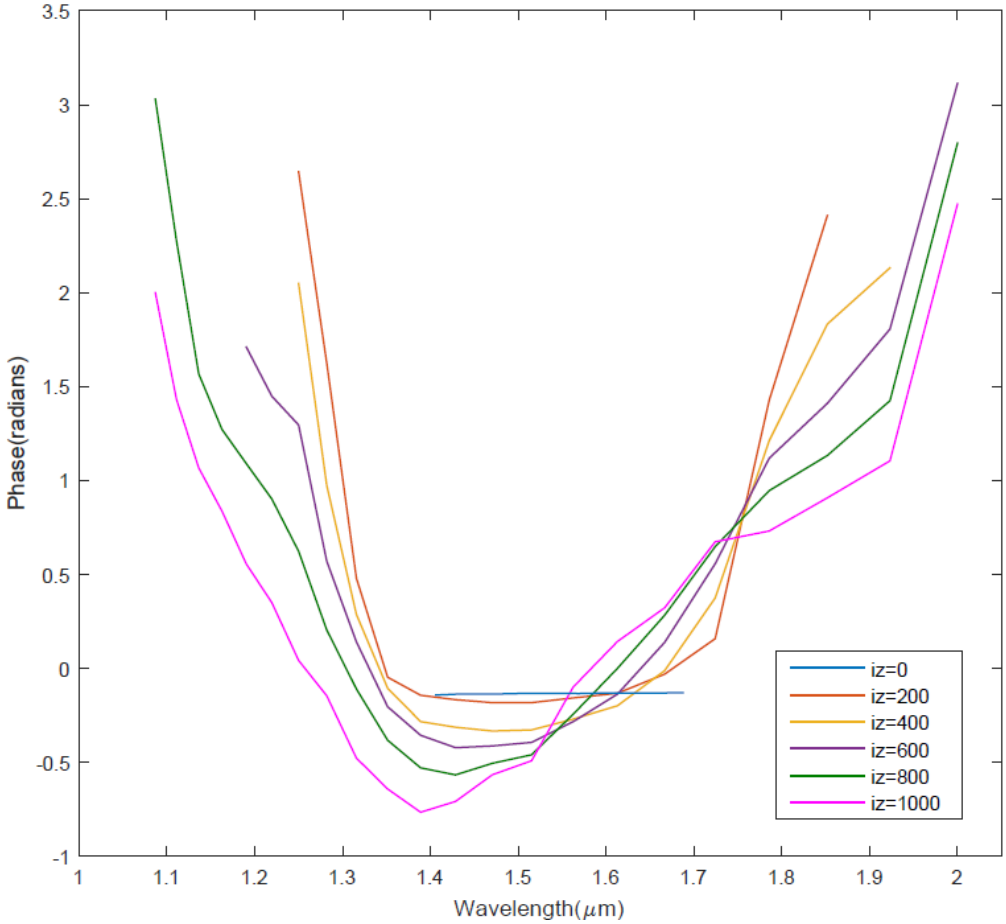

Fig. 4.27 Phase of the power spectrums of $Al_{0.25}Ga_{0.75}As$ waveguides with various propagation lengths in wavelength domain. The width of waveguide is 700nm. The lines represent the phase of wavelength components of the power propagated through the incident plane and cross-sections where the propagation lengths are 200Δz, 400Δz, 600Δz, 800Δz and 1000Δz, respectively.

In addition, Figure 4.27 depicts the corresponding phase of the power spectrums in Figure 4.26. In the incident plane, the phase of power pulse is zero, the same as the incident pulse. When the propagation distance increased, Kerr-type nonlinearity happened and new wavelength components were generated. The phase became quadratic, spread to a wider wavelength range

and shifted to the shorter wavelength range. The longer the propagation distance, the wider the wavelength range of phase. Kerr-type nonlinearity here is considered as FWM process. Therefore, the phenomenon shown in Figures 4.25-4.27 is caused by FWM.

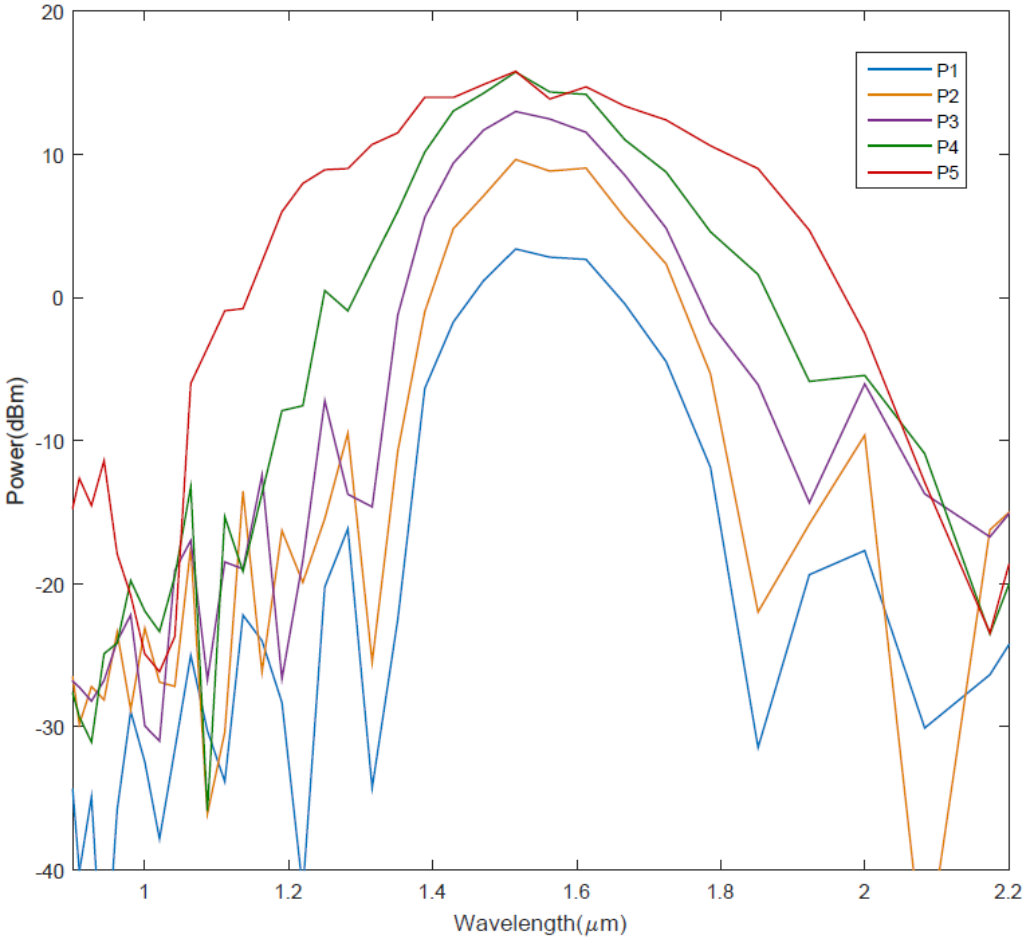

Fig. 4.28 Power spectrums of $Al_{0.25}Ga_{0.75}As$ waveguides with various incident powers in wavelength domain. The width is 700 nm and the propagation distance is 1000 cells. The blue line represents the lowest power while the red line represents the highest power.

Apart from the propagation distance, incident power also affects the efficiency of FWM. In Figure 4.28, the power spectrums are $Al_{0.25}Ga_{0.75}As$ waveguides with a range of incident power but a certain propagation distance is plotted. The width of the waveguide is 700 nm and the length is 1000 cells. Five lines represent five different incident powers. The blue line means the lowest power and the red line means the highest power. The yellow and purple lines do not make much difference when compared to the blue line. However, with regards to high power cases, such as the green and red lines, new wavelength components were produced so that the wavelength range was extended to a wider one. The red line represents the highest power so it also has the widest wavelength range. Again, in order to confirm the generation of wavelength components caused by FWM, Figure 4.29 indicates the phase of power spectrums plotted in

Figure 4.28 in wavelength domain. With regard to low power cases, the phases are close to zero value. When the power increases, the phase is described as quadratic curves and shifts to the shorter wavelength range, leading to a wider wavelength range. Therefore, it is FWM that causes the broadenings in wavelength domain of the pulses.

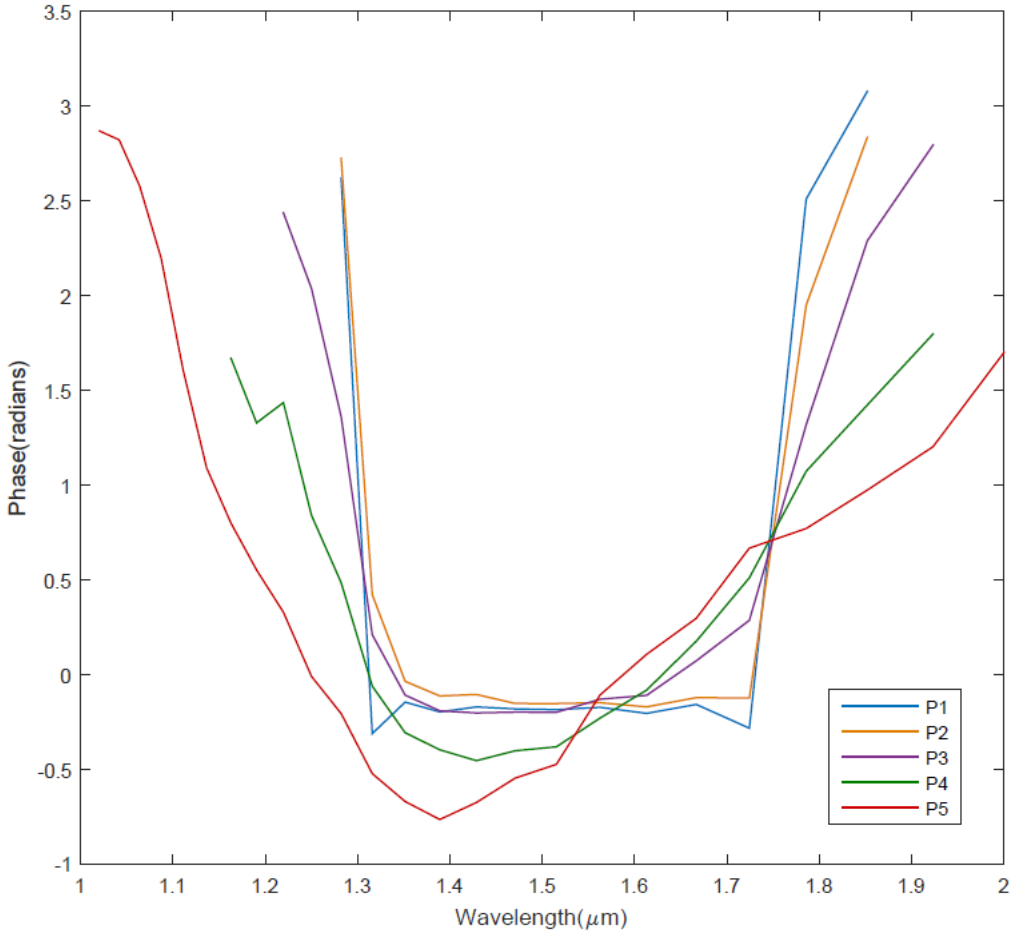

Fig. 4.29 Phase of the power spectrums of $Al_{0.25}Ga_{0.75}As$ waveguides with various incident powers in wavelength domain. The width is 700 nm and the propagation distance is 1000 cells. The blue line represents the lowest power while the red line represents the highest power.

To compare the efficiency of FWM in $Al_{0.25}Ga_{0.75}As$ waveguide with various widths and to demonstrate the importance of phase match condition, relatively long-distance propagation is simulated. Fig. 4.30 shows the comparison of the power spectrum of $Al_{0.25}Ga_{0.75}As$ waveguide with three widths of 600 nm, 700 nm and 800 nm in wavelength domain. The propagation length of waveguide is 7000 cells and is equal to 0.35 mm. The blue line represents the waveguide with a width of 600 nm. It has a wider wavelength range when compared with the original power spectrum of incident pulse as described in Figure 4.26. However, it has the smallest width of wavelength range in Figure 4.28. With regard to the green line, which represents the waveguide with a width of 800 nm, its wavelength range is wider than 600 case

but narrower than 700 nm case. Therefore, the waveguide with a width of 700 nm has the most efficient FWM process. The result agrees with the values of phase mismatch factor plotted in Figure 4.23. Considering the coherent length is 350 μm, the absolute value of Δk should be less than 0.0029 μm^{-1}. When the widths of waveguide are 600 nm and 800 nm, the wavelength ranges with required Δk are 1.46-1.65 and 1.45-1.66, respectively. With regard to the 700 nm case, Δk of the almost whole wavelength range 1.2-2.1 μm meets the requirement. Therefore, it is concluded that $Al_{0.25}Ga_{0.75}As$ waveguide with a width of 700 nm has the most wavelength components involved in the FWM process and achieves the most efficient FWM in TE fundamental mode at wavelength 1.55 μm.

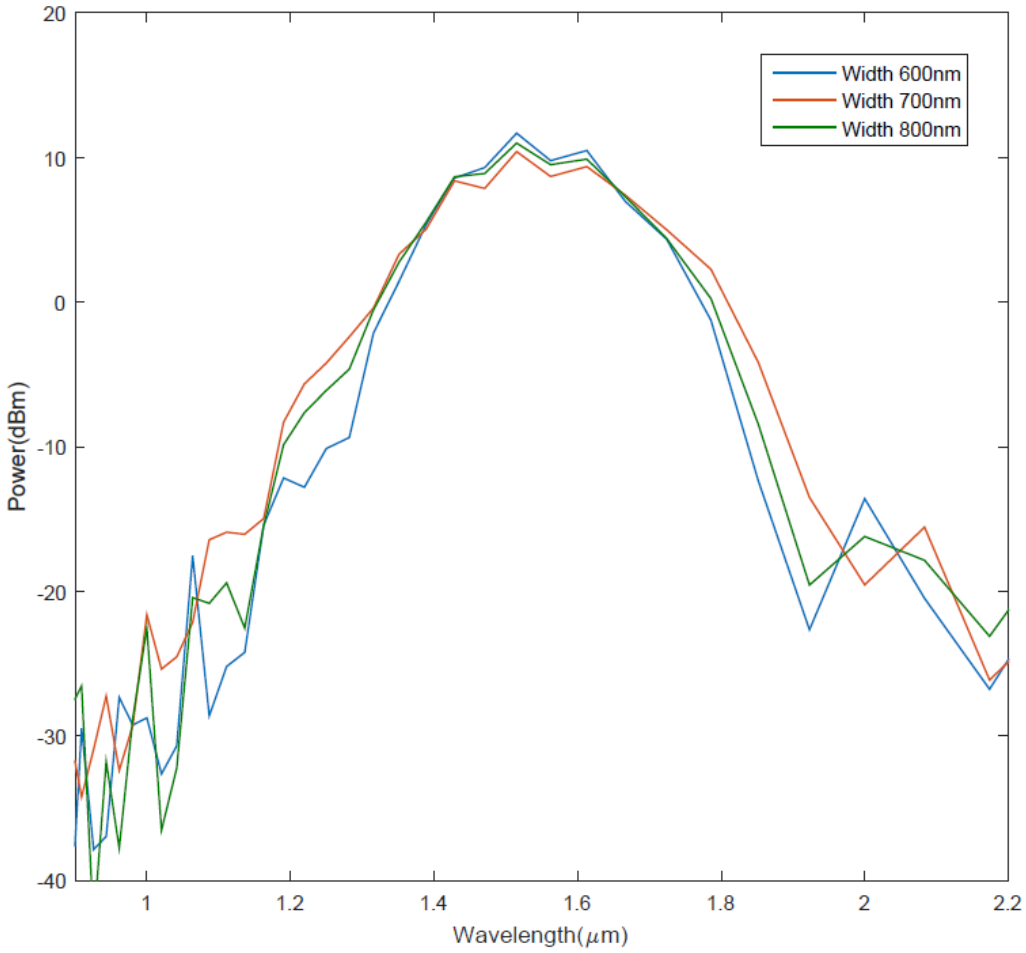

Fig. 4.30 Comparison of power spectrums of $Al_{0.25}Ga_{0.75}As$ waveguides with three widths 600 nm, 700 nm and 800 nm in wavelength domain. The propagation distance is 7000 cells.

4.2.6 Raman scattering

Though Kerr-type nonlinearity is dominant in the third-order frequency mixing process in $Al_{0.25}Ga_{0.75}As$ waveguide, it is worthwhile checking the effect of Raman scattering. Values of

Raman parameters of AlGaAs are inferred from the parameters of GaAs and AlAs that were demonstrated in reference [153]. Therefore, the optical phonon frequency $1/\tau_1$ and optical phonon lifetime τ_2 are obtained as follows:

$Al_{0.25}Ga_{0.75}As$: τ_1=114 fs; τ_2=8.77 ps (4.17a)

$Al_{0.75}Ga_{0.25}As$: τ_1'=98.47 fs; τ_2'==5.05 ps (4.17b)

Raman strength[154] has a linear relationship with Kerr nonlinearity. Therefore, the Raman response described in equation (2.73) was obtained and was incorporated in the simulation. In Figure 4.31, the effect of Raman scattering in third-order frequency mixing process of $Al_{0.25}Ga_{0.75}As$ waveguide is indicated. The width of waveguide is 700 nm and lines represent the cross-sections whose propagation lengths are 200 cells, 400 cells, 600 cells, 800 cells and 1000 cells, respectively. Figure 4.31a shows the Kerr effect and Figure 4.31b shows the Kerr effect and Raman scattering. The structures of waveguide and incident wave are the same in both simulations. The only difference is that the simulation of second sub-figure contains Raman scattering of $Al_{0.25}Ga_{0.75}As$ and $Al_{0.75}Ga_{0.25}As$. The primary trends of power spectrums in two graphs are similar, as well as the broadenings of wavelength range. It is possible to conclude that Raman scattering does not have a significant influence on the third-order frequency mixing process in $Al_{0.25}Ga_{0.75}As$ waveguide in TE fundamental mode at wavelength 1.55 μm.

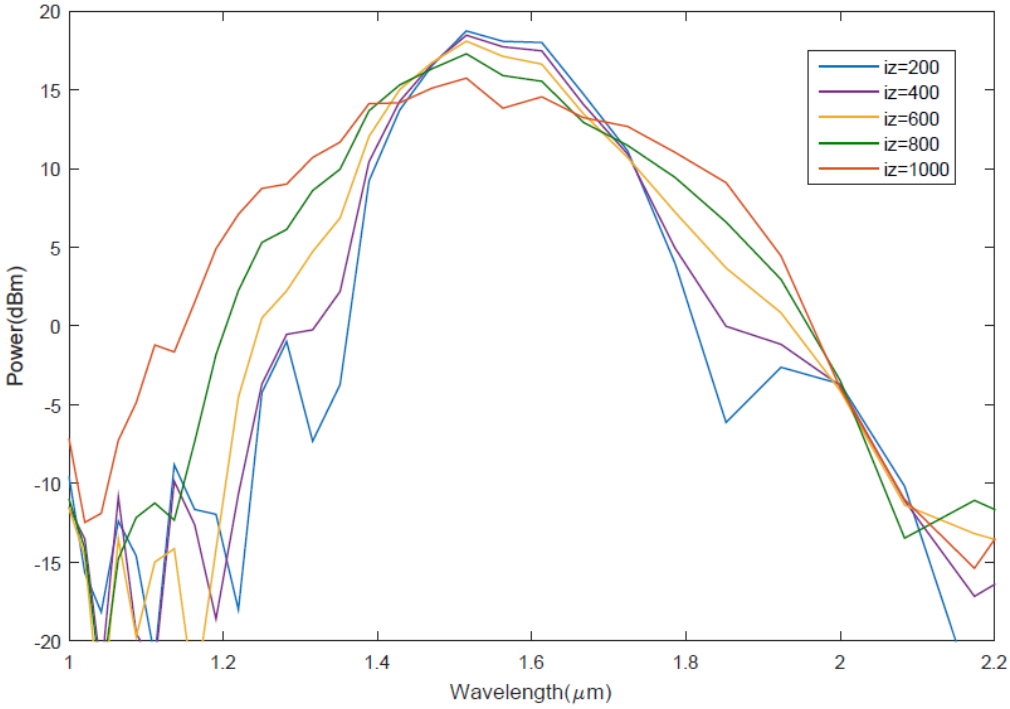

Fig. 4.31a Kerr effect of $Al_{0.25}Ga_{0.75}As$ waveguide with a width of 700 nm.

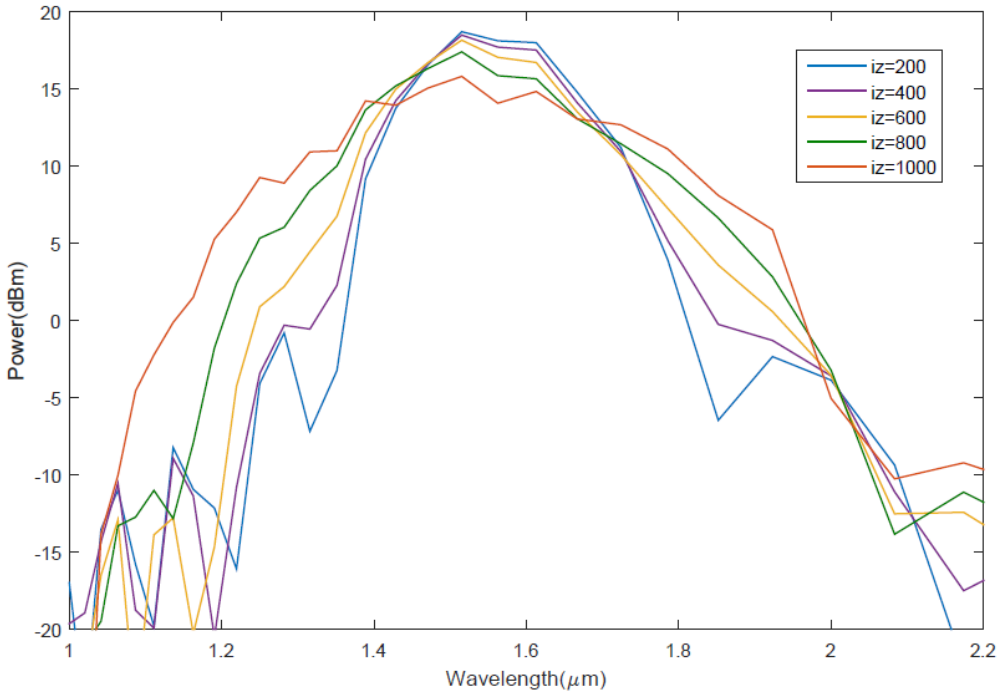

Fig. 4.31b Kerr effect and Raman scattering of $Al_{0.25}Ga_{0.75}As$ waveguide with a width of 700 nm.

4.2.7 Comparison with experimental results

Simulation results of $Al_{0.25}Ga_{0.75}As$ waveguide were a good match with the experimental data, although the length of waveguide in simulation is relatively short. Figure 4.30 indicates the power spectrums of $Al_{0.25}Ga_{0.75}As$ waveguide with a range of incident powers in the simulation. The width of waveguide is 600 nm and the length is 2000 cells, which is equal to 0.1 mm. In contrast, Figure 4.31 shows the experimental data of the same waveguide but with a longer length of 2.5 mm, which is provided by Stuart May. The input wave was defined in equation (4.2) with a central wavelength 1550 nm and the duration was determined by the optical laser that provides 120-fs (FWHM) optical pulses at a repetition rate of 82 MHz.

Figure 4.30 and Figure 4.31 compare the power spectrums of $Al_{0.25}Ga_{0.75}As$ waveguides with various incident powers in the shorter wavelength range between simulations and experiments. In Figure 4.30, dark blue line represents the lowest power (P1) while the purple line represents the highest power (P9). In both figures, in lower power cases, when the incident power increases, the power spectrum spreads to a broader wavelength range, such as the grey lines. With regards to the higher powers, the broadening becomes larger and a new pulse occurs at around wavelength 1.15 μm. When the incident power keeps increasing, the power spectrum maintains similar wavelength range, leading to the bunching of higher power curves in both

figures. In addition, in the two figures, the peak at wavelength 1.55 μm in low power cases becomes less obvious in higher power cases. Therefore, the simulation results of nonlinear frequency processes in $Al_{0.25}Ga_{0.75}As$ waveguide in agreement with the experimental data.

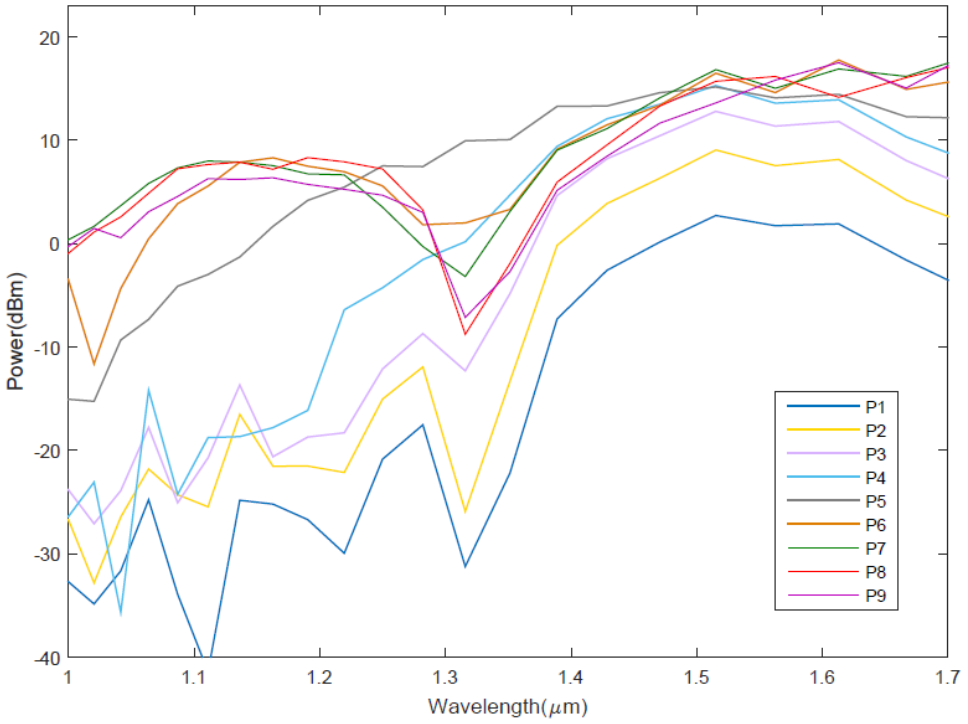

Fig. 4.32 Simulation results: power spectrums of $Al_{0.25}Ga_{0.75}As$ waveguides with various incident powers. The width is 600 nm and the propagation distance is 2000 cells.

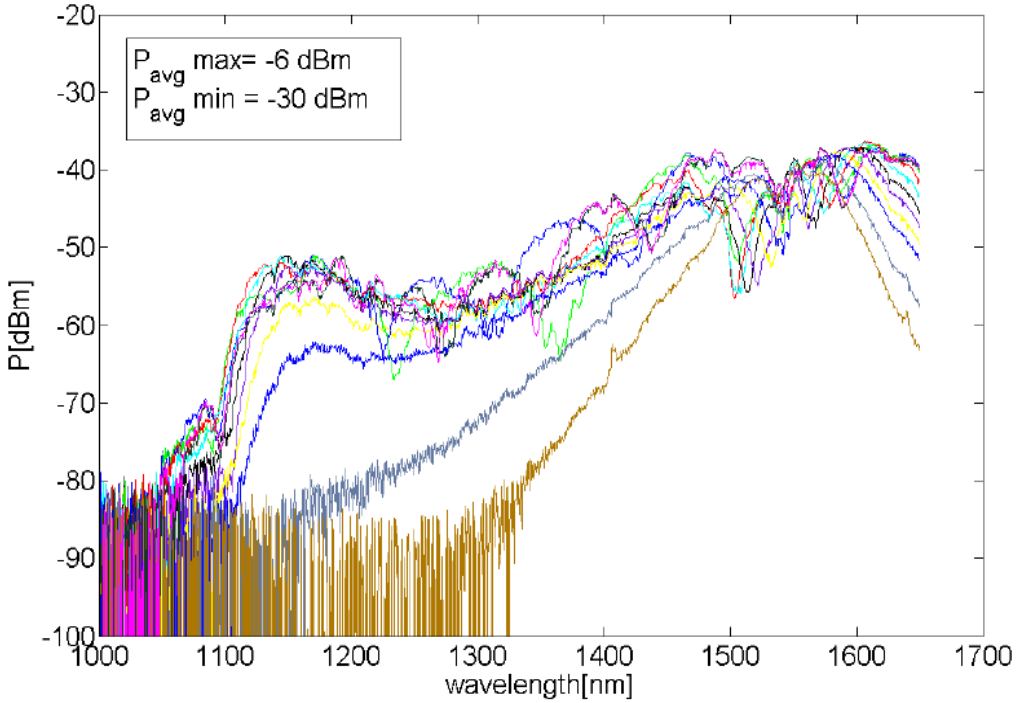

Fig. 4.33 Experimental results: power spectrums of $Al_{0.25}Ga_{0.75}As$ waveguides with various incident powers. The width is 600 nm and the propagation distance is 2.5 mm. Source: provided by Prof. Marc Sorel and Stuart May.

4.3 $Al_{0.3}Ga_{0.7}As$-on-insulator waveguide

This section presents the simulation of $Al_{0.3}Ga_{0.7}As$-on-insulator waveguide. $Al_{0.3}Ga_{0.7}As$ has a high refractive index (3.2 at wavelength 1550 nm) while silicon dioxide has a relatively low one (1.4 at wavelength 1550 nm). Strong refractive index contrast leads to mode confinement in the propagation of an optical pulse. Linear dispersion was incorporated in the simulation including material-dependent dispersion and geometry-dependent dispersion. GVD and phase mismatch factor were discussed to determine the phase matching condition of FWM in TE fundamental mode. Based on the large nonlinear refractive index of $Al_{0.3}Ga_{0.7}As$, FWM was observed in the $Al_{0.3}Ga_{0.7}As$-on-insulator waveguide.

4.3.1 Basic model

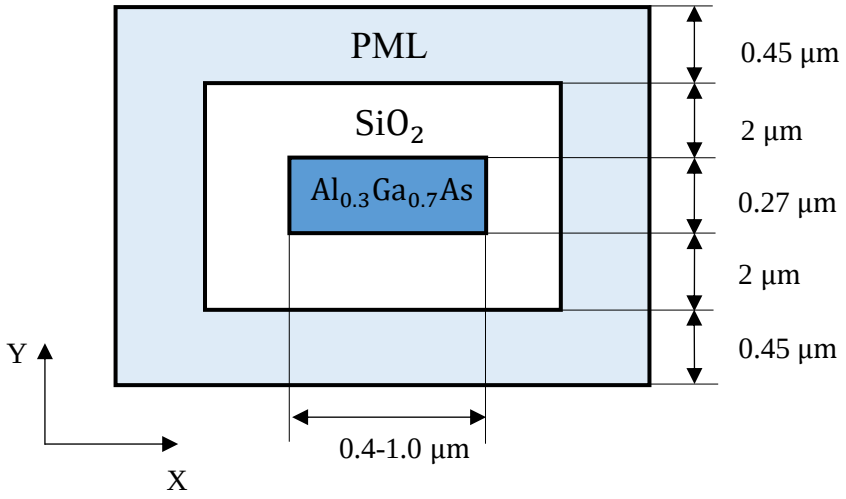

Fig. 4.34 Cross-section of $Al_{0.3}Ga_{0.7}As$-on-insulator waveguide in the simulation. Source: Stuart May.

Fig. 4.34 describes the cross-section of $Al_{0.3}Ga_{0.7}As$-on-insulator waveguide in the simulation. The core layer is $Al_{0.3}Ga_{0.7}As$ whose height is 0.27 μm and width is between 0.4 and 1 μm. The structure and height of core layer were suggested by Stuart May. Because the height of the core layer is small, the cladding layer-silicon dioxide-is set as thick as 2 μm to guarantee the mode confinement in waveguide. In addition, the outer layer is 10-cell thick PML, ensuring the problem domain is limited and the energy of radiation would be absorbed eventually. The grid sizes and time step are defined as:

Δx = 50 nm; Δy = 45 nm; Δz = 50 nm

$$\Delta t = \frac{\Delta y}{2c} \tag{4.18}$$

4.3.2 Excitation source

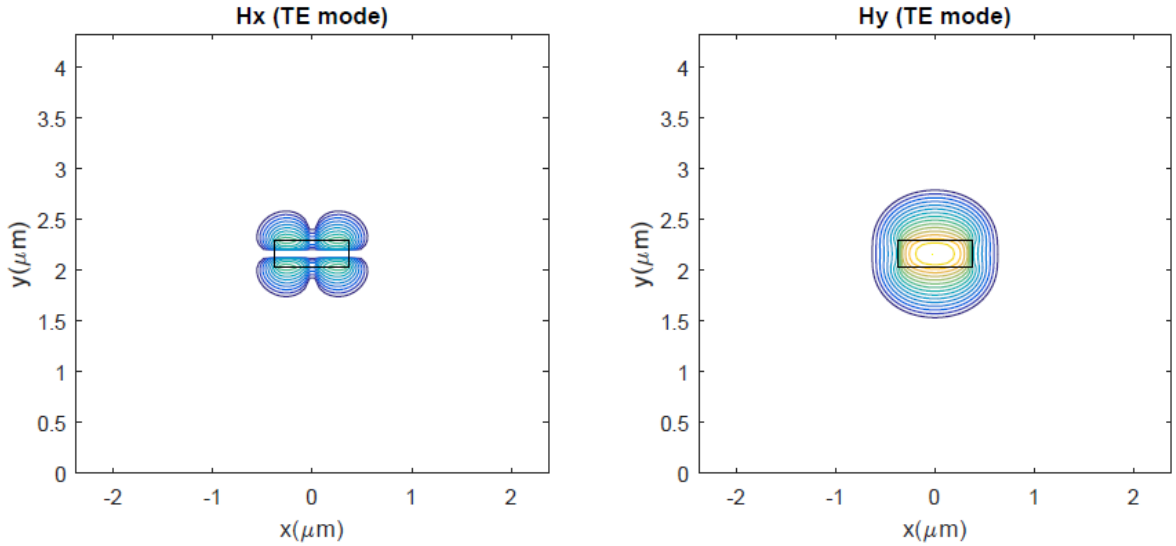

Fig. 4.35 Magnetic field in TE fundamental mode of *x-y* plane of $Al_{0.3}Ga_{0.7}As$-on-insulator waveguide at wavelength 1.55 μm. The width is 0.7 μm and the effective index of waveguide is 2.29.

Mode solver was used to incorporate geometric dispersion and to obtain the peak values of excitation source in the incident plane. Fig. 4.35 plots the values of the magnetic field in the incident *x-y* plane of $Al_{0.3}Ga_{0.7}As$-on-insulator waveguide with a width of 0.7 μm in TE fundamental mode at wavelength 1550 nm, whose effective index is 2.29. TE mode is well confined and main energy of optical pulse is propagated in the core layer. Consequently, the incident wave was obtained based on the Gaussian pulse and values of mode, which is defined in formulae (4.2) and (4.3). The duration and time delay are decided by the laser source used in the experiment which provides a source of 120-fs (FWHM) optical pulses at a repetition rate of 82 MHz.

4.3.3 Material dispersion

Material dispersion of AlGaAs was described as Lorentz resonance. In order to determine the resonances and parameters, the refractive index of $Al_{0.3}Ga_{0.7}As$ and silicon dioxide should be expressed as equation (3.7). According to the equation (4.13), a modified function for refractive index of $Al_{0.3}Ga_{0.7}As$ was obtained with four pole pairs when x is equal to 0.3. It was shown in the reference [24] that the refractive index of silicon dioxide was based on a Sellmeier

equation with three pole pairs. As a result, the relative permittivities and resonant frequencies of $Al_{0.3}Ga_{0.7}As$ and silicon dioxide can be obtained as follows:

$Al_{0.3}Ga_{0.7}As$:

$$\varepsilon_\infty = 3.6569;\ \varepsilon_{s1} = 3.6900;\ \varepsilon_{s2} = 9.9303;\ \varepsilon_{s3} = 5.1555;\ \varepsilon_{s4} = 4.2452 \quad (4.19a)$$

$$\omega_1 = 1.8627 \text{ eV}; \quad \omega_2 = 3.4011 \text{ eV};$$

$$\omega_3 = 0.0333 \text{ eV}; \quad \omega_4 = 0.04523 \text{ eV} \quad (4.19b)$$

Silicon dioxide:

$$\varepsilon_\infty = 1;\quad \varepsilon_{s1} = 1.6635;\quad \varepsilon_{s2} = 1.4407;\quad \varepsilon_{s3} = 1.8990 \quad (4.20a)$$

$$\omega_1 = 18.6523 \text{ eV}; \quad \omega_2 = 10.7875 \text{ eV}; \quad \omega_3 = 0.1253 \text{ eV} \quad (4.20b)$$

In Figure 4.36, the refractive indices in a wavelength range 1.2 - 2.0 μm have been plotted. The red line represents $Al_{0.3}Ga_{0.7}As$ and the blue line represents silicon dioxide, both of which decrease gradually when the wavelength increases. It is clear that the core layer has a higher refractive index than the cladding layer.

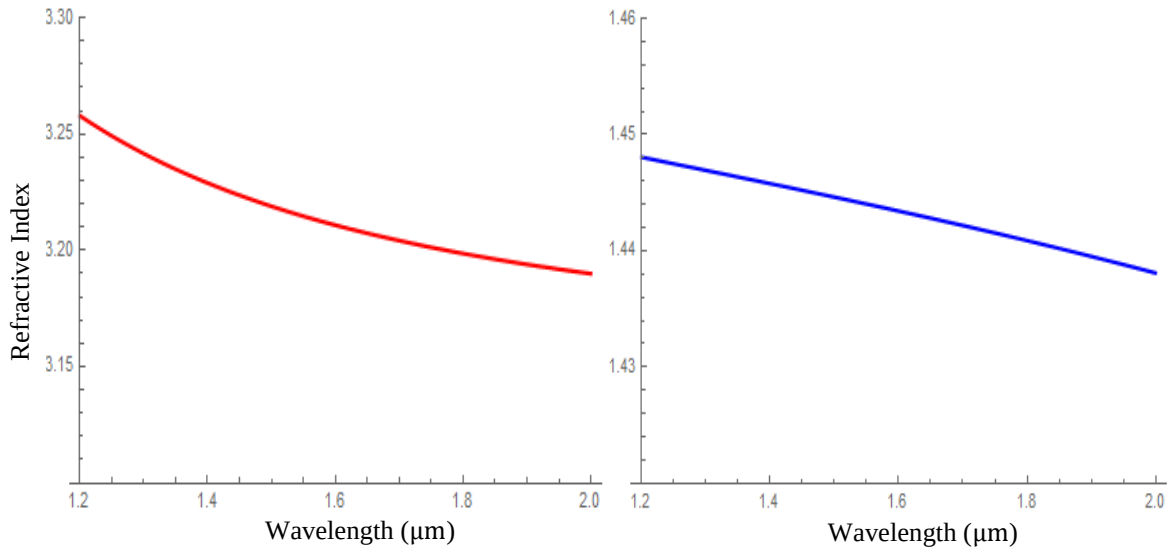

Fig. 4.36 Refractive index of AlGaAs and silicon dioxide in a wavelength range 1.2-2.0 μm. Red line represents $Al_{0.3}Ga_{0.7}As$ and blue line represents silicon dioxide.

Now that geometric dispersion can be incorporated in mode solver and material dispersion can be incorporated based on the equations (4.19-4.20), it is possible to simulate the linear dispersion of $Al_{0.3}Ga_{0.7}As$-on-insulator waveguide. In Figure 4.37, the propagation of energy flux, over time, of four cross-sections in $Al_{0.3}Ga_{0.7}As$-on-insulator waveguide is shown. Sub-

figure (a) represents the incident plane while (b)-(d) are cross-sections that are 400 cells, 800 cells and 1200 cells away from the incident plane, respectively. Compared to the input pulse in sub-figure (a), which has a peak value of 201 W and FWHM 48 fs, the pulses in subfigures (b)-(d) have smaller peak values but wider widths in time domain. The pulse with the smallest amplitude 97 W is in the sub-figure (d) and its FWHM is 55 fs. Therefore, the longer the distance the optical pulse is propagated, the lower peak value and wider width it has, and this is caused by linear dispersion.

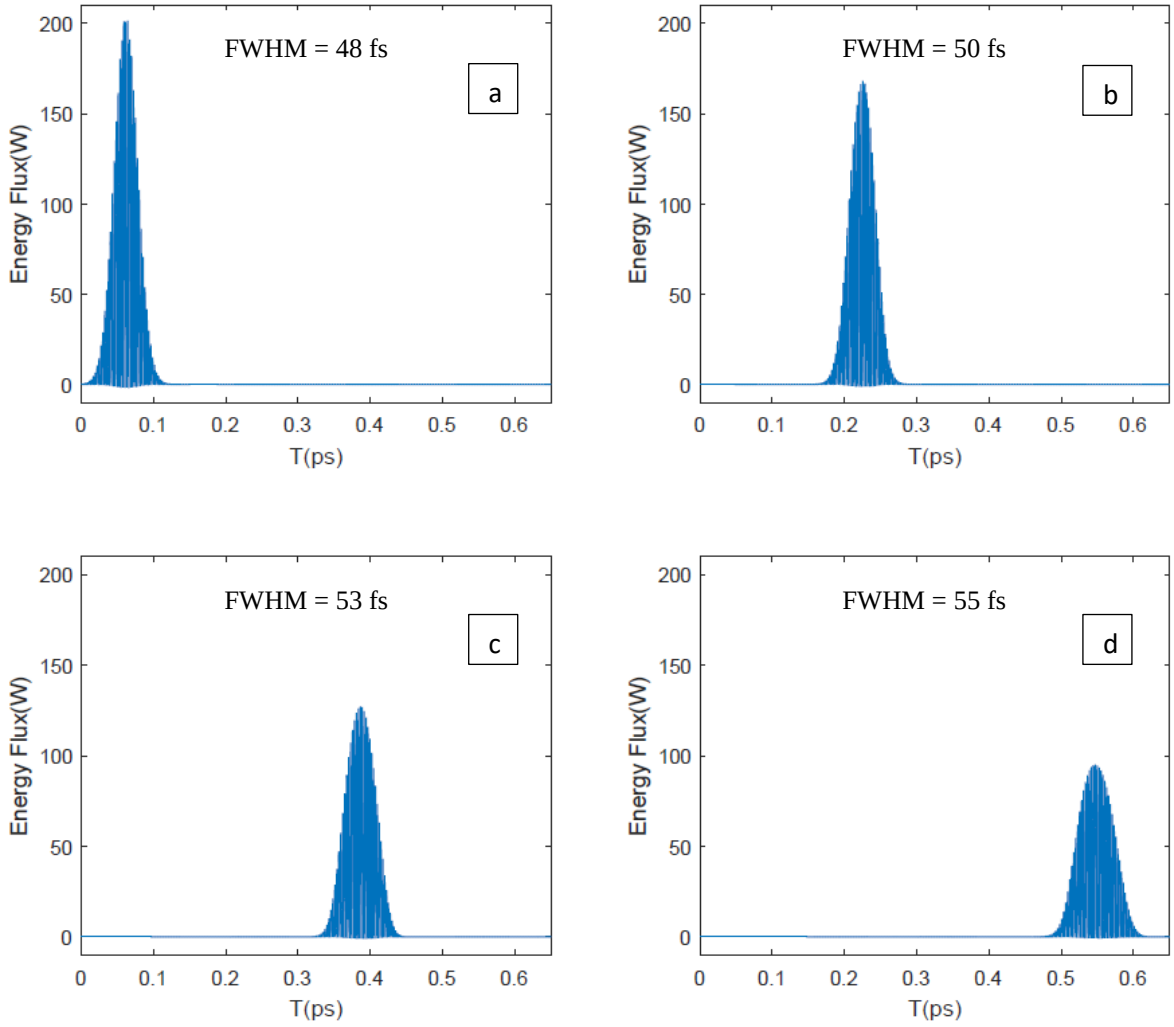

Fig. 4.37 Propagation of energy flux in $Al_{0.3}Ga_{0.7}As$-on-insulator waveguide in time domain. Energy flux of four cross-sections are described in time domain. Subfigure (a) is the incident plane and (b), (c) and (d) are cross-sections where the propagation lengths are 400Δz, 800Δz and 1200Δz, respectively.

4.3.4 Phase matching condition of FWM

In order to evaluate the nonlinear interactions and determine the phase matching condition of FWM, Figures 4.38 and 4.39 plot GVD, D and the phase mismatch factor Δk of $Al_{0.3}Ga_{0.7}As$-

on-insulator waveguide in TE fundamental mode. In Figure 4.38(b), GVD and D parameters of waveguides are shown with various widths at wavelength 1.55 μm. GVD starts from a positive value of 1.03 ps·ns/km at width 400 nm, then drops sharply to a negative value -0.42 ps·ns/km as the width increases to 500 nm. It then rises to a positive value of 0.42 ps·ns/km at width 900 nm. It is clear that there are two zero points of GVD in the figure; one is around 440 nm, the other one is 700 nm. To take a further comparison of the GVD of waveguides with these two widths, Figure 4.38(a) indicates the GVD of waveguides with various widths in TE fundamental modes in a wavelength range from 1.3-1.8 μm. Seven lines represent the waveguides with seven widths between 400 nm and 900 nm. When the width is as small as 440 nm, higher order terms of dispersion matter and GVD are dramatically affected by the change of wavelength. In contrast, with regards to 700 nm, the GVD has a more stable trend and keeps relatively small values in the whole wavelength range. Therefore, 700 nm is better than 440 nm for treatment as the zero point of GVD in TE fundamental mode at 1.55 μm.

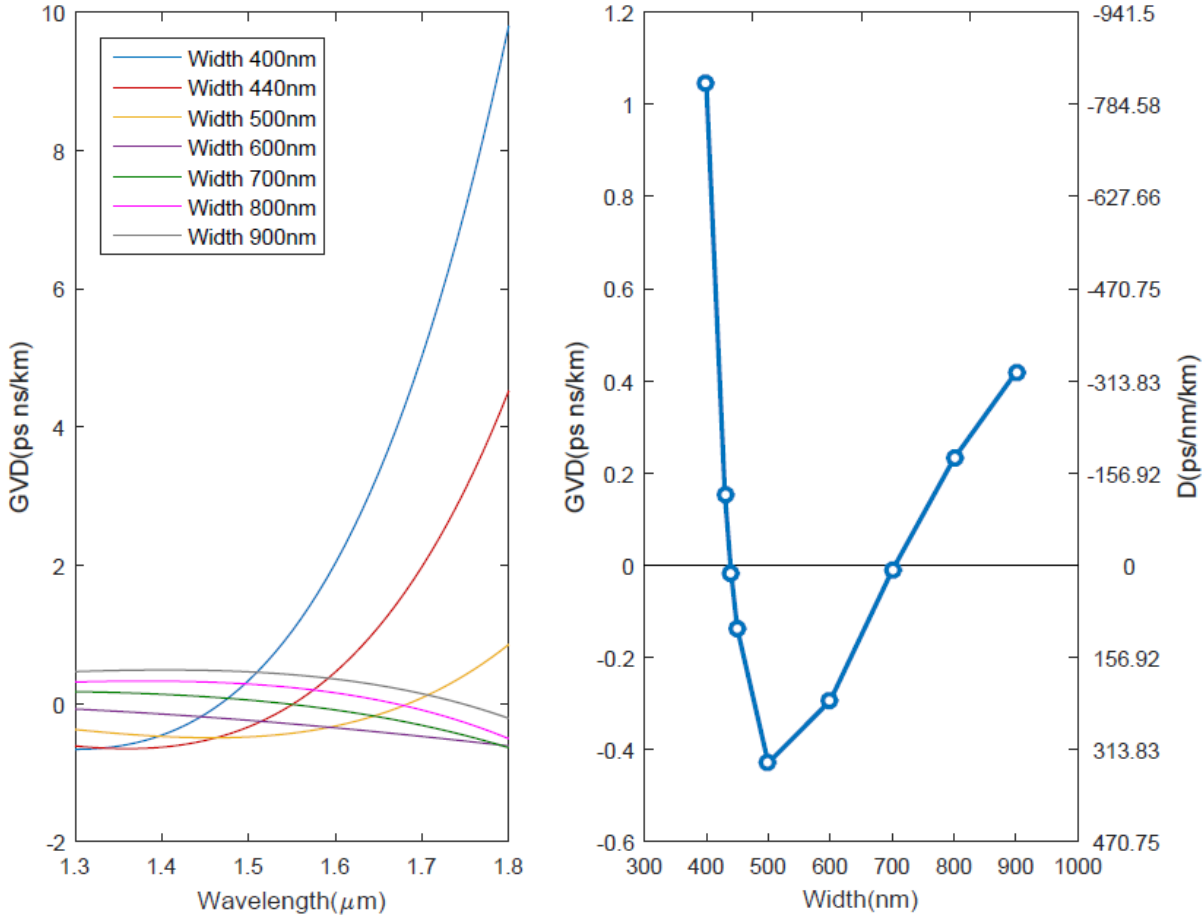

Fig. 4.38 (a) GVD of $Al_{0.3}Ga_{0.7}As$-on-insulator waveguides with various widths in TE fundamental mode at wavelength 1.3-1.8 μm; (b) GVD and D of $Al_{0.3}Ga_{0.7}As$-on-insulator waveguides with various widths in TE fundamental mode at wavelength 1.55 μm.

According to D parameter, the waveguide has normal dispersion when the width is less than 440 nm or larger than 700 nm; the waveguide has anomalous dispersion when the width is between 440 and 700 nm. In Figure 4.37, the width of simulated waveguide was 400 nm so it contained normal dispersion and the pulse was up-chirped. According to formula (4.9), the spreading of optical pulse could be calculated. The bandwidth of excitation source is $\frac{c}{\lambda_1} - \frac{c}{\lambda_2}$, where λ_1 and λ_2 are 1.1 and 2 μm, respectively. The GVD of waveguide with a width of 900 nm is 1.04 ps·ns/km and the propagation distance is 1200 cells. Therefore, the chirp is calculated as 6.9 fs, which confirmed the broadening 7 fs in Figure 4.37.

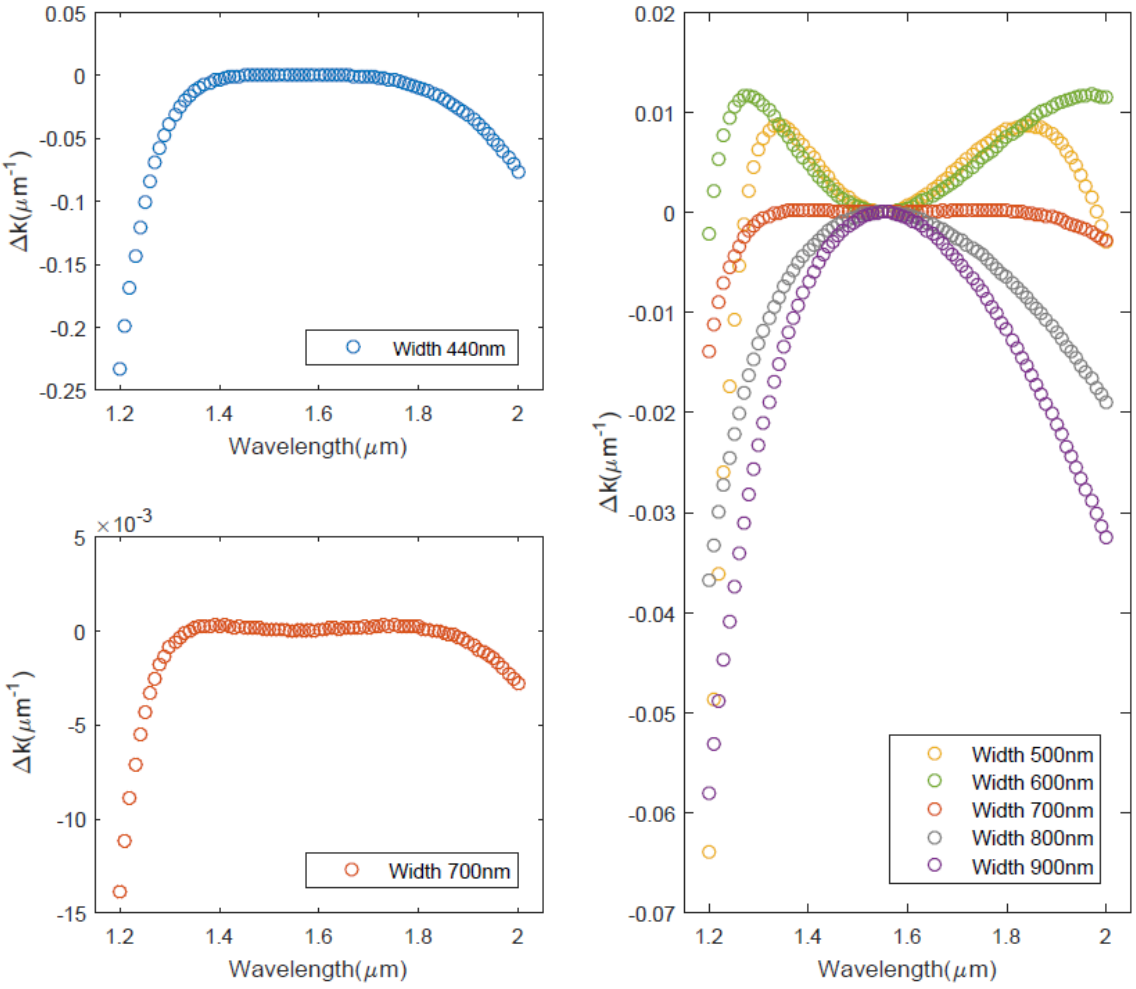

Fig. 4.39 Phase mismatch factors of $Al_{0.3}Ga_{0.7}As$-on-insulator waveguides with various widths in TE fundamental mode. The pump wavelength is 1.55 μm and the signal wavelength range is 1.2-2.0 μm.

In addition, Figure 4.39 compares the values of Δk of $Al_{0.25}Ga_{0.75}As$ waveguides with six widths in TE fundamental mode when the pump wavelength is 1.55 μm and the signal wavelength range is 1.2-2.0 μm. The widths of waveguides are 440 nm, 500 nm, 600nm, 700 nm, 800 nm and 900 nm, respectively. As was discussed above, 440 nm and 700 nm satisfy the

zero value of GVD so Δk in these two cases are quartic. When the width is 700 nm, Δk maintains small values in the whole wavelength range from 1.2-2.0 μm. However, in the 440 nm case, the absolute value of Δk is small in a relatively narrow wavelength range and increases significantly as the difference between the signal wavelength and pump wavelength grows. When the width is 800 nm and 900 nm, Δk is quadratic and its absolute value grows dramatically as the difference between the pump wavelength and signal wavelength increases. With regard to the widths 500 nm and 600 nm, Δk shows a quartic curve because the difference between 440 nm and 700 nm is small, as are their GVD values, but they still have a poorer situation for phase matching than the 700 nm case. In conclusion, compared with the 700 nm case, Δk of waveguides with those four widths have larger absolute values, leading to a shorter coherent length and a less efficient FWM process. As a consequence, it has been shown that the width 700 nm is the phase matching condition of FWM in $Al_{0.25}Ga_{0.75}As$ waveguide in TE fundamental mode at wavelength 1.55 μm.

4.3.5 Results of FWM

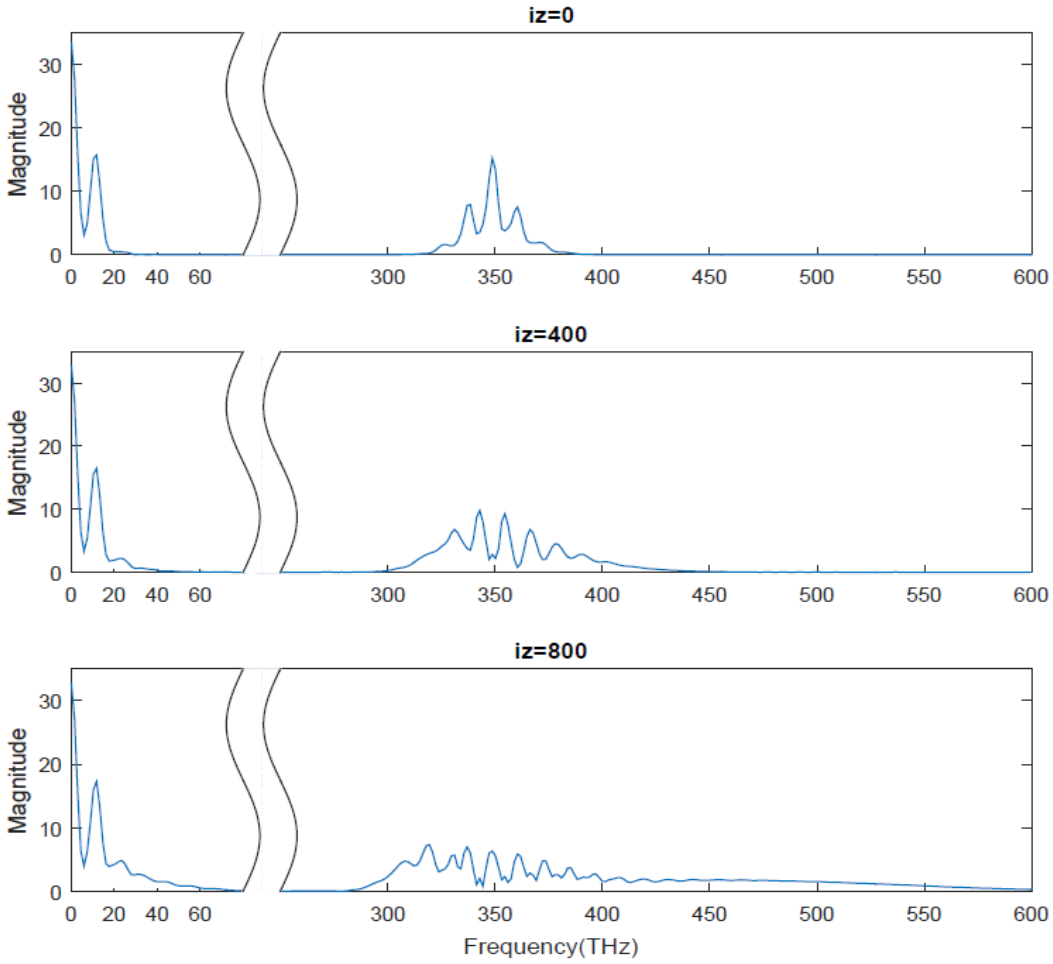

Fig. 4.40 FFT of energy flux in $Al_{0.3}Ga_{0.7}As$-on-insulator waveguide with a width of 700 nm. Sub-figures represent the incident plane and cross-sections where the propagation lengths are 400Δz and 800Δz, respectively.

According to the phase matching condition of FWM discussed in the previous section, the width of $Al_{0.3}Ga_{0.7}As$-on-insulator waveguide was set as 700 nm in TE fundamental mode at wavelength 1550 nm. The parameter of Kerr-type nonlinearity was obtained based on the nonlinear refractive index of AlGaAs[152]. In the simulation shown in Figure 4.40, the excitation source contains two frequencies. As depicted in the first sub-figure, the frequency components of the excitation source are 187.5 THz and 200 THz, where the corresponding wavelengths are 1.6 and 1.5 μm. Therefore, the FFT of energy flux shows the difference and sum of frequencies: 0 THz, 12.5 THz, 375 THz, 387.5 THz and 400 THz. When the propagation distance increases to 400 cells, pulses spread to wider frequency ranges and more peaks occur. The final sub-figure represents the cross-section that is 800 cells away from the incident plane, where the broadenings are more dramatic and pulses have the widest frequency range because of the generation of most new frequency components in FWM process.

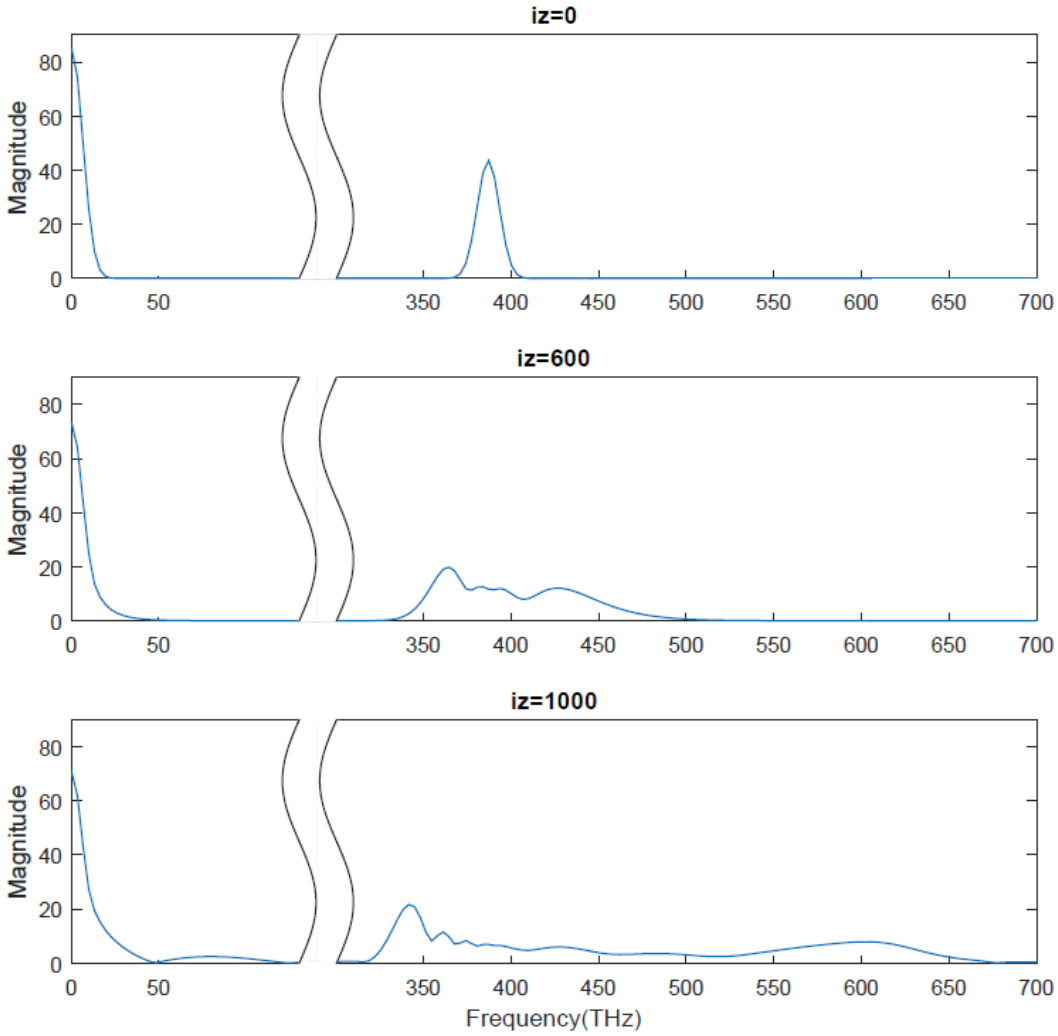

Fig. 4.41 FFT of energy flux over three cross-sections of $Al_{0.3}Ga_{0.7}As$-on-insulator waveguide with a width of 700 nm. Sub-figures represent the incident plane and cross-sections where the propagation lengths are 600Δz and 1000Δz, respectively.

The simulation in Figures 4.41-4.43 is different from the simulation in Figure 4.40 and has an excitation source which contains a narrow range of frequency components. Figure 4.41 illustrates the FFT of energy flux over three cross-sections of $Al_{0.3}Ga_{0.7}As$-on-insulator waveguide in the frequency domain. The first sub-figure represents the incident plane so that the frequency components are the same as the incident pulse. The central frequency is 194 THz and its corresponding wavelength is 1.55 μm. Therefore, the FFT of energy flux indicates a double-frequency pulse at 388 THz and a difference-frequency pulse at 0 THz. Then, the second cross-section is 600 cells away from the incident plane; its pulses have broadenings when compared with the original pulses. More peaks occur in the right pulse. When the propagation distance increases to 1000 cells, both pulses further spread so that the frequency ranges are the widest in the figure. Therefore, more wavelength components are produced when the pulse is propagated a longer distance in the $Al_{0.3}Ga_{0.7}As$-on-insulator waveguide.

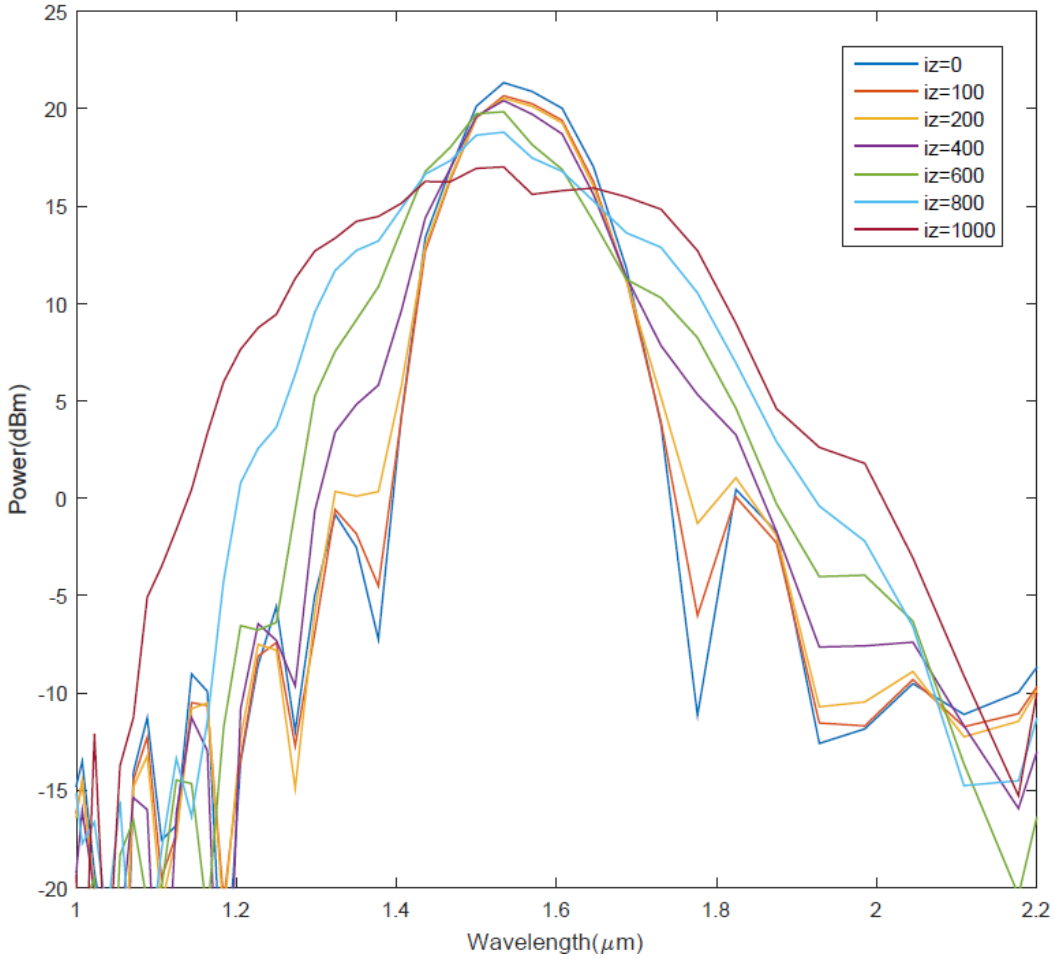

Fig. 4.42 Power spectrums of $Al_{0.3}Ga_{0.7}As$-on-insulator waveguides with various propagation lengths in wavelength domain. The width of waveguide is 700 nm. The lines represent wavelength components of the power propagates through the incident plane and cross-sections where the propagation lengths are 100Δz, 200Δz, 400Δz, 600Δz, 800Δz and 1000Δz, respectively.

To offer a clear view on the generation of wavelength components, Figure 4.42 plots the power spectrums of $Al_{0.3}Ga_{0.7}As$ -on-insulator waveguide with various propagation lengths in wavelength domain. In the incident plane, the power spectrum is described in the blue line and it is used as an initial power pulse for comparison. In short-distance cases, such as 100 and 200 cells, there are no obvious changes. When the propagation distance increases to 400 cells, broadenings occur on both sides of the power spectrum so that the wavelength range is extended. The broadenings keep spreading and the peak value keeps decreasing as the propagation distance grows to 600 cells, 800 cells and 1000 cells, respectively. The broadening on the left side - shorter wavelength range - is more significant than the one on the right side.

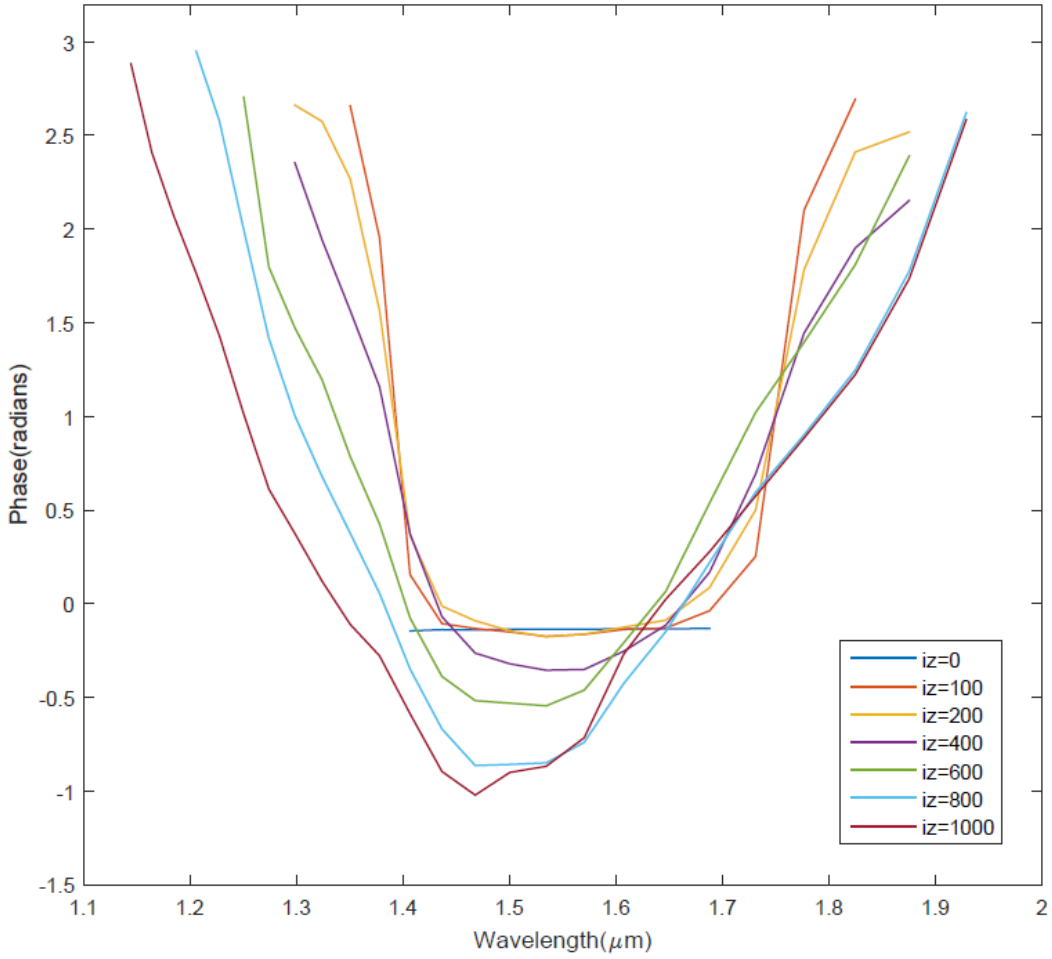

Fig. 4.43 Phase of the power spectrums of $Al_{0.3}Ga_{0.7}As$-on-insulator waveguides with various propagation lengths in wavelength domain. The width of waveguide is 700 nm. The lines represent the phase of wavelength components of the power propagates through the incident plane and cross-sections where the propagation lengths are 100Δz, 200Δz, 400Δz, 600Δz, 800Δz and 1000Δz, respectively.

In addition, the phase of power spectrums in Figure 4.42 is indicated in Figure 4.43. The phase of power pulse is zero in the incident plane and is quadratic for other cases. When the propagation distance is short, the phase is close to zero. In 400 cells case, the width of

wavelength range of phase becomes wider and it continues to grow and shift to the shorter wavelength range as the propagation distance increases to 600 cells, 800 cells and 1000 cells, respectively. This result explains the phenomenon in Figures 4.41 and 4.42 and confirms that the generation of new wavelength components is caused by FWM.

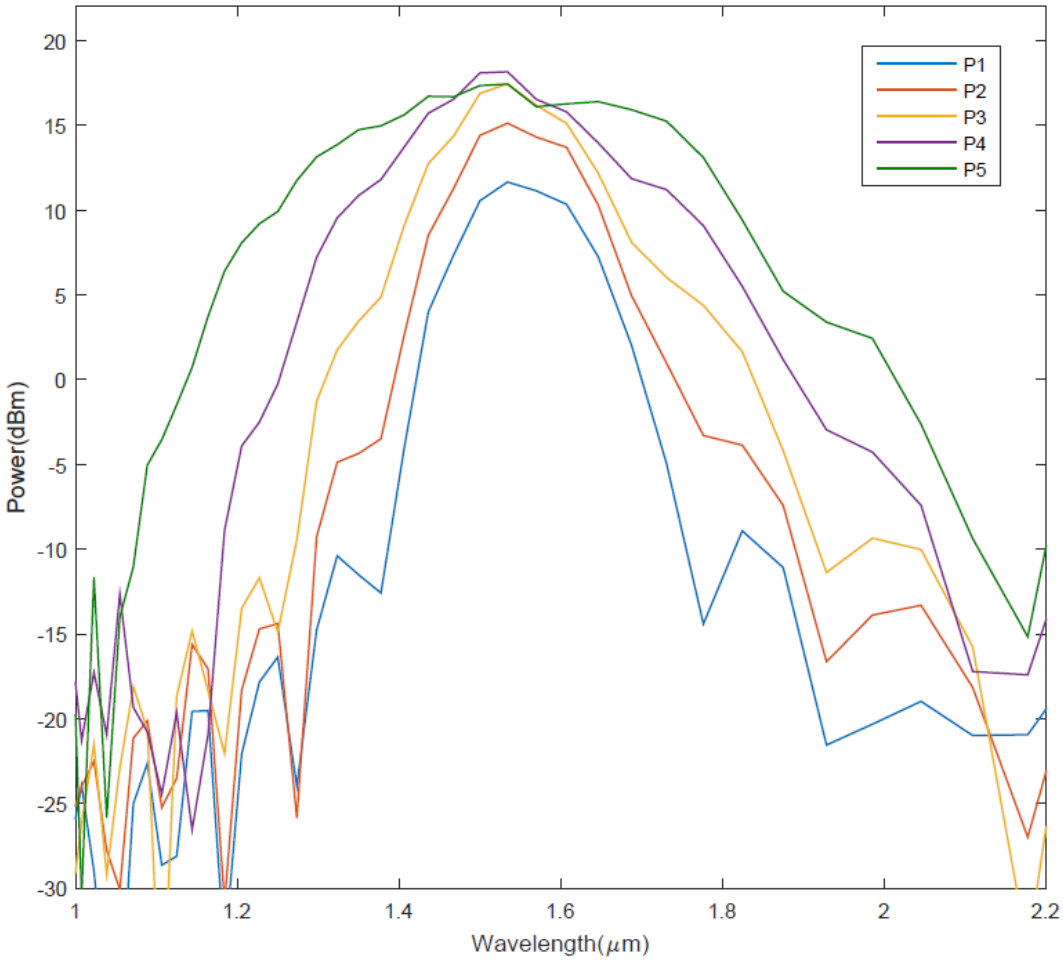

Fig. 4.44 Power spectrums of $Al_{0.3}Ga_{0.7}As$-on-insulator waveguides with various incident powers in wavelength domain. The width is 700 nm and the propagation distance is 1000 cells. The blue line represents the lowest power while the green line represents the highest power.

Figure 4.44 also compares the power spectrums of $Al_{0.3}Ga_{0.7}As$-on-insulator waveguide with various incident powers and a certain propagation distance. The width of the waveguide is 700 nm and the propagation distance is 1000 cells. Five lines represent five different incident powers, where the blue line means the lowest power and the green line means the highest power. The blue line has the smallest wavelength range and the red line does not show much difference. When the power increases to the yellow line, the broadenings occur on both sides of the power spectrum and the wavelength range becomes wider. With regards to the high power cases, such as the purple and green lines, the broadenings become more significant and the width of the wavelength range is further extended. In addition, the phase of the power spectrums in Figure

4.44 is illustrated in Figure 4.45. Phase is described as quadratic curves for all the cases. The higher the incident power, the wider the wavelength range of the phase is. Therefore, it is FWM that leads to the generation of new wavelength components in Figure 4.44.

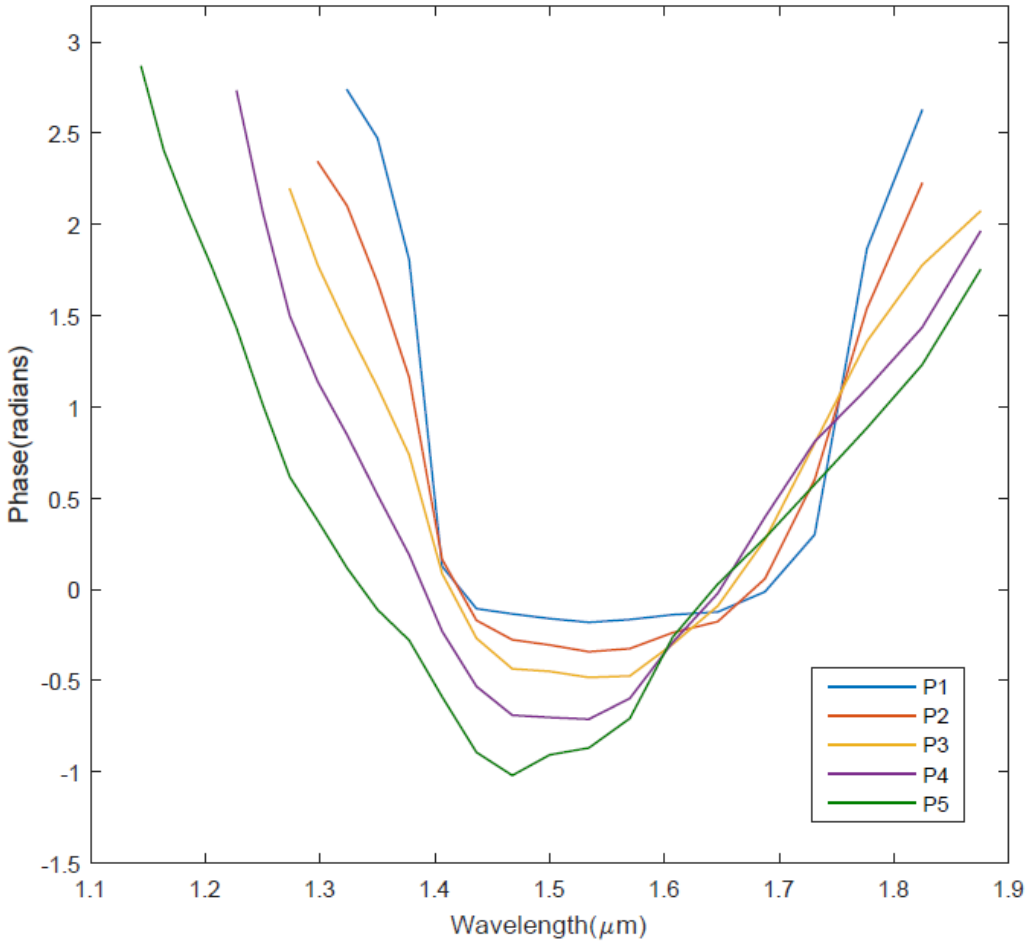

Fig. 4.45 Phase of the power spectrums of $Al_{0.3}Ga_{0.7}As$-on-insulator waveguides with various incident powers in wavelength domain. The width is 700 nm and the propagation distance is 1000 cells. The blue line represents the lowest power while the green line represents the highest power.

Furthermore, to prove the significance of phase matching condition, the FWM results of $Al_{0.3}Ga_{0.7}As$-on-insulator waveguide with various widths are compared. Three widths are 600 nm, 700 nm and 900 nm, where 700 nm satisfies the phase matching condition of FWM in $Al_{0.3}Ga_{0.7}As$-on-insulator waveguide in TE fundamental mode at wavelength 1.55 μm. The comparison of power spectrums of $Al_{0.3}Ga_{0.7}As$-on-insulator waveguide with three widths in the wavelength domain is shown in Figure 4.46. The propagation length of the waveguide is 4000 cells and is equal to 200 μm. The blue line represents the power spectrum of the waveguide with a width of 600 nm. It has a relatively wide wavelength range when compared with the initial power spectrum depicted in Figure 4.40. However, in Figure 4.46, the wavelength range of blue line is wider than 900 nm case but is narrower than 700 nm case.

Therefore, the waveguide with a width of 700 nm shows the most efficient FWM in the comparison. This result is also in agreement with the values of Δk plotted in Figure 4.39. The coherent length is 200 μm, so the absolute value of Δk should be less than 0.005 μm^{-1}. Therefore, as shown in Figure 4.39, the wavelength ranges of waveguides with widths 600 nm, 700 nm and 900 nm have the desired Δk are 1.39-1.74 μm, 1.24-2 μm and 1.42-1.7 μm, respectively. Therefore, $Al_{0.3}Ga_{0.7}As$-on-insulator waveguide with a width of 700 nm has the most wavelength components involved in nonlinear interaction in a coherent length of 200 μm and achieves the most efficient FWM process in TE fundamental mode at wavelength 1.55 μm.

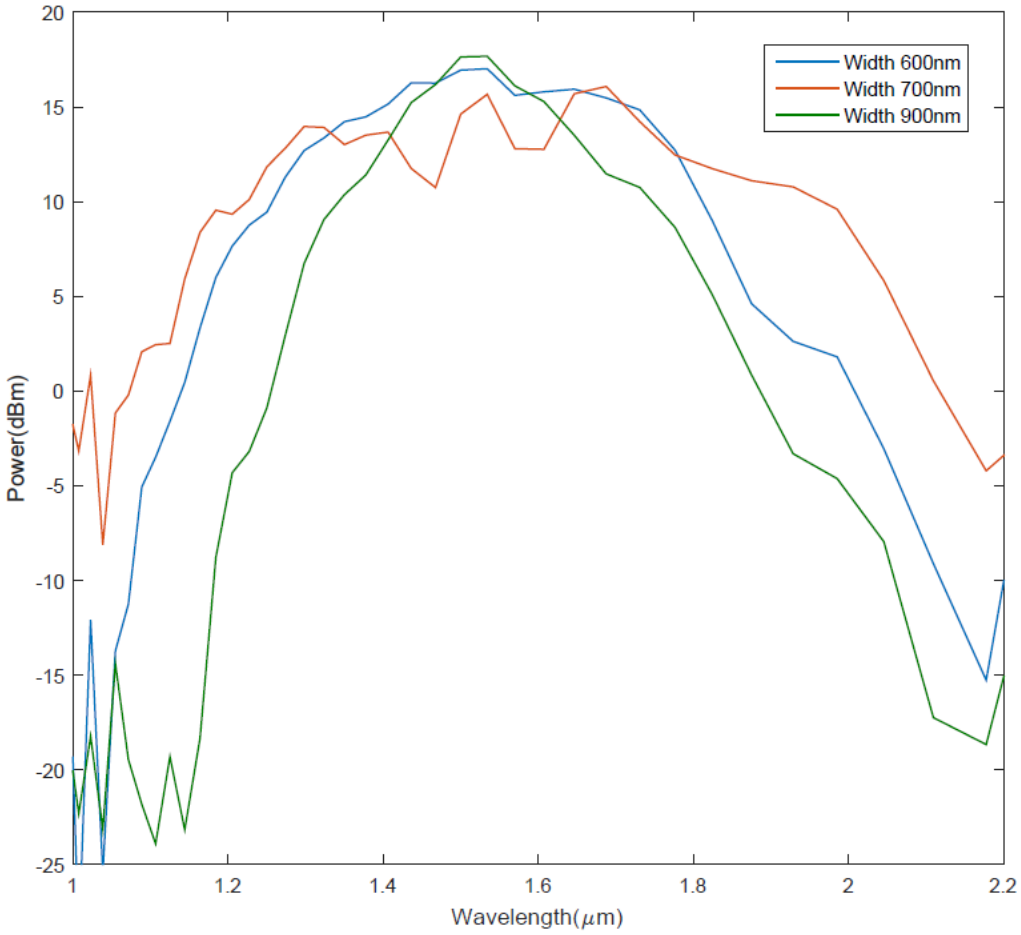

Fig. 4.46 Comparison of power spectrums of $Al_{0.3}Ga_{0.7}As$-on-insulator waveguide with three widths 600 nm, 700 nm and 900 nm in wavelength domain. The propagation distance is 4000 cells.

4.4 Conclusion

This chapter has introduced the simulations of FWM processes with FDTD algorithm discussed in previous two chapters in three waveguides: the GaAs suspended waveguide, the deep-etched multi-layer $Al_{0.25}Ga_{0.75}As$ waveguide and the $Al_{0.3}Ga_{0.7}As$ -on-insulator waveguide. The

excitation source was obtained through Gaussian pulse and TE mode at wavelength 1.55 μm. In these waveguides, there were two widths that satisfied zero-GVD and the waveguide with the smaller width was strongly affected by the high-order terms of dispersion, so that the bigger width was better and chosen for phase matching, which was proved by phase mismatch factor.

GaAs suspended waveguide was a relatively simple example. Because of the high refractive index and large co-efficient of Kerr-type nonlinearity of GaAs, super-continuum and generation of frequency comb based on FWM were realized when the width of waveguide was 760 nm and phase matching condition was achieved. However, TPA of GaAs was not taken into account and it may cause power loss and influence FWM. In contrast, AlGaAs has the advantages of GaAs and small TPA co-efficient, as well as the flexibility of adjusting refractive index in a wide range, so that it is ideal for real optical devices. In the simulation of the deep-etched multi-layer $Al_{0.25}Ga_{0.75}As$ waveguide, the results of GVD and phase matching condition of FWM were similar to the similar waveguides presented in the references. Power spectrums and their phases were analysed and compared between the waveguides with various propagation distances, incident powers or widths. Results of FWM were observed in the waveguide with a width of 700 nm. Although Kerr effect was dominant in the deep-etched multi-layer $Al_{0.25}Ga_{0.75}As$ waveguide, Raman scattering was incorporated to check its effect. The simulation results of the waveguide with a width of 600 nm showed a good agreement with the super-continuum in the experimental measurements. With regard to the $Al_{0.3}Ga_{0.7}As$-on-insulator waveguide, it has a newly designed structure and phase matching condition of FWM was fulfilled when the width was 700 nm. Comparisons of power spectrums and corresponding phases between the waveguides with various propagation distances, incident powers or widths were shown. It was demonstrated that efficient FWM was realized when the phase matching condition was satisfied.

Chapter 5

Four-Wave Mixing of Silicon-Based Waveguides

This chapter presents the simulations of four-wave mixing process for two silicon-based waveguides: the silicon-on-insulator waveguide and the silicon rich silicon nitride (SRSN)-on-insulator waveguide. Models and methods to incorporate linear dispersion and nonlinearity are demonstrated. Either linear dispersion or nonlinearity could be turned on or turned off so that it was flexible enough to check the linear and nonlinear characteristics. FWM was observed in both waveguides based on Kerr-type nonlinearity.

5.1 Silicon-on-insulator waveguide

A silicon-on-insulator waveguide is a typical waveguide because of the mature and low-cost fabrication technology of silicon, as well as the potential application in integrated circuits. The contrast of refractive index between silicon and silicon dioxide ensures strong mode confinement inside the waveguide. In simulation, both material-dependent dispersion and geometric-dependent dispersion are taken into account. Kerr-type nonlinearity is incorporated to simulate the FWM process. The phase matching condition of FWM is discussed based on the GVD and phase mismatch factor. Moreover, waveguides with various distances, incident powers or widths are compared to show the results of FWM.

5.1.1 Basic model

The structure of silicon-on-insulator waveguide in the simulation is depicted in Figures 5.1 and 3.1. *X*-*y* plane is bounded by PML absorbing boundary conditions while the *z*-direction has cyclic boundary conditions. Figure 5.1 depicts a cross-section of the silicon-on-insulator waveguide. The core layer is silicon, according to the suggestion from Professor David Hutchings, the thicknesses of silicon wafers in the experiments are 0.22 μm, 0.34 μm and 0.4 μm. The height is 0.22 μm and the width is between 0.3 and 0.8 μm because this set of values do not allow the existence of high-order modes in the waveguide and provide the

possibility of finding zero value of GVD when the excitation source is based on TE fundamental mode. In contrast, the cladding layer is 1-μm thick silicon dioxide and the thickness was decided in mode solver to make sure the mode was confined. To cut off the problem domain and absorb the energy escapes from the waveguide, the outer layer is 10-cell thick PML absorbing boundary. The grid sizes and the time step are defined as:

Δx = 50 nm; Δy = 44 nm; Δz = 50 nm

$$\Delta t = \frac{\Delta y}{2c} \tag{5.1}$$

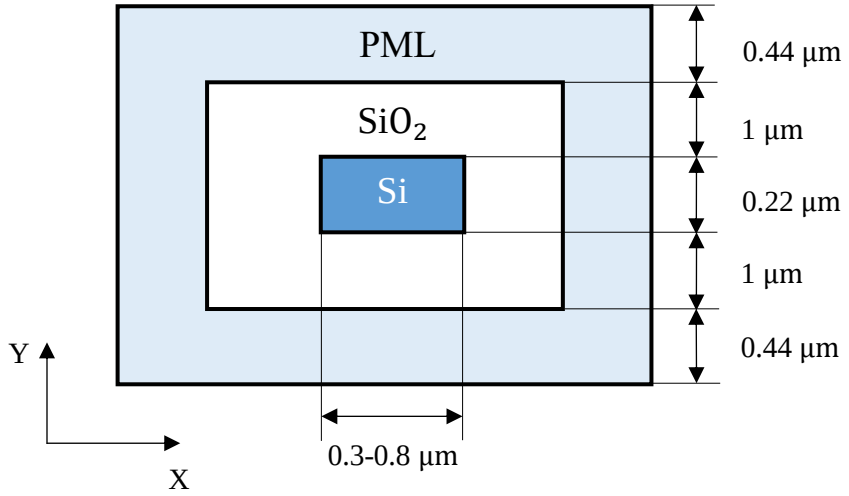

Fig. 5.1 Cross-section of silicon-on-insulator waveguide in the simulation.

5.1.2 Excitation source

To build an excitation source of waveguide for FDTD simulation, a mode solver toolbox is utilized to incorporate geometric dispersion and to calculate the TE fundamental mode. Figure 5.2 describes the peak values of the magnetic field in the incident *x*-*y* plane of silicon-on-insulator waveguide (width = 0.4 μm) in TE fundamental mode at wavelength 1550 nm with an effective index of 2.25. Apart from PML area, the core layer and the cladding layer of the waveguide have the initial values. In Figure 5.2, TE fundamental mode is well confined and the main energy of optical pulse is propagated in the core layer. According to the values of the magnetic field shown in Figure 5.2 and formula (4.2), the excitation source is determined. When simulating the FWM process, the duration and time-delay constant are decided by the laser source used in experiment, which provides a source of 120-fs (FWHM) optical pulses at a repetition rate of 82 MHz.

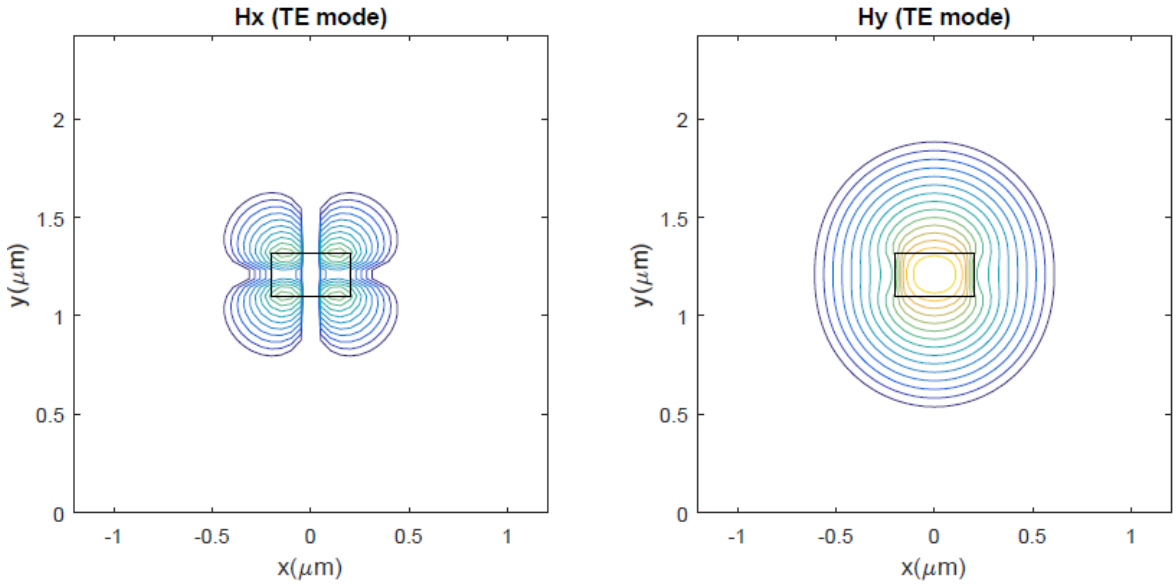

Fig. 5.2 Magnetic field in TE fundamental mode in *x*-*y* plane of silicon-on-insulator waveguide at wavelength 1.55 μm. The width of core layer is 0.4 μm and the effective index of waveguide is 2.25.

5.1.3 Material dispersion

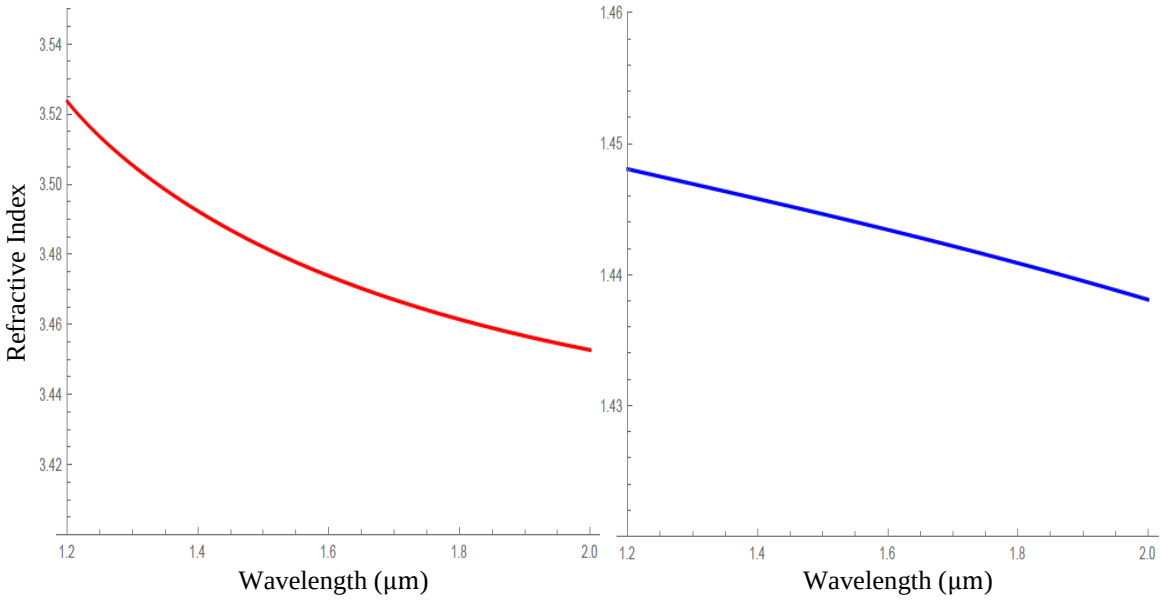

Fig. 5.3 Refractive index of silicon and silicon dioxide in a wavelength range 1.2-2.0 μm. The red line represents silicon and the blue line represents silicon dioxide.

Material dispersions of silicon and silicon dioxide are described as the sum of Lorentz resonances. In order to gain the parameters and incorporate the linear dispersion in the simulation, the refractive index should be expressed as a Sellmeier equation. The refractive index of silicon[24] is presented as a Sellmeier equation with three pole pairs. Therefore, the relative permittivities and resonant frequencies of silicon are obtained:

ε_∞=1; ε_{s1}=11.6684; ε_{s2}=1.0030; ε_{s3}=2.5413 (5.2a)

ω_1=4.1120 eV; ω_2=1.0926 eV; ω_3=0.0011 eV (5.2b)

The relative permittivities and resonant frequencies of silicon dioxide were presented in formulae (4.16-4.17). Based on the Sellmeier equations, the refractive indices of silicon and silicon dioxide over a limited wavelength range 1.2–2.0 μm are plotted in Figure 5.3. The red line represents silicon while the blue line represents silicon dioxide, both of which decrease slowly when the wavelength increases. At wavelength 1.55 μm, the refractive index of silicon and silicon dioxide are 3.478 and 1.444, respectively. Therefore, silicon has a much higher refractive index than silicon dioxide, leading to a strong refractive index contrast between the core layer, the cladding layer and mode confinement.

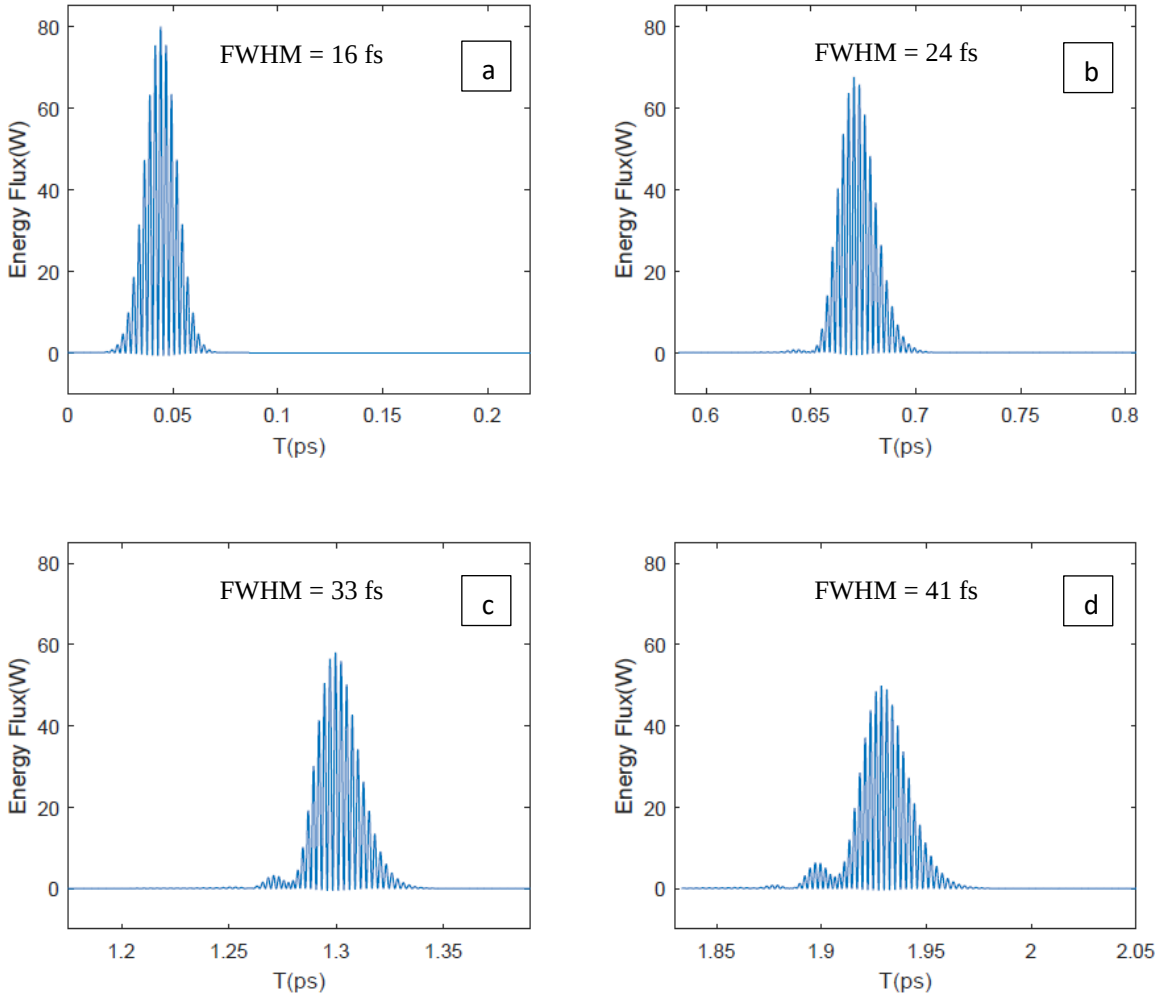

Fig. 5.4 Propagation of energy flux in silicon-on-insulator waveguide in time domain. Sub-figure (a) is the incident plane while (b), (c) and (d) are cross-sections where propagation lengths are 400Δz, 800Δz and 1200Δz, respectively.

Together with the mode solver, both geometric dispersion and material dispersion of silicon-on-insulator waveguide could be incorporated in the simulation. Group velocity dispersion is observed in Figure 5.4 where the pulse contains a range of frequency components. The propagation of energy flux over four cross-sections of silicon-on-insulator waveguide is shown in time domain. In addition, the FWHM of pulses in sub-figures was measured to compare the width. Sub-figure (a) represents the incident plane. It has a peak value of 79.8 W and FWHM 16 fs. When the propagation distance increases to 400 cells, 800 cells and 1200 cells in sub-figures (b) - (d), the magnitude of energy flux pulse drops gradually to 49.9 W while FWHM grows to 41 fs. This phenomenon is caused by linear dispersion, which causes a range of velocities among various frequencies: lower frequency components run faster than higher ones. Therefore, the FWHM of pulse in time domain becomes larger as the propagation distance increases.

5.1.4 Phase matching condition of FWM

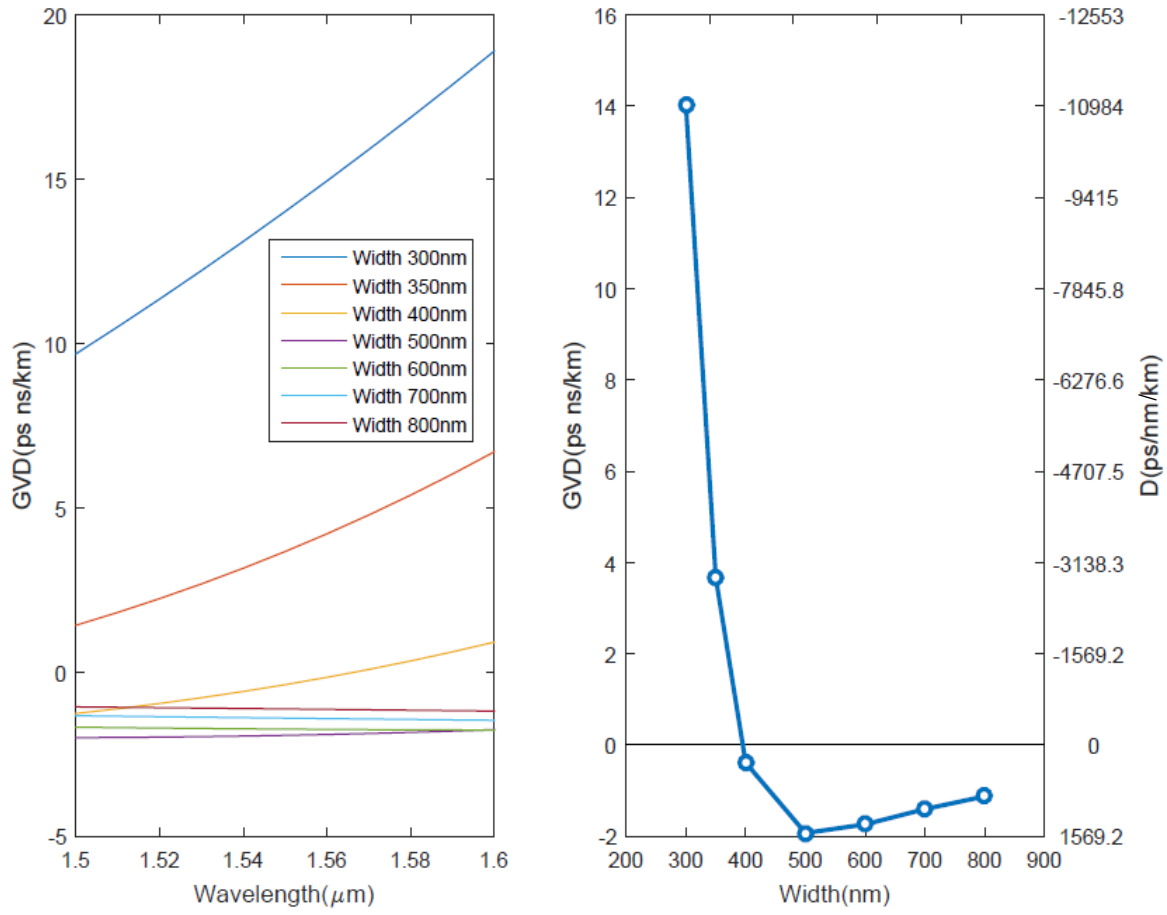

Fig. 5.5 (a) GVD of silicon-on-insulator waveguide with various widths in TE fundamental mode at wavelength 1.5-1.6 μm; (b) GVD and D of silicon-on-insulator waveguide with various widths in TE fundamental mode at wavelength 1.55 μm.

Similar to AlGaAs waveguides, in the silicon-on-insulator waveguide, GVD and phase mismatch factor Δk are also utilized to evaluate the overlap and nonlinear interactions among waves in FWM process as they are influenced by linear dispersion. As discussed in Chapter 3, Δk=0 is required for phase matching. For small frequency shifts, the odd terms in the Taylor expansion are cancelled and GVD is the leading term. Therefore, for small changes in frequency, Δk is generally a quadratic equation but it would become a quartic equation when GVD is approximately zero. According to the approach introduced in Section 3.5.1, the GVD of silicon-on-insulator waveguide with various widths in TE fundamental mode is obtained and plotted in Figure 5.5. D parameter, which is defined in equation (4.8), is also indicated in the second y-axis in sub-figure (b).

In Figure 5.5(a), seven lines represent the GVD of a silicon-on-insulator waveguide with widths of 300 nm, 350 nm, 400 nm, 500 nm, 600 nm, 700 nm and 800 nm, respectively. For short-width cases, such as 300 nm and 350 nm, GVD maintains positive values over the wavelength range 1.5-1.6 μm and rises sharply as the wavelength increases. When the width is 400 nm, GVD starts from a negative value of -1.1 ps·ns/km at wavelength 1.5 μm and increases gradually to a positive value of 0.9 ps·ns/km at wavelength 1.6 μm. As for larger widths such as 500 nm, 600 nm, 700 nm and 800 nm, GVD lines have relatively stable trends and keep negative values over the whole limited wavelength range. In addition, Figure 5.5(b) provides a clear comparison of GVD and D of silicon-on-insulator waveguides with several widths at wavelength 1.55 μm. GVD points start from a relatively large positive value of 14 ps·ns/km at short width 300 nm, then drops sharply at first and decreases more slowly afterwards to a negative value of -1.9 ps·ns/km as the width rises to 500 nm. When width is 400 nm, GVD approaches zero. From the smallest value at width 500 nm, GVD grows slowly as the width increases to 800 nm but it keeps its negative values. Theoretically, there are two zero-points of GVD: one is around 400 nm and the other one is larger than 800 nm. However, when the width is larger than 800 nm, high-order modes are propagated in the waveguide and this may cause radiation and the loss of power. Therefore, width 400 nm is chosen as the zero point of GVD for the further analysis of Δk.

With regard to D parameter, it is negative and the waveguide has normal dispersion when the width is less than 400 nm; it is positive and the waveguide has anomalous dispersion when the width is between 400 and 800 nm. In Figure 5.4, the width of simulated waveguide was 350 nm so it contained normal dispersion and the pulse was up-chirped. The bandwidth of

excitation source is $\frac{c}{\lambda_1} - \frac{c}{\lambda_2}$, where λ_1 and λ_2 are 1.1 and 2 μm, respectively. The GVD of waveguide with a width of 350 nm is 3.8 ps·ns/km and the propagation distance is 1200 cells. Therefore, the chirp is calculated as 24.6 fs, which confirmed the broadening 25 fs in Figure 5.4.

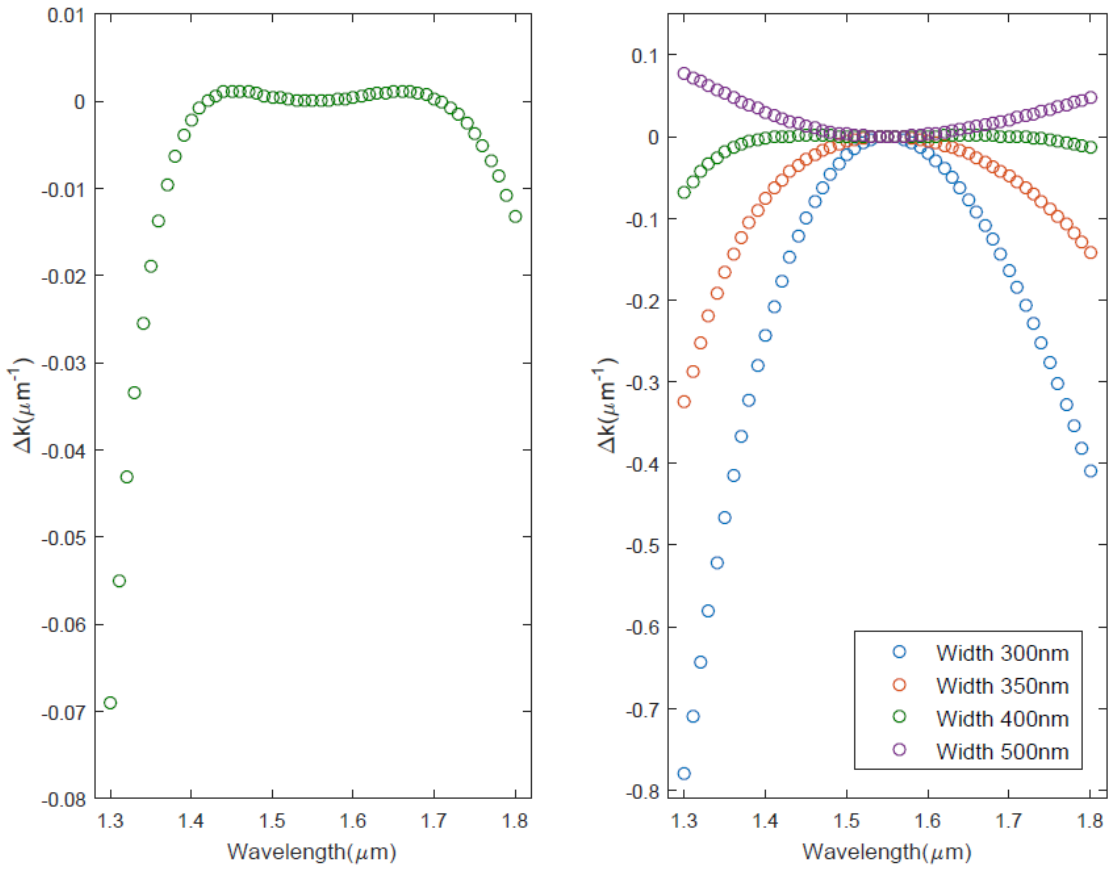

Fig. 5.6 Phase mismatch factors of silicon-on-insulator waveguides with various widths in TE fundamental mode. The pump wavelength is 1.55 μm and the signal wavelength range is 1.3-1.8 μm.

In Figure 5.6, Δk of silicon-on-insulator waveguide with various widths in TE fundamental mode is compared when the pump wavelength is 1.55 μm and the signal wavelength is 1.3-1.8 μm. Points with four colors represent widths of 300 nm, 350 nm, 400 nm and 500 nm, respectively. There is no significant difference between the four widths when the wavelength range is 1.54-1.56 μm and Δk is around zero, which is ideal for phase matching. However, apart from this narrow range, the values of Δk vary. As shown in the first sub-figure, when the width is 400 nm, Δk is a quartic equation of wavelength and maintains relatively small values in the whole range. In contrast, for the other three widths, Δk is quadratic and has larger absolute values, causing shorter coherent lengths. Now that phase matching condition is decided by Δk, it is possible to draw the conclusion that at wavelength 1.55 μm, width 400 nm

is a good choice for phase matching of FWM in TE fundamental mode. In reference [155], the observation of FWM phenomenon was reported in silicon wire waveguide with a similar structure: the height of core layer is 200 nm and the width is 400 nm, when the wavelength of the pump and idler light were 1546.9 nm and 1547.7 nm, respectively.

5.1.5 Results of FWM

The previous section discussed that a width of 400 nm satisfies the phase matching condition when the excitation source is based on the TE fundamental mode and the range of wavelength components is from 1.3 to 1.8 μm. Therefore, 400 nm is applied as the width of waveguide to simulate the FWM process. The Kerr effect is incorporated into the simulation. The nonlinear refractive index of silicon $n_2 = 4\times10^{-14}$ cm$^2 \cdot$ W^{-1} is demonstrated in the reference [34] and the real part of Kerr parameter is obtained according to formula (2.70).

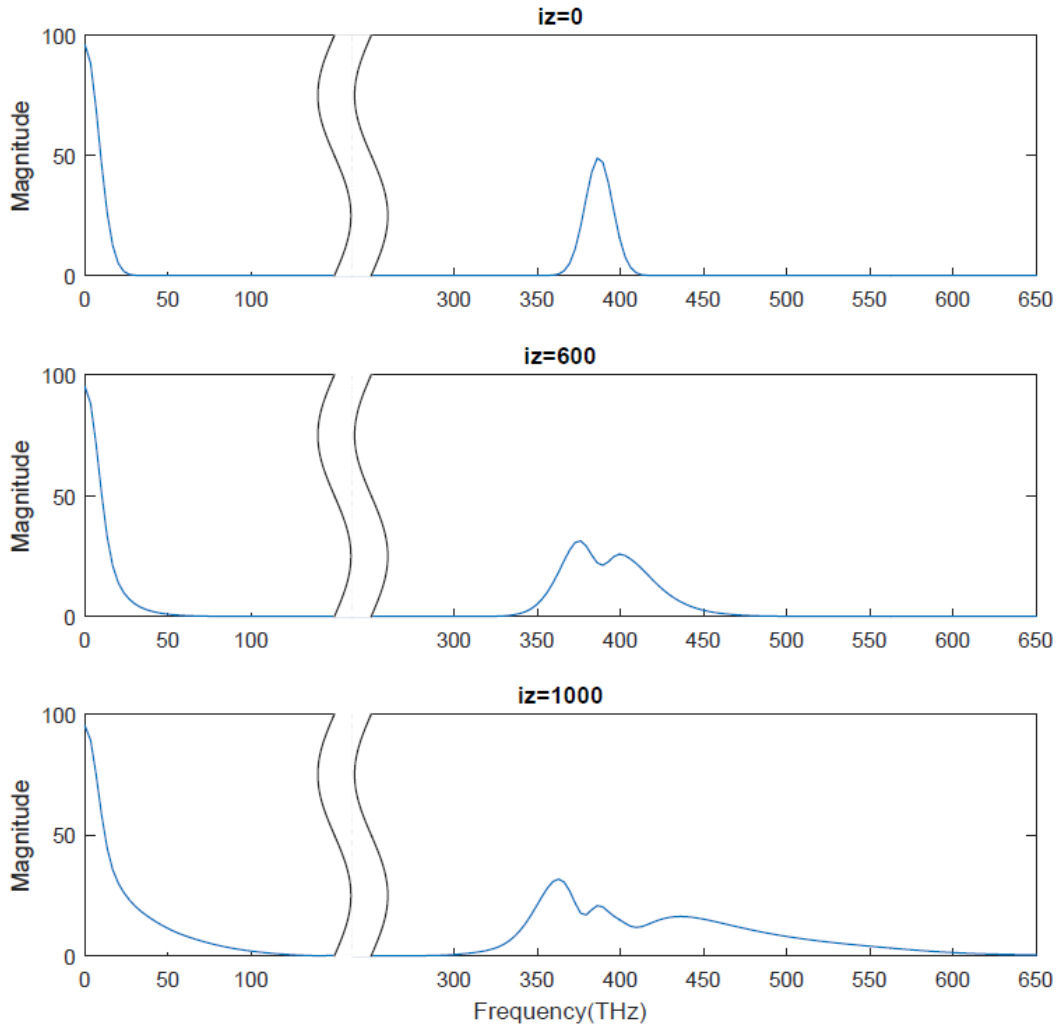

Fig. 5.7 FFT of energy flux over three cross-sections of silicon-on-insulator waveguide with a width of 400 nm. Sub-figures represent the incident plane and cross-sections where the propagation lengths are 600Δz and 1000Δz, respectively.

Figure 5.7 shows the FFT of energy flux over three cross-sections of a silicon-on-insulator waveguide. The first sub-figure represents the incident plane so that the frequency range is the same as the excitation source, which contains a narrow range of frequency components with the central frequency 194 THz, whose corresponding wavelength is 1.55 μm. As a result, the FFT of energy flux shows the sum frequency 388 THz in the right pulse and a difference frequency in the left pulse. In contrast, the cross-section in the second sub-figure is 600 cells away from the incident plane. The width of pulses becomes wider and two peaks occur in the double-frequency pulse. As for the third cross-section, the propagation distance increases to 1000 cells. The broadenings are more significant in pulses and more peaks occur in the double-frequency pulse because of the generation of new frequency components.

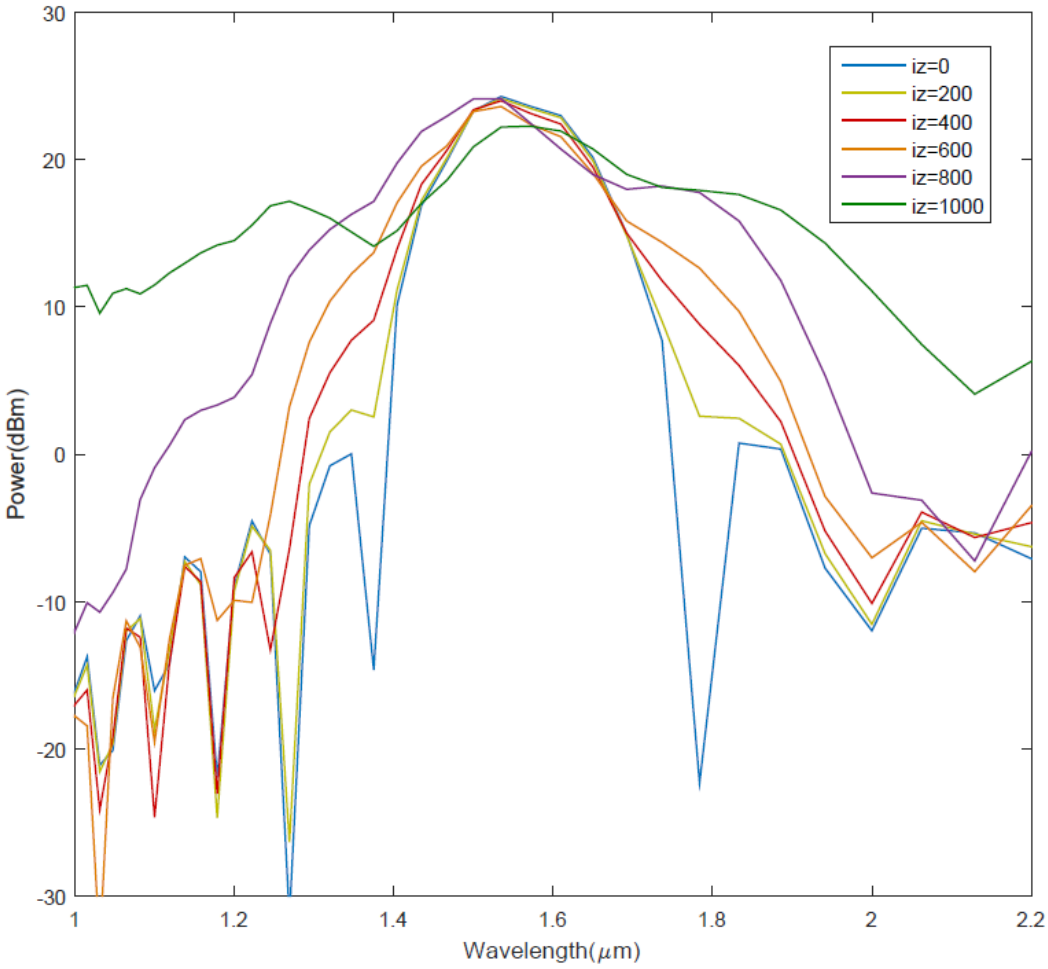

Fig. 5.8 Power spectrums of silicon-on-insulator waveguides with various lengths in wavelength domain. The width of waveguide is 400nm. The lines represent wavelength components of the power propagated through the incident plane and cross-sections where the propagation lengths are 200Δz, 400Δz, 600Δz, 800Δz and 1000Δz, respectively.

In order to have a better understanding of the FWM process in the silicon-on-insulator waveguide, Figure 5.8 compares the wavelength components of the power spectrums in various

cross-sections of silicon-on-insulator waveguide. Power is described in unit dBm, as being calculated by energy flux and parameters of laser source. The first blue line represents the incident plane and it provides an initial power spectrum for the comparison. The second line does not show much difference because of its short propagation length which is 200 cells. Then the third red line depicts the power spectrum of the cross-section which is 400 cells away from the incident plane. It has a wider wavelength range than the blue line with broadenings on both sides. The broadenings of pulse become wider as the distance of propagation increases to 600 and 800 cells. When the propagation length grows to 1000 cells, more pulses occur and more new wavelength components are generated.

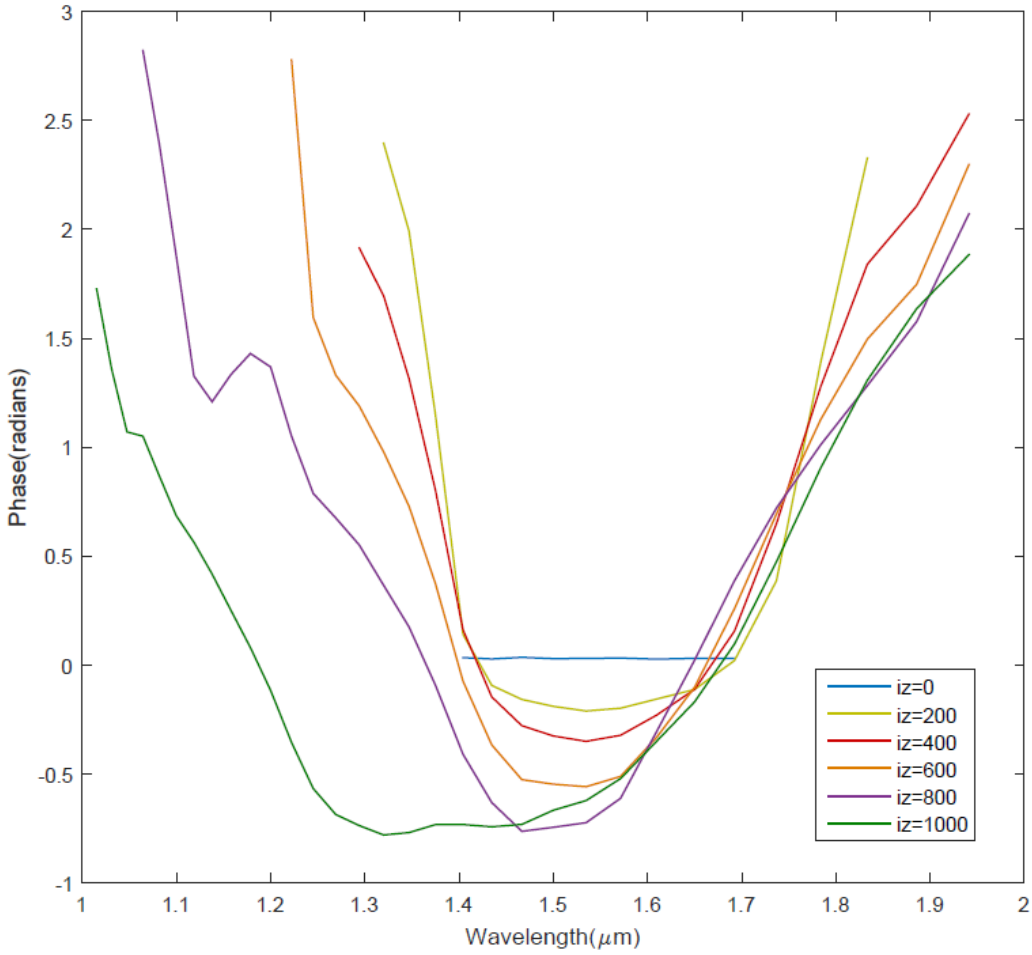

Fig. 5.9 Phase of the power spectrums of silicon-on-insulator waveguides with various lengths in wavelength domain. The width of waveguide is 400nm. The lines represent the phase of wavelength components of the power propagated through the incident plane and cross-sections where the propagation lengths are 200Δz, 400Δz, 600Δz, 800Δz and 1000Δz, respectively.

Furthermore, Figure 5.9 indicates the phase of power spectrums in Figure 5.8 in wavelength domain. For the incident pulse, the phase is zero in a wavelength range 1.4-1.7. When the propagation distance increases, the phase becomes a quadratic curve and the range of

wavelength components becomes wider. In addition, it shifts to the shorter wavelength range. Therefore, it is proved that the broadenings in Figures 5.7 and 5.8 are caused by Kerr-type nonlinearity, which is treated as FWM process here.

Other than the propagation distance, incident power is also a factor which affects the efficiency of FWM. Figure 5.10 indicates the power spectrums of silicon-on-insulator waveguides with a range of incident power but a certain propagation distance. The width of the waveguide is 400 nm and the length is 1000 cells. The five lines in the figure represent five different incident powers and the blue line means the lowest power and the green line means the highest power. Compared to the blue line, the red line and yellow line do not make much difference. However, when the power increases to the purple and green lines, broadenings occur on both sides and the wavelength ranges become wider, meaning more wavelength components were generated. Therefore, the higher the incident power is, the more efficient the FWM is.

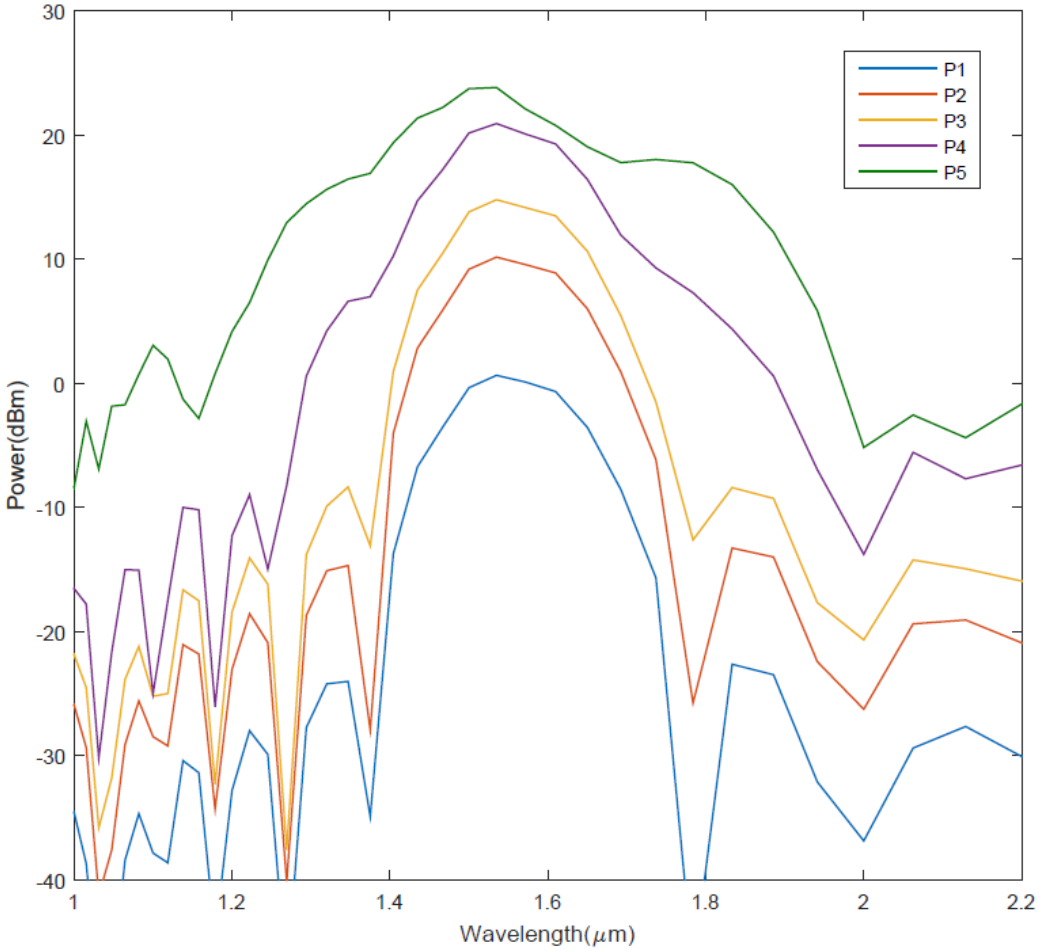

Fig. 5.10 Power spectrums of silicon-on-insulator waveguides with various incident powers in wavelength domain. The width is 400 nm and the propagation distance is 1000 cells. The blue line represents the lowest power while the green line represents the highest power.

Similarly, the corresponding phase of the power spectrums in Figure 5.10 is plotted in Figure 5.11 to determine the generation of wavelength components is resulted from FWM. In Figure 5.11, as for low power cases, phase is close to zero in the incident wavelength range. With regards to the relatively high power cases, such as purple and green lines, phase is shown as quadratic curve and the wavelength range is extended. In addition, the phase shifts to the shorter wavelength range. Therefore, the phenomenon described in Figures 5.10 is caused by FWM.

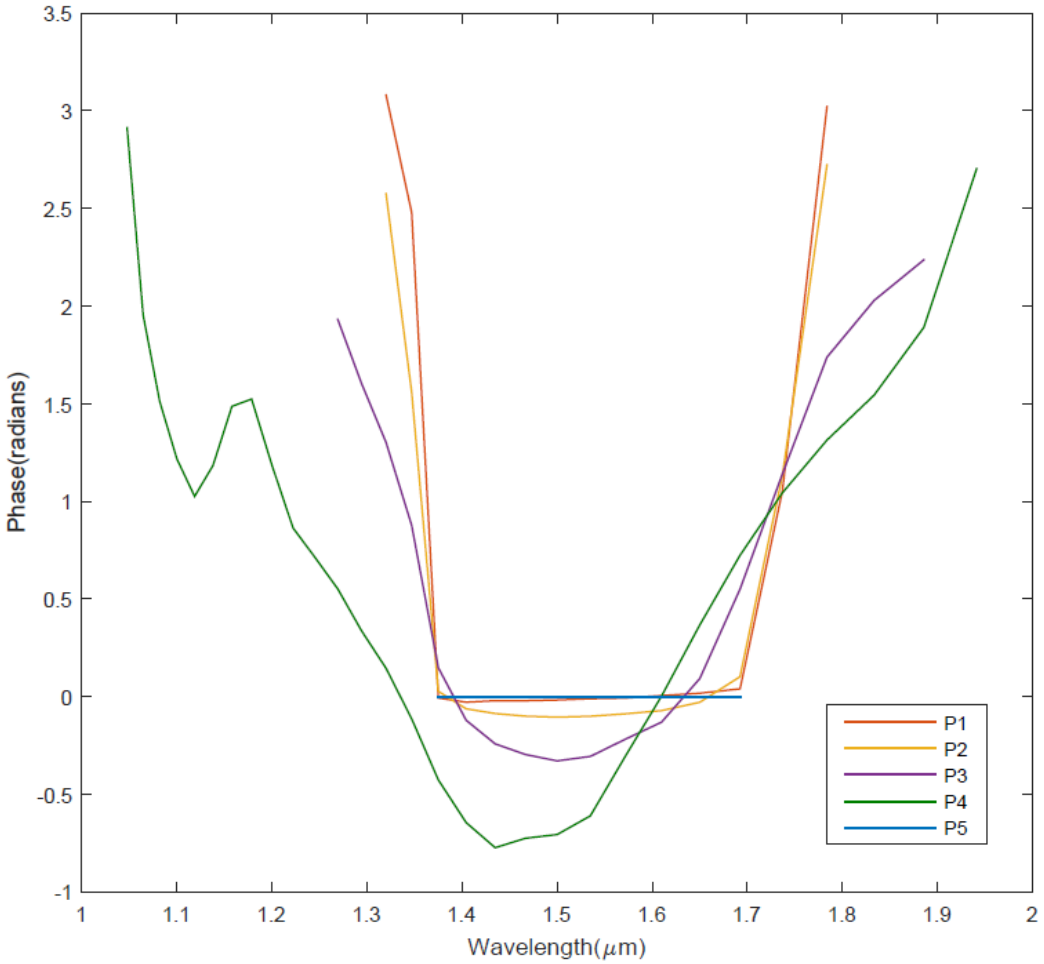

Fig. 5.11 Phase of the power spectrums of silicon-on-insulator waveguides with various incident powers in wavelength domain. The width is 400 nm and the propagation distance is 1000 cells. The blue line represents the lowest power while the green line represents the highest power.

To further compare the efficiency of FWM and prove the significance of phase matching in silicon-on-insulator waveguide, waveguides with various widths but the same incident power and propagation distance are simulated. According to the values of GVD and phase mismatch factor plotted in Figure 5.5 and 5.6, three widths of 300 nm, 400 nm and 500 nm were chosen, of which 400 nm is close to phase match condition. Figure 5.12 shows the comparison of power spectrums of silicon-on-insulator waveguide with these three widths in wavelength domain.

The length of the waveguide is 1000 cells and is equal to 50 μm. In Figure 5.12, when the width is 300nm, the power spectrum spreads but it still has a relatively narrow wavelength range. In the 500 nm case, the wavelength range of power pulse is wider than the one with 300 nm but is smaller than the one with 400 nm. Therefore, the power spectrum of the 400 nm case has the widest wavelength range with generated new pulses. The results discussed above are in agreement with the values of Δk in Figure 5.6. To gain a coherent length of 50 μm, the absolute value of Δk should be less than 0.02 μm^{-1}. When the width is 400 nm, the range of signal wavelength with the required Δk is the widest one: 1.35-1.85 μm. With regards to widths of 300 nm and 500 nm, the corresponding wavelength range is 1.51-1.61 μm and 1.42-1.70 μm, respectively. As a consequence, the silicon-on-insulator waveguide with a width of 400 nm has the most efficient FWM process in the TE fundamental mode at wavelength 1.55 μm.

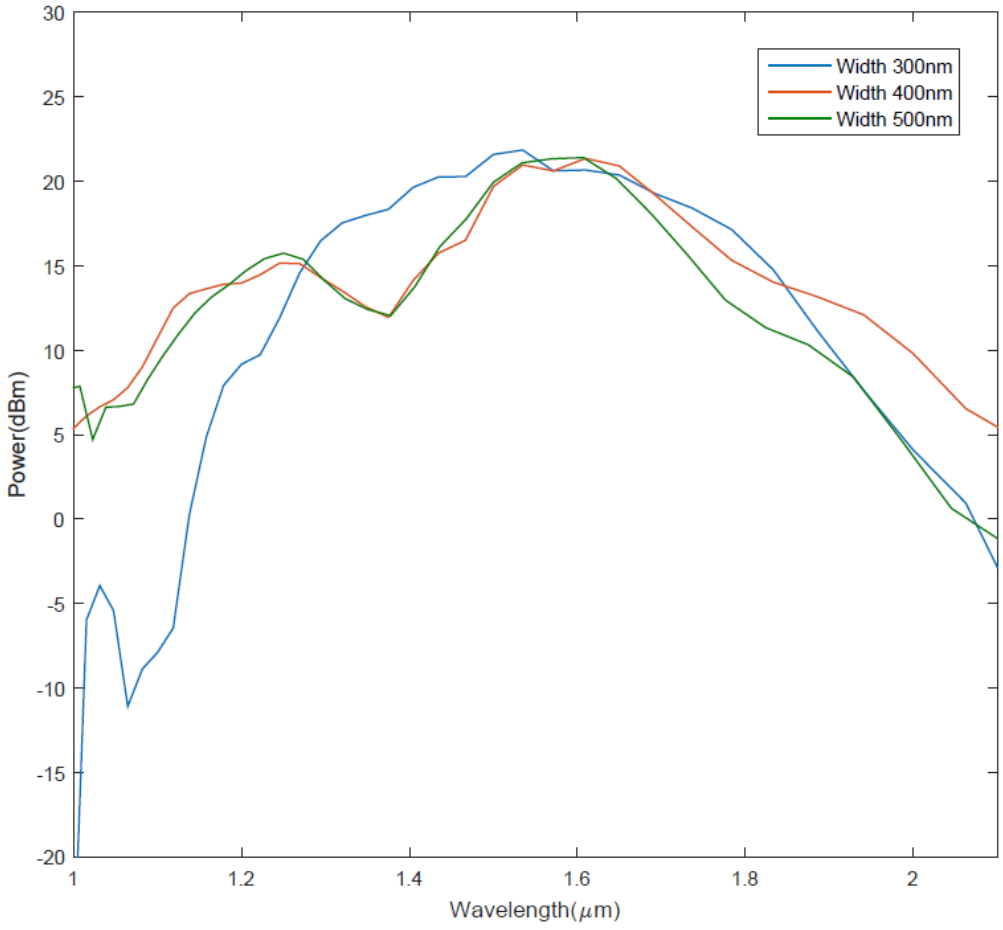

Fig. 5.12 Comparison of power spectrums of silicon-on-insulator waveguides with three widths 300 nm, 400 nm and 500 nm in wavelength domain. The propagation distance is 1000 cells.

5.2 Silicon rich silicon nitride-on-insulator waveguides

With a larger energy gap of material, silicon nitride is an alternative to silicon in SOI waveguide. Moreover, at a wavelength of 1550 nm, silicon nitride does not have TPA which exists in silicon. According to the variation in the SiH_4/N_2 flow ratio, the refractive index of silicon nitride could be adjusted in a wide range of 1.57-2.76. In this simulation, the refractive index depends on the measurement result provided by Stuart May in the experiment which is 2.42 at wavelength 1550 nm, meaning silicon nitride contains rich silicon. Therefore, silicon nitride here is called silicon rich silicon nitride. In the simulation of SRSN-on-insulator waveguide, both linear dispersion and Kerr-type nonlinearity were taken into consideration. Results of FWM were observed and the significance of phase matching condition is discussed.

5.2.1 Basic model

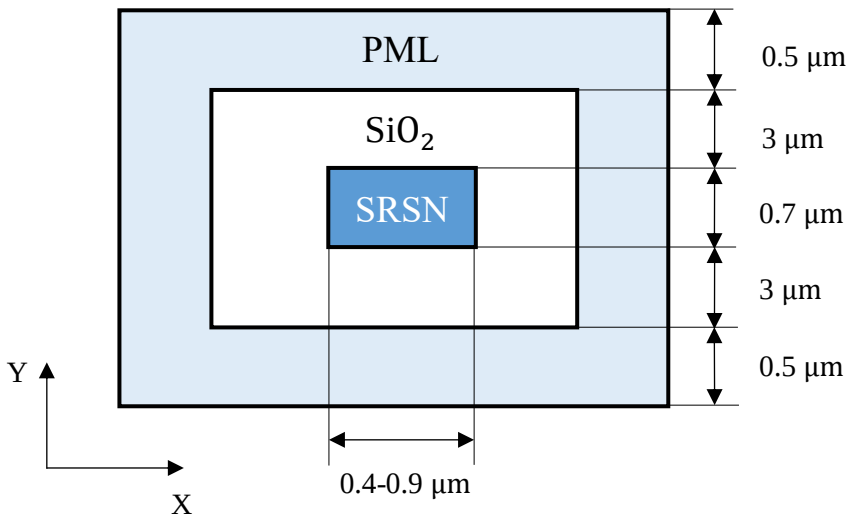

Fig. 5.13 Cross-section of SRSN-on-insulator waveguide in the simulation.

The cross-section - *x*-*y* plane - of SRSN-on-insulator waveguide in the simulation is described in Figure 5.13 and *z*-direction has cyclic boundary conditions. The core layer is SRSN the height of which is 0.7 µm and width is 0.4-0.9 µm. The height of SRSN was suggested by Stuart May based on the experimental condition. Because the refractive index contrast between SRSN and silicon dioxide is not as strong as that between silicon and silicon dioxide, the thickness of the cladding layer is set as 3 µm, ensuring the optical wave is propagated as a well confined mode inside the waveguide. In addition, the outer layer is 10-cell thick PML so that the problem domain is limited and energy escape away from the waveguide will be absorbed eventually. Based on the size of the waveguide and wavelength components of pulse, the grid size is uniform and the time step has been decided by the grid size:

$$\Delta x = \Delta y = \Delta z = 50 \text{ nm}; \qquad \Delta t = \frac{\Delta x}{2c} \tag{5.3}$$

5.2.2 Excitation source

The mode solver in MATLAB has been utilised to gain the TE fundamental mode of the SRSN-on-insulator waveguide. The SRSN core layer and silicon dioxide cladding layer have initial values while the initial value of the PML area is zero. Figure 5.14 shows the magnetic field in the incident *x-y* plane of waveguide (width = 0.5 μm) in TE fundamental mode at wavelength 1550 nm, where the effective index is 1.98. The TE mode is well confined and the main energy of the optical pulse is propagated in the core layer. In the simulation, the excitation source was a combination of Gaussian pulses and amplitude, which was determined by the values of fields in Figure 5.14. Formula (4.2) contains a range of frequency components and formula (4.3) contains two frequencies. The duration and time delay are decided by the laser source used in the experiment which provides a source of 120-fs (FWHM) optical pulses at a repetition rate of 82 MHz.

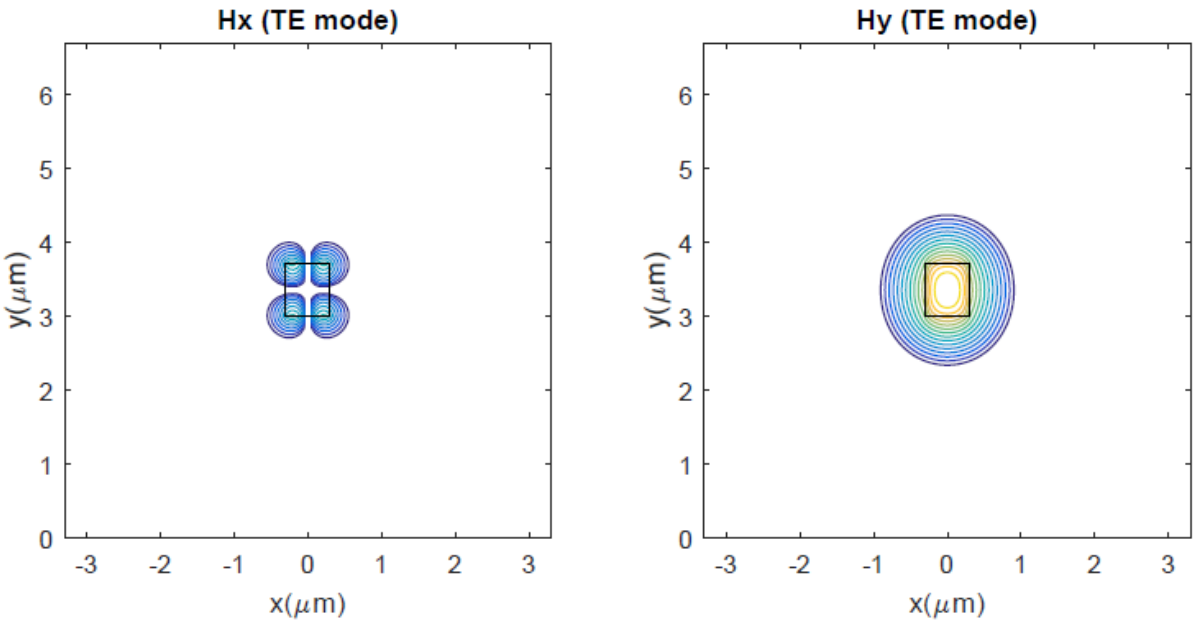

Fig. 5.14 Magnetic field in TE fundamental mode of *x-y* plane of silicon SRSN-on-insulator waveguide at wavelength 1.55 μm. The width of core layer is 0.5 μm and the effective index of waveguide is 1.98.

5.2.3 Material dispersion

Lorentz resonance is used to describe the material dispersion of SRSN and silicon dioxide. The relative permittivities and resonant frequencies of silicon dioxide were proposed in formulae

(4.16-4.17). With regard to silicon nitride, its refractive index has a wide range, being determined by the Si/N ratio. In this simulation, the refractive index of SRSN was based on a value measured in the experiment: 2.42 at wavelength 1.55 μm. To determine the ratio of Si/N and obtain a refractive index over a range of wavelength, a collinear relationship between stoichiometric co-efficients of silicon nitride and amorphous silicon was built. Firstly, the refractive index of Si_3N_4 is described as a Sellmeier equation with two pole pairs [61]:

$$n^2_{Si_3N_4} = A1 + \frac{A2*\lambda^2}{\lambda^2 - A3} + \frac{A4*\lambda^2}{\lambda^2 - A5} \tag{5.4}$$

where A1=1; A2=3.0249; A3=0.1350^2; A4=40314; A5= 1239.8420^2. Secondly, the refractive index of amorphous silicon is described as a Sellmeier equation with one pole pair[156]:

$$n^2_{a-Si} = B1 + \frac{B2*\lambda^2}{\lambda^2 - B3} \tag{5.5}$$

where B1=2.3961; B2=8.9468; B3= 0.1843. Then, the collinear relationship is expressed as:

$$\begin{aligned} y1 &= x*A1+(1-x)*B1; \\ y2 &= x*A2+(1-x)*B2; \\ y3 &= x*A3+(1-x)*B3; \\ y4 &= x*A4; \\ y5 &= A5; \end{aligned} \tag{5.6}$$

And the refractive index of SRSN is described as the Sellmeier equation with these co-efficients:

$$n^2_{SRSN} = y1 + \frac{y2*\lambda^2}{\lambda^2 - y3} + \frac{y4*\lambda^2}{\lambda^2 - y5} \tag{5.7}$$

According to the single point of the refractive index in the measurement, the value of x is 0.7538 and the composition of SRSN is determined. The relative permittivities and resonant frequencies of SRSN are obtained:

ε_∞ = 1.3437; ε_{s1} = 5.8267; ε_{s2} = 40315.3; (5.8a)

ω_1 = 5.0997 eV; ω_2 = 0.0012 eV (5.8b)

Figure 5.15 shows the refractive index of SRSN based on equation (5.7) in the first sub-figure and shows the refractive index of silicon dioxide in the second sub-figure in a wavelength range of 0.8-2.0 μm. Both lines decrease gradually as the wavelength increases and the core layer has a higher refractive index than the cladding layer. The refractive index of SRSN and silicon dioxide are 2.42 and 1.44 when the wavelength is 1.55 μm.

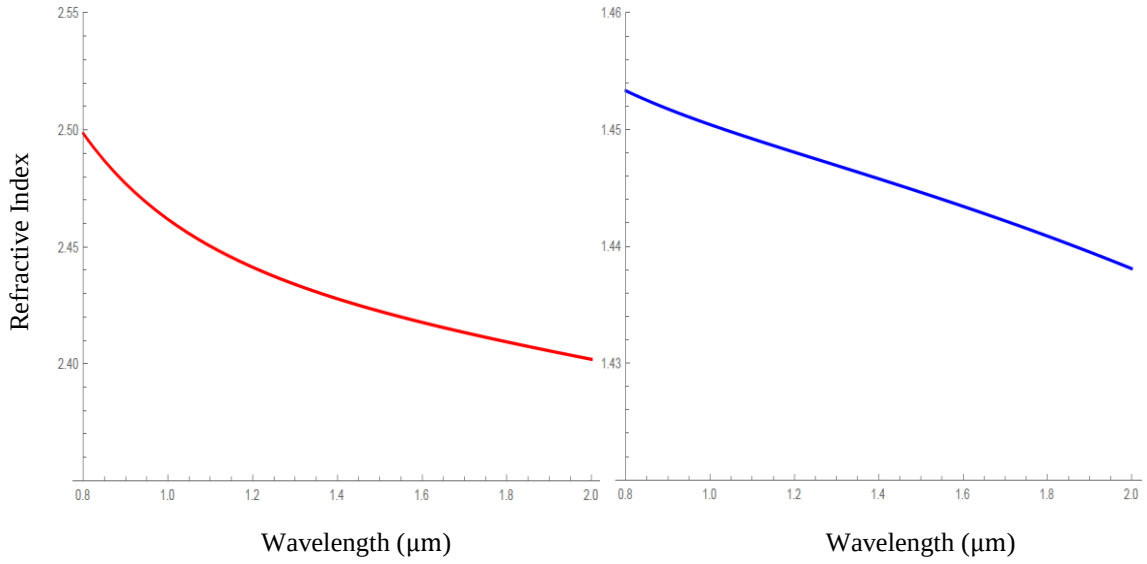

Fig. 5.15 Refractive index of SRSN and silicon dioxide at wavelength 0.8-2.0 μm. The red line represents SRSN and the blue line represents silicon dioxide.

Material dispersion is incorporated with Sellmeier equations and the geometric dispersion is incorporated in mode solver. The linear dispersion of the SRSN-on-insulator waveguide is involved in the simulation and group velocity dispersion is observed in Figure 5.16 through the propagation of energy flux over various cross-sections in the time domain. Sub-figure (a) represents the incident plane and it has the highest peak value at 17.3 W and the smallest at FWHM 30 fs. When the propagation distance is 400 cells, the pulse shown in sub-figure (b) becomes wider and the peak value decreases. Over time, the propagation distance of the optical pulse increases to 800 cells and 1200 cells in sub-figures (c) and (d). The peak value continues to drop to 3.9 W while the FWHM grows to 60 fs. This phenomenon has resulted from linear dispersion where lower frequency components run faster than higher ones. Therefore, as the propagation distance grows, the pulse becomes wider in time domain.

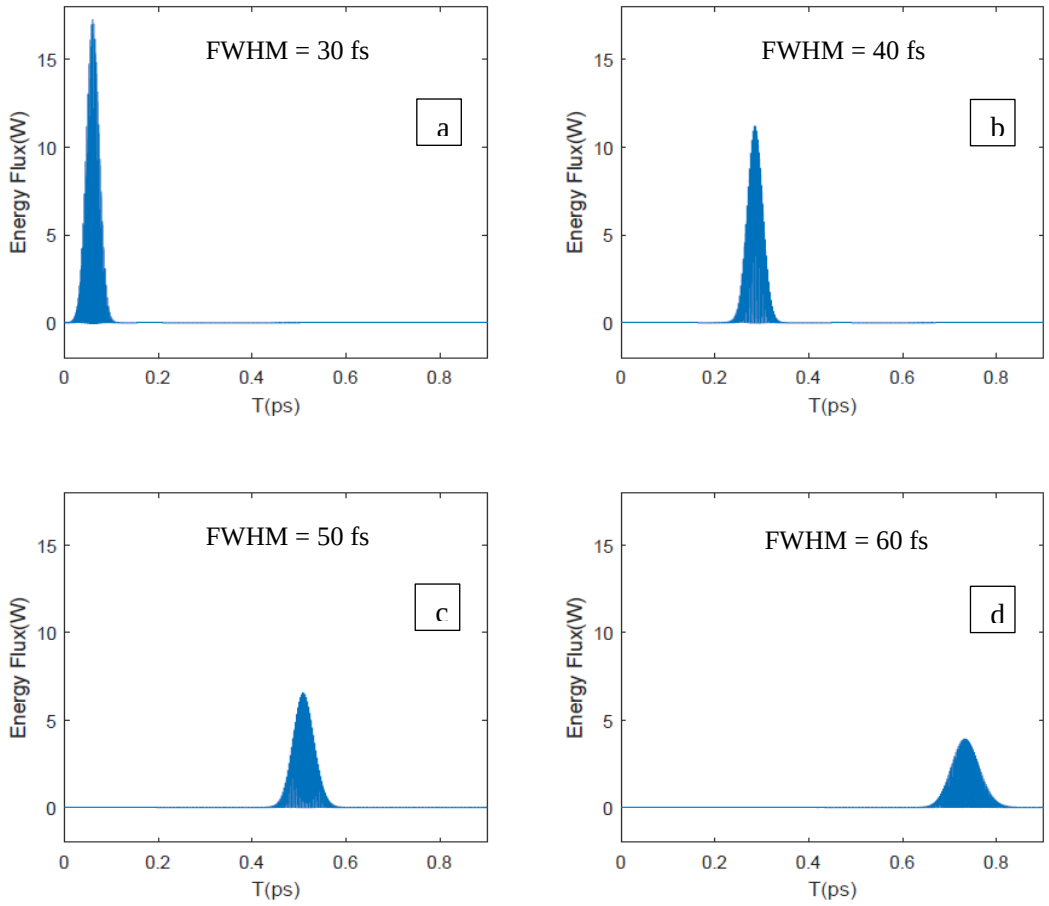

Fig. 5.16 Propagation of energy flux in SRSN-on-insulator waveguide in time domain. Sub-figure (a) is the incident plane while (b), (c) and (d) are cross-sections where propagation lengths are 400Δz, 800Δz and 1200Δz, respectively.

5.2.4 Phase matching condition of FWM

To determine the phase matching condition of FWM in the SRSN-on-insulator waveguide and to achieve efficient nonlinear interactions, GVD, D and phase mismatch factor Δk are plotted in Figures 5.17 and 5.18. Figure 5.17(a) shows the GVD of the SRSN-on-insulator waveguide with various widths in TE fundamental mode in a limited wavelength range 1.5-1.6 μm. Seven lines represent the waveguide with seven widths. GVD maintains positive values over the whole wavelength range when the widths are 400 nm and 450 nm. As for the widths 600 nm, 700 nm, 800 nm and 900 nm, GVD maintains negative values over the whole wavelength range. Only when the width is 500 nm, does GVD increase gradually from a negative value of -0.8 ps·ns/km at wavelength 1.5 μm to 0.5 ps·ns/km at wavelength 1.6 μm. In Figure 5.17(b), GVD of waveguides with various widths at wavelength 1.55 μm are compared. Another expression of GVD - D parameter - is also plotted in the right y-axis in sub-figure (b). GVD has the largest value of 4.1 ps·ns/km at width 400 nm, then drops dramatically to 1.6 ps·ns/km at width 450

nm. After that, GVD continues to drop to a negative value of -0.2 ps·ns/km at width 500 nm. For bigger widths 600 nm, 700 nm, 800 nm and 900 nm, GVD stays negative and far away from zero when compared to the GVD at width 500 nm. Theoretically, there are two zero-points of GVD: one is around 500 nm and the other is larger than 900 nm. However, when the width is larger than 900 nm, high-order modes occur and this may cause radiation and the loss of power. Consequently, a width of 500 nm is chosen as the zero point of GVD for the further analysis of Δk in Figure 5.18.

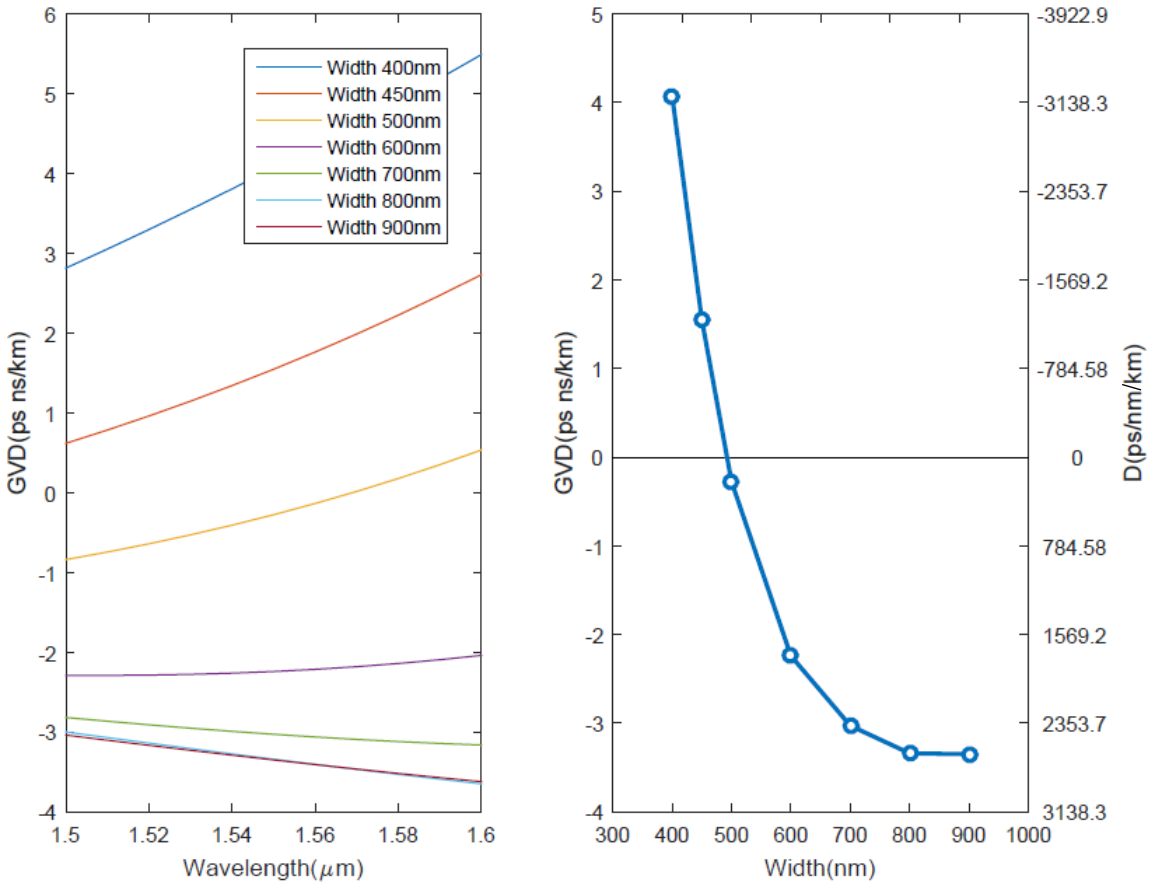

Fig. 5.17 (a) GVD of SRSN-on-insulator waveguide with various widths in TE fundamental mode at wavelength 1.5-1.6 μm; (b) GVD and D of SRSN-on-insulator waveguide with various widths in TE fundamental mode at wavelength 1.55 μm.

According to D parameter, the waveguide has normal dispersion when the width is less than 500 nm; the waveguide has anomalous dispersion when the width is between 500 and 900 nm. In Figure 5.16, the width of simulated waveguide was 400 nm so it contained normal dispersion and the pulse was up-chirped. The bandwidth of excitation source is $\frac{c}{\lambda_1} - \frac{c}{\lambda_2}$, where λ_1 and λ_2 are 1.1 and 2 μm, respectively. The GVD of waveguide with a width of 400 nm is 4.1 ps·ns/km and the propagation distance is 1200 cells. Therefore, the chirp is calculated as 30.2 fs, which confirmed the broadening 30 fs in Figure 5.16.

Figure 5.18 shows the Δk of the SRSN-on-insulator waveguide with various widths in TE fundamental mode at signal wavelength 1.3-1.8 μm. The pump wavelength is 1.55 μm. Points with five colours represent five widths 400 nm, 450 nm, 500 nm, 600 nm and 800 nm, respectively. In the limited central wavelength range 1.545-1.555 μm, the difference between the five widths is negligible and the value of phase mismatch factor is approximately zero, which satisfies the phase matching. However, in a wider wavelength range, Δk is a quadratic equation of wavelength where the widths are 400 nm, 450 nm, 600 nm and 800 nm so that the absolute value of Δk increases as the difference between wavelength and central wavelength 1.55 μm increases. In contrast, Δk is a quartic equation in 400 nm case and has relatively small values in the whole range, ensuring long coherent length. It is possible to conclude that the SRSN-on-insulator waveguide with width 500 nm is suitable for the phase matching of FWM in TE fundamental mode at wavelength 1.55 μm.

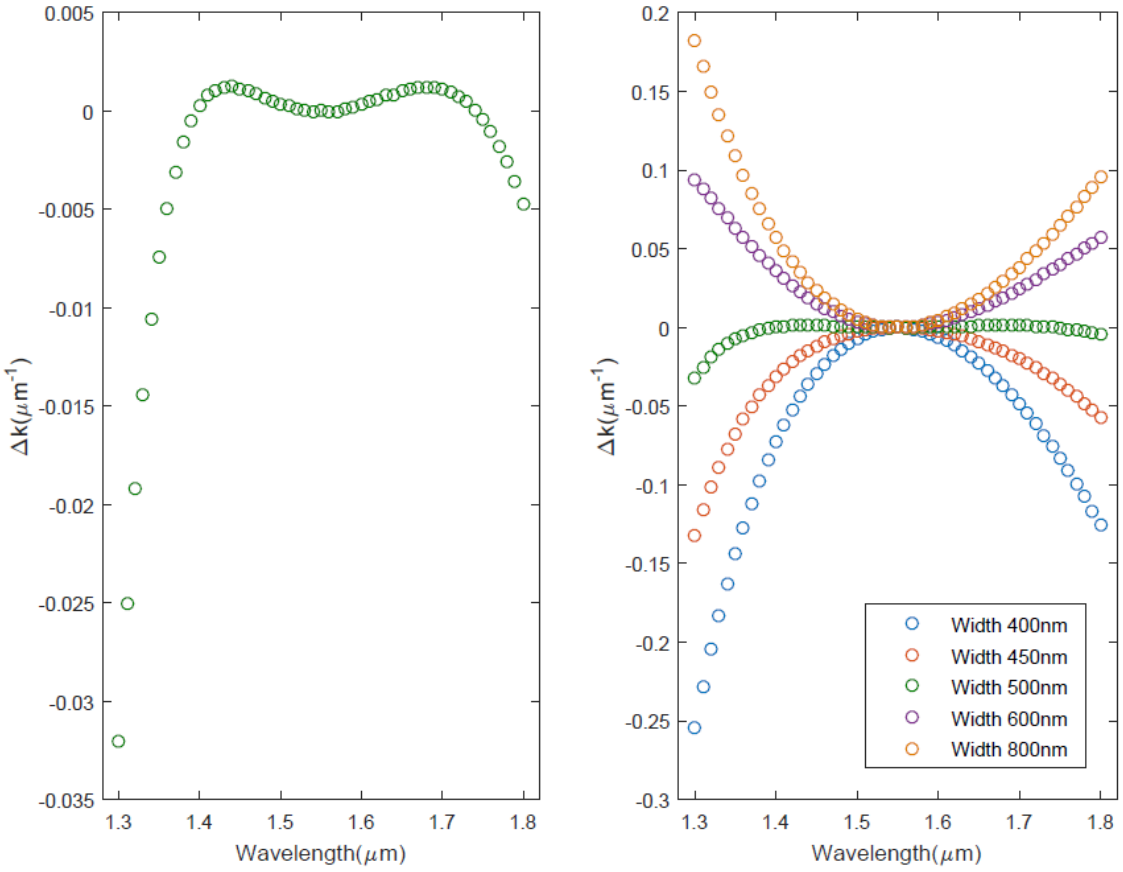

Fig. 5.18 Phase mismatch factors of SRSN-on-insulator waveguide with various widths in TE fundamental mode at wavelength 1.5-1.6 μm.

5.2.5 Results of FWM

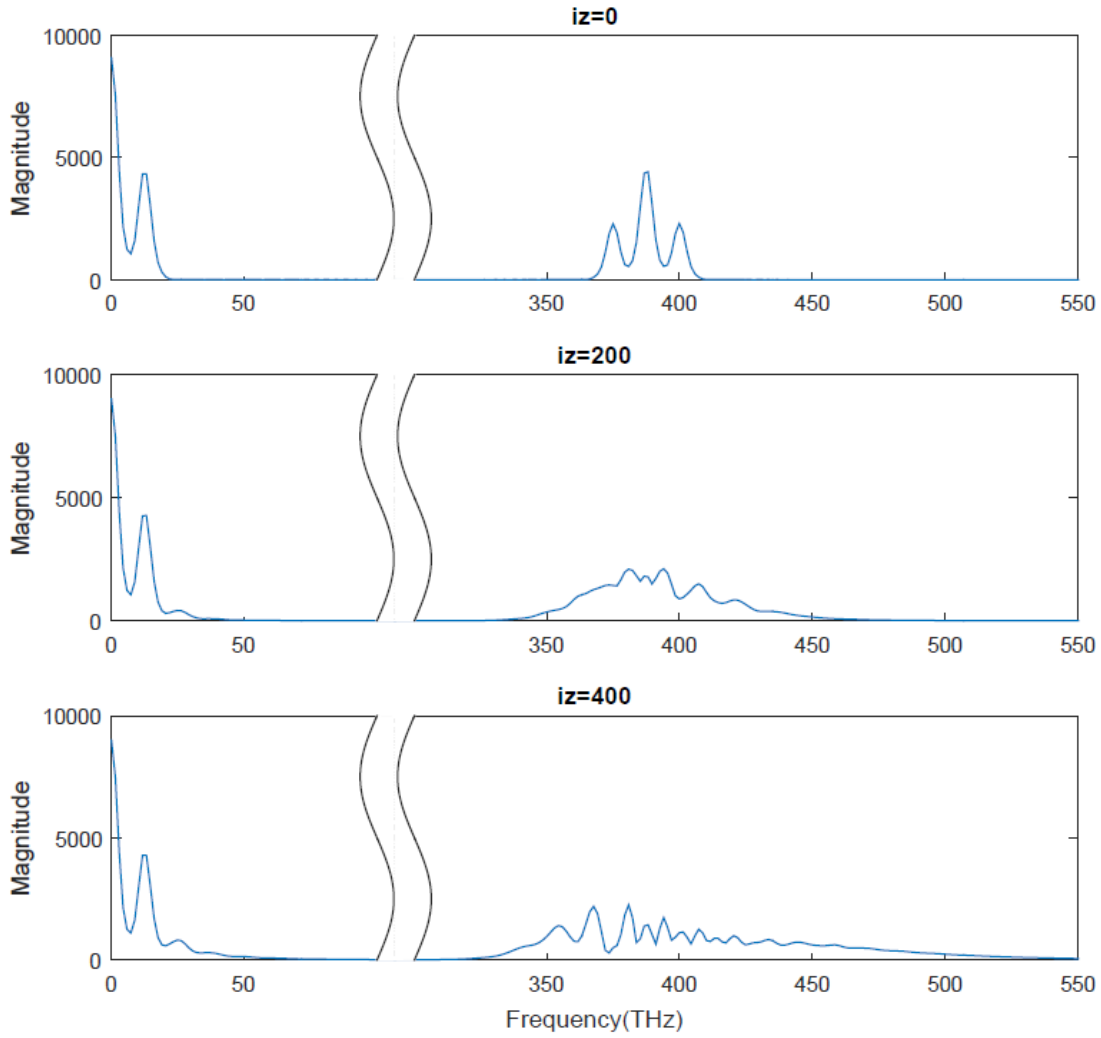

Fig. 5.19 FFT of energy flux in SRSN-on-insulator waveguide with a width of 500 nm. Sub-figures represent the incident plane and cross-sections where the propagation lengths are 200Δz and 400Δz, respectively.

As was discussed in the previous section, a width of 500 nm was chosen for the phase matching in TE fundamental mode at a wavelength of 1.55 μm. Therefore, the width of SRSN-on-insulator waveguide was set as 500 nm to simulate the FWM process based on Kerr-type nonlinearity. The nonlinear refractive index of silicon nitride $n_2 = 4\times10^{-14}$ $\text{cm}^2 \cdot \text{W}^{-1}$ is presented in the reference [69] and the real part of Kerr parameter has been obtained according to formula (2.70). In this simulation of FWM, the excitation source contains two frequencies or one narrow frequency range. In Figure 5.19, the FFT of energy flux over three cross-sections of the SRSN-on-insulator waveguide is shown. The first cross-section is the incident plane so that the frequency range is the same as the excitation source, which contains two frequencies - 187.5 THz and 200 THz - where the corresponding wavelengths are 1.6 and 1.5 μm, respectively. Therefore, the FFT of energy flux shows the sum of any two frequency components: 375 THz, 387.5 THz and 400 THz, as well as the difference in any two frequency

components: 0 THz and 12.5 THz. In the second cross-section which is 200 cells away from the incident plane, the frequency ranges of pulses have been extended and more peaks occur in the sum-frequency pulse. When the propagation distance increases to 400 cells in the third cross-section, the broadening of pulses are much more significant, meaning more frequency components were generated as a result of FWM.

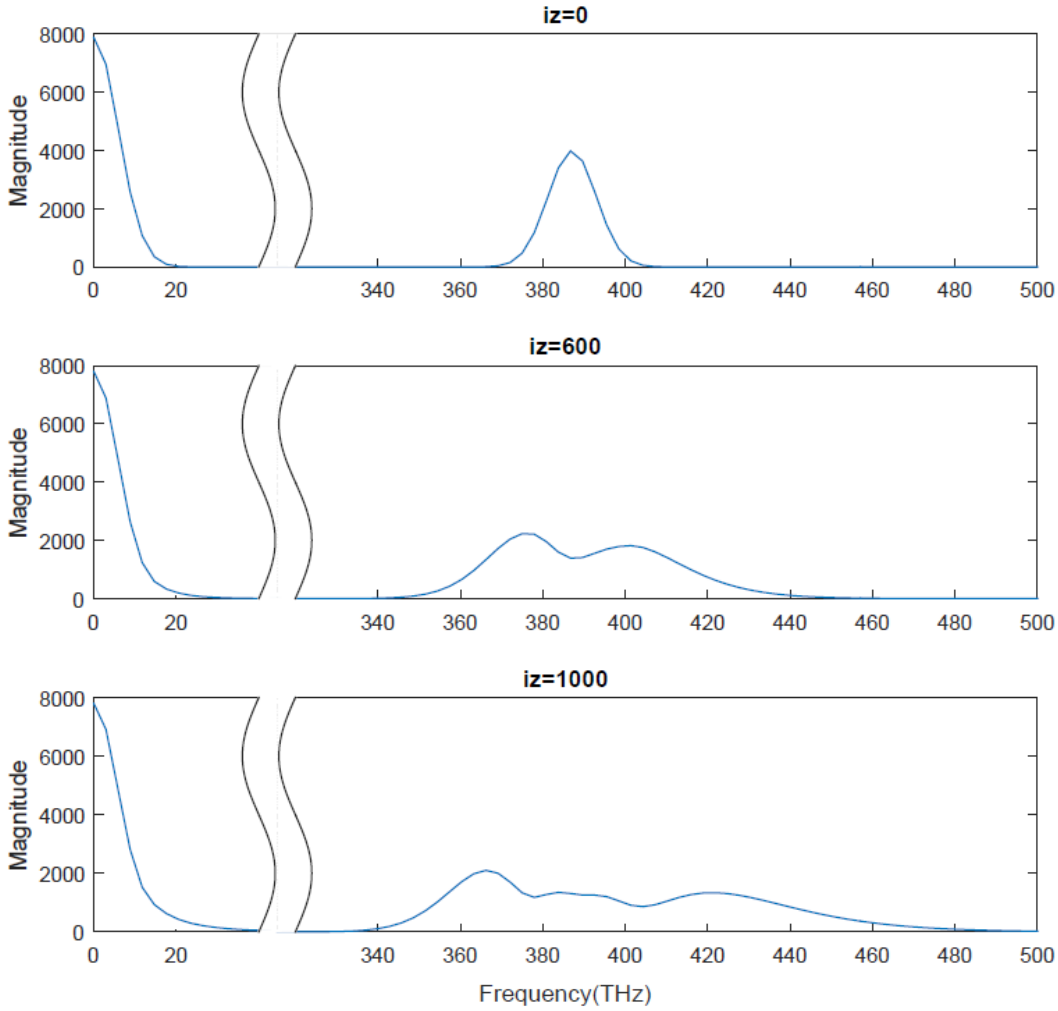

Fig. 5.20 FFT of energy flux over three cross-sections of SRSN-on-insulator waveguide with a width of 500 nm. Sub-figures represent the incident plane and cross-sections where the propagation lengths are 600Δz and 1000Δz, respectively.

An obvious FWM process was observed in Figures 5.19 where the excitation source contains two frequencies. In contrast, in the simulation shown in Figures 5.20-5.22, the excitation source contains one frequency range. Figure 5.20 shows the FFT of energy flux over three cross-sections of SRSN-on-insulator waveguide with width 500 nm. The first sub-figure represents the incident plane so that the frequency range is the same as the excitation source, containing a frequency range with a central frequency of 194 THz, whose corresponding wavelength is 1.55 μm. Therefore, the FFT of energy flux shows the sum frequency 388 THz in the right

pulse and the difference frequency in the left pulse. Then, in the second cross-section which is 600 cells away from the incident plane, the peak value of sum frequency pulse drops but two peaks occur and the central pulse spreads slightly. As for the last cross-section, the propagation length is 1000 cells. It has wider broadenings and more peaks occur in sum frequency pulse, which is caused by the generation of more frequency components.

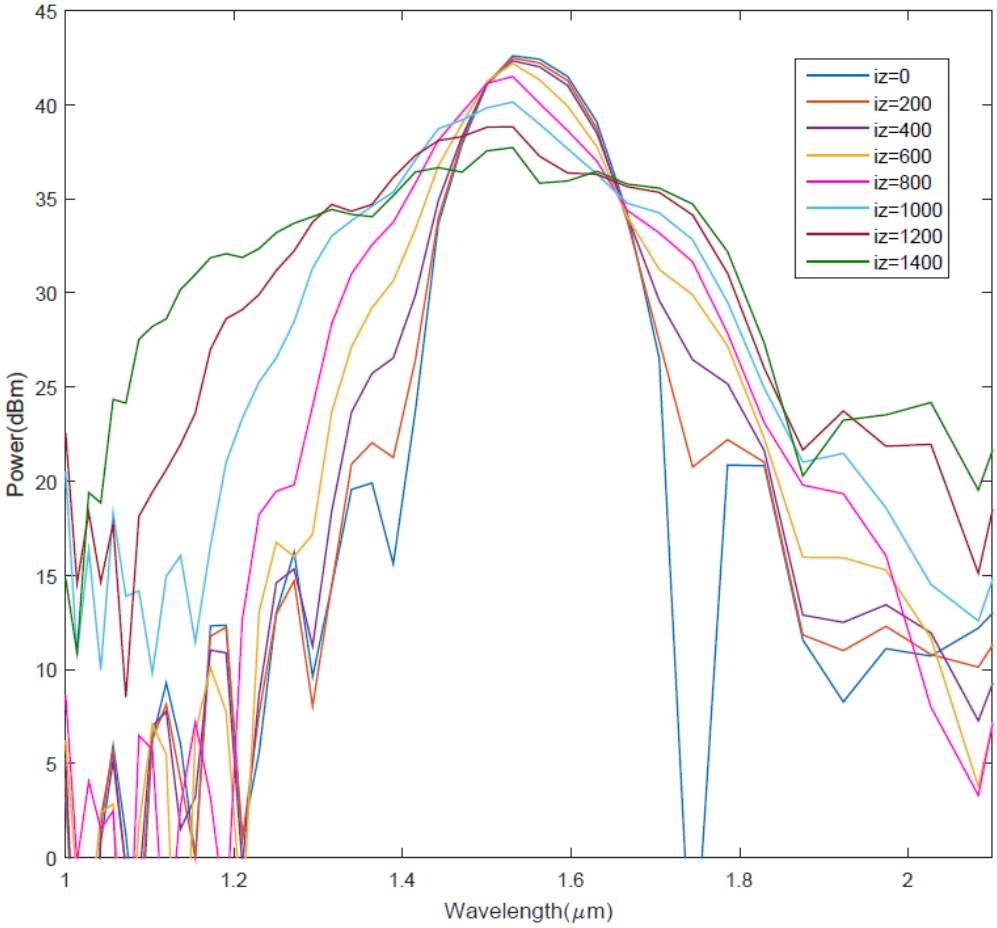

Fig. 5.21 Power spectrums of SRSN-on-insulator waveguides with various propagation lengths in wavelength domain. The width of waveguide is 500nm. The lines represent wavelength components of the power propagated through the incident plane and cross-sections where the propagation lengths are 200Δz, 400Δz, 600Δz, 800Δz, 1000Δz, 1200Δz and 1400Δz, respectively.

Figure 5.21 illustrates the power spectrums over various cross-sections of SRSN-on-insulator waveguide to further check the wavelength components and to determine the existence of the FWM process. Power is described in unit dBm based on the laser source. The blue line represents the incident plane and it is utilized as the original pulse for comparison. The red line represent the cross-section which is 200 cells away from the incident plane and the pulse show slight broadenings on both sides. When the propagation distances increase to 400 cells, 600 cells, 800 cells, 1000 cells, 1200 cells and 1400 cells, the peak value of power spectrum drops and the broadenings keep spreading. The broadening in the short wavelength range in more

significant than the one in the other side. Therefore, the wavelength range of the power spectrum becomes wider as the propagation distance increases.

Moreover, Figure 5.22 indicates the corresponding phase of the power spectrums plotted in Figure 5.21. The phase of power pulse is zero in the incident plane and is quadratic for other cases. The wavelength range of phase becomes wider as the propagation distance increases from 0 to 1400 cells and it is in agreement with the power spectrums. The phase shifts to the shorter wavelength range and the corresponding phenomenon in Figure 5.21 is the broadening of power spectrums in shorter wavelength. As a result, it is FWM that cause the generation of new wavelength components in Figure 5.21.

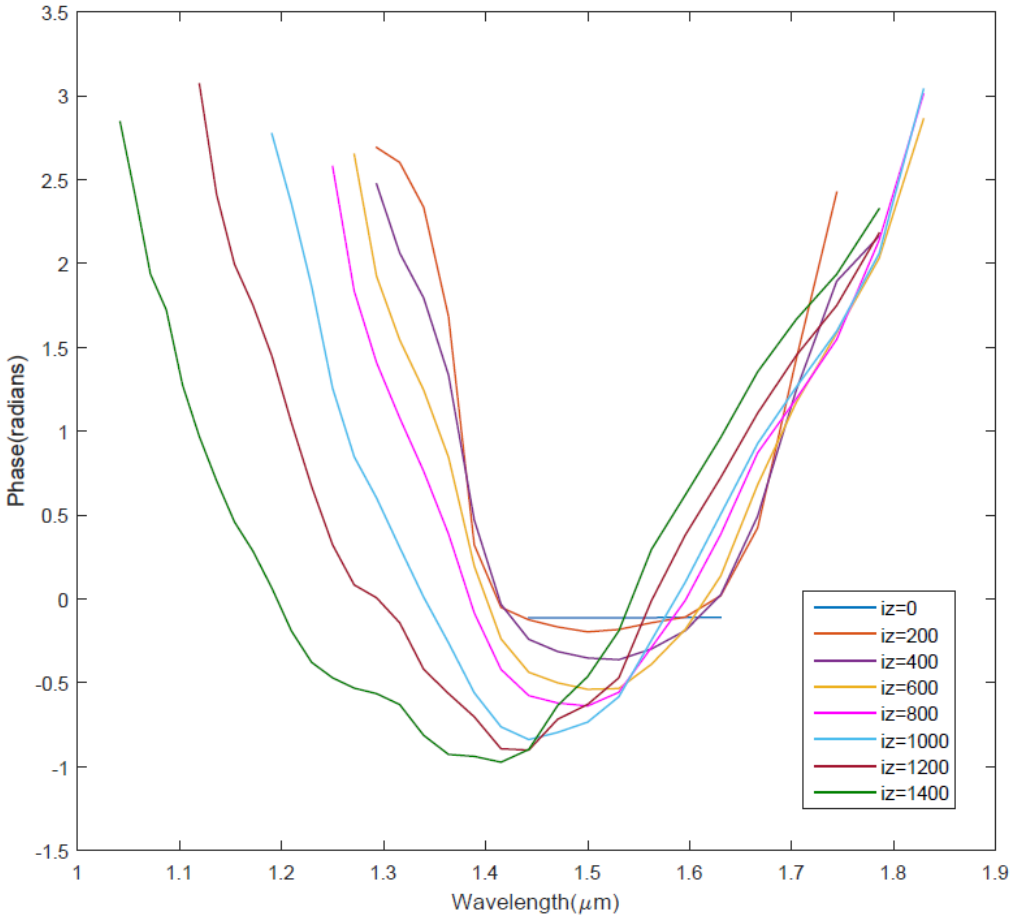

Fig. 5.22 Phase of the power spectrums of SRSN-on-insulator waveguides with various propagation lengths in wavelength domain. The width of waveguide is 500nm. The lines represent the phase of wavelength components of the power propagated through the incident plane and cross-sections where the propagation lengths are 200Δz, 400Δz, 600Δz, 800Δz, 1000Δz, 1200Δz and 1400Δz, respectively.

Furthermore, in Figure 5.23, the power spectrums of SRSN-on-insulator waveguides with various incident powers are shown but a certain propagation distance, is compared. The width of the waveguide is 500 nm and the propagation distance is 1000 cells. Five lines represent five

different incident powers, where the blue line means the lowest power and the green line means the highest power. The blue pulse has the smallest wavelength range and the red line does not show much difference. With higher powers in the yellow and purple lines, the broadenings occur on both sides and the wavelength range becomes wider. These changes are more significant in the green line, which has the highest power and widest frequency range. Besides, the phase of the power spectrums in Figure 5.23 is indicated in Figure 5.24. Phase is close to zero in low power case and described as quadratic curves in high power cases. The higher the incident power is, the wider the wavelength range is, which matches the power spectrums. Consequently, new wavelength components generated in Figure 5.23 is caused by FWM.

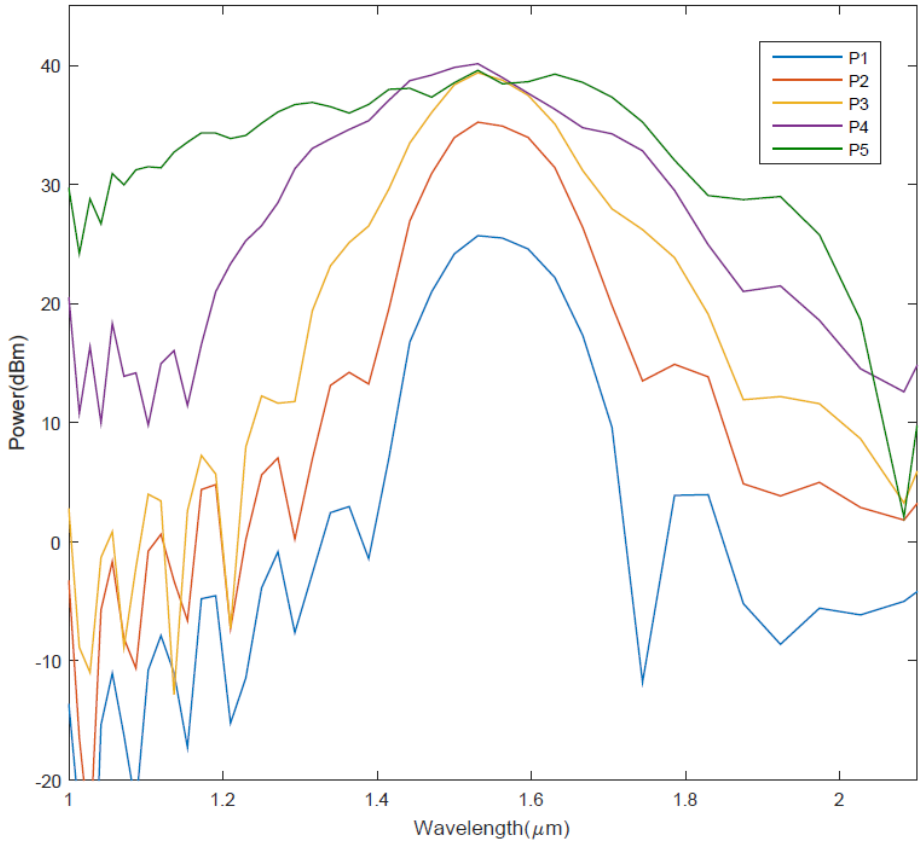

Fig. 5.23 Power spectrums of SRSN-on-insulator waveguides with various incident powers in wavelength domain. The width is 500 nm and the propagation distance is 1000 cells. The blue line represents the lowest power while the green line represents the highest power.

In order to confirm the significance of phase matching in the SRSN-on-insulator waveguide, waveguides with various widths but the same incident power and propagation length are simulated and compared. Three widths of 400 nm, 500 nm and 800 nm are chosen based on the values of GVD and the phase mismatch factor plotted in Figures 5.17 and 5.18, in which

500 nm is close to zero value of GVD and maintains a small Δk in the wavelength range 1.3-1.8 μm.

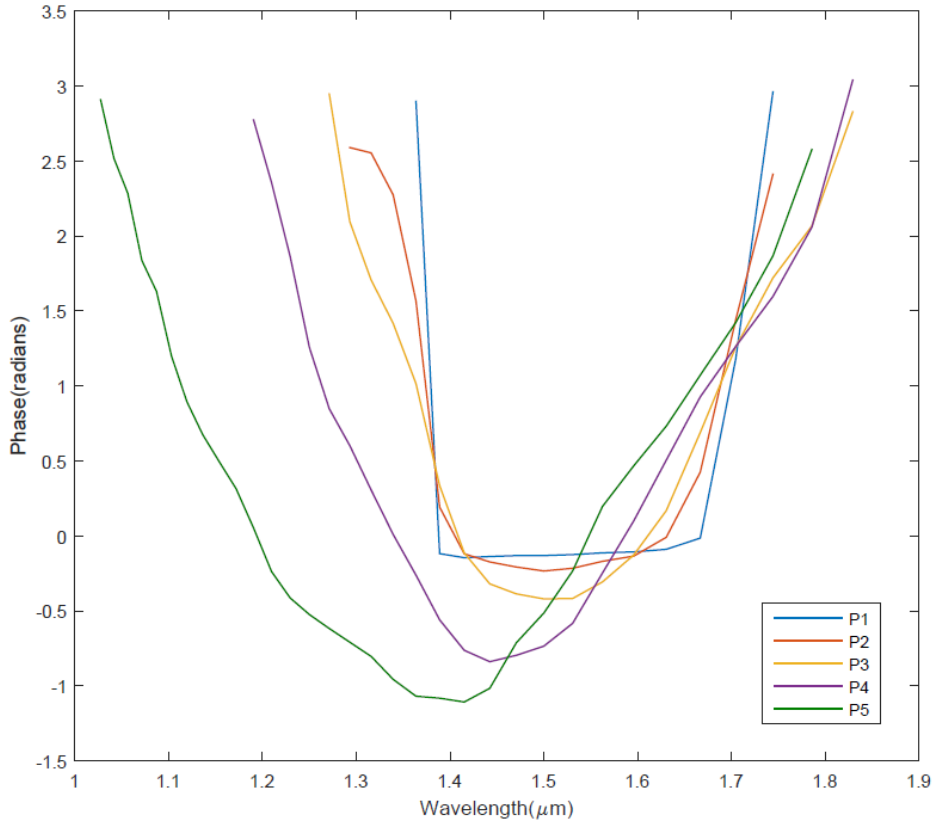

Fig. 5.24 Phase of the power spectrums of SRSN-on-insulator waveguides with various incident powers in wavelength domain. The width is 500 nm and the propagation distance is 1000 cells. The blue line represents the lowest power while the green line represents the highest power.

Figure 5.25 compares the power spectrums of SRSN-on-insulator waveguides with the above three widths in wavelength domain. The propagation length of the waveguide is 1400 cells and is equal to 70 μm. The blue and green lines represent the waveguides with widths of 400 nm and 800 nm, respectively. They have broadenings on both sides when compared to the similar original power spectrum shown in Figure 5.21. However, they show a smaller wavelength range than 500 nm case. Therefore, the waveguide with a width of 500 nm shows the most efficient FWM in the comparison, which matches the values of Δk plotted in Figure 5.18. Considering the coherent length is 70 μm, the absolute value of Δk should be less than 0.014 μm^{-1}. As for widths 400 nm and 800 nm, the ranges of signal wavelength with desired Δk are 1.48-1.63 μm and 1.47-1.64 respectively. When the width of the waveguide is 500 nm, the value of Δk is satisfied in the almost whole wavelength range plotted in Figure 5.18. Therefore, SRSN-on-insulator waveguide with a width of 500 nm has the most wavelength components

involved in nonlinear interaction in a coherent length of 70 μm and achieves the most efficient FWM process in TE fundamental mode at wavelength 1.55 μm.

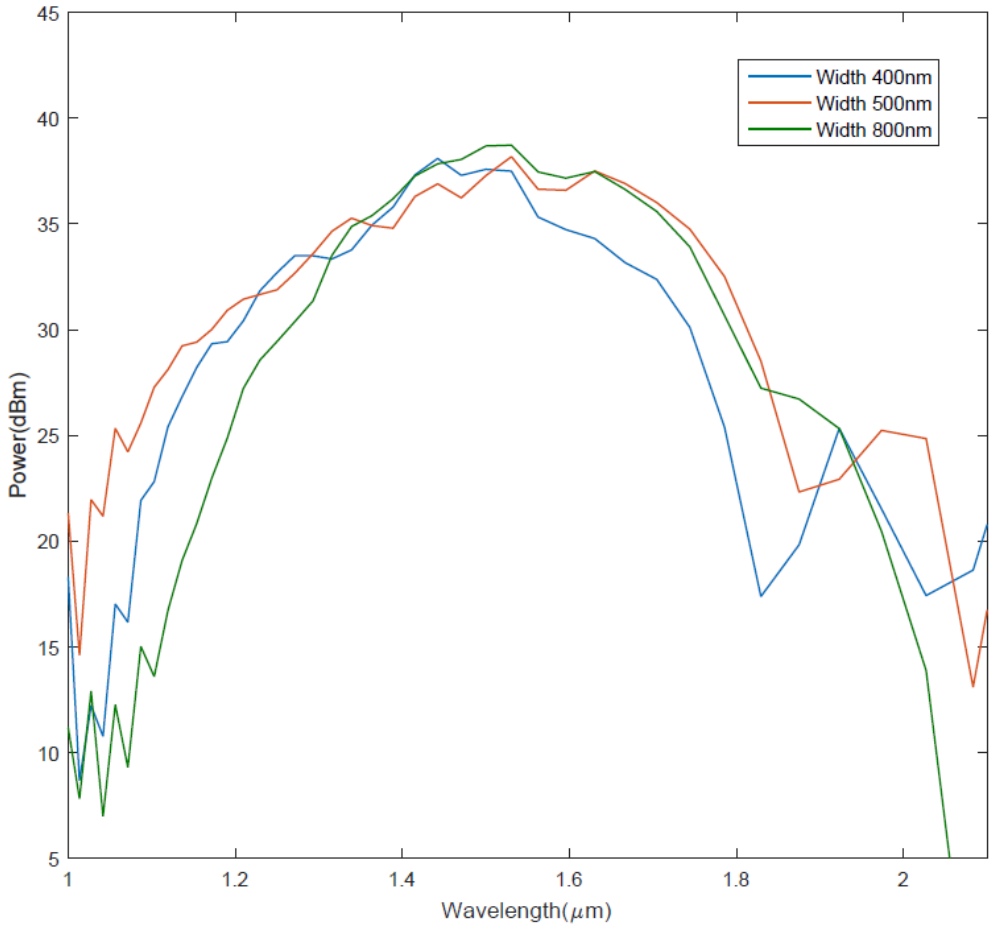

Fig. 5.25 Comparison of power spectrums of SRSN-on-insulator waveguides with three widths 400 nm, 500 nm and 800 nm in wavelength domain. The propagation distance is 1400 cells.

5.3 Conclusion

This chapter has presented the simulations of FWM processes with FDTD algorithm for two silicon-based waveguides: the silicon-on-insulator waveguide and the SRSN-on-insulator waveguide. The excitation source was based on Gaussian pulse and TE mode at wavelength 1.55 μm. In these waveguides, there were two widths that satisfied zero-GVD and the waveguide with the bigger width allowed the existence of high-order modes, so that the smaller width was chosen for phase matching.

According to the thicknesses of wafers in fabrication, the heights of silicon-on-insulator waveguide and SRSN-on-insulator waveguide were designed as 220 nm and 700 nm, respectively. GVD and phase mismatch factors were discussed and phase matching conditions

of FWM in two waveguides were achieved when the widths were 400 nm and 500 nm, respectively. In the simulations of two waveguides, power spectrums and their phases of the waveguides with various propagation distances, incident powers or widths were compared. Broadening in the power spectrums were much bigger in the shorter wavelength range. Efficient FWM was realized when the phase matching condition was satisfied.

Chapter 6

Second-Harmonic Generation of Highly Birefringent AlGaAs Waveguide

This chapter introduces a simulation of SHG in a highly birefringent $Al_{0.3}Ga_{0.7}As$-on-insulator waveguide. Basic models and material dispersion of waveguide are presented. Because of the strong contrast in the refractive index between $Al_{0.3}Ga_{0.7}As$ and silicon dioxide, an optical wave is propagated as a well-confined mode in the waveguide. Mode solver was applied to obtain TE and TM modes and type-I phase matching condition of SHG was achieved. The incorporated nonlinearities included second-order nonlinearity and third-order Kerr-type nonlinearity. Efficient SHG was observed in a suitably designed waveguide.

6.1 Basic model

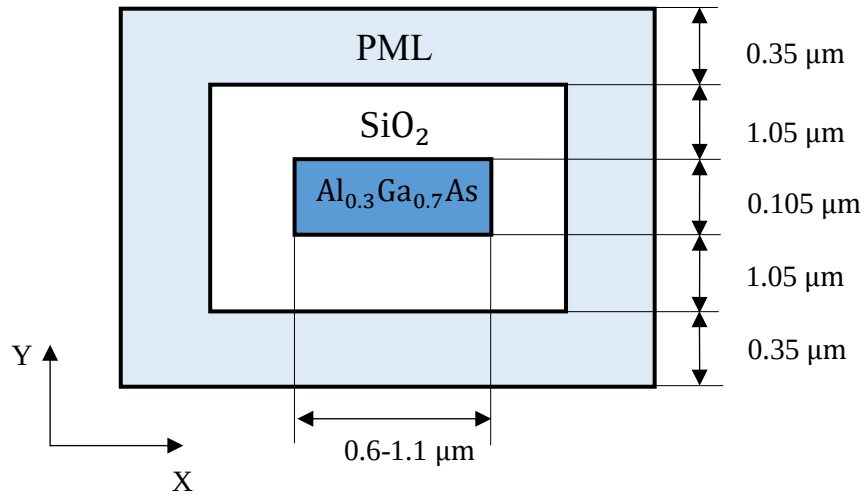

Fig. 6.1 Cross-section of highly birefringent $Al_{0.3}Ga_{0.7}As$ waveguide in the simulation.

Figure 6.1 describes the cross-section of highly birefringent $Al_{0.3}Ga_{0.7}As$ waveguide in the simulation and $Al_{0.3}Ga_{0.7}As$ is the core layer with a height of 105 nm and the width is between 0.6 and 1.1 µm. The cladding layer is silicon dioxide with a thickness of 1.05 µm, caused by a low refractive index and offers COMS compatibility. In addition, the outer layer of *x*-*y* plane

is 10-cell thick PML, ensuring the problem domain is bounded and that the radiation energy would eventually be absorbed. The grid sizes and the time step (which is determined by the smallest grid size) are defined as follows:

Δx = 50 nm; Δy = 35 nm; Δz = 50 nm

$$\Delta t = \frac{\Delta y}{2c} \tag{6.1}$$

6.2 Linear dispersion

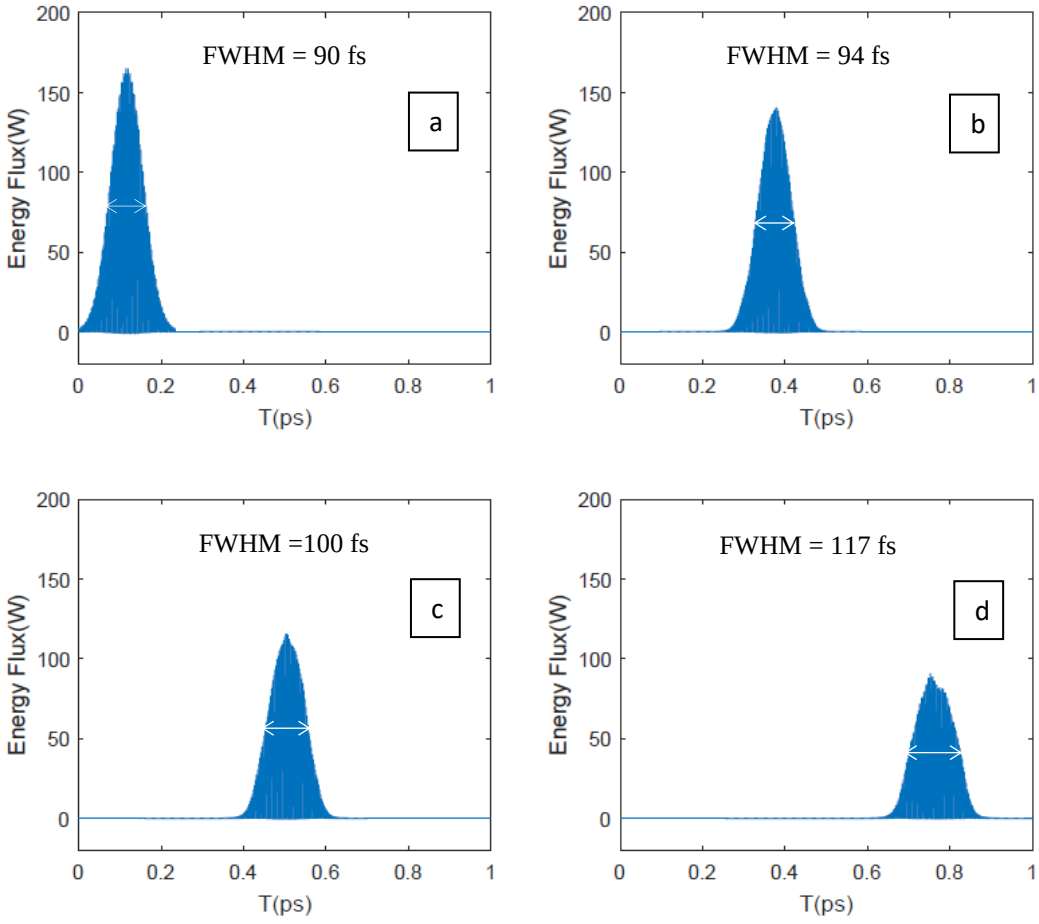

Fig. 6.2 Propagation of energy flux in highly birefringent $Al_{0.3}Ga_{0.7}As$ waveguide in time domain. Subfigure (a) is the incident plane while (b), (c) and (d) are cross-sections where propagation lengths are 400Δz, 600Δz and 1000Δz, respectively.

The simulation of FWM in a $Al_{0.3}Ga_{0.7}As$-on-insulator waveguide was demonstrated in Chapter 4, where the refractive index of $Al_{0.3}Ga_{0.7}As$ and silicon dioxide was plotted in Figure 4.34, and the parameters of Lorentz dispersion were described in the equations (4.19 and 4.20). Different from the $Al_{0.3}Ga_{0.7}As$-on-insulator waveguide in Chapter 4, this waveguide has a

different structure with a smaller height and this simulation not only considers the third-order nonlinearity but also the second-order nonlinearity.

Figure 6.2 depicts the group velocity dispersion of a highly birefringent $Al_{0.3}Ga_{0.7}As$ waveguide. It reflects the propagation of energy flux in four cross-sections in the time domain. Sub-figure (a) represents the incident plane while (b) - (d) are cross sections that are 400 cells, 600 cells and 1000 cells away from the incident plane, respectively. In addition, the FWHM of pulses are also indicated in four sub-figures. The input wave in the sub-figure (a) has the largest peak value (165 W) and the smallest FWHM (90 fs). Over time, the propagation distance increases in sub-figure (b) – (d), and the peak value gradually drops from to 91 W while the FWHM grows to 117 fs. This phenomenon is caused by linear dispersion. The excitation source contains a range of frequency components and in the Lorentz medium, the lower frequency components run faster than the higher ones, resulting in the broadening of the pulse in the time domain.

6.3 Phase matching condition of SHG

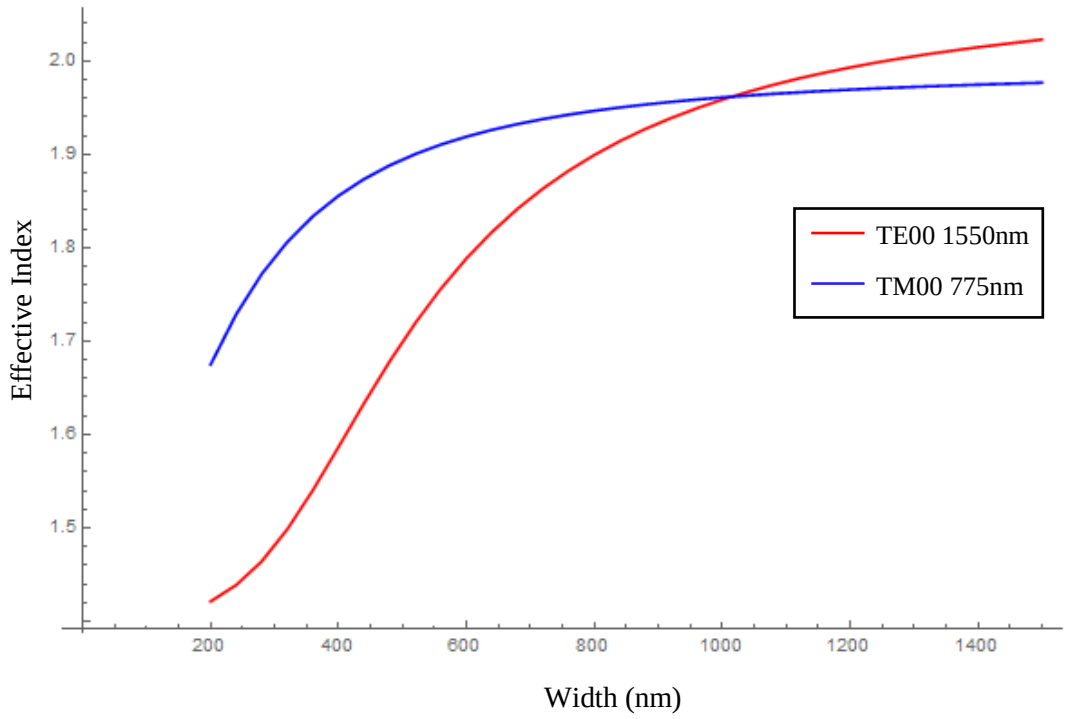

Fig. 6.3 Type-I phase matching condition of SHG in highly birefringent $Al_{0.3}Ga_{0.7}As$ waveguide. The red line represents the effective indices of TE fundamental mode at wavelength 1550 nm and the blue line represents the effective indices of TM fundamental mode at wavelength 775 nm in the waveguides with various widths.

The effective index of highly birefringent $Al_{0.3}Ga_{0.7}As$ waveguide is dependent on the polarization; for instance, effective indices are different in the TE and TM mode. It was highlighted in Chapter 3 that there are two types of phase matching conditions of SHG. As shown in Figure 6.3, Type-I phase matching condition is achieved when that width is 1050 nm. The red and blue lines represent the effective indices of TE fundamental mode at 1550 nm and those of TM fundamental mode at 775 nm of waveguides with a variety of widths, respectively. When the width of waveguide increases, both lines grow. The red line starts at a lower initial value about 1.42 while the blue line starts from 1.67. With a faster growth, the red line catches up with the blue line at the width 1050 nm with the effective index 1.97, and overtakes it at larger widths. The goal is the point of intersection and this satisfies the Type-I phase matching condition.

6.4 TE mode and TM mode

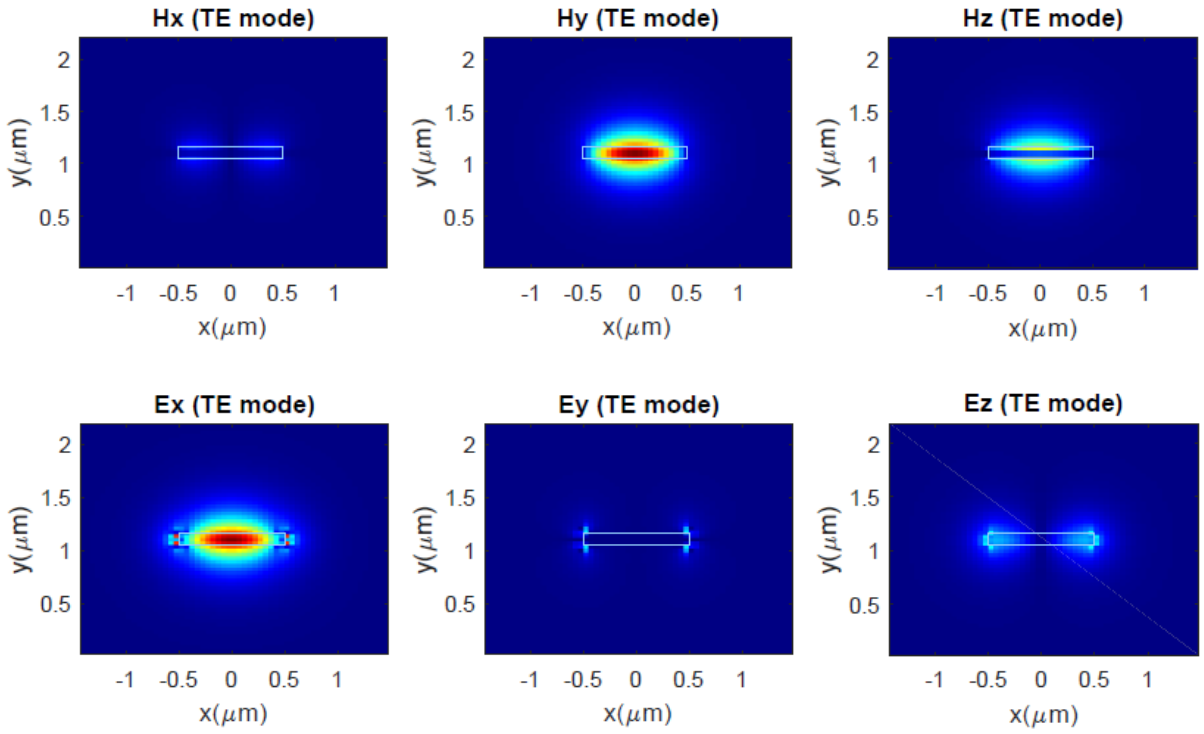

Fig. 6.4 Magnetic and electric fields in TE fundamental mode of *x*-*y* plane in highly birefringent $Al_{0.3}Ga_{0.7}As$ waveguide at wavelength 1550 nm. The width is 1050 nm and the effective index of waveguide is 1.97.

With mode solver, the values of six field components were obtained. Apart from the PML area, the $Al_{0.3}Ga_{0.7}As$ core layer and surrounded silicon dioxide layer have initial values. Figure 6.4 describes the TE fundamental mode in both magnetic and electric fields in the *x*-*y* plane of

highly birefringent $Al_{0.3}Ga_{0.7}As$ waveguide (width = 1050 nm) at wavelength 1550 nm, where the effective index is 1.97. Six sub-figures represent six components of magnetic and electric fields. It is shown that the TE mode is well confined in the central part of the waveguide and the main energy of optical pulse is propagated in H_y and E_x.

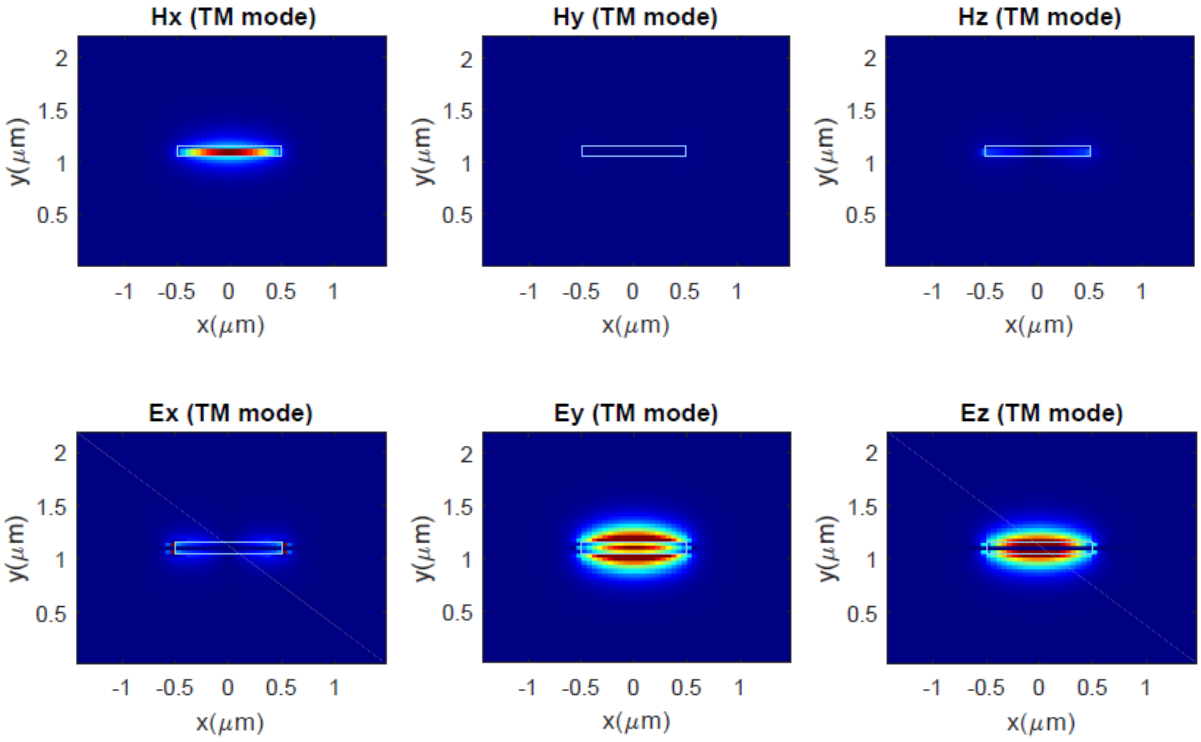

Fig. 6.5 Magnetic and electric fields in TM fundamental mode of *x-y* plane in highly birefringent $Al_{0.3}Ga_{0.7}As$ waveguide at wavelength 775 nm. The width is 1050 nm and the effective index of waveguide is 1.97.

Figure 6.5 shows the TM fundamental mode in both magnetic and electric fields in the *x-y* plane of highly birefringent $Al_{0.3}Ga_{0.7}As$ waveguide width = 1050 nm) at wavelength 775 nm, where the effective index is 1.97. Six sub-figures represent six components of magnetic and electric fields. TM mode is also well confined and the main energy of optical pulse is propagated in E_y and H_x.

6.5 Results of SHG

Based on the discussion of phase matching condition in the previous section, in order to simulate the efficient SHG, the width of the waveguide was set as 1050 nm. According to the type-I phase matching condition, the excitation source is TE fundamental mode at 1550 nm while the output is TM fundamental mode at 775 nm. Therefore, in this simulation, the

excitation source consists of TE fundamental mode at wavelength 1550 nm and Gaussian pulse which is defined in the formula (4.2). The output of simulation of the values of E_y is over the whole cross-section. Kerr-type third-order nonlinearity of AlGaAs was incorporated based on the value of nonlinear refractive index n_2 given in Chapter 4. Second-order susceptibility $\chi^{(2)}$ of AlGaAs is 180pm/V[67] and was incorporated to simulate three-wave mixing in highly birefringent $Al_{0.3}Ga_{0.7}As$ waveguide. In general, second-order nonlinearity causes sum and difference frequency generation, where SHG is a special case of SFG. If the phase of SHG is not matched, SHG power would grow at first, drop and then grow again, as shown in Figure 3.5. Therefore, efficient SHG could be realized when the phase matching condition is fulfilled.

Other than the phase matching condition, another major issue that affects the efficiency of SHG is the interaction length. It is noted that it is not an issue if the excitation source is CW plane-wave sources. With regards to ultrashort pulses, frequency conversion is influenced by the effective interaction length, which is determined by the duration of incident pulse and group velocity mismatch (GVM). GVM can lead to temporal walk-off, which means the temporal overlaps between the waves with various group velocities are lost after a certain propagation distance. GVM is defined as follows:

$$V_1 = \frac{\partial \omega_1}{\partial k_1} \; ; \; V_2 = \frac{\partial \omega_2}{\partial k_2} \tag{6.2}$$

$$\beta = \frac{1}{V_2} - \frac{1}{V_1} \tag{6.3}$$

where V_1 and V_2 are group velocities of the fundamental pulse and the second-harmonic pulse and β is the GVM. Then the interaction length is expressed as:

$$l = \frac{t_p}{\beta} \tag{6.4}$$

where t_p is the FWHM of incident pulse. Therefore, the duration of incident pulse should be decided reasonably to ensure an adequate interaction length. Otherwise, a walk-off effect occurs and undermines the efficiency of SHG.

Figure 6.6 indicates the FFT of E_y component over six cross-sections of a highly birefringent $Al_{0.3}Ga_{0.7}As$ waveguide with a width of 1050 nm, which nearly satisfies the phase matching

condition. The incident pulse was based on TE fundamental mode at wavelength 1550 nm (corresponding frequency is 194 THz) with a duration of 117 fs, so its primary energy was propagated in E_x and H_y components. In contrast, the newly generated frequency in SHG process was twice that of the initial frequency and the polarization was TM fundamental mode at 775 nm (corresponding frequency is 388 THz), where E_y and H_x carried the main energy. Therefore, the FFT of E_y illustrates the power of SHG. In Figure 6.6, sub-figures represent the cross-sections that are 20 cells, 40 cells, 60 cells, 80 cells, 100 cells and 120 cells away from the incident plane, respectively. It is known that, in the incident plane, the magnitude of E_y at frequency 388 THz is zero. When the propagation distance increases to 120 cells, magnitude of E_y at frequency 388 THz keeps growing to 7.23×10^9 V/m.

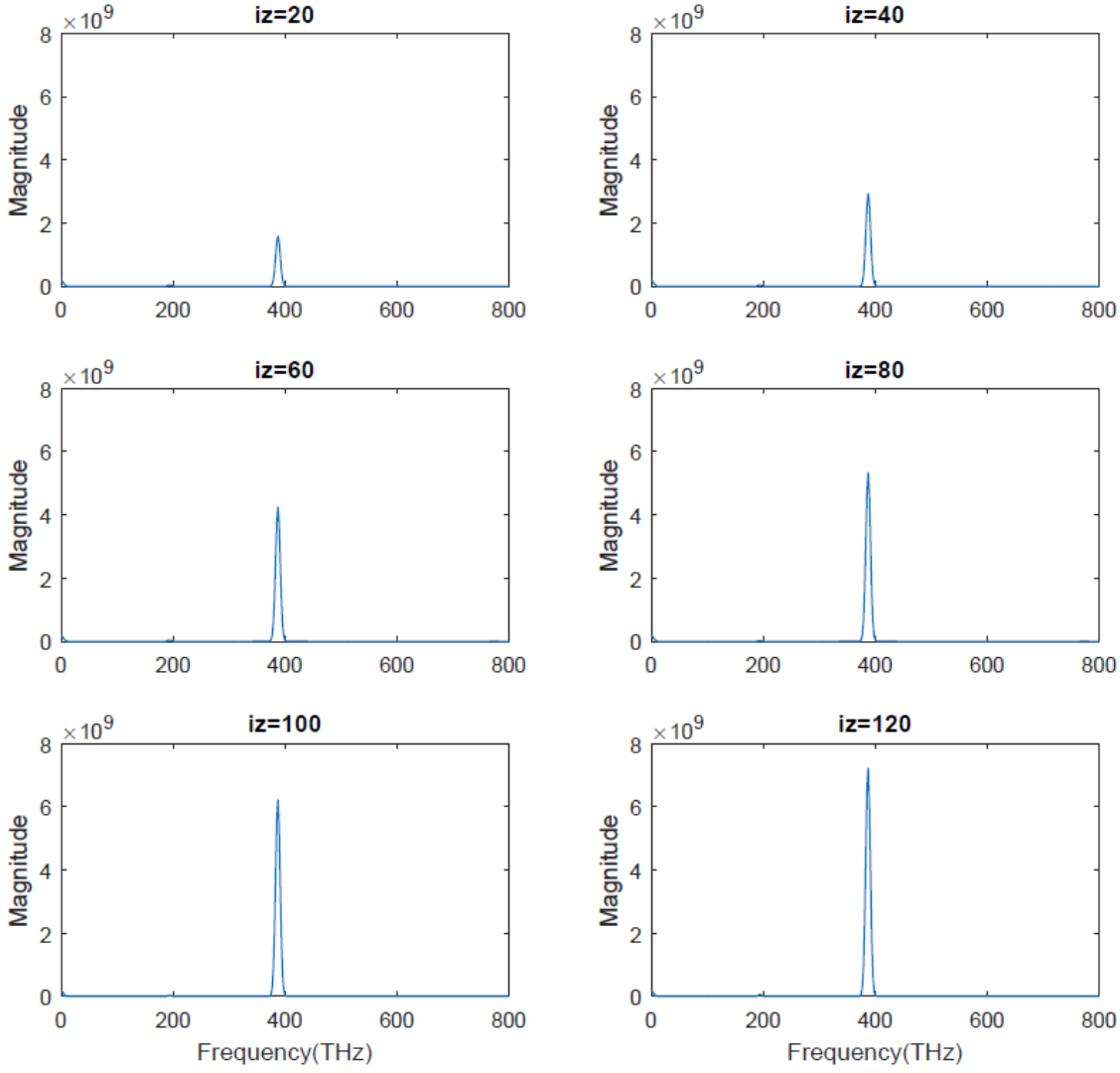

Fig. 6.6 FFT of E_y component over cross-sections in highly birefringent $Al_{0.3}Ga_{0.7}As$ waveguide with a width of 1050 nm. Sub-figures are cross sections where the propagation lengths are 20Δz, 40Δz, 60Δz, 80Δz, 100Δz and 120Δz respectively.

To further prove the significance of phase matching, the result of SHG in a phase-mismatched highly birefringent $Al_{0.3}Ga_{0.7}As$ waveguide with a width of 600 nm is also plotted for comparison with the phase matched example. According to the equations (3.9-3.10), the coherent length is infinite in a phase-matched waveguide. With regard to the width 600 nm, the coherent length is:

$$l_c = \frac{\pi}{2k_1 - k_2} = \frac{\pi}{\frac{4\pi n_{\omega_1}}{\lambda_1} - \frac{2\pi n_{2\omega_1}}{\lambda_2}} \approx 58\ \Delta z \tag{6.5}$$

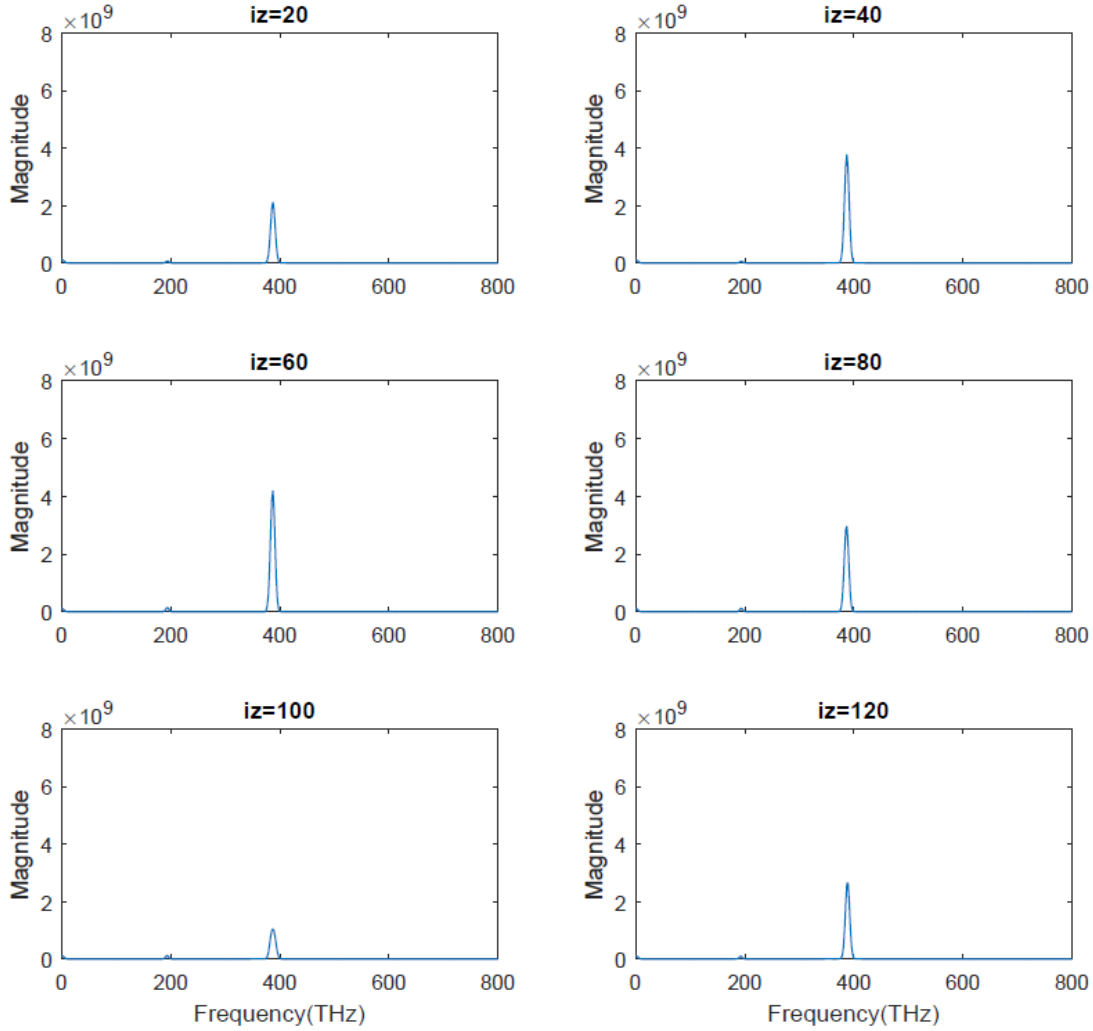

Fig. 6.7 FFT of E_y component over cross-sections in highly birefringent $Al_{0.3}Ga_{0.7}As$ waveguide with a width of 600 nm. Sub-figures are cross sections where the propagation lengths are 20Δz, 40Δz, 60Δz, 80Δz, 100Δz and 120Δz respectively.

Figure 6.7 shows the FFT of E_y component over six cross-sections of highly birefringent $Al_{0.3}Ga_{0.7}As$ waveguide with a width of 600 nm. Initially, the magnitude of E_y produced in SHG rises from zero at the incident plane to 4.19×10^9 V/m at a distance of 60 cells in the third

sub-figure. Then, the value decreases to 1.05×10^{9} V/m as the distance increases to 100 cells. After that, it starts to rise again in a longer propagation distance. This phenomenon is caused by the limited coherent length, which is between 50 and 60 cells. With regards to the results of the phase-matched highly birefringent $Al_{0.3}Ga_{0.7}As$ waveguide in Figure 6.6, the value of E_y at the newly generated frequency in SHG process never drops. Therefore, phase matching condition ensures efficient SHG.

6.6 Conclusion

This chapter has introduced a simulation of SHG process with FDTD algorithm in a highly birefringent $Al_{0.3}Ga_{0.7}As$-on-insulator waveguide. Linear dispersion, second- and third-order nonlinearities were incorporated. The height of this waveguide was 105 nm and Type-I phase matching condition was achieved when the width was 1050 nm: the effective index of waveguide in TE fundamental mode at 1550 nm was equals to the effective index of waveguide in TM fundamental mode at 775 nm.

In addition, GVM was discussed in case the efficiency of SHG would be undermined by the temporal walk-off. In the phase-matched waveguide, the SHG power grew as the propagation distance increased. In contrast, in the phase-mismatched case, the SHG power was limited by the coherent length. It grew as the propagation distance increased from zero to the coherent length, after which, the SHG power dropped when the propagation distance increased from one coherent length to two coherent lengths. It was concluded that efficient SHG was realized when the Type-I phase matching condition was satisfied.

Chapter 7

Conclusion and Future Work

7.1 Conclusion

This thesis has presented the simulations of six optical waveguides, based on FDTD algorithms with the incorporation of linear dispersion (including geometric and material dispersions) and nonlinearity through the PLRC method. Basic models of waveguides were built with an outer PML absorbing boundary condition in an *x*-*y* plane and with circular boundary conditions in a *z*-direction. The excitation source was defined as a combination of Gaussian pulse and TE fundamental mode, which was generated by mode solver. Material dispersion was described as Lorentz medium and incorporated through Sellmeier equations. Second- and third-order nonlinearities were incorporated in order to simulate SHG, FWM and Raman scattering.

GaAs suspended waveguide was designed and simulated as a simple example. GVD, D and phase mismatch factors were discussed in order to determine the phase matching condition of FWM. The structure could be engineered to achieve zero-GVD. When the width was 760 nm, the phase matching condition of FWM in TE fundamental mode at wavelength 1.55 μm was satisfied. Results of FWM were observed through the FFT of energy flux in Figures 4.8 – 4.10, where super-continuum and the generation of frequency comb were realized.

In the simulations of deep-etched $Al_{0.25}Ga_{0.75}As$ waveguide and $Al_{0.3}Ga_{0.7}As$-on-insulator waveguide, material dispersions were expressed in the form of Sellmeier equations with four pole pairs. GVD, D and phase mismatch factors were discussed and, as a result, the widths that fulfilled phase matching conditions of FWM in TE fundamental mode at wavelength 1.55 μm were obtained: both were 700 nm. When the excitation source had high intensity, FWM happened in both waveguides. Power spectrums and their phases of waveguides with various propagations or incident powers were plotted and compared. The broadening in the shorter wavelength range was much larger. In addition, Raman scattering was also taken into consideration in $Al_{0.25}Ga_{0.75}As$ waveguide but it did not make much difference because the Kerr-effect was dominant. Moreover, simulation results of this waveguide were in strong agreement with the experimental measurements in Figures 4.30 and 4.31.

With regard to the simulations of silicon-on-insulator waveguides and silicon nitride-on-insulator waveguides, following the discussion of GVD, D and phase mismatch factors, widths of waveguides achieved phase matching conditions of FWM in TE fundamental mode at wavelength 1.55 μm were 400 nm and 500 nm, respectively. Power spectrums and their phases of waveguides with various propagations or incident powers were plotted and compared in order to determine the generation of new wavelength components in FWM process. The power spectrums spread further in a shorter wavelength range.

As for the simulation of highly birefringent AlGaAs waveguides, it was not only linear dispersion and Kerr-type nonlinearity, but also second-order nonlinearity, which was incorporated. With an analysis of effective indices of waveguides with various widths in TE and TM fundamental modes, type-I phase matching condition of SHG was found: when the width was 1050 nm, the effect of the waveguide in TE fundamental mode at wavelength 1550 nm was equal to the one in TM fundamental mode at wavelength 775 nm. GVM was discussed in order to ensure the enough interaction length and avoid walk-off in the simulation. In the comparison between the phase-matched and phase-mismatched waveguides, it was demonstrated that SHG power was limited by the coherent length and efficient SHG was realized when the phase matching condition was achieved.

In conclusion, in the simulation of FWM process in TE fundamental mode at wavelength 1.55 μm, GaAs/AlGaAs waveguides had two zero-GVD points and the larger widths were confirmed as phase matching condition because the smaller ones were affected significantly by the higher-order term of dispersion. In contrast, in the simulations of silicon-based waveguides, there were also two zero-GVD points but the larger widths allowed the existence of higher-order modes of optical wave. Thus, phase matching conditions were satisfied when the widths were decided as the smaller ones. Therefore, phase mismatch factors of GaAs/AlGaAs waveguides were much smaller than those of silicon-based waveguides when the phase matching conditions of FWM were fulfilled, leading to the wider broadenings in the power spectrums in wavelength domain. The observation of FWM results in all these five optical waveguides were indicated through the broadenings of power spectrums when the excitation sources contain a single or two frequency components. Among the GaAs/AlGaAs waveguides, $Al_{0.3}Ga_{0.7}As$-on-insulator waveguide has the most efficient frequency conversion caused by FWM process. Silicon nitride-on-insulator waveguide has a higher FWM efficiency than that of silicon-on-insulator waveguide.

Therefore, it is proved that this simulation framework is capable of simulating a wide range of optical waveguides with various materials and structures. Not only linear dispersion, but also nonlinearity (including second- and third-order nonlinear effects) could be taken into consideration to simulate SHG, FWM and Raman scattering. The size of grid could be adjusted flexibly based on the structure and the wavelength of excitation source. The simulation results could give some advices on fabrication, such as the designed structure and materials of waveguide, the duration of excitation sources, the wavelength range of generated super-continuum and the comparisons of the efficiency of FWM/SHG between the waveguides with various widths.

7.2 Future work

The simulation demonstrated in this thesis can be widely applied for many optical waveguides and is suitable for linear dispersive, nonlinear, isotropic and anisotropic materials. It could be used for simulating linear dispersion, second- and third-order nonlinear frequency mixing processes. However, there is still room for improvement.

The first goal would be to incorporate propagation loss and TPA. Both cause power loss in the propagation of optical waves in waveguides. To take propagation loss into consideration, permittivity should be treated as a complex number rather than a real number. With regard to TPA effect, the nonlinear polarization due to TPA should be expressed based on TPA co-efficient and incorporated in FDTD algorithm[156]. As a result, more realistic simulation can be achieved when TPA and propagation loss are taken into account.

The second goal would be increase the lengths of waveguides in the simulations. Parallel computation and HPC resource are crucial parts because the programs for long-distance simulation are time- and memory-consuming. Then, to maintain the stability of FDTD algorithm in long-time simulation, CPML should be utilized to replace normal PML.

The third goal would be to extend the simulation for magneto-optic materials. This involves incorporating magneto-optical susceptibility to simulate the rotation of polarization in the optical waveguides, which is known as the Faraday Effect. Typical applications are optical isolators and circulators[157].

References

[1] S.R. Forrest, “Optoelectronic integrated circuits XV,” *Proc. IEEE*, vol. 75, no. 11, pp. 1488–1497, 1987.

[2] Lotfia M. EI-Nadi and M. S. Mansour, *Laser Science and Applications: Proceedings of the Sixth International Conference*. National Institute of Laser Enhanced Sciences, Cairo University, Giza, Egypt, 2007.

[3] J. L. Hall, “Defining and measuring optical frequencies (Nobel lecture),” *Rev. Mod. Phys.*, vol. 78, no. 4, p. 1279, 2006.

[4] T. W. Hänsch, “Passion for precision (Nobel lecture),” *ChemPhysChem*, vol. 7, no. 6, pp. 1170–1187, 2006.

[5] “The Nobel Prize in Physics 2005,” 2005. [Online]. Available: https://www.nobelprize.org/nobel_prizes/physics/laureates/2005/index.html.

[6] B. Kuyken, T. Ideguchi, and S. Holzner, “An octave spanning mid-infrared frequency comb generated in a silicon nanophotonic wire waveguide,” *Nat. Commun.*, vol. 6, p. 6310, 2015.

[7] D. T. U. Fotonik, P. Engineering, O. Society, and A. Ocis, “Efficient frequency comb generation in AlGaAs-on-insulator,” *Optica*, vol. 3, no. 8, pp. 823–826, 2016.

[8] Y. O. N. G. Y. Ang *et al.*, “Four-wave mixing parametric oscillation and frequency comb generation at visible wavelengths in a silica microbubble resonator,” *Opt. Lett.*, vol. 41, no. 22, pp. 5266–5269, 2016.

[9] B. Stern, X. Ji, Y. Okawachi, A. L. Gaeta, and M. Lipson, “Fully integrated ultra-low power Kerr comb generation,” *arXiv Prepr. arXiv*, 2018.

[10] R. Wu, V. Torres-company, D. E. Leaird, and A. M. Weiner, “Supercontinuum-based 10-GHz flat-topped optical frequency comb generation,” *Opt. Express*, vol. 21, no. 5, pp. 6045–6052, 2013.

[11] J. M. C. Boggio *et al.*, “Optical frequency comb generated by four-wave mixing in highly nonlinear fibers,” *Opt. Soc. Am.*, pp. 100–101, 2009.

[12] A. J. Metcalf, V. Torres-company, D. E. Leaird, S. Member, A. M. Weiner, and A. Broadband, “High-power broadly tunable electrooptic frequency comb generator,” *IEEE J. Sel. Top. Quantum Electron.*, vol. 19, no. 6, pp. 231–236, 2013.

[13] M. Yan, P. Luo, K. Iwakuni, G. Millot, T. W. Hänsch, and N. Picqué, “Mid-infrared dual-comb spectroscopy with electro-optic modulators,” *Nat. Publ. Gr.*, vol. 6, no. 10, pp. 4–11, 2017.

[14] A. Parriaux, K. Hammani, and G. Millot., “Two-micron all-fibered dual-comb spectrometer based on electro-optic modulators and wavelength conversion,” *Commun. Phys.*, vol. 1, no. 1, p. 17, 2018.

[15] F. Adler, K. Moutzouris, A. Leitenstorfer, H. Schnatz, B. Lipphardt, and G. Grosche, “Phase-locked two-branch erbium-doped fiber laser system for long-term precision measurements of optical frequencies,” *Opt. Express*, vol. 12, no. 24, pp. 5872–5880, 2004.

[16] A. Fülöp *et al.*, “High-order coherent communications using mode-locked dark-pulse Kerr combs from microresonators,” *arXiv Prepr. arXiv*, 2018.

[17] S. Y. Zhang *et al.*, “Direct frequency comb optical frequency standard based on two-photon transitions of thermal atoms,” *Sci. Rep.*, vol. 5, p. 15114, 2015.

[18] B. J. Bloom *et al.*, “An optical lattice clock with accuracy and stability at the 10-18 level,” *Nature*, vol. 506, no. 7486, p. 71, 2014.

[19] T. L. Nicholson *et al.*, “Comparison of two independent Sr optical clocks with 1× 10− 17 stability at 10 3 s,” *Phys. Rev. Lett.*, vol. 109, no. 23, p. 230801, 2012.

[20] C. W. Chou, D. B. Hume, J. C. J. Koelemeij, D. J. Wineland, and T. Rosenband, “Frequency comparison of two high-accuracy Al+ optical clocks,” *Phys. Rev. Lett.*, vol. 104, no. 7, p. 070802, 2010.

[21] R. Le Targat, R., Lorini, L., Le Coq, Y., Zawada, M., Guéna, J., Abgrall, M., ... & Gartman, “Experimental realization of an optical second with strontium lattice clocks,” *Nat. Commun.*, vol. 4, p. 2019, 2013.

[22] T. W. Hänsch and N. Picqué, “Laser spectroscopy and frequency combs,” *IOP Publ.*, vol. 467, no. 1, p. 012001, 2013.

[23] R. Soref, “The past, present, and future of silicon photonics,” *IEEE J. Sel. Top. Quantum Electron.*, vol. 12, no. 6, pp. 1678–1687, 2006.

[24] B. Tatian, “Fitting refractive-index data with the Sellmeier dispersion formula,” *Appl. Opt.*, vol. 23, no. 24, pp. 4477–4485, 1984.

[25] Q. Lin, O. J. Painter, and G. P. Agrawal, “Nonlinear optical phenomena in silicon waveguides: modeling and applications,” *Opt. Express*, vol. 15, no. 25, pp. 16604–16644, 2007.

[26] X. Liu *et al.*, “Self-phase modulation and nonlinear loss in silicon nanophotonic wires near the mid-infrared two-photon absorption edge,” *Opt. Express*, vol. 19, no. 8, pp. 7778–7789, 2011.

[27] E. Dulkeith, Y. a Vlasov, X. Chen, N. C. Panoiu, and R. M. Osgood, Jr., “Self-phase-modulation in submicron silicon-on-insulator photonic wires,” *Opt. Express*, vol. 14, no. 12, pp. 5524–5534, 2006.

[28] L. Yin and G. P. Agrawal, “Impact of two-photon absorption on self-phase modulation in silicon waveguides,” *Opt. Lett.*, vol. 32, no. 14, pp. 2031–2033, 2007.

[29] O. Boyraz, T. Indukuri, and B. Jalali, “Self-phase-modulation induced spectral broadening in silicon waveguides,” *Opt. Express*, vol. 12, no. 5, pp. 829–834, 2004.

[30] I. Hsieh, X. Chen, J. I. Dadap, N. C. Panoiu, and R. M. Osgood, “Cross-phase modulation-induced spectral and temporal effects on co-propagating femtosecond pulses in silicon photonic wires,” *Opt. Express*, vol. 15, no. 3, pp. 1135–1146, 2007.

[31] W. Astar *et al.*, “Tunable wavelength conversion by XPM in a silicon nanowire, and the potential for XPM-multicasting,” *J. Light. Technol.*, vol. 28, no. 17, pp. 2499–2511, 2010.

[32] K. Yamada, H. Fukuda, T. Tsuchizawa, T. Watanabe, T. Shoji, and S. Itabashi, “All-optical efficient wavelength conversion using silicon photonic wire waveguide,” *IEEE Photonics Technol. Lett.*, vol. 18, no. 9, pp. 1046–1048, 2006.

[33] M. a Foster, A. C. Turner, J. E. Sharping, B. S. Schmidt, M. Lipson, and A. L. Gaeta, “Broad-band optical parametric gain on a silicon photonic chip.,” *Nature*, vol. 441, no. 7096, pp. 960–963, 2006.

[34] W. Mathlouthi, H. Rong, and M. Paniccia, “Characterization of efficient wavelength conversion by four-wave mixing in sub-micron silicon waveguides,” *Opt. Express*, vol. 16, no. 21, pp. 16735–16745, 2008.

[35] A. Pasquazi *et al.*, “Efficient wavelength conversion and net parametric gain via four wave mixing in a high index doped silica waveguide,” *Opt. Express*, vol. 18, no. 8, pp. 7634–7641, 2010.

[36] S. Zlatanovic *et al.*, “Mid-infrared wavelength conversion in silicon waveguides using ultracompact telecom-band-derived pump source,” *Nat. Photonics*, vol. 4, no. 8, pp. 561–564, 2010.

[37] Y. Ding, J. Xu, H. Ou, and C. Peucheret, “Mode-selective wavelength conversion based on four-wave mixing in a multimode silicon waveguide.,” *Opt. Express*, vol. 22, no. 1, pp. 127–135, 2014.

[38] Q. Lin, J. Zhang, P. M. Fauchet, and G. P. Agrawal, “Ultrabroadband parametric generation and wavelength conversion in silicon waveguides,” *Opt. Express*, vol. 14, no. 11, pp. 4786–4799, 2006.

[39] H. Hu *et al.*, “Ultra-high-speed wavelength conversion in a silicon photonic chip.,” *Opt. Express*, vol. 19, no. 21, pp. 19886–94, 2011.

[40] R. Adams *et al.*, “Wavelength conversion of 28 GBaud 16-QAM signals based on four-wave mixing in a silicon nanowire.,” *Opt. Express*, vol. 22, no. 4, pp. 4083–4090, 2014.

[41] I. Avrutsky and R. Soref, “Phase-matched sum frequency generation in strained silicon waveguides using their second- order nonlinear optical susceptibility,” *Opt. Express*, vol. 19, no. 22, pp. 21707–21716, 2011.

[42] L. Bianco, F., Cazzanelli, M., Yeremyan, A., Ghulinyan, M., Pucker, G., Modotto, D., ... & Pavesi, “Mid-infrared difference-frequency generation in silicon waveguides strained by silicon nitride,” *Eur. Conf. Lasers Electro-Optics. Opt. Soc. Am.*, 2013.

[43] C. G. Nesic, A., Palmer, R., Koeber, S., Korn, D., Koenig, S., Elder, D. L., ... & Koos, “Demonstration of difference frequency generation in a silicon slot waveguide,” *CLEO Sci. Innov. Opt. Soc. Am.*, 2014.

[44] M. Cazzanelli, “Second-harmonic generation in silicon waveguides strained by silicon nitride,” *Nat. Mater.*, vol. 11, no. 2, pp. 148–154, 2011.

[45] B. Chmielak *et al.*, “Pockels effect based fully integrated , strained silicon electro-optic modulator,” *Opt. Express*, vol. 19, no. 18, pp. 17212–17219, 2011.

[46] C. Schriever *et al.*, “Second-order optical nonlinearity in silicon waveguides : inhomogeneous stress and interfaces,” *Adv. Opt. Mater.*, vol. 3, no. 1, pp. 129–136, 2015.

[47] L. Zhang, Q. Lin, Y. Yue, Y. Yan, R. G. Beausoleil, and A. E. Willner, “Silicon waveguide with four zero-dispersion wavelengths and its application in on-chip octave-spanning supercontinuum generation,” *Opt. Express*, vol. 20, no. 2, pp. 1685–1690, 2012.

[48] B. Kuyken, X. Liu, R. M. Osgood Jr., R. Baets, G. Roelkens, and W. M. J. Green, “Mid-infrared to telecom-band supercontinuum generation in highly nonlinear silicon-on-insulator wire waveguides,” *Opt. Express*, vol. 19, no. 21, pp. 20172–20181, 2011.

[49] R. K. W. Lau, M. R. E. Lamont, A. G. Griffith, Y. Okawachi, M. Lipson, and A. L. Gaeta, “Octave-spanning mid-infrared supercontinuum generation in silicon nanowaveguides,” *Opt. Lett.*, vol. 39, no. 15, pp. 4518–21, 2014.

[50] X. Liu, R. M. Osgood, Y. a. Vlasov, and W. M. J. Green, “Mid-infrared optical parametric amplifier using silicon nanophotonic waveguides,” *Nat. Photonics*, vol. 4, no. 8, pp. 557–560, 2010.

[51] F. Li *et al.*, “Error-free all-optical demultiplexing at 160Gb/s via FWM in a silicon nanowire,” *Opt. Express*, vol. 18, no. 4, pp. 3905–3910, 2010.

[52] H. Ji *et al.*, “Optical waveform sampling and error-free demultiplexing of 1.28 tb/s serial data in a nanoengineered silicon waveguide,” *J. Light. Technol.*, vol. 29, no. 4, pp. 426–431, 2011.

[53] S. Mas, J. Caraquitena, J. V Galán, P. Sanchis, and J. Martí, “Tailoring the dispersion behavior of silicon nanophotonic slot waveguides,” *Opt. Express*, vol. 18, no. 20, pp. 20839–20844, 2010.

[54] A. C. Turner *et al.*, “Tailored anomalous group-velocity dispersion in silicon waveguides,” *Conf. Lasers Electro-Optics 2006 Quantum Electron. Laser Sci. Conf. CLEO/QELS 2006*, vol. 14, no. 10, pp. 4357–4362, 2006.

[55] Y. Lianghong, L. Qiang, and G. P. Agrawal, “Dispersion tailoring and soliton propagation in Si waveguides,” *Conf. Lasers Electro-Optics 2006 Quantum Electron. Laser Sci. Conf. CLEO/QELS 2006*, vol. 31, no. 9, pp. 1295–1297, 2006.

[56] J. Zhang, Q. Lin, G. Piredda, R. W. Boyd, G. P. Agrawal, and P. M. Fauchet, “Optical solitons in a silicon waveguide,” *Opt. Soc. Am.*, vol. 15, no. 12, pp. 1295–1297, 2007.

[57] D. T. H. Tan, K. Ikeda, P. C. Sun, and Y. Fainman, “Group velocity dispersion and self phase modulation in silicon nitride waveguides,” *Appl. Phys. Lett.*, vol. 96, no. 6, pp. 1–4, 2010.

[58] D. S. Kim, S. G. Yoon, G. E. Jang, S. J. Suh, H. Kim, and D. H. Yoon, “Refractive index properties of SiN thin films and fabrication of SiN optical waveguide,” *J. Electroceramics*, vol. 17, no. 2–4, pp. 315–318, 2006.

[59] D. H. Yoon, S. G. Yoon, and Y. T. Kim, “Refractive index and etched structure of silicon nitride waveguides fabricated by PECVD,” *Thin Solid Films*, vol. 515, no. 12, pp. 5004–5007, 2007.

[60] C. Santiago, “Optical properties of amorphous hydrogenated silicon nitride thin films,” *Opt. Eng.*, vol. 45, no. 12, p. 123802, 2006.

[61] K. Luke, Y. Okawachi, M. R. Lamont, A. L. Gaeta, M. Lipson, “Broadband mid-infrared frequency comb generation in a Si3N4 microresonator,” *Opt. Lett.*, vol. 40, no. 21, pp. 4823–4826, 2015.

[62] H. Zhao *et al.*, “Visible-to-near-infrared octave spanning supercontinuum generation in a silicon nitride waveguide,” *Opt. Lett.*, vol. 40, no. 10, pp. 2177–2180, 2015.

[63] A. R. Johnson *et al.*, “Octave-spanning coherent supercontinuum generation in a silicon nitride waveguide,” *Opt. Lett.*, vol. 40, no. 21, p. 5117, 2015.

[64] J. S. Levy, M. a Foster, A. L. Gaeta, and M. Lipson, “Harmonic generation in silicon nitride ring resonators,” *Opt. Express*, vol. 19, no. 12, pp. 11415–11421, 2011.

[65] G. I. Stegeman *et al.*, “AlGaAs below half bandgap: the silicon of nonlinear optical materials,” *Int. J. Nonlinear Opt. Phys.*, vol. 3, no. 03, pp. 347–371, 1994.

[66] S. Gehrsitz, F. K. Reinhart, C. Gourgon, N. Herres, A. Vonlanthen, and H. Sigg, “The refractive index of AlxGa1−xAs below the band gap: Accurate determination and empirical modeling,” *J. Appl. Phys.*, vol. 87, no. 11, pp. 7825–7837, 2000.

[67] K. A. Rutkowska, D. Duchesne, M. Volatier, R. Arès, and V. Aimez, “Second harmonic generation in AlGaAs nanowaveguides,” *Acta Phys. Pol. A.*, vol. 120, no. 4, 2011.

[68] J. S. Aitchison, D. C. Hutchings, J. U. Kang, G. I. Stegeman, and A. Villeneuve, “The nonlinear optical properties of AlGaAs at the half band gap,” *IEEE J. Quantum Electron.*, vol. 33, no. 3, pp. 341–348, 1997.

[69] K. Ikeda, R. E. Saperstein, N. Alic, and Y. Fainman, “Thermal and Kerr nonlinear properties of plasma-deposited silicon nitride/ silicon dioxide waveguides,” *Opt. Express*, vol. 16, no. 17, p. 12987, 2008.

[70] K. Dolgaleva, W. C. Ng, L. Qian, and J. S. Aitchison, “Compact highly-nonlinear AlGaAs waveguides for efficient wavelength conversion,” *Opt. Express*, vol. 19, no. 13, pp. 12440–12455, 2011.

[71] S. T. Ho, C. E. Soccolich, M. N. Islam, W. S. Hobson, A. F. J. Levi, and R. E. Slusher, “Large nonlinear phase shifts in low-loss AlxGa1-xAs waveguides near half-gap,” *Appl. Phys. Lett.*, vol. 59, no. 20, pp. 2558–2560, 1991.

[72] Z. Yang *et al.*, “Enhanced second-harmonic generation in AlGaAs microring resonators,” *Opt. Lett.*, vol. 32, no. 7, pp. 826–828, 2007.

[73] X. Yu, L. Scaccabarozzi, J. S. Harris, P. S. Kuo, and M. M. Fejer, “Efficient continuous wave second harmonic generation pumped at 1.55 μm in quasi-phase-matched AlGaAs waveguides,” *Opt. Express*, vol. 13, no. 26, pp. 10742–10748, 2005.

[74] M. Savanier *et al.*, “Large second-harmonic generation at 1.55 μmin oxidized AlGaAs waveguides,” *Opt. Lett.*, vol. 36, no. 15, pp. 2955–2957, 2011.

[75] D. Duchesne *et al.*, “Second harmonic generation in AlGaAs photonic wires using low power continuous wave light,” *Opt. Express*, vol. 19, no. 13, pp. 12408–12417, 2011.

[76] J. Ota, W. Narita, I. Ohta, T. Matsushita, and T. Kondo, “Fabrication of periodically-inverted AlGaAs waveguides for quasi-phase-matched wavelength conversion at 1.55 μm,” *Jpn. J. Appl. Phys.*, vol. 48, no. 4S, pp. 0–4, 2009.

[77] J. Han, P. Abolghasem, B. J. Bijlani, and A. S. Helmy, “Continuous-wave sum-frequency generation in AlGaAs Bragg reflection waveguides,” *Opt. Lett.*, vol. 34, no. 23, pp. 3656–3658, 2009.

[78] L. Lanco *et al.*, “Backward difference frequency generation in an AlGaAs waveguide,” *Appl. Phys. Lett.*, vol. 89, no. 3, pp. 3–6, 2006.

[79] J. Han, P. Abolghasem, D. Kang, B. J. Bijlani, and A. S. Helmy, “Difference-frequency generation in AlGaAs Bragg reflection waveguides,” *Opt. Lett.*, vol. 35, no. 14, pp. 2334–2336, 2010.

[80] K. Dolgaleva, W. C. Ng, L. Qian, J. S. Aitchison, M. C. Camasta, and M. Sorel, “Broadband self-phase modulation, cross-phase modulation, and four-wave mixing in 9-mm-long AlGaAs waveguides.,” *Opt. Lett.*, vol. 35, no. 24, pp. 4093–4095, 2010.

[81] D. Duchesne *et al.*, “Nonlinear photonics in AlGaAs photonics nanowires: Self phase and cross phase modulation,” *Conf. Proc. Int. Symp. Signals, Syst. Electron.*, pp. 475–478, 2007.

[82] W. Astar, P. Apiratikul, T. E. Murphy, S. Member, and G. M. Carter, “Wavelength conversion of 10-Gb/s RZ-OOK using filtered XPM in a passive GaAs–AlGaAs waveguide,” *IEEE Photonics Technol. Lett.*, vol. 22, no. 9, pp. 637–639, 2010.

[83] B. M. Cannon *et al.*, “All-optical amplitude-phase transmultiplexing of RZ-OOK and RZ-BPSK to RZ-QPSK by polarization-insensitive XPM using a nonlinear birefringent AlGaAs waveguide,” *Opt. Express*, vol. 21, no. 17, pp. 19885–19899, 2013.

[84] K. Dolgaleva *et al.*, “Tuneable four-wave mixing in AlGaAs nanowires,” *Opt. Express*, vol. 23, no. 17, pp. 22477–22493, 2015.

[85] T. Mahmood *et al.*, “Polarization-insensitive wavelength conversion by FWM of 100-GHz-spaced DWDM 4×10 Gbs RZ-BPSK signals in a birefringent nonlinear AlGaAs waveguide,” *IEEE J. Quantum Electron.*, vol. 50, no. 2, pp. 74–84, 2014.

[86] P. Apiratikul *et al.*, “Enhanced continuous-wave four-wave mixing efficiency in nonlinear AlGaAs waveguides,” *Opt. Express*, vol. 22, no. 22, p. 26814, 2014.

[87] J. J. Wathen *et al.*, “Efficient continuous-wave four-wave mixing and self-phase modulation in a bandgap-engineered AlGaAs waveguide,” *Lasers Electro-Optics (CLEO), 2012 Conf. on. IEEE*, pp. 1–2, 2012.

[88] J. J. Wathen, P. Apiratikul, C. J. K. Richardson, G. a Porkolab, G. M. Carter, and T. E. Murphy, “Efficient continuous-wave four-wave mixing in bandgap-engineered AlGaAs waveguides,” *Opt. Lett.*, vol. 39, no. 11, pp. 3161–4, 2014.

[89] J. Meier, W. S. Mohammed, A. Jugessur, L. Qian, M. Mojahedi, and J. S. Aitchison, “Group velocity inversion in AlGaAs nanowires,” *Opt. Express*, vol. 15, no. 20, pp. 12755–12762, 2007.

[90] R. El-Ganainy, S. Mokhov, K. G. Makris, D. N. Christodoulides, G. I. Stegeman, and R. Morandotti, “Solitons in dispersion-inverted AlGaAs nanowires,” *Conf. Lasers Electro-Optics 2006 Quantum Electron. Laser Sci. Conf. CLEO/QELS 2006*, vol. 14, no. 6, pp. 2277–2282, 2006.

[91] P. Sumithra and D. Thiripurasundari, “Review on Computational Electromagnetics,” *Adv. Electromagn.*, vol. 6, no. 1, pp. 42–55, 2017.

[92] R. Courant, “Variational methods for the solution of problems of equilibrium and vibrations,” *Bull. Am. Math. Soc.*, vol. 49, no. 1, pp. 1–24, 1943.

[93] E. L. & G. T. G .Dhatt, *Finite element method*. John Wiley & Sons, 2012.

[94] O. C. Zienkiewicz and R. L. . Taylor, *The finite element method*. London: McGraw-hill, 1977.

[95] G. Strang & G. Fix, *An analysis of the finite element method*. Prentice-Hall, 1973.

[96] T. J. Hughes, *The finite element method: linear static and dynamic finite element analysis*. Courier Corporation, 2012.

[97] K. S. Yee, “Numerical solution of initial boundary value problems involving Maxwell’s equations in isotropic media,” *IEEE Trans. Antennas Propag.*, vol. 14, no. 3, pp. 302–307, 1966.

[98] A. Taflove, “Application of the Finite-Difference Time-Domain Method to Sinusoidal Steady-State Electromagnetic-Penetration Problems,” *IEEE Trans. Electromagn. Compat.*, vol. EMC-22, no. 3, pp. 191–202, 1980.

[99] G. Mur, “Absorbing boundary conditions for the finite-difference approximation of the time-domain electromagnetic-field equations,” *IEEE Trans. Electromagn. Compat.*, vol. EMC-23, no. 4, pp. 377–382, 1981.

[100] D. H. Choi and W. J. Hoefer, “The finite-difference-time-domain method and its application to eigenvalue problems,” *IEEE Trans. Microw. Theory Tech.*, vol. 34, no. 12, pp. 1464–1470, 1986.

[101] R. B. S. & M. S. R. Luebbers, F. P. Hunsberger, K. S. Kunz, “A frequency-dependent finite-difference time-domain formulation for dispersive materials,” *Electromagn. Compat. IEEE Trans.*, vol. 32, no. 3, pp. 222–227, 1990.

[102] R. M. Joseph, S. C. Hagness, and A. Taflove, “Direct time integration of Maxwell’s equations in linear dispersive media with absorption for scattering and propagation of femtosecond electromagnetic pulses,” *Opt. Lett.*, vol. 16, no. 18, p. 1412, 1991.

[103] K. T. and F. Ichiro, “A treatment by the FD-TD method of the dispersive characteristics associated with electronic polarization,” *Microw. Opt. Technol. Lett.*, vol. 3, no. 6, pp. 203–205, 1990.

[104] P. M. Goorjian and A. Taflove, “Direct time integration of Maxwell’s equations in nonlinear dispersive media for propagation and scattering of femtosecond electromagnetic solitons,” *Opt. Lett.*, vol. 17, no. 3, pp. 180–182, 1992.

[105] R. M. Joseph and A. Taflove, “Spatial soliton deflection mechanism indicated by FD-TD Maxwell’s equations modeling,” *IEEE Photonics Technol. Lett.*, vol. 6, no. 10, pp. 1251–1254, 1994.

[106] J.-P. Berenger, “A perfectly matched layer for the absorption of electromagnetic waves,” *J. Comput. Phys.*, vol. 114, no. 2, pp. 185–200, 1994.

[107] E. T. Thiele and A. Taflove, “Validation and Extension to Three Dimensions of the Berenger PML Absorbing Boundary Condition for FD-TD Meshes,” *IEEE Microw. Guid. Wave Lett.*, vol. 4, no. 8, pp. 268–270, 1994.

[108] C. L. Xu, W. P. Huang, S. K. Chaudhuri, and J. Chrostowski, “A full-vectorial beam propagation method for anisotropic waveguides,” *J. Light. Technol.*, vol. 12, no. 11, pp. 1926–1931, 1994.

[109] N. Kumar Das, Y. Yamayoshi, and H. Kawaguchi, “Analysis of basic four-wave mixing characteristics in a semiconductor optical amplifier by the finite-difference beam propagation method,” *IEEE J. Quantum Electron.*, vol. 36, no. 10, pp. 1184–1192, 2000.

[110] K. Saitoh, M. Koshiba, and S. Member, “Full-vectorial imaginary-distance beam propagation method based on a finite element scheme: application to photonic crystal fibers,” *IEEE J. Quantum Electron.*, vol. 38, no. 7, pp. 927–933, 2002.

[111] H. DeVoe, “Optical properties of molecular aggregates. I. Classical model of electronic absorption and refraction,” *J. Chem. Phys.*, vol. 41, no. 2, p. 393, 1964.

[112] E. M. . Purcell and C. R. . Pennypacker, “Scattering and absorption of light by nonspherical dielectric grains,” *Astrophys. J.*, vol. 186, p. 705, 1973.

[113] George H. Goedecke and Sean G. O’Brien, “Scattering by irregular inhomogeneous particles via the digitized Green’s function algorithm,” *Appl. Opt.*, vol. 27, no. 12, pp. 2431–2438, 1988.

[114] M. a. Yurkin and A. G. Hoekstra, “The discrete dipole approximation: An overview and recent developments,” *J. Quant. Spectrosc. Radiat. Transf.*, vol. 106, no. 1–3, pp. 558–589, 2007.

[115] B. T. Draine and P. J. Flatau, “User guide for the discrete dipole approximation code DDSCAT 7.3,” *arXiv Prepr. arXiv1305.6497*, 2013.

[116] J. C. Lachat and J. O. Watson, “Effective numerical treatment of boundary integral equations: A formulation for three-dimensional elastostatics,” *Int. J. Numer. Methods Eng.*, vol. 10, no. 5, pp. 991–1005, 1976.

[117] A. H. D. Cheng and D. T. Cheng, “Heritage and early history of the boundary element method,” *Eng. Anal. Bound. Elem.*, vol. 29, no. 3, pp. 268–302, 2005.

[118] E. D. Caballero, H. Esteban, U. P. De Valencia, A. Belenguer, and D. I. Electrica, “On the analysis of radiation losses in substrate integrated waveguide using mode-matching and method of moments,” *Microw. Conf.*, pp. 398–401, 2014.

[119] G. Apaydin and L. Sevgi, “Method of Moments (MoM) modeling of wave propagation inside a wedge waveguide,” *Appl. Comput. Electromagn. Soc. J.*, vol. 29, no. 8, 2014.

[120] G. Karagounis, D. De Zutter, and D. Vande Ginste, “Full-wave simulation of optical waveguides via truncation in the method of moments using PML absorbing boundary conditions,” *Opt. Express*, vol. 24, no. 25, p. 28326, 2016.

[121] K. M. Fujisawa T, “Finite-element mode-solver for nonlinear periodic optical waveguides and its application to photonic crystal circuits,” *J. Light. Technol.*, vol. 23, no. 1, p. 382, 2005.

[122] P. C. Circuits, T. Fujisawa, and M. Koshiba, “Finite-element mode-solver for nonlinear periodic optical waveguides and its application to photonic crystal circuits,” *J. Light. Technol.*, vol. 23, no. 1, pp. 382–387, 2005.

[123] H. P. Uranus and H. J. W. M. Hoekstra, “Modelling of microstructured waveguides using a finite-element-based vectorial mode solver with transparent boundary conditions,” *Opt. Express*, vol. 12, no. 12, pp. 2795–2809, 2004.

[124] P. Pintus, “Accurate vectorial finite element mode solver for magneto-optic and anisotropic waveguides,” *Opt. Express*, vol. 22, no. 13, pp. 15737–15756, 2014.

[125] Chiang Y C, Chiou Y P, Chang H C, “Improved full-vectorial finite-difference mode solver for optical waveguides with step-index profiles,” *J. Light. Technol.*, vol. 20, no. 8, p. 1609, 2002.

[126] J. Xiao, H. Ni, and X. Sun, “Full-vector mode solver for bending waveguides based on the finite-difference frequency- domain method in cylindrical coordinate systems,” *Opt. Lett.*, vol. 33, no. 16, pp. 1848–1850, 2008.

[127] R. Courant, K. Friedrichs, and H. Lewy, “On the partial difference equations of mathematical physics,” *IBM J. Res. Dev.*, vol. 11, no. 2, pp. 215–234, 1967.

[128] R. Luebbers and K. Kunz, “FDTD calculation of scattering from frequency-dependent materials,” *IEEE Trans. Antennas Propag.*, vol. 41, no. 9, pp. 1249–1257, 1993.

[129] J.-P. Berenger, “Perfectly matched layer for the FDTD solution of wave-structure interaction problems,” *IEEE Trans. Antennas Propag.*, vol. 44, no. 1, pp. 110–117, 1996.

[130] J.-P. Berenger, “Three-dimensional perfectly matched layer for the absorption of electromagnetic waves,” *J. Comput. Phys.*, vol. 127, no. 2, pp. 363–379, 1996.

[131] J.-P. Berenger, “A perfectly matched layer for the absorption of electromagnetic waves,” *J. Comput. Phys.*, vol. 114, no. 2, pp. 185–200, 1994.

[132] S. D. Gedney, “An anisotropie perfectly matched layer-absorbing medium for the truncation of FDTD lattices,” *IEEE Trans. Antennas Propag.*, vol. 44, no. 12, pp. 1630–1639, 1996.

[133] I. Transactions and O. N. Antennas, “Evanescent Waves in PML’s Origin of the Numerical Reflection in. Wave-Structure Interaction Problems,” *IEEE Trans. Antennas Propag.*, vol. 47, no. 10, pp. 1497–1503, 1999.

[134] J. A. Roden and S. D. Gedney, “Convolution PML (CPML): An efficient FDTD implementation of the CFS-PML for arbitrary media,” *Microw. Opt. Technol. Lett.*, vol. 27, no. 5, pp. 334–339, 2000.

[135] M. Kuzuoglu and R. Mittra, “Frequency dependence of the constitutive parameters of causal perfectly matched anisotropie absorbers,” *IEEE Microw. Guid. Wave Lett.*, vol. 6, no. 12, pp. 447–449, 1996.

[136] W. C. Chew and W. H. Weedon, “A 3D perfectly matched medium from modified maxwell’s equations with stretched coordinates,” *Microw. Opt. Technol. Lett.*, vol. 7, no. 13, pp. 599–604, 1994.

[137] R. J. Luebbers, “FDTD for Nth-order dispersive media,” *Antennas Propagation, IEEE …*, vol. 40, no. 11, pp. 1297–1301, 1992.

[138] V. D. AZ Elsherbeni, *The finite-difference time-domain method for electromagnetics with MATLAB simulations*. The Institution of Engineering and Technology, 2016.

[139] R.M.Hill and L.A.Dissado, “Debye and non-Debye relaxation,” *J. Phys. C Solid State Phys.*, vol. 18, no. 19, pp. 3829–3836, 1985.

[140] D. F. Kelley and R. J. Luebbers, “Piecewise linear recursive convolution for dispersive media using FDTD,” *Antennas Propagation, IEEE Trans.*, vol. 44, no. 6, pp. 792–797, 1996.

[141] G. S. He, *Nonlinear optics and photonics*. OUP Oxford, 2014.

[142] R.W.Hellwarth, “Third-order optical susceptibilities of liquids and solids,” *Prog. Quantum Electron.*, vol. 5, pp. 1–68, 1977.

[143] R. Singh, “CV Raman and the discovery of the Raman effect,” *Phys. Perspect.*, vol. 4, no. 4, pp. 399–420, 2002.

[144] P. Weinberger, “John Kerr and his effects found in 1877 and 1878,” *Philos. Mag. Lett.*, vol. 88, no. 12, pp. 897–907, 2008.

[145] John Kerr, “XL. A new relation between electricity and light: Dielectrified media birefringent,” *Philos. Mag.*, vol. 50, no. 332, pp. 337–348, 1875.

[146] A. B. Fallahkhair, S. Member, K. S. Li, T. E. Murphy, and S. Member, “Vector finite difference modesolver for anisotropic dielectric waveguides,” *J. Light. Technol.*, vol. 26, no. 11, pp. 1423–1431, 2008.

[147] A. Taflove and S. C. Hagness, “Computational Electrodynamics: The Finite-Difference Time-Domain Method, Third Edition,” *Artech House*. p. 1038, 2005.

[148] R. Paschotta, *Encyclopedia of laser physics and technology*. Berlin: Wiley-vch, 2008.

[149] C. Lacava, V. Pusino, P. Minzioni, M. Sorel, and I. Cristiani, “Nonlinear properties of AlGaAs waveguides in continuous wave operation regime,” *Opt. Express*, vol. 22, no. 5, pp. 5291–5298, 2014.

[150] C. (Ed. . Rulliere, *Femtosecond Laser Pulses: Principles and Experiments*. 2005.

[151] T. Skauli *et al.*, “Improved dispersion relations for GaAs and applications to nonlinear optics Improved dispersion relations for GaAs and applications to nonlinear optics,” *J. Appl. Phys.*, vol. 94, no. 10, pp. 6447–6455, 2003.

[152] C. Lacava, V. Pusino, P. Minzioni, M. Sorel, and I. Cristiani, “Nonlinear properties of AlGaAs waveguides in continuous wave operation regime,” *Opt. Express*, vol. 22, no. 5, pp. 5291–5298, 2014.

[153] D. J. Lockwood, G. Yu, and N. L. Rowell, “Optical phonon frequencies and damping in AlAs , GaP , GaAs , InP , InAs and InSb studied by oblique incidence infrared spectroscopy,” *Solid State Commun.*, vol. 136, no. 7, pp. 404–409, 2005.

[154] Y. Kao, M. N. Islam, J. M. Saylor, F. L. E. Slusher, and W. S. Hobson, “Raman effect in AlGaAs waveguides for subpicosecond pulses,” *J. Appl. Phys.*, vol. 78, no. 4, pp. 2198–2203, 1995.

[155] H. Fukuda *et al.*, “Four-wave mixing in silicon wire waveguides,” *Opt. Express*, vol. 13, no. 12, p. 4629, 2005.

[156] D. T. Piercet and W. E. Spicer, “Electronic structure of amorphous Si from photoemission and optical studies,” *Phys. Rev. B*, vol. 5, no. 8, pp. 3017–3029, 1972.

[157] N. Bahlmann, O. Zhuromskyy, M. Hammer, L. Wilkens, R. Gerhardt, and P. Hertel, “Applications of magneto-optical waveguides in integrated optics,” *JOSA B*, vol. 22, no. 1, pp. 240–253, 2005.